

Low Reynolds Number Swimming In Complex Environments

A thesis presented for the degree of
Doctor of Philosophy of Imperial College London
and the
Diploma of Imperial College
by

Ophir Samson

Department of Mathematics
Imperial College
180 Queen's Gate, London SW7 2BZ

JUNE 23, 2010

I certify that this thesis, and the research to which it refers, are the product of my own work, and that any ideas or quotations from the work of other people, published or otherwise, are fully acknowledged in accordance with the standard referencing practices of the discipline.

Signed:

Copyright

Copyright in text of this thesis rests with the Author. Copies (by any process) either in full, or of extracts, may be made **only** in accordance with instructions given by the Author and lodged in the doctorate thesis archive of the college central library. Details may be obtained from the Librarian. This page must form part of any such copies made. Further copies (by any process) of copies made in accordance with such instructions may not be made without the permission (in writing) of the Author.

The ownership of any intellectual property rights which may be described in this thesis is vested in Imperial College, subject to any prior agreement to the contrary, and may not be made available for use by third parties without the written permission of the University, which will prescribe the terms and conditions of any such agreement. Further information on the conditions under which disclosures and exploitation may take place is available from the Imperial College registry.

“A poet once said, “The whole universe is in a glass of wine.” We will probably never know in what sense he meant that, for poets do not write to be understood. But it is true that if we look at a glass of wine closely enough we see the entire universe.

“There are the things of physics: the twisting liquid which evaporates depending on the wind and weather, the reflections in the glass, and our imagination adds the atoms. The glass is a distillation of the Earth’s rocks, and in its composition we see the secrets of the universe’s age, and the evolution of stars. What strange arrays of chemicals are in the wine? How did they come to be? There are the ferments, the enzymes, the substrates, and the products. There in wine is found the great generalization: all life is fermentation. Nobody can discover the chemistry of wine without discovering, as did Louis Pasteur, the cause of much disease. How vivid is the claret, pressing its existence into the consciousness that watches it!

“If our small minds, for some convenience, divide this glass of wine, this universe, into parts - physics, biology, geology, astronomy, psychology, and so on - remember that Nature does not know it! So let us put it all back together, not forgetting ultimately what it is for. Let it give us one more final pleasure: drink it and forget it all!”

Richard P. Feynman

To my parents, Smadar and Ilan.

Abstract

The study of swimming micro-organisms has been of interest not just to biologists, but also to fluid dynamicists for over a century. As they are rarely in isolation, much interest has been focused on the study of the swimmers' interaction with their environment. By virtue of the typically small sizes of these organisms and their swimming protocols, the characteristic Reynolds number of the motion of the fluid around them is small. Hence they reside in a Stokes flow regime where viscous forces dominate inertial effects and where far-field interactions (e.g. with nearby walls) can have a significant effect on the swimmer's dynamical evolution.

This thesis provides a detailed investigation of idealised models of low Reynolds number swimmers in a variety of wall-bounded fluid domains. Our approach employs a combination of analytical and numerical techniques.

A simple two-dimensional point singularity is used to model a swimmer. We first study its dynamics when placed in the half-plane above an infinite no-slip wall and find it to be in qualitative agreement with numerical and experimental studies. The success of the model in this case encourages its use to study the swimmer's dynamics in more complicated domains. Specifically, we next explore the dynamics of the same swimmer above an infinite straight wall with a single gap, or orifice. Using techniques of complex analysis and conformal mapping theory, a dynamical system governing the swimmer's motion is explicitly derived. This analysis is then extended to the case in which the swimmer evolves near an infinite straight wall with two gaps.

We are also interested in how the presence of background flows can affect the swimmer's dynamics in these confined geometries. We therefore employ the same techniques of complex analysis and conformal mappings to find analytical expressions for pressure-driven flows near a wall with either one or two gaps. We then extend this to find new solutions for the shear flows and stagnation point flows in the same geometry. The effect of a background shear flow on the swimmer's dynamics is then explored.

Finally, while there have been a number of studies of Stokes flows within domains which are simply connected, the doubly connected analogues are rather rare. By building upon the analytical techniques presented in this thesis, we present numerical solutions to such problems, including that of the Weis-Fogh mechanism in the low Reynolds number regime.

Acknowledgements

Mathematics is a social subject and I am deeply indebted to the academic and nurturing support of those around me. I would therefore like to take this opportunity to show my profound appreciation for the people who have been key to ensuring the past few years have been happy ones.

Firstly, I am sincerely grateful for the help and guidance from my supervisor, Darren Crowdy. It has been inspiring to be in the presence of such a talented mathematician and teacher. The rigour and precision that he has taught me has cast an impression that extends into areas of my life far beyond those of equations and graphs. I would also like to thank John Gibbons for his continuing support and useful discussion throughout the programme. I am also grateful to the Massachusetts Institute of Technology for their kind hospitality and, in particular, to John Bush, Anette (“Peko”) Hosoi, Thomas Peacock and Roman Stocker for making me feel so welcome there.

There are many other friends who have been hugely generous with their time and support throughout the past few years. In particular, I would like to express my deepest gratitude to (in alphabetical order): Alex (Stormont); Aliko (Chis-er-wick); Andréa (Lobsters); Anna (La Llave); Anto (Athens); Arek (Lymington); Chris (Études-Tableaux); Danya (Lemongrass); Ed (Christmas); Hai-Yen (mince-pies); Joe (Rhythm Enterprises); Ksenia (post-it); Lara (Tropicoco); Laura (Bruins); Marilyn (Shabbat); Martina (teeth); Mike (risotto); Owen (620); Sumayya (James) and Sungyon (Pfft). The individual experiences I have shared with each has defined me and I look forward to a future with many more.

Ophir Samson

Table of contents

Abstract	6
1 An introduction to swimming in low Reynolds numbers.	19
2 Application of singularity theory to low Reynolds number swimming.	26
2.1 Complex variable methods in Stokes flows.	26
2.1.1 Representation of field variables using Goursat functions.	28
2.2 Singularity model for swimmers.	31
2.2.1 Modelling swimmers using Goursat singularities.	32
2.2.2 The Crowdy and Or point singularity model [1].	34
2.3 A swimmer above an infinite wall in the presence of a background shear flow.	40
2.4 Summary	41
3 Stokes flows past a gap in a wall.	44
3.1 Introduction	44
3.2 Stokes flow near the end of a plate.	49
3.3 Shear flow past a wall with a gap.	50
3.3.1 Mathematical formulation	50
3.3.2 Conformal mapping: a wall with a single gap.	51
3.3.3 Determining $\hat{F}(\zeta)$ and $\hat{G}(\zeta)$ from the no-slip boundary condition.	54
3.3.4 Comparison to Smith's solution [2].	56
3.4 Stagnation point flow past a wall with a gap.	61
3.4.1 Mathematical formulation	61
3.4.2 Determining $\hat{F}(\zeta)$ and $\hat{G}(\zeta)$ from the no-slip boundary condition.	63
3.4.3 Results: streamlines of stagnation point flow near a wall with a gap.	65
3.4.4 Comparison to Ko and Jeong's solution [3].	67
3.5 Summary	70
4 Swimming in low Reynolds numbers near a wall with a gap.	72
4.1 Introduction	72
4.1.1 The point swimmer model.	73
4.2 Swimming near a gap in a wall.	74

4.2.1	Mathematical formulation.	74
4.2.2	The Goursat functions for a swimmer near a wall with a gap.	75
4.2.3	Determining $\hat{F}(\zeta)$ and $\hat{G}(\zeta)$ from the no-slip boundary condition.	76
4.2.4	Equations of motion.	81
4.3	Dynamics of a swimmer near an orifice.	82
4.3.1	Deflection from the wall.	83
4.3.2	Jumping over the gap.	83
4.3.3	Rebounding from the gap.	84
4.3.4	Trapping near the gap: equilibrium points.	85
4.3.5	Escaping the gap region.	89
4.4	Bifurcation analysis in the parameter ϵ	89
4.5	Background shear effects on a swimmer near a wall with a gap.	92
4.6	Summary	97
5	Stokes flows past a wall with two gaps.	103
5.1	Introduction	103
5.2	The force on a central plate in a Stokes flow.	105
5.3	Conformal mapping: a wall with two gaps.	105
5.4	Shear flows past a wall with two gaps.	110
5.4.1	Limit of diminishing central plate length: comparison to Smith [2].	114
5.4.2	Results: shear flow past a wall with two gaps.	116
5.5	Stagnation point flow past a wall with two gaps.	116
5.5.1	Limit of diminishing central plate length: comparison to Ko and Jeong [3].	121
5.5.2	Results: stagnation point flow past a wall with two gaps.	122
5.6	Summary	127
6	Swimming in low Reynolds numbers near a wall with two gaps.	129
6.1	Introduction	129
6.2	Conformal mapping: the symmetric double gap.	130
6.3	Swimming near two gaps.	131
6.3.1	The Goursat functions for swimming near a wall with two gaps.	131
6.3.2	Determining the Goursat functions from the no-slip boundary condition.	132
6.3.3	The form of $\hat{F}(\zeta)$ and $\hat{G}(\zeta)$	133
6.3.4	Determining the constants of $\hat{F}(\zeta)$	135
6.3.5	The blocking effect.	137
6.4	Dynamical system of a swimmer near a wall with two gaps.	138
6.4.1	Stationary points and their linear stability.	139
6.4.2	Varying the parameter ϵ with fixed gap separation.	139
6.4.3	Varying gap separation with fixed ϵ	146
6.5	Summary	153

7	Numerical solutions to Stokes flows in complex geometries.	155
7.1	Introduction	155
7.2	Slow viscous shear flow past a cylinder above a wall.	156
7.2.1	Conformal map: a cylinder above a plane.	157
7.2.2	Constructing the Goursat functions.	158
7.2.3	The no-slip boundary conditions.	159
7.2.4	Numerical procedure	161
7.2.5	Results: shear flow past a cylinder above a wall.	162
7.3	Shear flow past a finite perpendicular plate above a wall.	165
7.3.1	Conformal mapping: finite plate above a wall	167
7.3.2	Constructing the Goursat functions	169
7.3.3	The no-slip boundary conditions	170
7.3.4	Results: shear flow past a finite plate above a wall.	171
7.3.5	Limiting case: diminishing gap width.	173
7.4	Shear flow past a finite inclined plate above a wall.	177
7.5	The Weis-Fogh mechanism: the low Reynolds number limit	181
7.6	Summary	190
8	Conclusions and future work.	192
A	Analysis of single gap conformal map.	196
B	Analysis of double gap conformal map.	199
C	Derivation of conformal map for a cylinder above a plane.	201
	References	209

List of Figures

2.1	Dynamics for $\epsilon = 0$ for different initial orientations. When $\theta(0) = 0$, the swimmer moves directly down and crashes into the wall.	38
2.2	Three examples of bouncing orbit trajectories for a treadmilling swimmer with $\epsilon = 0.2$. Here, $z_d(0) = i, \theta(0) = -2\pi/5$ (black, dashed), $z_d(0) = 0.8i, \theta(0) = -\pi/3$ (black, dotted) and $z_d(0) = 0.6i, \theta(0) = -\pi/5$ (blue, solid).	39
2.3	Phase space portrait in (θ, y) space as given by equation (2.45) for a treadmilling swimmer with $\epsilon = 0.2$ [4].	40
2.4	Trajectories of swimmer (with $\epsilon = 0.2, z_d(0) = 0.4i, \theta(0) = 0.7\pi$) in the presence of a background shear flow of varying strength: $\gamma = 0$ (Black, solid), $\gamma = 0.15$ (Blue, dashed), $\gamma = 0.4$ (black, dash-dot) and $\gamma = 0.6$ (blue, dash-dot).	42
2.5	Trajectories of a swimmer (with $\epsilon = 0.2, z_d(0) = 0.55i, \theta(0) = 4\pi/5$) in the presence of a background shear flow of varying strength: $\gamma = 0.5$ (Black, solid) and also $\gamma = 0.75$ (Red, dash). We see that the combined effect of the shear with the image singularity interaction gives rise to “spiralling” orbits.	43
2.6	Trajectories of the swimmer ($\epsilon = 0.05$) in the presence of a strong background shear flow ($\gamma = 8.5$) at different heights (bottom to top): $\text{Im}[z_d(0)] = 0.2, 0.4, 0.6, 0.8, 1$	43
3.1	Streamlines for a stagnation point flow. If the flow was unbounded, there would be a natural stagnation point at the origin (hence the name of the flow). This is equivalent to a linear straining flow.	47
3.2	Conformal mapping from the interior of the unit disk (in the ζ -plane) to the exterior of an infinite horizontal wall with a gap between $x = \pm 1$ (in the fluid z -plane).	52
3.3	Streamlines of shear flow past a single gap. The fluid in the lower half plane is only driven by the shear flow in the upper half plane and hence, if there was no gap, it would remain stationary.	57

3.4	Streamlines for a flow through a gap driven only by a downwardly directed pressure gradient. Here $\Delta P = 1$ and $k = 0$ so that there is no stagnation point flow. This corresponds to $N = \infty$, as defined by Ko and Joeng [3].	66
3.5	Streamlines for a stagnation point flow above a gap with no added pressure gradient and so $\Delta P = N = 0$ with $k = 1$. A single saddle stagnation point appears at the origin while two viscous eddies, both extending to infinity, are formed symmetrically in the lower half plane below the gap and the wall.	66
3.6	Streamlines when the added pressure gradient is in the same direction as the stagnation point flow. Here $k = \Delta P = 1$, and the fluid is pushed through the gap. There are no viscous eddies formed.	67
3.7	Streamlines when the added pressure gradient is in the opposite direction to the stagnation point flow. Here $\Delta P = N = -0.5$ with $k = 1$. There is one saddle stagnation point appearing above the gap while two viscous eddies formed underneath the edges of the plates and above the streamline which separates from the edge.	68
3.8	Streamlines for $k = 1$ and $\Delta P = 0.07$. The effect of the added (slight) downward directed pressure gradient is to reduce the size of the symmetric viscous eddies, visualised in Figure 3.5.	68
4.1	The two sheets of the Riemann surface associated with the conformal map (4.6). The upper sheet corresponds to the “physical” fluid domain, in which the swimmer resides. The lower sheet is the non-physical sheet, in which swimmer’s image will remain. In the analysis, the two sheets are glued together along the branch cuts taken as the walls: here the sheets are shown “unglued” along the walls to indicate that the image singularity is at the swimmer’s reflection in the wall on the lower sheet.	77
4.2	A swimmer moving away from a gap (positioned at $x = \pm 1$) above a wall, with $z_d(0) = -3 + 0.3i$, $\epsilon = 0.2$ and has initial orientation $\theta(0) = 0.24$. The swimmer is placed away from the gap and is initially oriented away from it. As the effect of the gap is small, the swimmer’s trajectory is reminiscent of the bouncing orbits exhibited by Crowdy and Or [1].	84
4.3	Two swimmers starting at $z_d(0) = \pm 5 + i$, both initially directed downwards with $\theta(0) = \pi/2$. The presence of the gap “breaks” the symmetry and the swimmer results in moving away from the gap. It then continues along the a bouncing orbit in the respective direction.	85
4.4	The gap provides a “switching mechanism” from one bouncing periodic orbit to another. The dynamics near the gap region are shown. Upper right figure: The orbit switches to a trajectory which is close to the steadily translating state found in [16]. Bottom right figure: The approaching and departing orbits (before and after the gap, respectively) are almost identical. Clockwise from top left $\theta(0) = 0.15\pi, 0.25\pi, 0.3\pi, 0.1\pi$ with initial positions $z_d(0) = 6.8 + i, 8 + 0.21i, 5 + 0.3i, 10.5 + 0.6i$	86

- 4.5 The gap may act to repel the swimmer, sending it back in the direction from which it came from. Here, we have $\theta(0) = 0.1\pi$ with initial condition $z_d(0) = 3.4 + 0.5i$ 87
- 4.6 For some choices of initial conditions, the swimmer may become trapped in the gap region. The swimmers spiral into one of, at most, four attracting points. Clockwise from top left to bottom left, we have: $\theta(0) = 0.3, 0.25\pi, 0.05\pi, 0.75$ with initial positions $z_d(0) = 3.6 + 0.8i, 10.2 + i, 0.6i, 0.6i$ 88
- 4.7 The swimmer may also escape the gap region to take a bouncing orbit on either side of the gap and wall. The two trajectories on the left correspond to $\theta(0) = 0.05$ with $z_d(0) = 0.1 + 0.5i, 0.5i$ (above and below the wall, respectively) while the two on the right correspond to $\theta(0) = \pm 0.05$ with $z_d(0) = -0.1 + 0.5i, 0.5i$ (also, above and below, respectively). Note the sensitivity of the swimmer's ultimate path on its initial conditions; all starting configurations are very close to each other here. 89
- 4.8 Stationary point locations before (upper figure) and after (lower figure) the Hopf bifurcation when $\epsilon = \epsilon_H^{(1)} = 0.3584$. As ϵ passes through this value, the two stable spirals become unstable spirals surrounded by fixed periodic orbits. Only the points in the upper half plane are displayed. 91
- 4.9 Growth of the periodic fixed orbits associated with two of the (unstable) stationary points in the upper half plane. When ϵ reaches the gluing bifurcation value ($\epsilon_g^{(1)} = 0.36895$), the two fixed orbits make contact on the imaginary axis, together with the saddle point (which was also on the imaginary axis for all $\epsilon < \epsilon_g^{(1)}$). The stationary points are shown for $\epsilon = \epsilon_g^{(1)}$ 92
- 4.10 Location of stationary points just after the gluing bifurcation ($\epsilon > \epsilon_g^{(1)}$). This shows the well defined "figure of eight" fixed orbit formed after the gluing of two separate periodic orbits. 93
- 4.11 Typical periodic orbits just after the ungluing bifurcation at $\epsilon = \epsilon_g^{(2)}$, when the single figure of eight periodic orbit has split into two separate orbits, each containing an unstable spiral around both fixed points. 94
- 4.12 Two projections of the periodic orbits for $\epsilon = \epsilon_g^{(1)-} = 0.3689$, just before the gluing bifurcations. These are visualised in three-dimensional space ($\text{Re}[z_d], \text{Im}[z_d], \theta$). 95
- 4.13 Two projections of the newly formed figure of eight orbits, just after the gluing bifurcation [73] where $\epsilon = \epsilon_g^{(1)+} = 0.369$. These are also shown in three-dimensional space ($\text{Re}[z_d], \text{Im}[z_d], \theta$). 96
- 4.14 The stability diagram for one of the complex eigenvalues σ associated with the stationary point in the first quadrant as ϵ is increased. There is also another complex conjugate eigenvalue and a negative real eigenvalue, both of which are not shown here. 97

4.15	The effect of increasing the strength of a background shear flow above the wall: without shear the swimmer proceeds along the same bouncing orbit towards one of the attracting points. Increasing the shear rate further leads to the swimmer eventually moving away from the gap in another periodic bouncing orbit.	98
4.16	Closed periodic orbit within the gap. Without any background shear, the swimmer moves towards one of the four stable spiral. As the shear flow is introduced and increased in strength, there exists a close periodic orbit in the gap's vicinity. This orbit is not symmetric about the real axis (which is to be expected, as there is a background shear flow only in the upper half plane). As the shear rate increases further the swimmer leaves the gap region and enters into a spiral orbit.	99
4.17	Closed periodic orbit in the gap when a uniform background shear (with $\gamma = 0.128$) flow is introduced symmetrically above and below the wall. The diamond-shaped orbit is now up-down symmetric.	100
5.1	Central plate length ($2r$) in the fluid domain as a function of ρ , the radius of the inner circle of the annulus in the ζ -plane.	106
5.2	Total horizontal force on the central plate for varying plate length, for an oncoming shear flow. There is no vertical force on this.	115
5.3	Typical streamlines for shear flow above a wall with two gaps, with varying central plate length of 0.3 (top), 1 (middle) and 1.9 (bottom). These may be qualitatively compared to Figures 1 and 2 in Smith [2].	117
5.4	Total vertical force on the central plate as a function of varying plate length, where the fluid is driven by a far field stagnation point flow of strength $k = 1$ (with $\mu = 1$) as well as an added pressure gradient with $\Delta P = 1$ in the downward direction. Due to the symmetry of the geometry together with that of the forcing flows, there is no horizontal force on the plate. . . .	121
5.5	Flow streamlines for $N = 1$ and central plate length = 0.3, 1, 1.9 (top to bottom). This corresponds to an additional (downward directed) pressure gradient. The effect of this pressure gradient is to incline the viscous eddies inwards beneath the central plate.	124
5.6	Flow streamlines for $N = 0.07$ and central plate length = 0.3, 1, 1.9 (top to bottom). In this case, $\Delta P = 0.07$ and hence there is almost no additional pressure gradient and the flow is predominantly driven by the far field stagnation point flow. In this case, the viscous (Moffatt-type) eddies are almost vertically oriented below the gaps.	125
5.7	Flow streamlines for $N = -0.5$ and central plate length = 0.3, 1, 1.9 (top to bottom). In this case, a pressure gradient is introduced in the upward direction, against the oncoming (downward) stagnation point flow. The effect of this is to orient the viscous eddies away from the central plate and beneath the sidewalls.	126

6.1	Here $\epsilon = 0.1$. The point C (and its corresponding reflections in the real and imaginary axes) are the only stable points.	141
6.2	Here $\epsilon = 0.115$. The points B and D, both of which are unstable points, are near to each other. They meet and cancel each other out when ϵ reaches the value of 0.1175. The point C is still the only stable point.	142
6.3	Two figure-of-eight fixed orbits when $\epsilon = 0.18 > \epsilon_h^{(1)}$. Each one is the projection on to the $(\text{Re}[z_d], \text{Im}[z_d])$ plane of the orbit which lies in the three-dimensional space (where the third axis corresponds to the swimmer's orientation, θ). Point F has emerged as a result of a saddle-node bifurcation.	142
6.4	Fixed orbit around the stagnation point C when $\epsilon = 0.18$. It does not cross itself. Projecting this onto the $(\text{Re}[z_d], \text{Im}[z_d])$ plane retrieves one of the figure-of-eight orbits drawn in Figure 6.3.	143
6.5	Eigenvalues, σ , for the linear stability of point C as ϵ is increased. When $\text{Re}[\sigma] < 0$, it is a stable spiral point while when $\text{Re}[\sigma] > 0$, the points become unstable.	144
6.6	A saddle point bifurcation: the points A, A_2 and A_3 all lie on the horizontal axes inside the gaps. Any swimmer placed inside a gap with initial orientation $\theta = \pi/2$ will only swim horizontally. Here we chart the horizontal swimming velocity as a function of its position as ϵ is increased. Both $\dot{\theta}$ and $\text{Im}[\dot{z}_d]$ are zero at all times and so a stagnation point is attained when the horizontal velocity is zero. We see that when ϵ approaches the value $\epsilon_m = 0.3183$, A and A_2 cancel each other out. This is an example of a saddle-node bifurcation.	145
6.7	The positions of the only remaining stationary points when $\epsilon > \epsilon_s = 0.4343$ (here $\epsilon = 0.5$), and all points are unstable. There are no more saddle-node bifurcations as ϵ increases further.	146
6.8	The stationary points around two widely separated gaps ($r_0 = 5$) with unit width. The stars highlight the stationary points which are stable while the crosses correspond to unstable stagnation points. ϵ is fixed at 0.1.	147
6.9	A close-up view of the stationary points in Figure 6.8 with $r_0 = 5$. Points C and D are stable spiral points, B is an unstable saddle point while the others are unstable points. Point E (not shown) is on the imaginary axis above the center of the plate and is an unstable point.	148
6.10	Stagnation points as the length of the central plate diminishes. Here we have $r_0 = 0.1 > r_h^{(1)}$ and the stagnation points have the same stability structure as those in Figure 6.8. The presence of the other gap, however, moves them off slightly off the "standard" positions, as seen in Figure 6.8.	149
6.11	Here $r_0 = 0.02 < r_h^{(1)}$, just before points B and D meet and cancel each other out during a saddle-node bifurcation. Here, the stability of point D has changed from a stable spiral to that of an unstable spiral.	150
6.12	Here $r_0 = 0.01$, just after points B and D have met.	150

6.13	As r_0 is decreased further to 2×10^{-5} , two new points are born on the imaginary axis. The upper stagnation point, E_3 is an unstable saddle point while the lower stationary point, E_2 is an unstable point.	151
6.14	Even when r_0 is exponentially small, the blocking effect (top figure) ensures that the flow is altered from the single gap counterpart, (bottom figure), where r_0 is exactly zero. The effect of the blocking effect is highlighted by the dotted circle.	152
7.1	Here the cylinder is far away from the no-slip wall and hence the wall's effect on the fluid around the cylinder is minimal. The cylinder is centered above the origin with height $\alpha = 2.7$ and $r = 0.4$. The streamlines are attracted slightly downwards towards the plane before and after the cylinder.	163
7.2	As the cylinder is brought downwards, the effect of the wall on the fluid around the cylinder becomes more evident. Here, $\alpha = 0.8$ and $r = 0.4$	164
7.3	Streamlines for when the ratio of gap width to cylinder radius is 0.935. Eddies have not formed yet.	165
7.4	Eddies begin to form as the cylinder is brought towards the plane. Here $\alpha = 0.5$ and $r = 0.4$	166
7.5	When the ratio of the gap width to cylinder radius is much less than the critical value of 0.865 (as found by Davis and O'Neill [54]) the eddies become fully formed. Here $\alpha = 0.43$ and $r = 0.4$	166
7.6	When the plate is far away from the wall, the streamlines behave similarly to when in a free space shear flow past a plate. Here $a = 2$ and $b = 3$	172
7.7	When the plate is brought further down, the effect of the wall becomes more evident and streamlines are pulled downwards towards it. Here $a = 1$ and $b = 2$, and so the plate is unit length.	172
7.8	The plate is of unit length and the gap width is 0.7. The effect of wall becomes even more pronounced as the plate is brought down further. The plate has unit length.	173
7.9	Eddies begin to form as the plate becomes close to the wall. Here, the gap width is 0.5 and the plate's length is 1.5.	174
7.10	Here the gap between the plate and the plane is 0.3 and the plate's length is 1.8. The eddies become more pronounced as the plate is brought even further down towards the wall.	174
7.11	The plate length is 1.5 and the gap width is further reduced to 0.1. At this stage the separation of the streamlines create eddies which prevent the fluid from travelling through the small gap between the plate and the wall.	175
7.12	Force on the plate as a function of gap width (solid, blue). We see that as the width is reduced to zero, the force tends to the value of 5.817 (dashed, red) as predicted by Kim [5].	177
7.13	Schematic diagram of the shear flow past an inclined plate above a wall. The on-coming shear flow has strength $U = 1$	178

7.14	A plate, inclined at angle of $\pi/3$ from the horizontal is gradually brought downwards towards the no-slip wall. Here the gap has widths 0.26, 0.08 and 0.02 (top to bottom). As the gap becomes narrower, less fluid may pass through it and the resulting viscous eddies increase in size.	182
7.15	As the plate is made longer $L = 3$ and kept very close to the wall, with gap width 0.02 (and inclined with $\phi = \pi/3$), a secondary set of eddies appear in the immediate vicinity of the wedge, to the right of the plate.	183
7.16	Typical streamlines around a plate with varying inclination angle. In all cases, $r_0 = 0.2$ and $r_0 + L = 2$, and $\phi = \pi/10, \pi/5, 3\pi/5, 9\pi/10$ (top to bottom, respectively).	184
7.17	Schematic diagram for the spreading out phase of the Weis-Fogh mechanism. Both wings are separated by an angle $\phi(t)$ at their lowest point and move away from each other with relative speed $2U$	185
7.18	Typical streamlines around two wings during the “opening” phase of the Weis-Fogh mechanism. They rotate with angular velocity U until reaching a separation angle of $\phi = \pi/3$. Here they are pictured at separation angles $\phi = 0.2, \pi/9, \pi/6$ (top to bottom). The wings have unit length and their lower corners are at a distance of 0.1 away from each other (or 10% of the wing’s length).	188
7.19	Typical streamlines around two wings during the “spreading” phase. They are inclined with separation angle $\phi = \pi/3$ and move with speed $U = 1$ away from each other.	189

Chapter 1

An introduction to swimming in low Reynolds numbers.

The locomotion of small microorganisms has been of interest to fluid dynamicists and biologists for many years. While their motion occurs within fluids of non-negligible kinematic viscosity, they do so at very small length scales and speeds. The Reynolds number associated with these motions is therefore very small and so they reside in a world where inertial forces are negligible in comparison to the viscous effects of the fluid. For example, the Reynolds number associated with *Escherichia coli* (E. Coli) motion is approximately $\mathcal{O}(10^{-4})$ while that of a spermatozoan is roughly $\mathcal{O}(10^{-2})$.

As a consequence of this, any velocity perturbation on their boundary is diffused much more rapidly into the fluid relative to the speed at which the fluid particles are, themselves, carried by the flow. The fluid's response to the motion of the swimmer's body is therefore nearly instantaneous and so the rate of change of the swimmer's momentum is completely negligible in comparison to the typical magnitudes of the surrounding viscous forces. Because of this, the force and torque on the swimmer's body from the fluid is instantaneously balanced by the external forces and torques. However, in most cases there are no external forces and so the fluid exerts no force on the swimmer. Also, unless the swimmer is a nose or bottom-heavy cell (both cases we shall not consider), there will be no torque on the swimmer either.

Recently, a large amount of attention has been placed on understanding swimming dynamics in *unbounded* low Reynolds number flows [6, 7, 8]. This has been used to explain the methods which the swimmers adopt in order to propel themselves through the fluid. In reality, however, most organisms are typically in the vicinity of other bodies or boundaries, where the hydrodynamic interaction with these has a significant effect on their motion. Therefore, in order to gain a complete understanding of low Reynolds number swimming, one must also study the hydrodynamic interaction between swimmers and their boundaries.

The boundaries of the fluid may either take the form of a deformable interface between two different fluids [9, 10] or, alternatively, a solid boundary. On the former, fluid stress is continuous across the interface while the fluid remains stationary on the surface of the latter. Free surfaces generally move with the local fluid and so their positions are harder to control than a solid boundary (which may be fixed in place): it is because of this that we restrict our attention to how swimmers interact with solid surfaces.

There have been a number of recent investigations into how a swimming micro-organism interacts with solid surfaces. Lauga *et al.* [11] have shown that due to the hydrodynamic interaction with solid boundaries around them, *E. Coli* swim in a clockwise circular motion when placed near to a wall, while Cosson *et al.* [12] and Berke *et al.* [13] demonstrate how spermatozoa and *E. Coli* are attracted to solid boundaries that confine their domain. More recently, Drescher *et al.* [14] have presented some interesting steady states of circular *Volvox* algae when placed next to a wall, where pairs of cells “dance” around each other, while Zilman *et al.* [4] have studied the shear induced orbits of ocean larvae. Much theoretical work in this area has focused on quantifying the change in swimming speed and energetics near solid boundaries [15, 16, 17, 18].

In order to investigate the effects of solid boundaries on a low Reynolds number swimmer’s trajectory, a number of authors began by considering the interaction of such a swimmer with the simplest domain possible; that of a fluid bounded by an infinite flat wall. This wall is

referred to as a *no-slip boundary* due to the fact that any viscous fluid remains stationary on a solid surface, or moves with the surface's own velocity. Moreover, it is the swimmer's hydrodynamic interaction with this wall that may allow it to undertake an interesting swimming trajectory and so authors have devised experiments and theoretical models in order to study this interaction. In particular, it is a well known fact that swimmers in a low Reynolds number regime tend to be attracted towards no-slip surfaces [19, 20, 15, 21, 22, 13]. Berke *et al.* [13] investigated the hydrodynamics of *E. Coli* cells and their subsequent attraction to solid boundaries by placing a cell mixture in a density matched fluid between two parallel plates. Once the cells had been given time to settle, their distribution was photographed and recorded as a function of distance away from one of the plates, where it can be seen that there is an overall tendency for the cells to move towards one of the surfaces and then swim along it, in agreement with a previous experiment carried out by Rothschild [19].

To provide a physical explanation to these results, Berke *et al.* [13] model a single swimmer near a no-slip boundary as a force-free and torque-free prolate spheroid under a force dipole (a stresslet) model and find that the vertical component of the velocity is given by

$$u_y = -\frac{3p}{64\pi\eta y^2}(1 - 3\cos^2\theta) \quad (1.1)$$

where y is the distance from the wall in the normal direction, p is the dipole strength, η is the viscosity (either positive or negative corresponding to whether the swimmer is a "pusher" or "puller" [13]) and θ is the angle of the head's orientation, measured from the vertical.

When $\theta = \pi/2, 3\pi/2$, the swimmer is aligned with the wall and will swim parallel to it. The authors find that the evolution of this head angle is governed by

$$\frac{d\theta}{dt} = -\frac{3p \cos\theta \sin\theta}{64\pi\eta y^3} \left[1 + \frac{(\gamma^2 - 1)}{2(\gamma^2 + 1)}(1 + \cos^2\theta) \right] \quad (1.2)$$

where γ is the aspect ratio for the spheroid. In the case of a sphere, this parameter is equal to 1 and hence $d\theta/dt = -3p \cos\theta \sin\theta / (64\pi\eta y^3)$. While the authors did not perform the full

dynamical calculations, they were able to deduce that the swimmers will always reorient themselves with the boundary whatever their initial orientation is. While this simple model captures the general attraction of the swimmers to walls, it also predicts that they will crash into them in finite time, in contrast with experimental findings.

Or and Murray [23] have studied the dynamics of a fully three-dimensional swimmer when placed in such a geometry. The authors constructed a theoretical swimmer by connecting up to three rigid spheres using thin rods. This model was then submerged in a quiescent viscous fluid next to a long flat wall. The sphere's centers lie in the $x - y$ plane and all motion was constrained to that plane. Next, two (and sometimes three) of the spheres were made to rotate about an axis parallel to the z -axis in order to generate a motion.

The equations of motion imply that forces and torques on the sphere are linearly related to their linear and angular velocities via a mobility (or resistance) matrix. In the case of spherical particles near a planar wall, this matrix has been found by Swan and Brady [24]. While Or and Murray [23] do not compute this matrix exactly, they use scaling arguments to approximate it. In doing so, Or and Murray [23] show that in some cases the swimmer may take an interesting oscillating periodic orbit. Here, the swimmer moves towards the wall and, once it gets close to it, spends some time moving parallel to it. During this time spent in parallel motion, it reorients itself and then moves away from the wall again. This process is then repeated and is interpreted as a steady orbit within the solution space of the governing dynamics. In other cases, the swimmer will form "spiralling" motions along the wall. This is shown diagrammatically in Figure 2 of [23].

To verify this, the authors built a macro-scale version of this swimmer with up to three rotating spheres, and placed it in a viscous bath of fluid next to a wall [25]. The periodic orbits, predicted by their theory [23] can clearly be seen in their experiments. While this is a three-dimensional model, all the motion is coplanar and hence lends itself well to study in two dimensions.

Other authors have also studied the effect of an ambient background flow on the motion of

swimmers near planar walls. Zilman, Novak and Benayahu [4] construct a hydrodynamic model for the motion of marine larvae in the presence of a background linear shear flow near flat solid boundaries. By accounting for the flow vorticity and the swimmers' own method of self-propulsion, the authors find that if the swimmers are sufficiently close to the wall, they may undergo interesting spiralling trajectories, similar to those found by Or and Murray [23].

However, while Zilman *et al.* [4] take the wall as a reference point for the shear flow (where the shear velocity is zero), they do not take into account the hydrodynamic interaction that the swimmer has with the wall itself. Their results nevertheless give a qualitative insight into the trajectories when the shear rate is high and hence its effect plays a more dominant role in the swimmer's motion than the interaction with the wall.

There has also been much attention placed on the class of circular swimmers that do not change their shape but produce a purely tangential velocity field on their boundaries. This is often referred to as *treadmilling* [26] and is associated with the presence of cilia on the organism's body. Similar models have been used to capture the collective action of short cilia on the surface of motile cells such as *Opalina* and *Volvox* [27, 28]. Swimmers of these form were first considered by Blake [27] who demonstrated how a circular swimmer with an imposed tangential and normal velocity on its body can propel itself in an unbounded Stokes flow. The surface velocities, or surface waves, are viewed as an "envelope" (or a smooth approximation) to the motion of the tips of all the cilia on the body's surface [29, 30, 28]. The advantage of this model is that it ignores the added complication of shape variation and focuses only on the interaction with its environment. Blake [27] demonstrated that even a purely tangential velocity profile may produce a net displacement for the swimmer.

Since the Stokes equations are linear, the superposition of appropriately chosen singularities have also been used in order to solve for the flow and pressure around a swimming organism. In particular, Blake [27] used a distribution of Stokeslet singularities to model the collective action of cilia on the surface of a slender body. This model also demonstrated that a tangential velocity profile was much more effective at providing a propulsive force

than a normal velocity component.

This thesis is motivated by the study of swimmers which do not have any means to propel themselves through the fluid without the assistance of an external boundary. In other words, these organisms would not be able to move if they were placed in an unbounded fluid. Restricting the study to swimmers of this form will isolate the effect that solid surfaces have on low Reynolds number locomotion. Recently, Crowdy and Or [1] have proposed a singularity model for such swimmers when placed near a solid boundary. Their model, which will be discussed in chapter 2, was based on a circular treadmilling swimmer which had no means of self-propulsion. The authors then found the appropriate Stokes singularities that represented the flow field that this treadmiller created in the global fluid. By studying the interaction between these singularities and the no-slip wall, they were able to infer the dynamics of a low Reynolds number swimmer in the same geometry.

Blake and Chwang [31] has also used singularity models such as these to explain the motion of swimming microorganisms in the vicinity of flat walls. In general, the singularities themselves will not satisfy the no-slip condition on the boundary. Therefore, a superposition of those singularities together with their images is often necessary in order to satisfy the boundary conditions. This method is similar to that used in electrostatics where image charges may be placed throughout the domain in order to satisfy a constant-potential condition on a given surface. For example, in the case of a point charge above a flat wall, the boundary condition is satisfied by simply placing an equal and opposite charge at the point of reflection in the wall. Within the context of low Reynolds number swimming, the zero horizontal and vertical velocity requirements constitute two boundary conditions which the singularities must satisfy. Determining which singularities are appropriate may be more challenging and less straight-forward than within problems of electrostatics, whose boundary conditions are scalar. For example, in documenting various image systems in the vicinity of a no-slip boundary in a Stokes flow, Blake and Chwang [31] showed a Stokeslet generated not only an image Stokeslet, but also an image force dipole as well as a source dipole flow field.

In this thesis, we will adopt the singularity model proposed by Crowdy and Or [1] in order to represent a low Reynolds number swimmer. Using this singularity model within domains of geometric complexity will shed light on how a swimmer, such as the type modelled by Crowdy and Or [1], will behave in such surroundings. This thesis appears to be the first study to present a systematic and flexible approach to modelling low Reynolds number swimming in confined environments.

The thesis will be structured as follows: chapter 2 will begin with a general description of Stokes flows within the framework of complex variables and will then introduce, in greater detail, the Crowdy and Or [1] singularity model for a low Reynolds number swimmer. Our attention will then turn towards domains which are more complicated than those considered by Crowdy and Or [1] and Blake [27, 31]. In chapter 3, we introduce a new method using conformal mapping theory in order to retrieve, in a unified fashion, previously discovered exact solutions of Stokes flows past a wall with a gap. Chapter 4 will then extend this method in a natural way to incorporate the swimming model of Crowdy and Or [1]. This will enable us to write down the dynamical system of a low Reynolds number swimmer near a wall with a gap explicitly and categorise the different swimming trajectories which it may undertake. We will then add a further degree of complication to the fluid domain by introducing a second gap in the wall. Chapter 5 will then present exact solutions to various Stokes flow problems near these two gaps by using complex variable techniques in this doubly connected domain. In chapter 6, we extend these solutions by reintroducing the Crowdy and Or [1] singularity model in order to find the dynamical system which governs a swimmer's motion near a wall with two gaps explicitly. Finally, in contrast to the exact, analytical solutions we present in the previous chapters, chapter 7 will discuss various numerical approaches to Stokes flows problems within multiply connected domains.

Chapter 2

Application of singularity theory to low Reynolds number swimming.

2.1 Complex variable methods in Stokes flows.

We begin our study of swimming near solid boundaries with a review of the complex variable formulation of two-dimensional Stokes flows. We shall use this formulation, as well as the models within, when solving similar problems throughout the thesis.

In the limit of zero Reynolds number, the Navier-Stokes equations reduce to

$$\begin{aligned}\nabla p(\mathbf{x}) &= \mu \nabla^2 \mathbf{u}(\mathbf{x}) \\ \nabla \cdot \mathbf{u}(\mathbf{x}) &= 0\end{aligned}\tag{2.1}$$

where \mathbf{u} is the velocity of the fluid at a point $\mathbf{x} \in \mathbb{R}^3$ and μ is the dynamic viscosity. These are the *Stokes equations* and are the governing equations of fluid mechanics in flow environments where either the kinematic viscosity of the fluid is very high, or the typical speed or length scale of the flow is very low. Taking the curl of equation (2.1) results in

$$\nabla \wedge \nabla p(\mathbf{x}) = \mu \nabla \wedge \nabla^2 \mathbf{u}(\mathbf{x}).\tag{2.2}$$

As the curl of a gradient field is zero (assuming that the pressure is a continuous function)

Chapter 2. Application of singularity theory to low Reynolds number swimming. 27

and after invoking the second equation of (2.1), the right hand side of this becomes

$$0 = \mu \nabla^2 (\nabla \wedge \mathbf{u}). \quad (2.3)$$

Defining the *vorticity field*, $\boldsymbol{\omega}(\mathbf{x})$, of a fluid as the curl of the velocity field, we arrive at the alternative form of the Stokes equation

$$0 = \nabla^2 \boldsymbol{\omega}(\mathbf{x}). \quad (2.4)$$

When the flow is purely two-dimensional, with $\mathbf{u} = (u, v)$ and $\mathbf{x} = (x, y)$, the vorticity is directed out of the plane and given by

$$\boldsymbol{\omega}(\mathbf{x}) = (0, 0, \omega(x, y)). \quad (2.5)$$

Next, as the velocity satisfies the second equation of (2.1), there exists a scalar function $\psi(x, y)$ such that $\mathbf{u} = \nabla \wedge (0, 0, \psi)$, or

$$(u, v) = \left(\frac{\partial \psi}{\partial y}, -\frac{\partial \psi}{\partial x} \right). \quad (2.6)$$

The function $\psi(x, y)$ is called the *stream function* and exists for all two-dimensional incompressible flows. Taking the curl of the velocity field gives

$$\boldsymbol{\omega}(x, y) = (0, 0, -\nabla^2 \psi(x, y)), \quad (2.7)$$

from which we see that the stream function satisfies

$$\nabla^2 \psi(x, y) = -\omega(x, y). \quad (2.8)$$

However, equation (2.4) revealed that the vorticity satisfies the Laplace equation and so, after taking the Laplacian of equation (2.8), we deduce that the stream function is governed by the biharmonic equation

$$\nabla^4 \psi(x, y) = 0. \quad (2.9)$$

We will now use a representation of the biharmonic operator using complex variables. Define the variable $z = x + iy$. Using this, we have that

$$\frac{\partial}{\partial z} = \frac{1}{2} \left(\frac{\partial}{\partial x} - i \frac{\partial}{\partial y} \right), \quad \frac{\partial}{\partial \bar{z}} = \frac{1}{2} \left(\frac{\partial}{\partial x} + i \frac{\partial}{\partial y} \right) \quad (2.10)$$

and so it is easy to show that the Laplace operator is given by

$$\nabla^2 = 4 \frac{\partial^2}{\partial z \partial \bar{z}} \quad (2.11)$$

with $\bar{z} = x - iy$ being the complex conjugate of z and hence the biharmonic equation is given by

$$0 = \frac{\partial^4 \psi}{\partial z^2 \partial \bar{z}^2}. \quad (2.12)$$

By integrating this equation four times, it can be shown to have the general solution

$$\psi(z, \bar{z}) = \text{Im}[\bar{z}f(z) + g(z)] \quad (2.13)$$

The functions $f(z)$ and $g(z)$ are called the *Goursat functions* and are analytic everywhere inside the fluid domain. This was shown by Muskhelishvili [32] in the context of elasticity problems where ψ was an Airy stress function. Richardson [33] demonstrated its usefulness for Stokes flow problems when considering the dynamics of two-dimensional bubbles in zero Reynolds number regimes. In order to solve a Stokes flow problem in two dimensions it is sufficient to determine $f(z)$ and $g(z)$, and these are usually found from the boundary conditions.

2.1.1 Representation of field variables using Goursat functions.

From this representation, one can deduce various physical quantities of the fluid such as the velocity, vorticity, pressure and the surface stress.

Velocity

From the definition of the stream function, the horizontal and vertical components of the velocity are given by ψ_y and $-\psi_x$ respectively. Therefore, using relation (2.10), we have

$$u + iv = \frac{\partial\psi}{\partial y} - i\frac{\partial\psi}{\partial x} = -i\left(\frac{\partial\psi}{\partial x} + i\frac{\partial\psi}{\partial y}\right) = -2i\frac{\partial\psi}{\partial\bar{z}}. \quad (2.14)$$

Next, using the definition of $\psi(z, \bar{z})$, we see that the velocity is given by

$$u + iv = -f(z) + z\bar{f}'(\bar{z}) + \bar{g}'(\bar{z}) \quad (2.15)$$

where $f'(z) = df/dz$.

Pressure and Vorticity

It can be seen directly from the Stokes equation (2.1) that

$$\frac{1}{\mu}\frac{\partial p}{\partial x} = \nabla^2 u, \quad \frac{1}{\mu}\frac{\partial p}{\partial y} = \nabla^2 v. \quad (2.16)$$

Therefore, forming a complex combination of these gives

$$\frac{1}{\mu}\left(\frac{\partial p}{\partial x} + i\frac{\partial p}{\partial y}\right) = \nabla^2(u + iv). \quad (2.17)$$

Again using relation (2.10) together with relation (2.15) gives

$$\frac{2}{\mu}\frac{\partial p}{\partial\bar{z}} = 4\frac{\partial^2}{\partial z\partial\bar{z}}\left[-f(z) + z\bar{f}'(\bar{z}) + \bar{g}'(\bar{z})\right]. \quad (2.18)$$

Integrating this and adding the constant function $4f'(z)$ to make the pressure real-valued, gives

$$\frac{p}{\mu} = 2\left[f'(z) + \bar{f}'(\bar{z})\right]. \quad (2.19)$$

Next, using the fact that $\omega = -\nabla^2\psi$, we have that

$$\omega = 2i\frac{\partial^2}{\partial z\partial\bar{z}}\left[\bar{z}f(z) + g(z) - z\bar{f}'(\bar{z}) - \bar{g}'(\bar{z})\right] = 2i\left[f'(z) - \bar{f}'(\bar{z})\right]. \quad (2.20)$$

Putting this together with (2.19) gives

$$\frac{p}{\mu} - i\omega = 4f'(z) \quad (2.21)$$

which we shall refer to throughout the thesis.

Fluid Stress

The fluid stress on a surface is given by

$$-pn_j + 2\mu e_{ij}n_j \quad (2.22)$$

where n_i denotes the components of the unit normal vector to the boundary and e_{ij} is the usual fluid rate of strain tensor. Writing $N = n_1 + in_2$ then, upon using the continuity equation, it can be seen that both components (corresponding to $j = 1, 2$) are satisfied by the real and imaginary parts of

$$-pN + 2\mu(e_{11} + ie_{12})\bar{N} \quad (2.23)$$

respectively. Noting that $e_{11} = \partial u/\partial x$ and that $e_{12} = (1/2)(\partial u/\partial y + \partial v/\partial x)$ and following a similar method used to derive (2.15), we find that

$$e_{11} + ie_{12} = z\bar{f}''(\bar{z}) + \bar{g}''(\bar{z}). \quad (2.24)$$

Furthermore, the complexified normal is given by $N = -ie^{i\theta} = -iz_s$ where s is an element of arc length along the boundary. Also, from (2.21), we have that

$$p = 4\mu\text{Re}[f'(z)]. \quad (2.25)$$

Putting this together with (2.24) in (2.23) gives

$$-pN + 2\mu(e_{11} + ie_{12})\bar{N} = 2i\mu z_s \left[\bar{f}'(\bar{z}) + f'(z) \right] + 2i\mu \bar{z}_s \left[z\bar{f}''(\bar{z}) + \bar{g}''(\bar{z}) \right]. \quad (2.26)$$

It is a remarkable fact the right hand side of this is an exact derivative,

$$2i\mu \frac{dH}{ds} \quad (2.27)$$

where

$$H(z, \bar{z}) = f(z) + z\bar{f}'(\bar{z}) + \bar{g}'(\bar{z}) \quad (2.28)$$

and we shall make use of this relation within a number of different studies later in this thesis.

2.2 Singularity model for swimmers.

We must take special care when considering two-dimensional Stokes flow problems analytically due to the well-known Stokes paradox, which states that it is impossible to find an exact two-dimensional solution for flow past an isolated body in such a way that its velocity decays at infinity. The presence of the non-vanishing far field velocity is due to the presence of a net force on the body. Therefore, in order to study this area analytically, we must restrict our attention to Stokes flow problems in which there is no such force exerted by the fluid on the objects within it.

These are not rare nor difficult to find. A characteristic feature of swimming microorganisms in low Reynolds numbers is that they produce a sequence of changing body shapes, often referred to as “squirming”. As discussed in the introduction, it does so in such a way that the body remains force and torque free as, in a Stokes flow, the rate of change of momentum and angular momentum is zero. Therefore we have that

$$\oint_{\partial B} F(z, \bar{z}) ds = \oint_{\partial B} F(z, \bar{z})(z - z_d) ds = 0 \quad (2.29)$$

where F is the force of the fluid on a body ∂B (with infinitesimal arc length ds) and z_d a point inside B . From equation (2.28), the condition that the swimmer experiences no net torque or force is a crucial one as it means that $H(z, \bar{z})$, which shall be used to solve various swimming problems, must not include any logarithmic singularities. As these

are precisely the singularities that are at the heart of the Stokes paradox, avoiding these means that problems of swimming microorganisms lends itself well to analytic study in two dimensions.

Any swimmer in a low Reynolds number flow will locally generate a flow which may equivalently be modelled by a distribution of Stokes flow singularities positioned either inside, or on the boundary of, the swimmer. In our study we adopt a similar approach where the swimming micro-organism is represented by a superposition of two-dimensional point singularities.

2.2.1 Modelling swimmers using Goursat singularities.

A swimming micro-organism will generate a flow around it. In order to determine the stream function $\psi(z, \bar{z})$ for that flow, one must find the appropriate Goursat functions $f(z)$ and $g(z)$ which are associated with it. These functions are analytic everywhere inside the fluid domain except, possibly, at a set of isolated singularities introduced to model the swimmer. We begin the search for an appropriate singularity description by supposing that the swimmer is located at $z = z_d$ and also that the Goursat function $f(z)$ is allowed to admit a logarithmic singularity there. Hence, to leading order, this function takes the form

$$f(z) = \lambda \log(z - z_d) \quad (2.30)$$

where $\lambda \in \mathbb{C}$ is the strength of the singularity. Upon substitution into (2.15), the velocity is then

$$\begin{aligned} u + iv &= -\lambda \log(z - z_d) + \frac{\bar{\lambda}z}{\bar{z} - \bar{z}_d} + \bar{g}'(\bar{z}) \\ &= -\lambda \log(z - z_d) + \frac{\bar{z}(z - z_d)}{\bar{z} - \bar{z}_d} + \frac{\bar{\lambda}z_d}{\bar{z} - \bar{z}_d} + \bar{g}'(\bar{z}). \end{aligned} \quad (2.31)$$

Chapter 2. Application of singularity theory to low Reynolds number swimming. 33

Therefore, in order to ensure that the velocity is both single valued and, at most, logarithmically singular (and does not have a simple pole at z_d), we must choose

$$g'(z) = -\frac{\lambda \bar{z}_d}{(z - z_d)} - \bar{\lambda} \log(z - z_d). \quad (2.32)$$

Therefore, if locally to z_d we have

$$\begin{aligned} f(z) &= \lambda \log(z - z_d) + \text{analytic function}, \\ g'(z) &= -\frac{\bar{\lambda} z_d}{(z - z_d)} - \bar{\lambda} \log(z - z_d) + \text{analytic function}, \end{aligned} \quad (2.33)$$

then we have a stokeslet [34] near z_d , which we have seen is the key to the Stokes paradox. This is also clear by noticing that the velocity here takes the form

$$u + iv \sim -\lambda \log |z - z_d| \quad (2.34)$$

and hence grows logarithmically as $z \rightarrow \infty$. Also note that enforcing $f(z)$ to take certain singularities forces $g'(z)$ to take singularities too.

If, instead, $f(z)$ is allowed to admit a simple pole singularity at z_d ,

$$f(z) = \frac{\lambda}{z - z_d}, \quad (2.35)$$

then following a similar argument to that above, $g'(z)$ must be chosen as

$$g'(z) = \frac{\lambda \bar{z}_d}{(z - z_d)^2} \quad (2.36)$$

in order to ensure that the velocity scales as $\mathcal{O}(1/|z - z_d|)$ rather than $\mathcal{O}(1/|z - z_d|^2)$. This corresponds to an irrotational dipole contribution of strength $-\lambda \bar{z}_d$ (a dipole is represented

by a simple pole of $g(z)$). We say that if the Goursat functions take the local form

$$\begin{aligned} f(z) &= \frac{\lambda}{z - z_d} + \text{analytic function}, \\ g'(z) &= \frac{\lambda \bar{z}_d}{(z - z_d)^2} + \text{analytic function}, \end{aligned} \quad (2.37)$$

then $f(z)$ has a *stresslet singularity* at z_d of strength λ . Again we see that including a simple pole into $f(z)$ imposes a double pole into $g'(z)$: an “associated” stresslet-dipole. Said another way, $g'(z)$ may be chosen to admit independent singularities from $f(z)$, but not conversely. Specifically, allowing $g'(z)$ to admit a logarithmic singularity

$$g'(z) = c \log(z - z_d) \quad (2.38)$$

where $c \in \mathbb{R}$ represents a source (or sink) at z_d while if $c \in i\mathbb{R}$ then this is a rotlet at z_d . A double pole of $g'(z)$ corresponds to an irrotational dipole singularity, a triple pole corresponds to an irrotational quadrupole and so on. With regard to modelling a swimming micro-organism, we are free to choose any combination of Stokes flow singularities that is deemed appropriate for the problem at hand. However, each of these singularities will be a (potentially complicated) function of the swimmer’s size, shape, its swimming protocol and its local effect on the fluid around it. The attention is therefore focused on which specific combination of singularities can be used to accurately model a physical swimmer.

2.2.2 The Crowdy and Or point singularity model [1].

In order to rationalise the three-dimensional numerical [23] and laboratory [25] experiments of Murray *et al.* of a three-linked swimmer near a flat solid wall, Crowdy and Or [1] adopt a singularity model to represent the swimmer by a combination of Stokes flow singularities. By arguing that the mechanical motion in the above experiments are coplanar, they propose that many of the qualitative dynamics recorded within may be retrieved by modelling the swimmer using an appropriate singularity configuration inside an infinite two-dimensional fluid. This fluid fills the upper half of a complex plane above a no-slip wall, on which the fluid’s velocity is zero. Furthermore, changing the actuation rates of

Chapter 2. Application of singularity theory to low Reynolds number swimming. 35

the spheres simply corresponds to tweaking the corresponding choice and strength of the singularities that will replace them.

Their specific choice of singularity structure is motivated by the swimming protocol of a treadmilling micro-organism of radius ϵ in an unbounded fluid. This acts as a sensible first approximation to how a treadmilling swimmer would behave when in the vicinity of a boundary. The swimmer is assumed to induce a tangential velocity profile of the form

$$U(\phi, \theta, t) = 2V \sin(2(\phi - \theta(t))) \quad (2.39)$$

where ϕ is the angle measured from the positive x -direction and $\phi = \theta$ is an angle from the horizontal which is interpreted as the distinguished direction of the swimmer's head. The magnitude of the constant V sets the timescale for the treadmilling motion. Notice that while an organism may produce a time-dependent tangential velocity profile, the Stokes equations imply that the fluid reacts instantaneously to it.

The singularity structure that they propose is that of a stresslet of strength

$$\lambda(t) = \exp(2i\theta(t)). \quad (2.40)$$

Due to the presence of this stresslet, the associated stresslet-dipole has strength $\lambda \bar{z}_d$ at the swimmer's image position. In addition to this, the authors' [1] model also includes an irrotational quadrupole of strength $2\epsilon^2\lambda$. Interestingly, note that the orientation of the stresslet singularity is twice the orientation of the swimmer. This differs from [13] who assume that their stresslet direction is in the same as that of the body. In the language of Goursat functions, this means that near $z = z_d$,

$$\begin{aligned} f(z, t) &= \frac{\lambda(t)}{z - z_d(t)} + f_0(t) + f_1(t)(z - z_d(t)) + \mathcal{O}(z - z_d(t))^2, \\ g'(z, t) &= \frac{2\epsilon^2\lambda(t)}{(z - z_d(t))^3} + \frac{\lambda(t)\overline{z_d(t)}}{(z - z_d(t))^2} + g_0(t) + \mathcal{O}(z - z_d(t)). \end{aligned} \quad (2.41)$$

From here on, we will suppress any explicit time dependence on the parameters and func-

tions for convenience (and so $z_d(t)$ will simply be written as z_d , $f(z, t)$ as $f(z)$, and so on).

It should be noted that while this singularity configuration depicts a non-self propagating treadmilling swimmer in free-space well, it is unlikely to model its behaviour accurately when effected by another external entity such as a solid boundary or another swimmer. In order to model this accurately, the effective singularity description of the swimmer would have to change in response to its surroundings. However, as a first model and in order not to over-complicate the dynamics, Crowdy and Or [1] assume that the swimmer is passive with respect to its surroundings and thus takes the same singularity structure whether in free space or in a more complicated surrounding. Previous authors have made similar assumptions [26]. Within the context of this model, this means that their swimmers will *always* be modelled using a stresslet of strength λ together with a superposed quadrupole of strength $2\lambda\epsilon^2$, no matter what their surroundings are.

Once this singularity model has been chosen, the authors place it at the point $z_d(0)$ and endow the swimmer with an initial head orientation, $\theta(0)$. Due to the simplicity of the domain, it is clear that an image singularity should be placed at the point of the swimmer's reflection in the wall, \bar{z}_d . Using this, the authors find that in addition to the stresslet singularity at the swimmer's position, the Goursat function $f(z)$ must admit up to a third order pole at the *image* position, too. This is an important result which we refer to throughout the thesis.

Using the method of images, the authors allow z_d and θ to evolve as a result of the swimmer's interaction with its image. In doing so, the velocity and rotation of the swimmer is deduced from the finite part of the fluid velocity and (half of the) fluid vorticity at the swimmer's position. The resulting dynamical system is then given in closed form by

$$\frac{dz_d}{dt} = -\frac{2\lambda}{(z_d - \bar{z}_d)} - 2\epsilon^2 \frac{(\bar{\lambda} + 3\lambda)}{(z_d - \bar{z}_d)^3} \quad (2.42)$$

$$\frac{d\theta}{dt} = -i \left[\frac{\bar{\lambda} - \lambda}{(z_d - \bar{z}_d)^2} + 6\epsilon^2 \frac{(\bar{\lambda} - \lambda)}{(z_d - \bar{z}_d)^4} \right] \quad (2.43)$$

The authors are able to retrieve many of the qualitative swimming dynamic that are recorded by Murray *et al.* [23] [25]. In the limit $\epsilon \rightarrow 0$ (the zero-area swimmer as considered by Berke *et al.* [13]) the model is one of a stresslet only with no superposed quadrupole and hence (2.42) and (2.43) reduce to

$$\frac{dz_d}{dt} = -\frac{2\lambda}{(z_d - \bar{z}_d)} \quad \text{and} \quad \frac{d\theta}{dt} = \frac{i(\lambda - \bar{\lambda})}{(z_d - \bar{z}_d)^2}. \quad (2.44)$$

Solving these equations numerically (using a Newton solver which marches forward in time) does not allow any solutions where the swimmer moves parallel to the wall in either a rectilinear motion (or a more complicated one). Instead, whatever its initial orientation is, the swimmer eventually reorients itself and finally crashes into the wall, see Figure 2.1. This is consistent with the findings of Berke *et al.* [13] who claim that while a swimmer will initially either move away or towards the wall (depending on its initial orientation), the hydrodynamic effects will reorient the swimmer in such a way that it will always swim towards the wall.

When $\epsilon \neq 0$, the swimmer's dynamics reveal interesting trajectories where it takes a wave-like motion along the wall, a few of which are shown in Figure 2.2 for different initial conditions. These are interpreted as nonlinear period solutions of the dynamical system (2.42) and (2.43). For all initial orientations $\theta(0) \neq 0$, the swimmer will always reorient itself such that it swims towards the wall. It then spends a period of time swimming on an approximately rectilinear trajectory at a distance of approximately ϵ from the wall. While it does so, its orientation is still in evolution and, after a while, the swimmer “takes off” from the wall again only to later be reoriented back towards it, and so on. The swimmer continues this cycle indefinitely. This motion should be compared with Figures 2(c) and 4(c) of Or and Murray [23]. From here on, we shall refer to these as *bouncing orbits*.

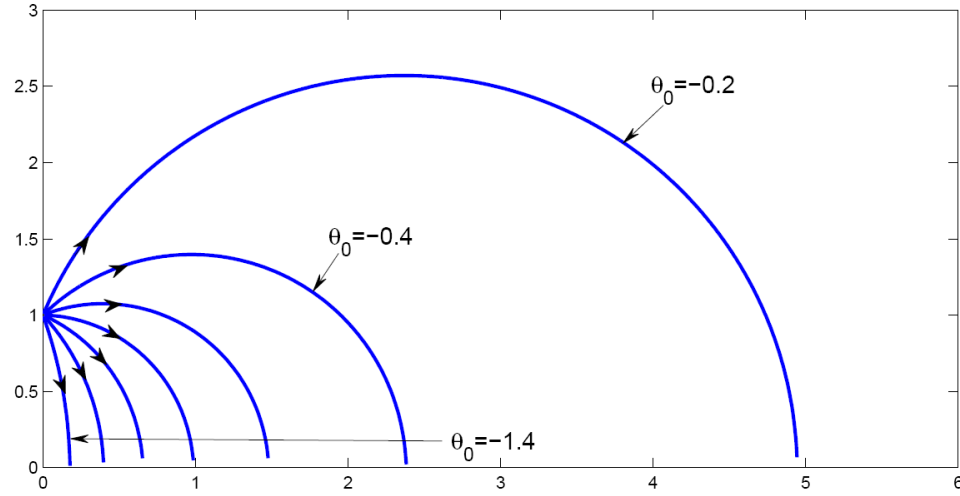


Figure 2.1: Dynamics for $\epsilon = 0$ for different initial orientations [1]. When $\theta(0) = 0$, the swimmer moves directly down and crashes into the wall.

Finally, we note that Berke *et al.* [13] predicted various qualitative properties of the swimmer's trajectory but did not perform the full dynamic calculations. The above is a complete model dynamical system that can provide detailed predictions of the swimmer's evolution.

Interestingly, the dynamical system defined by equations (2.42) and (2.43) is integrable with solution

$$\theta(y) = \frac{1}{2} \arcsin \left[\sin(2\theta_0) \exp \left(\frac{3}{2} \log \frac{y}{y_0} - \frac{1}{4} \log \frac{y^2 - \epsilon^2}{y_0^2 - \epsilon^2} \right) \right], \quad (2.45)$$

where (θ_0, y_0) is an initial point on the trajectory. Figure 2.3 is a phase space portrait of the possible swimming trajectories in the (θ, y) space for $\epsilon = 0.2$ and in the range of $-90^\circ \leq \theta \leq 90^\circ$. When $-90^\circ \leq \theta < 0$, the swimmer moves to the right while when $0 < \theta \leq 90^\circ$ the swimmer moves to the left. The separating line $\theta = 0$ corresponds to when the swimmer moves directly away from the wall while those at $\theta = \pm 90^\circ$ are for the cases when the swimmer moves directly towards the wall. The dynamics are π periodic and hence this diagram gives a complete description of the phase space for the swimming motion by a wall. For comparison, note the close similarity to Figure 2(b) presented in [23] for a three-dimensional swimmer propelled by two actuated spheres.

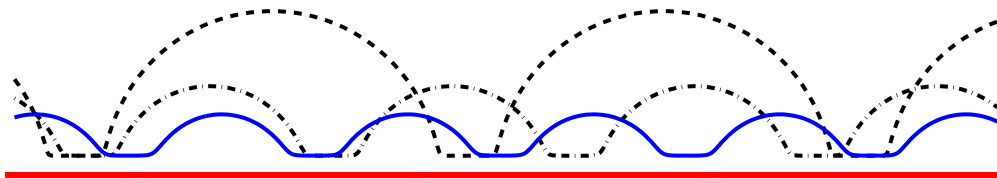


Figure 2.2: Three examples of bouncing orbit trajectories for a treadmilling swimmer with $\epsilon = 0.2$. Here, $z_d(0) = i, \theta(0) = -2\pi/5$ (black, dashed), $z_d(0) = 0.8i, \theta(0) = -\pi/3$ (black, dotted) and $z_d(0) = 0.6i, \theta(0) = -\pi/5$ (blue, solid).

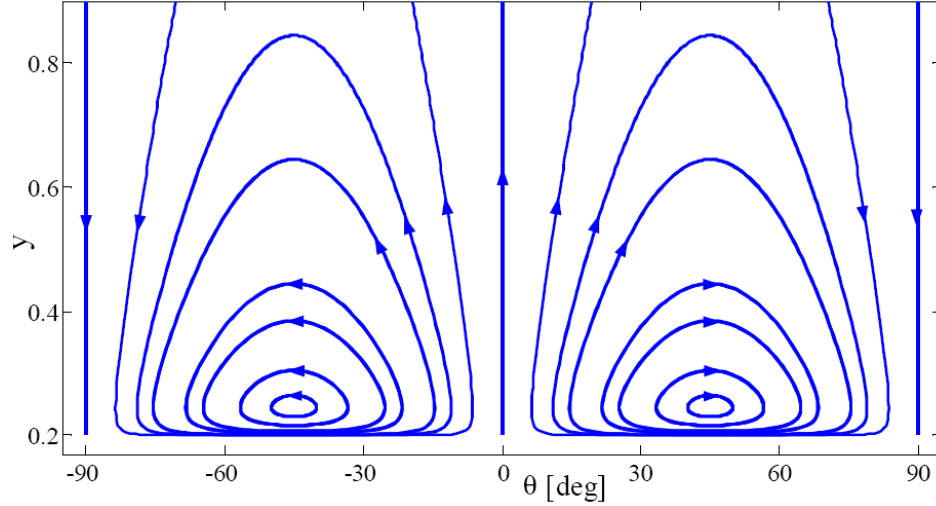


Figure 2.3: Phase space portrait in (θ, y) space as given by equation (2.45) for a tread-milling swimmer with $\epsilon = 0.2$ [4].

2.3 A swimmer above an infinite wall in the presence of a background shear flow.

Using the above solution for a swimmer above an infinite flat wall in an otherwise ambient background flow, we now explore situations with different background flows. Consider, for example, the swimmer placed in a background shear flow of the form

$$\psi = \gamma y^2, \quad (u, v) = (2\gamma y, 0) \quad (2.46)$$

where U is the strength of the shear flow and $y = \text{Im}[z]$. Hence the velocity is given by $u + iv = 2\gamma y = -i2\gamma(z - \bar{z})/2$ and, comparing with (2.15) we see that the corresponding Goursat functions for this are

$$f(z) = \frac{i\gamma}{2}z, \quad g'(z) = -i\gamma z. \quad (2.47)$$

Chapter 2. Application of singularity theory to low Reynolds number swimming. 41

Due to the linearity of the Stokes equations, the resulting dynamics are a superposition of the above solution for the swimmer in an ambient flow with that of a swimmer in an unbounded shear flow. In this case, both the image singularity and the background shear flow drive the swimmer and there is therefore a natural competition between these two effects. For larger shear rates, 2γ , the shear flow effect is more dominant and acts to draw out the “wavelengths” of the bouncing orbits, see Figures 2.4, 2.5 and 2.6.

Interestingly, when the shear rate is low, the swimmer’s interaction with its image dominates its dynamics and undergoes the familiar bouncing orbits. As the shear rate is increased it is possible for the swimmer to undergo a spiralling motion. The trajectories for larger shear rates should be compared with Figure 9 in [4], however it should be noted that Zilman *et al.* do not seem to take into account the swimmer’s own hydrodynamic interaction with the wall (i.e. the interaction with the image singularity). Therefore, the comparison is only valid for higher shear rates, when the shearing effect dominates the wall-interaction effect.

2.4 Summary

We have presented the model of Crowdy and Or [1] used to describe the hydrodynamic interaction between a two-dimensional (circular) treadmilling swimmer and an infinite flat surface. While this two-dimensional model was not as realistic as a three-dimensional one, it afforded the authors the opportunity to tackle these problems with analytic tools. Furthermore, many of the three-dimensional dynamics of swimming problems are quasi two-dimensional in that the motion takes place predominantly in some plane. Therefore, many of the qualitative phenomena are preserved within the two-dimensional description.

An important implication of the above model is the contribution of the quadrupole singularity. Other authors have used a force dipole (stresslet) model to simulate micro-organism swimming, however we have seen that if the swimmer is modelled with this singularity alone, it will generically crash into the wall. The inclusion of the superposed quadrupole singularity appears to prevent this from happening and leads to bouncing orbits. These are

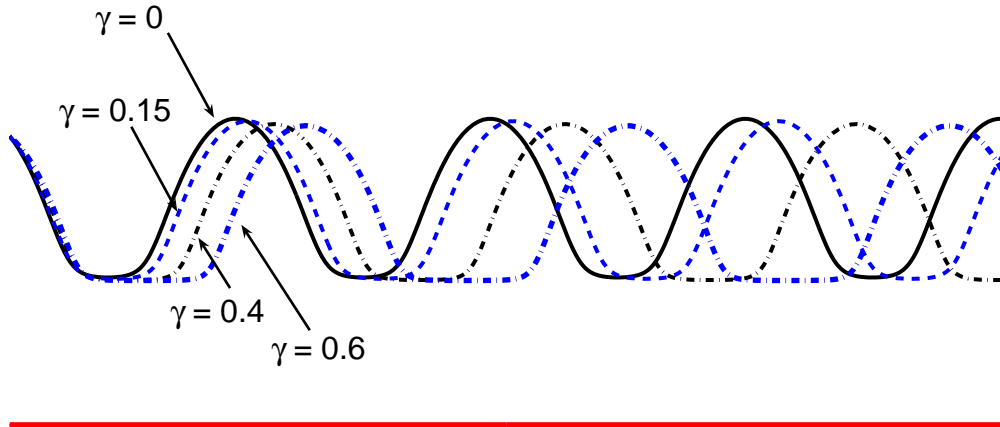


Figure 2.4: Trajectories of swimmer (with $\epsilon = 0.2$, $z_d(0) = 0.4i$, $\theta(0) = 0.7\pi$) in the presence of a background shear flow of varying strength: $\gamma = 0$ (Black, solid), $\gamma = 0.15$ (Blue, dashed), $\gamma = 0.4$ (black, dash-dot) and $\gamma = 0.6$ (blue, dash-dot).

interpreted as stable, nonlinear, period orbits of the resulting dynamical system.

We have shown that the model presented by Crowdy and Or [1] captures the physical phenomena observed by Murray and Or [23] and Murray *et al.* [25] for similar experiments within an numerical and laboratory setup, respectively. That Crowdy and Or [1] have done so using an independent method suggests that this model is a useful one and supports the idea that many qualitative phenomena of two-dimensional low Reynolds number swimming can be captured by this model. Indeed it can be expected that it may be used to predict the behaviour of similar swimmers in more complicated geometries: this will be the focus of the next two chapters.

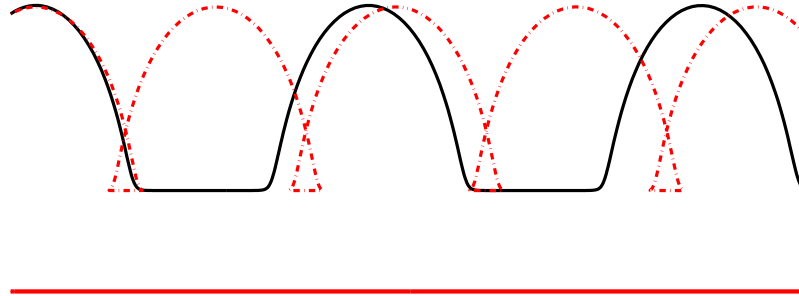


Figure 2.5: Trajectories of a swimmer (with $\epsilon = 0.2$, $z_d(0) = 0.55i$, $\theta(0) = 4\pi/5$) in the presence of a background shear flow of varying strength: $\gamma = 0.5$ (Black, solid) and also $\gamma = 0.75$ (Red, dash). We see that the combined effect of the shear with the image singularity interaction gives rise to “spiralling” orbits.

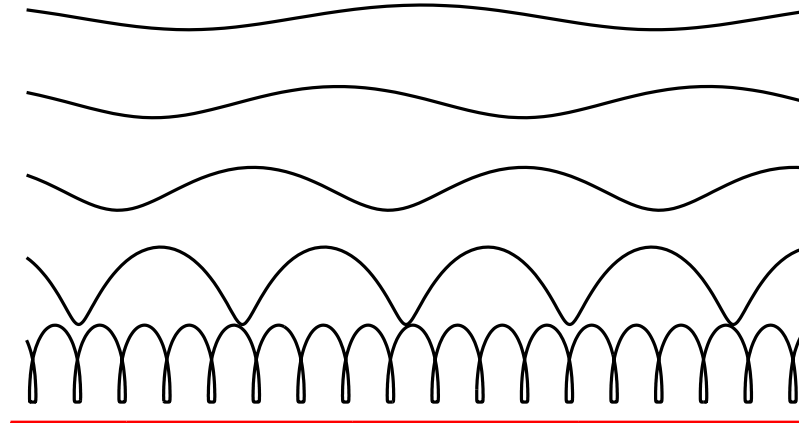


Figure 2.6: Trajectories of the swimmer ($\epsilon = 0.05$) in the presence of a strong background shear flow ($\gamma = 8.5$) at different heights (bottom to top): $\text{Im}[z_d(0)] = 0.2, 0.4, 0.6, 0.8, 1$.

Chapter 3

Stokes flows past a gap in a wall.

3.1 Introduction

In chapter 2 we saw that much attention has been recently paid to the study of swimming dynamics near a solid boundary. Crowdy and Or [1] have shown that it is the hydrodynamic interaction between the swimming micro-organism and the infinite flat boundary that determines its subsequent motion and allows “bouncing orbits”. It is likely that these dynamics may be altered by a change in the solid boundary that the swimmer interacts with. Problems of swimming near more geometrically complicated domains are therefore of interest. However, this does not appear to have been previously studied in any detail.

As a first step towards doing so, a careful study of how a general Stokes flow behaves in the presence of such boundaries is necessary. For example, it is straight-forward to write down the solution for the shear flow of a fluid in the upper half plane above an infinite flat wall, but it is not immediately clear how the resulting streamlines would be altered when near a more complicated no-slip surface.

As a natural extension to the simple half plane we consider the case where the flat wall admits a finite gap, or orifice. In this case the fluid fills the entirety of the complex plane, above and below this wall which now has a gap in the interval $[-1, 1]$. Only the fluid in the upper half plane will be driven by some far field flow, while the fluid far below the wall in

the lower half plane is assumed to remain at rest.

In the past, problems of fluid flow past an aperture have been notoriously difficult due to the fact that no boundary condition can be set *a priori* in the gap region, except that the velocities and stresses must be continuous across this region (however, this is a basic physical requirement across any line in the fluid). For example, Weinbaum [35] indicated that there may not be a separation streamline, defined by a contour on which the stream function vanishes, emanating from a sharp corner. Dagan *et al.* [36] have demonstrated the difficulty associated with fixing a boundary condition when a net flux across a slit is present.

We will focus our attention on two cases: one where the fluid is driven by a far field uniform shear flow and one where it is forced by a stagnation point flow. Analytical solutions to both of these cases have been previously found, though by rather different methods. We shall aim to develop a new mathematical approach using conformal mapping theory which will provide exact solutions to these problems in a unified fashion, so that only minor changes to the method are required in order to solve both problems. Furthermore, we would like our method to also accommodate the cases where the flow is driven by other singularities too, either at a point inside the fluid (such as a Crowdy-Or singularity model [1]) or by one at infinity.

Smith [2] found the solution for a uniform Stokes flow past a wall with a gap, such that the stream function approached that of a uniform shear flow

$$\psi \rightarrow Uy^2 \quad (3.1)$$

or, alternatively,

$$(u, v) \rightarrow \begin{cases} (2Uy, 0), & \text{as } z \rightarrow \infty^+ \\ (0, 0), & \text{as } z \rightarrow \infty^- \end{cases} \quad (3.2)$$

in the far field. Here we write ∞^+ to represent the region far above the wall such that $y \rightarrow +\infty$, while ∞^- corresponds $y \rightarrow -\infty$. Here $y = \text{Im}[z]$ and U is the strength of

the shear flow, which Smith [2] takes as unity. Smith [2] then wrote the global flow as the addition of a symmetric and an antisymmetric stream function. The antisymmetric stream function was an odd function of y , and as the velocity was therefore an even function of y , this represented the behaviour when the direction of the shear flow above the wall was exactly the same as that beneath the wall. The symmetric part, an even function of y , described the shear flow which was in opposite directions on both sides of the boundary and could be directly written as $y^2/2$. The antisymmetric stream function was found by taking the Fourier transform (in x) of the biharmonic equation, applying the no-slip boundary conditions and expressing the solution in terms of the first Bessel function. The solution was then inverted using a result of Erdelyi [37] and, upon adding both stream function contributions together, eventually gave the exact solution

$$\psi(x, y) = \frac{1}{2}y^2 + \frac{y}{2\sqrt{2}} \left\{ y^2 - x^2 + a^2 + [(y^2 + x^2)^2 + 2a^2(y^2 - x^2) + a^4]^{\frac{1}{2}} \right\}^{\frac{1}{2}} \quad (3.3)$$

where a is half the gap width (and hence is equal to one in the geometrical configurations of this chapter). The first term accounts for the antisymmetric velocity while the second accounts for the symmetric one. The flows in the lower half plane, which were in opposite directions, cancelled each other out and the resulting solution was the desired one. This agrees with the results of O'Neill [38] and Wakiya [39] who considered slow viscous flows above a plane with a cylindrical trough, when the limit of infinite cylindrical depression is taken.

We will also consider the a stagnation point flow of the form

$$\psi(x, y) = kxy^2 \quad (3.4)$$

near the same geometry, where k is a real constant which determines the strength of the flow. We see that the origin is a natural stagnation point of this flow and that this stream function is the equivalent of a uniform straining flow, see Figure 3.1.

The stagnation point flow (3.4) has the associated velocity profile $(u, v) = (2kxy, -ky^2)$

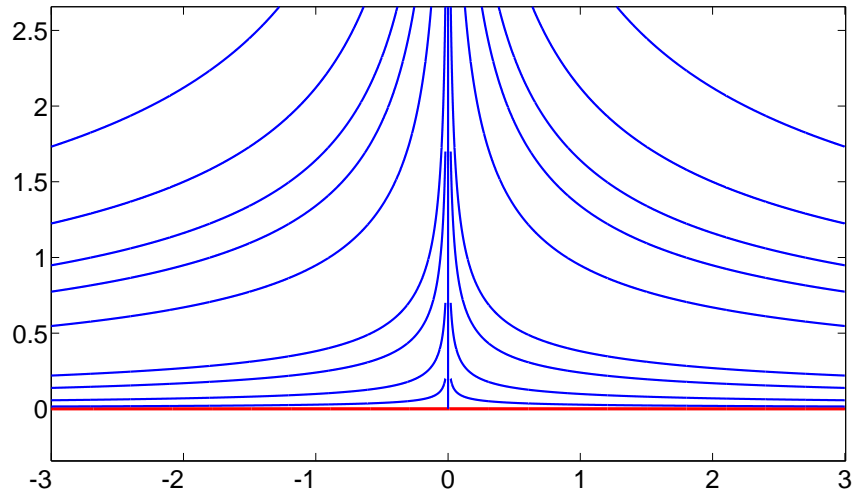


Figure 3.1: Streamlines for a stagnation point flow. If the flow was unbounded, there would be a natural stagnation point at the origin (hence the name of the flow). This is equivalent to a linear straining flow.

and hence, from the Stokes equations (2.1) we see that the pressure is given by

$$p(x, y) = -2ky \quad (3.5)$$

plus a possible constant. Aside from this linearly decreasing pressure which is associated with the driving stagnation point flow, the pressure at the upstream infinity can be set higher than that at the lower infinity by a value $2\Delta P$ which may cause a discharge through the gap in the wall.

The problem of stagnation point flow above a wall with a hole or a gap has been previously solved by Ko and Jeong [3]. The authors approached this problem by expressing the stream function as a combination of analytic functions

$$\psi_J(z, \bar{z}) = \text{Im} \left[\int F_J(z) dz + \int G_J(z) dz + (\bar{z} - z) G_J(z) \right] \quad (3.6)$$

where these analytic functions satisfy

$$u + iv = \overline{F}_J(\overline{z}) + (z - \overline{z})\overline{F}'_J(\overline{z}) - G_J(z). \quad (3.7)$$

Applying this form of the velocity to the boundary conditions on either side of the walls, they find that

$$\begin{aligned} 0 &= [F_J + \overline{G}_J]_+ - [F_J + \overline{G}_J]_- \\ 0 &= [F_J + \overline{G}_J]_+ + [F_J + \overline{G}_J]_- \end{aligned} \quad (3.8)$$

where $[\cdot]_{\pm}$ evaluates the relevant expression above and below the real line respectively. This is a Riemann-Hilbert problem for the two analytic functions $F_J(z), G_J(z)$. To find them, they assume that these functions take the form

$$\begin{aligned} F_J(z) + \overline{G}_J(z) &= A_0 + A_1z + A_2z^2 \\ F_J(z) - \overline{G}_J(z) &= (z^2 - 1)^{1/2}(B_0 + B_1z) \end{aligned} \quad (3.9)$$

where they choose the branch cut to lie along the two walls, which is identical to selecting

$$-\pi < \arg(z + 1) < \pi, \quad 0 < \arg(z - 1) < 2\pi. \quad (3.10)$$

Therefore, the functions remain single-valued across the gap. Consequently, Ko and Jeong [3] find that

$$\begin{aligned} F_J(z) &= -\frac{ikz}{8} [z + (z^2 - 1)^{1/2}] + \frac{\Delta P}{4\mu} (z^2 - 1)^{1/2} \\ G_J(z) &= \frac{ikz}{8} [z + (z^2 - 1)^{1/2}] + \frac{\Delta P}{4\mu} (z^2 - 1)^{1/2}. \end{aligned} \quad (3.11)$$

Notice that, from (3.7), we see that this solution is valid up to an additive constant, as the translations $F_J \rightarrow F_J(z) + c$ and $G_J \rightarrow G_J(z) + \bar{c}$ leave the velocity unchanged.

Interestingly, while this work is similar in nature to that of Smith [2] (who considered exactly the same geometry only with a driving shear flow, as opposed to stagnation point

flow), Ko and Jeong [3] seem to be unaware of Smith's work [2]. An interesting test on Ko and Jeong's method would be to use it to solve Smith's problem. While both of these problems above were solved using rather different methods, they will serve as a useful check on the formulation that we will present in this chapter.

Due to the sharp corners at the start and end of the gap, special attention must be drawn to the structure of the flow there. The approach we take here originates from the description of the singularity structure at a sharp corner, first proposed by Dean and Montagnon [40]. They showed that near a sharp corner with interior angle 2π , the stream function takes the form

$$\psi(r, \theta) \sim r^{\frac{3}{2}} \quad (3.12)$$

where r is the radial distance from the corner. We use this results to argue the structure of the Goursat functions around corners.

While we focus our attention on flows which are purely two-dimensional, it should be noted that by solving a pair of dual integral equations, Davis [41] was able to find exact solutions to the axisymmetric analogue of the problem considered by Smith [2]. In this problem, Davis considers a uniform shear flow above an infinite wall which admits a circular orifice (as opposed to a rectilinear slit, as in Smith's problem). Davis' [41] work was motivated by the study of fluid skimming and particle entrainment performed by Yan *et al.* [42] and is a generalization of the classical solution of Sampson flow past a circular orifice in a wall [43].

3.2 Stokes flow near the end of a plate.

Consider two infinite walls conjoined at $z = z_0$ with internal angle 2α . When this separation angle is 2π , the walls lie along the same line and wedge corner becomes the end of a plate. Based on the above leading order form of the stream function (3.12) together with (2.13), the Goursat function $f(z)$ can be shown to take the form

$$f(z) \sim a_0(z - z_0)^{1/2} + \mathcal{O}(z - z_0) \quad (3.13)$$

with a_0 constant, in the vicinity of this corner. From the no-slip velocity condition (2.15), it follows that $g'(z)$ takes the form

$$g'(z) \sim b_0(z - z_0)^{-1/2} \quad (3.14)$$

with b_0 constant, near $z = z_0$ so that the velocity does not diverge there. Knowledge of the Goursat functions' singularity structure around the sharp end of a plate will be crucial in our study of Stokes flows around complex geometries in this, as well as later, chapters.

3.3 Shear flow past a wall with a gap.

Using conformal mapping techniques, we will now attempt to find an exact solution to the problem considered by Smith [2]: that of a uniform shear flow above an infinite no-slip wall with a gap.

3.3.1 Mathematical formulation

We want to find a stream function, ψ which satisfies the biharmonic equation everywhere in the fluid,

$$\nabla^4 \psi(z, \bar{z}) = 0 \quad (3.15)$$

such that the velocity is zero along the walls $|x| > 1$ and that, as we move far above the wall, the flow behaves as a regular shear flow with strength $U = 1$,

$$\psi(x, y) \rightarrow y^2 \quad \text{as} \quad z \rightarrow \infty^+. \quad (3.16)$$

In this case, the far field velocity is given by

$$u + iv = \psi_y - i\psi_x = 2y = -i(z - \bar{z}). \quad (3.17)$$

Next, recall that we express the stream function which satisfies the biharmonic equation as

$$\psi(z, \bar{z}) = \text{Im}[\bar{z}f(z) + g(z)] \quad (3.18)$$

where $f(z)$ and $g(z)$ are analytic functions of z with the velocity relation

$$u + iv = -f(z) + z\bar{f}'(\bar{z}) + \bar{g}'(\bar{z}). \quad (3.19)$$

Equating this to (3.17), our functions take the far field form

$$f(z) \sim \begin{cases} iz/2 & \text{as } z \rightarrow \infty^+ \\ f_\infty & \text{as } z \rightarrow \infty^-, \end{cases} \quad (3.20)$$

and

$$g'(z) \sim \begin{cases} -iz & \text{as } z \rightarrow \infty^+ \\ g_\infty & \text{as } z \rightarrow \infty^- \end{cases} \quad (3.21)$$

where f_∞ and g_∞ are constants.

3.3.2 Conformal mapping: a wall with a single gap.

Let us now introduce an analytic function which maps the interior of a disk with unit radius in a complex plane, whose coordinates are measured by the complex variable ζ , to the physical fluid domain, which has the usual z -coordinates. This is an example of a *conformal map*; an angle preserving function at all points where it has non-zero derivative. We construct this map as a composition of a Möbius map and a reciprocal map: the Möbius map,

$$\eta(\zeta) = \frac{1}{2} (\zeta^{-1} + \zeta) \quad (3.22)$$

maps the interior of the unit disk in the ζ -plane to the exterior of a slit of length 2 in the complex η -plane. The reciprocal map

$$z(\eta) = \frac{1}{\eta} = \frac{2\zeta}{\zeta^2 + 1} \quad (3.23)$$

therefore maps the interior unit ζ -disk to the exterior of the fluid domain. Chosen in this way, we ensure that

$$z(1) = 1 \quad \text{and} \quad z(-1) = -1. \quad (3.24)$$

Note also that the points $\zeta = \pm i$ both map to infinity. However, it is $\zeta = +i$ which corresponds to $z = \infty^+$ and hence it will be here that the far field shear flow condition shall be imposed in the ζ -plane. Figure 3.2 shows a schematic diagram of the mapped regions.

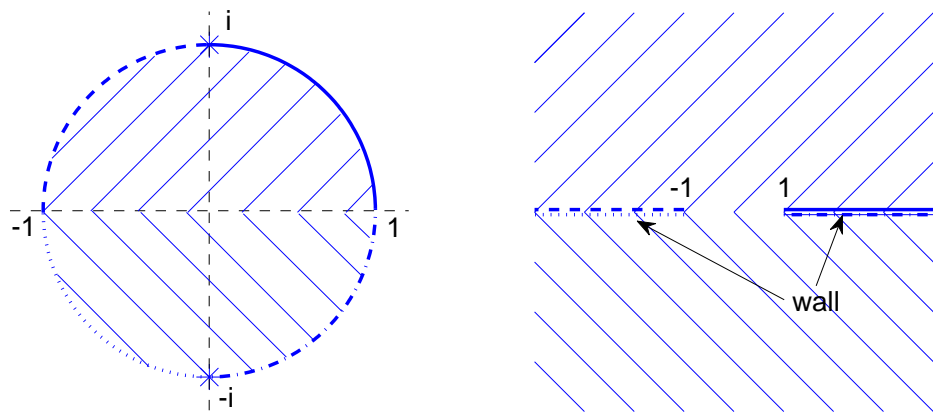


Figure 3.2: Conformal mapping from the interior of the unit disk (in the ζ -plane) to the exterior of an infinite horizontal wall with a gap between $x = \pm 1$ (in the fluid z -plane).

It is possible to invert this map (3.23) explicitly to give

$$\zeta(z) = \frac{1 - (1 - z^2)^{1/2}}{z}. \quad (3.25)$$

The negative square root is taken to ensure that the origin in the fluid domain is the image of a point inside the unit disk in the ζ -plane. This map has two branch points, at $z = \pm 1$; the two ends of the gaps. The branch cuts are taken to lie along the walls and so there will not be any discontinuities across the gap. Also notice that the Taylor expansion of $z(\zeta)$

reveals that

$$\zeta \mp 1 = \mathcal{O}((z \mp 1)^{1/2}) \quad (3.26)$$

near the point $z = \pm 1$. Therefore $\zeta(z)$ *also* has square root branch point singularities of exactly the same type that is required of the Goursat functions $f(z)$ and $g'(z)$. This is a crucial observation for the analysis as it follows that ζ may serve as a uniformisation variable for the problem. Therefore, the problem of determining the multi-valued functions $f(z)$ and $g'(z)$, which admit branch cuts in the physical domain, reduces to finding the single-valued, analytic functions $F(\zeta)$ and $G(\zeta)$ defined by

$$F(\zeta) \equiv f(z(\zeta)) \quad \text{and} \quad G(\zeta) \equiv g'(z(\zeta)) \quad (3.27)$$

where ζ is a point in the unit disk.

As a conformal map is analytic, we may form a Taylor expansion about the point $\zeta = 1$, corresponding to one of the corners, as

$$z(\zeta) = z(1) + z'(1)(\zeta - 1) + \frac{1}{2}z''(1)(\zeta - 1)^2 + \dots \quad (3.28)$$

However, the derivative of a conformal map vanishes at the corners,

$$z'(\pm 1) = 0 \quad (3.29)$$

as this is a point of non-conformality. Hence we have

$$z - 1 = (\zeta - 1)^2 \left[\frac{1}{2}z''(1) + \mathcal{O}(\zeta - 1) + \dots \right] = (\zeta - 1)^2 P(\zeta) \quad (3.30)$$

where $P(\zeta)$ is analytic everywhere inside the disk. Substituting this into (3.13), we have that

$$f(z(\zeta)) \equiv (\zeta - 1)[P(\zeta)]^{\frac{1}{2}}H(z(\zeta)). \quad (3.31)$$

As $H(z(\zeta))$ is also analytic, this can be written as

$$F(\zeta) = (\zeta - 1)H_1(\zeta) \quad (3.32)$$

where $H_1(\zeta)$ is also an analytic function. As we have two corners at $z = \pm 1$ in our problem, $f(z)$ takes the form

$$f(z) = (z^2 - 1)^{\frac{1}{2}}H(z) \quad (3.33)$$

which, by a similar argument to that above, can be written as

$$F(\zeta) \equiv (\zeta^2 - 1)H_2(\zeta). \quad (3.34)$$

Note that as $H_2(\zeta)$ is an analytic function of ζ , so is $F(\zeta)$. By a similar argument we also have that

$$G(\zeta) = \frac{K_2(\zeta)}{(\zeta^2 - 1)} \quad (3.35)$$

for analytic $K_2(\zeta)$. Keeping this in mind we rewrite the Goursat functions as

$$F(\zeta) = \frac{(\zeta^2 - 1)(\zeta - i)H_2(\zeta)}{(\zeta - i)} = \frac{\hat{F}(\zeta)}{\zeta - i} \quad (3.36)$$

and

$$G(\zeta) = \frac{\hat{G}(\zeta)}{(\zeta - i)(\zeta^2 - 1)} \quad (3.37)$$

where now $\hat{F}(\zeta)$ and $\hat{G}(\zeta) = K_2(\zeta)(\zeta - i)$ are two functions to be found: they are analytic and single-valued on the inside, and on the boundary, of the unit disk.

3.3.3 Determining $\hat{F}(\zeta)$ and $\hat{G}(\zeta)$ from the no-slip boundary condition.

We now use the fact that the fluid is stationary on the walls, which correspond to the boundary of the unit disk in the ζ -plane, or where

$$\bar{\zeta} = \frac{1}{\zeta}. \quad (3.38)$$

Writing the no-slip condition (3.19) in the ζ -coordinates gives

$$u + iv = 0 = -F(\zeta) + \frac{z(\zeta)}{\bar{z}'(1/\zeta)} \bar{F}'(1/\zeta) + \bar{G}(1/\zeta). \quad (3.39)$$

Next, we have that

$$\frac{z(\zeta)}{\bar{z}'(1/\zeta)} = \frac{1 + \zeta^2}{\zeta(\zeta^2 - 1)} \quad (3.40)$$

and so upon substitution of the ansatz (3.37) and the conformal map into this, we have

$$0 = -\frac{\hat{F}(\zeta)}{(\zeta - i)} + \frac{(1 + \zeta^2)}{\zeta(\zeta^2 - 1)} \left[\frac{\zeta^2 \bar{\hat{F}}(1/\zeta)}{(\zeta - i)^2} - \frac{i\zeta \bar{\hat{F}}'(1/\zeta)}{(\zeta - i)} \right] + \frac{\zeta^3 \bar{\hat{G}}(1/\zeta)}{(1 + i\zeta)(1 - \zeta^2)}. \quad (3.41)$$

Rearranging this, we see that

$$0 = -\zeta(\zeta^2 - 1)(\zeta - i)\hat{F}(\zeta) + \zeta^2(1 + \zeta^2)\bar{\hat{F}}(1/\zeta) - i(1 + \zeta^2)\zeta(\zeta - i)\bar{\hat{F}}'(1/\zeta) + i\zeta^4(\zeta - i)\bar{\hat{G}}(1/\zeta). \quad (3.42)$$

From this it is clear that

$$\hat{F}(\zeta) = F_0 + F_1\zeta \quad (3.43)$$

only, as any term of $\mathcal{O}(\zeta^2)$ cannot be balanced by any other terms and hence is not present.

Furthermore, this implies that

$$F(\zeta) = \frac{F_0 + F_1\zeta}{\zeta - i} = F_1 + \frac{F_0 + iF_1}{\zeta - i} \quad (3.44)$$

and so we can set $F_1 = 0$ without loss of generality, as the velocity condition (3.19) shows that $f(z)$ has an additive degree of freedom. The constant F_0 may be found from the far field condition (3.20) which, in ζ -plane, is that

$$F(\zeta) \rightarrow \frac{i}{2}z(\zeta) = \frac{i\zeta}{(\zeta^2 + 1)} = \frac{i\zeta}{(\zeta + i)(\zeta - i)} \quad (3.45)$$

and hence, as $\zeta \rightarrow +i$,

$$F(\zeta) \rightarrow \left(\frac{i}{2}\right) \frac{1}{\zeta - i}. \quad (3.46)$$

This implies that $F_0 = i/2$ and so

$$F(\zeta) = \frac{i}{2(\zeta - i)}. \quad (3.47)$$

Similarly it can be shown that

$$G(\zeta) \rightarrow -iz(\zeta) = (-i)\frac{1}{\zeta - i}. \quad (3.48)$$

Next, we rearrange (3.42) to give

$$\hat{G}(\zeta) = i\zeta(1 - \zeta^2)\overline{\hat{F}}(1/\zeta) + \zeta(1 + \zeta^2)\hat{F}'(\zeta) - \zeta(\zeta + i)\hat{F}(\zeta). \quad (3.49)$$

But, from (3.46) we know that $\hat{F}(\zeta) = i/2$, and so relation (3.49) reveals that

$$\hat{G}(\zeta) = \frac{1}{2} [2\zeta - i\zeta^2 - \zeta^3]. \quad (3.50)$$

In summary, we have that

$$F(\zeta) = \frac{i}{2(\zeta - i)} \quad \text{and} \quad G(\zeta) = \frac{2\zeta - i\zeta^2 - \zeta^3}{2(\zeta - i)(\zeta^2 - 1)}. \quad (3.51)$$

Additionally, note that

$$G(\zeta) \rightarrow \frac{4i}{(-4)} \frac{1}{\zeta - i} = -\frac{i}{\zeta - i} \quad (3.52)$$

as $\zeta \rightarrow i$ which is consistent with (3.48).

Now that we have the Goursat functions everywhere in the unit disk (and hence in the physical domain, via the conformal map), expression (3.19) gives the velocity everywhere. The streamlines for this flow are shown in Figure 3.3.

3.3.4 Comparison to Smith's solution [2].

Smith [2] found that (3.3) is the stream function for the problem of a uniform shear flow past a wall with a gap. As a check on our solution, we retrieve his from ours. Using our

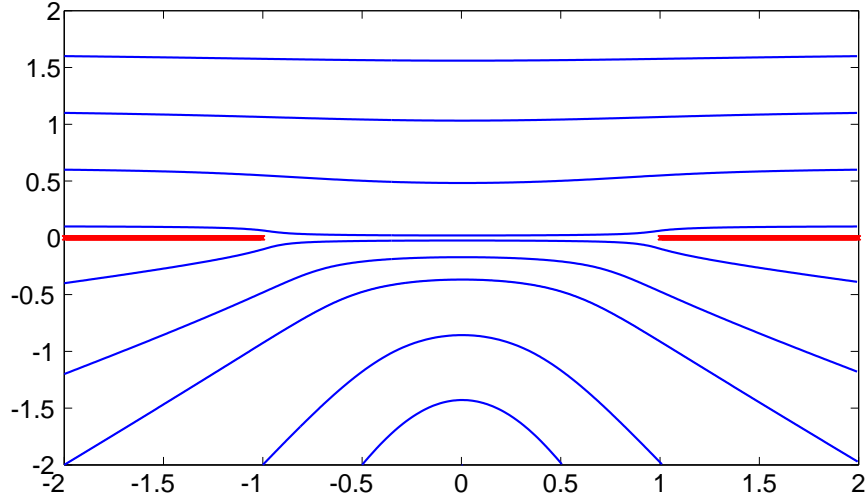


Figure 3.3: Streamlines of shear flow past a single gap. The fluid in the lower half plane is only driven by the shear flow in the upper half plane and hence, if there was no gap, it would remain stationary.

solution in the velocity condition (3.19) gives the velocity at any given point in the flow as a function of ζ and its conjugate, $\bar{\zeta}$. Specifically, using (3.42) we have

$$\begin{aligned}
 u + iv &= -\frac{i}{2(\zeta - i)} + \frac{i\zeta(1 + \bar{\zeta}^2)^2}{2(\zeta^2 + 1)(1 - \bar{\zeta}^2)(\bar{\zeta} + i)^2} + \frac{2\bar{\zeta} + i\bar{\zeta}^2 - \bar{\zeta}^3}{2(\bar{\zeta} + i)(\bar{\zeta}^2 - 1)} \\
 &= -\frac{i}{2(\zeta - i)} + \frac{i\zeta(1 + \bar{\zeta}^2)(\bar{\zeta} + i)(\bar{\zeta} - i)}{2(1 + \zeta^2)(1 - \bar{\zeta}^2)(\bar{\zeta} + i)^2} + \frac{(2\bar{\zeta} + i\bar{\zeta}^2 - \bar{\zeta}^3)(\bar{\zeta} - i)(1 + \zeta^2)}{2(1 + \zeta^2)(1 + \bar{\zeta}^2)(\bar{\zeta}^2 - 1)} \\
 &= \kappa(\zeta, \bar{\zeta}) \left[2i\zeta^2\bar{\zeta}^3 - 2i\zeta^2\bar{\zeta} + 3\zeta^2\bar{\zeta}^2 + 2i\bar{\zeta}^3 - 2i\bar{\zeta} + 3\bar{\zeta}^2 - 2i\zeta\bar{\zeta}^4 - 2\zeta\bar{\zeta}^3 \right. \\
 &\quad \left. + 2i\zeta - 2\zeta\bar{\zeta} - \zeta^2\bar{\zeta}^4 - 1 \right]
 \end{aligned}$$

where

$$\kappa(\zeta, \bar{\zeta}) = \frac{1}{2(1 + \zeta^2)(1 + \bar{\zeta}^2)(\bar{\zeta}^2 - 1)}. \quad (3.53)$$

This describes the velocity anywhere inside the fluid. It has been written in this way for ease of comparison to Smith's solution (3.3).

Next, we may write Smith's solution (3.3) as

$$\psi = \frac{1}{2}y^2 + \frac{y}{2\sqrt{2}}\alpha(x, y) \quad (3.54)$$

where

$$\alpha(x, y) = \left[y^2 - x^2 + 1 + \{(y^2 + x^2)^2 + 2(y^2 - x^2) + 1\}^{\frac{1}{2}} \right]^{\frac{1}{2}}. \quad (3.55)$$

Introducing the complex variable $z = x + iy$ gives

$$\psi = -\frac{1}{8}(z - \bar{z})^2 - \frac{i}{4\sqrt{2}}(z - \bar{z})\alpha(z, \bar{z}). \quad (3.56)$$

From this, the velocity can be deduced as

$$u + iv = -2i \frac{\partial \psi}{\partial \bar{z}} \quad (3.57)$$

and hence is

$$\begin{aligned} u + iv|_S &= \frac{i}{2}(\bar{z} - z) + \frac{1}{2\sqrt{2}} \left\{ \alpha + (\bar{z} - z) \frac{\partial \alpha}{\partial \bar{z}} \right\} \\ &= i \left[\frac{\bar{\zeta}}{\bar{\zeta}^2 + 1} - \frac{\zeta}{\zeta^2 + 1} \right] + \frac{1}{2\sqrt{2}} \left\{ \alpha + 2 \left(\frac{\bar{\zeta}}{\bar{\zeta}^2 + 1} - \frac{\zeta}{\zeta^2 + 1} \right) \frac{\partial \alpha}{\partial \bar{z}} \right\} \end{aligned} \quad (3.58)$$

where $|_S$ denotes the velocity found by Smith [2]. Let us now explore the function $\alpha(z, \bar{z})$ in order to simplify the above expression. Note that

$$y^2 - x^2 = -\frac{1}{2}(z^2 + \bar{z}^2) \quad \text{and} \quad y^2 + x^2 = z\bar{z}. \quad (3.59)$$

Using these in the definition of $\alpha(x, y)$ gives

$$\begin{aligned}\alpha(z, \bar{z}) &= \left[1 - \frac{1}{2}(z^2 + \bar{z}^2) + \{z^2\bar{z}^2 - z^2 - \bar{z}^2 + 1\}^{\frac{1}{2}} \right]^{\frac{1}{2}} \\ &= \frac{1}{\sqrt{2}} \left[2 - z^2 - \bar{z}^2 + 2(z^2 - 1)^{\frac{1}{2}}(\bar{z}^2 - 1)^{\frac{1}{2}} \right]^{\frac{1}{2}}.\end{aligned}$$

Next, using the definition of $z(\zeta)$ we have that

$$z^2 - 1 = -\frac{(\zeta^2 - 1)^2}{(\zeta^2 + 1)^2}. \quad (3.60)$$

Thus, taking the square root of this gives

$$(z^2 - 1)^{\frac{1}{2}} = \pm i \frac{(\zeta^2 - 1)}{(\zeta^2 + 1)} \quad \text{and} \quad (\bar{z}^2 - 1)^{\frac{1}{2}} = \mp i \frac{(\bar{\zeta}^2 - 1)}{(\bar{\zeta}^2 + 1)}. \quad (3.61)$$

Using this in the above expression for α gives

$$\begin{aligned}\alpha(z, \bar{z}) &= \frac{1}{\sqrt{2}} \left[2 - \left(\frac{4\zeta^2}{(\zeta^2 + 1)^2} + \frac{4\bar{\zeta}^2}{(\bar{\zeta}^2 + 1)^2} \right) + 2 \frac{(\zeta^2 - 1)(\bar{\zeta}^2 - 1)}{(\zeta^2 + 1)(\bar{\zeta}^2 + 1)} \right]^{\frac{1}{2}} \\ &= \frac{1}{\sqrt{2}(\zeta^2 + 1)(\bar{\zeta}^2 + 1)} [2(\zeta^2 + 1)^2(\bar{\zeta}^2 + 1)^2 - 4\zeta^2(\bar{\zeta}^2 + 1)^2 - \\ &\quad - 4\bar{\zeta}^2(\zeta^2 + 1)^2 + 2(\zeta^4 - 1)(\bar{\zeta}^4 - 1)] \\ &= \frac{1}{\sqrt{2}(\zeta^2 + 1)(\bar{\zeta}^2 + 1)} [4\zeta^4\bar{\zeta}^4 - 8\zeta^2\bar{\zeta}^2 + 4]^{\frac{1}{2}} \\ &= \sqrt{2} \frac{(\zeta^2\bar{\zeta}^2 - 1)}{(\zeta^2 + 1)(\bar{\zeta}^2 + 1)}.\end{aligned}$$

Next, we can differentiate (3.60) with respect to \bar{z} to give

$$\frac{\partial \alpha}{\partial \bar{z}} = \frac{1}{2\alpha} \left[-\bar{z} + \frac{\bar{z}(z^2 - 1)^{\frac{1}{2}}}{(\bar{z}^2 - 1)^{\frac{1}{2}}} \right] = -\frac{\bar{z}}{2\alpha} \left[1 - \left(\frac{z^2 - 1}{\bar{z}^2 - 1} \right)^{\frac{1}{2}} \right]. \quad (3.62)$$

Using relations (3.61), we have that

$$\begin{aligned} \frac{\partial \alpha}{\partial \bar{z}} &= -\frac{\bar{z}}{2\alpha} \left[1 + \frac{(\zeta^2 - 1)(\bar{\zeta}^2 + 1)}{(\zeta^2 + 1)(\bar{\zeta}^2 - 1)} \right] \\ &= -\frac{\bar{z}}{2\alpha(\zeta^2 + 1)(\bar{\zeta}^2 - 1)} \left[(\zeta^2 + 1)(\bar{\zeta}^2 - 1) + (\zeta^2 - 1)(\bar{\zeta}^2 + 1) \right] \\ &= -\frac{\bar{z}(\zeta^2 \bar{\zeta}^2 - 1)}{\alpha(\zeta^2 + 1)(\bar{\zeta}^2 - 1)}. \end{aligned}$$

When we use the above expression for α , we get

$$\frac{\partial \alpha}{\partial \bar{z}} = \frac{\sqrt{2} \bar{\zeta}}{\bar{\zeta}^2 - 1}. \quad (3.63)$$

Using this in the expression for Smith's velocity (3.58) gives

$$\begin{aligned} u + iv|_S &= i \left[\frac{\bar{\zeta}}{\bar{\zeta}^2 + 1} - \frac{\zeta}{\zeta^2 + 1} \right] - \frac{(\zeta^2 \bar{\zeta}^2 - 1)}{2(\zeta^2 + 1)(\bar{\zeta}^2 + 1)} \\ &\quad + \frac{\bar{\zeta}}{(\bar{\zeta}^2 - 1)} \left(\frac{\bar{\zeta}}{\bar{\zeta}^2 + 1} - \frac{\zeta}{\zeta^2 + 1} \right) \\ &= \left[\frac{\bar{\zeta}}{\bar{\zeta}^2 + 1} - \frac{\zeta}{\zeta^2 + 1} \right] \left(i + \frac{\bar{\zeta}}{\bar{\zeta}^2 - 1} \right) - \frac{\zeta^2 \bar{\zeta}^2 - 1}{2(\zeta^2 + 1)(\bar{\zeta}^2 + 1)} \end{aligned}$$

which may be written as

$$\begin{aligned}
u + iv_S &= \kappa(\zeta, \bar{\zeta}) \left[\left\{ \bar{\zeta}(\zeta^2 + 1) - \zeta(\bar{\zeta}^2 + 1) \right\} \left\{ 2i(\bar{\zeta}^2 - 1) + 2\bar{\zeta} \right\} \right] \\
&\quad - \kappa(\zeta, \bar{\zeta}) \left[(\zeta^2 \bar{\zeta}^2 - 1)(\bar{\zeta}^2 - 1) \right] \\
&= \kappa(\zeta, \bar{\zeta}) \left[2i\zeta^2 \bar{\zeta}^3 - 2i\zeta^2 \bar{\zeta} + 3\zeta^2 \bar{\zeta}^2 + 2i\bar{\zeta}^3 - 2i\bar{\zeta} + 3\bar{\zeta}^2 - 2i\zeta \bar{\zeta}^4 - 2\zeta \bar{\zeta}^3 \right. \\
&\quad \left. + 2i\zeta - 2\zeta \bar{\zeta} - \zeta^2 \bar{\zeta}^4 - 1 \right]
\end{aligned}$$

with $\kappa(\zeta, \bar{\zeta})$ given by (3.53). This is exactly the same as our solution and hence we have shown that our solution is identical to that of Smith [2], although both were found using different techniques.

3.4 Stagnation point flow past a wall with a gap.

We have shown how the use of complex variable techniques greatly simplified the task of determining the solution for a uniform shear flow past an infinite no-slip wall with a gap, compared to the method taken by Smith [2]. We now use our method to find the stagnation point flow, defined in (3.4), past the same geometry as above. The fluid in the lower half plane is driven only by the flow in the upper half plane, and is quiescent far beneath the wall. Our method offers a new approach to solving the same problem which was previously solved by Ko and Jeong [3].

3.4.1 Mathematical formulation

We want to find a stream function, ψ , which satisfies the biharmonic equation everywhere in the fluid such that the velocity is zero along the walls $|x| > 1$ and that, as we move far above the wall, the flow becomes a regular stagnation point flow with velocity

$$u + iv \rightarrow \begin{cases} 2kxy - icy^2, & \text{as } z \rightarrow \infty^+ \\ 0 & \text{as } z \rightarrow \infty^- \end{cases} \quad (3.64)$$

Furthermore, we require that the pressure takes the form

$$p \rightarrow \begin{cases} -2ky + \Delta P, & \text{as } z \rightarrow \infty^+ \\ -\Delta P, & \text{as } z \rightarrow \infty^-. \end{cases} \quad (3.65)$$

Consider first the limiting form of the velocity far above the wall. Here, we have that $u + iv = ky(2x - iy)$ so upon using the fact that $x = (z + \bar{z})/2$ and $y = -i(z - \bar{z})/2$, we have

$$u + iv = -\frac{ik}{4}z^2 - \frac{ik}{2}z\bar{z} + \frac{3ik}{4}\bar{z}^2. \quad (3.66)$$

From (3.19) we see that the far field forms of the velocity $f(z)$ and $g'(z)$ are therefore

$$f(z) \rightarrow \frac{ikz^2}{4}, \quad g'(z) \rightarrow -\frac{3ikz^2}{4}. \quad (3.67)$$

However, given that there is an additional pressure (which has no velocity contribution) at the upper and lower infinities, and that $p = 4\mu\text{Re}[f'(z)]$ (where μ is the viscosity), we see that the limiting forms of the Goursat functions are

$$f(z) \rightarrow \begin{cases} ikz^2/4 + \Delta Pz/4\mu + \mathcal{O}(1), & \text{as } z \rightarrow \infty^+ \\ -\Delta Pz/4\mu + \mathcal{O}(1), & \text{as } z \rightarrow \infty^- \end{cases} \quad (3.68)$$

and

$$g'(z) \rightarrow \begin{cases} -3ikz^2/4 + \mathcal{O}(1), & \text{as } z \rightarrow \infty^+ \\ \mathcal{O}(1), & \text{as } z \rightarrow \infty^-. \end{cases} \quad (3.69)$$

We again introduce the conformal map (3.23) and recall that $\zeta \rightarrow +i$ as we move away from the wall towards ∞^+ . Here, $f(z)$ has both a double pole (for the velocity) and a single pole (for the additional pressure), while $g'(z)$ only has a double pole. At the lower infinity, corresponding to $\zeta = -i$, $f(z)$ only admits a simple pole while $g'(z)$ is, at most, a constant there. The only other singularities in the functions arise by virtue of the corners at the end of the plates at which point $f(z(\zeta))$ is analytic while $g'(z(\zeta))$ admits a simple pole. Putting this together, we again define $F(\zeta) \equiv f(z(\zeta))$ and $G(\zeta) \equiv g'(z(\zeta))$ and assume the ansatz

$$F(\zeta) = \frac{\hat{F}(\zeta)}{(\zeta - i)^2(\zeta + i)}, \quad G(\zeta) = \frac{\hat{G}(\zeta)}{(\zeta^2 - 1)(\zeta - i)^2} \quad (3.70)$$

where $\hat{F}(\zeta)$ and $\hat{G}(\zeta)$ are the two functions to be found: again they are analytic and single-valued in the closure of the unit disk.

3.4.2 Determining $\hat{F}(\zeta)$ and $\hat{G}(\zeta)$ from the no-slip boundary condition.

We again refer to the fact that the fluid is stationary on the walls, which correspond to the boundary of the unit disk in the ζ -plane where $\bar{\zeta} = 1/\zeta$. The no-slip velocity condition reads

$$0 = -F(\zeta) + \frac{z(\zeta)}{\bar{z}'(1/\zeta)} \bar{F}'(1/\zeta) + \bar{G}(1/\zeta). \quad (3.71)$$

Upon substitution of the ansatz (3.70) and the conformal map into this, we have

$$\begin{aligned} 0 = & -\frac{F(\zeta)}{(\zeta - i)^2(\zeta + i)} \\ & + \frac{(1 + \zeta^2)}{\zeta(\zeta^2 - 1)} \left[\frac{-i\zeta^3 \bar{F}'(1/\zeta)}{(\zeta - i)^2(\zeta + i)} + \frac{2\zeta^4 \bar{F}(1/\zeta)}{(\zeta - i)^3(\zeta + i)} - \frac{\zeta^4 \bar{F}(1/\zeta)}{(\zeta - i)^2(\zeta + i)^2} \right] \\ & + \frac{\zeta^4 \bar{G}(1/\zeta)}{(\zeta - i)^2(\zeta^2 - 1)}. \end{aligned} \quad (3.72)$$

Rearranging this, we see that

$$\begin{aligned} 0 = & -(\zeta^2 - 1)\hat{F}(\zeta) - i\zeta^2(1 + \zeta^2)\bar{F}'(1/\zeta) + 2\zeta^3(\zeta + i)\bar{F}(1/\zeta) \\ & - \zeta^3(\zeta - i)\bar{F}(1/\zeta) + \zeta^4(\zeta + i)\bar{G}(1/\zeta). \end{aligned} \quad (3.73)$$

From this it can be seen that $\hat{F}(\zeta)$ is at most a cubic as any term of $\mathcal{O}(\zeta^4)$ cannot be balanced by any other terms and hence is not present. With this in mind, we may write

$$F(\zeta) = A + \frac{B}{(\zeta - i)^2} + \frac{C}{\zeta - i} + \frac{D}{\zeta + i}, \quad (3.74)$$

where A, B, C and D are constants. Again, we may set the $A = 0$ without loss of generality from the additive degree of freedom. The other constants can be found from the far field

condition (3.68) and (3.69) as the map takes the form

$$z(\zeta) = \frac{1}{\zeta - i} \left[\frac{2\zeta}{\zeta + i} \right] \quad (3.75)$$

which can be expanded around $\zeta = -i$ to give

$$z(\zeta) = \frac{1}{\zeta - i} - \frac{i}{2} + \dots \quad (3.76)$$

while around $\zeta = +i$ the map takes the form

$$z(\zeta) = \frac{1}{\zeta + i} + \dots \quad (3.77)$$

Hence, the far field forms of $f(z)$ are

$$\begin{aligned} F(\zeta) &\rightarrow \frac{ik}{4} \frac{1}{(\zeta - i)^2} + \frac{k/\mu + \Delta P}{4} \frac{1}{(\zeta - i)} + \dots \\ F(\zeta) &\rightarrow -\frac{\Delta P}{4} \frac{1}{(\zeta + i)} + \dots \end{aligned} \quad (3.78)$$

as we move to infinity in the upward and downward directions respectively. Writing these limiting forms in this way means that we may read off the constants in (3.74) as

$$B = \frac{ik}{4}, \quad C = \frac{1}{4} \left(\frac{k}{\mu} + \Delta P \right), \quad D = -\frac{\Delta P}{4\mu} \quad (3.79)$$

and hence we have the full expression for $f(z)$,

$$F(\zeta) = \frac{ik}{4} \frac{1}{(\zeta - i)^2} + \left[\frac{\Delta P}{4\mu} + \frac{k}{4} \right] \frac{1}{(\zeta - i)} - \frac{\Delta P}{4\mu} \frac{1}{(\zeta + i)}. \quad (3.80)$$

By rearranging (3.71), we then have $G(\zeta)$ given by

$$G(\zeta) = \bar{F}(1/\zeta) - \frac{\bar{z}(1/\zeta)}{z'(\zeta)} F'(\zeta) \quad (3.81)$$

Note that from (3.73) we see that when $\zeta \rightarrow i$, $\hat{G}(\zeta)$ takes the value

$$\hat{G}(i) = \frac{3ik}{2}. \quad (3.82)$$

Note also that this is consistent with (3.69) as

$$G(\zeta) \rightarrow -\frac{3ik}{4}z^2 = -\left(\frac{3ik}{4}\right)\frac{1}{(\zeta - i)^2} + \dots \quad (3.83)$$

and so, given (3.70) we can expect that $G(\zeta) = 3ik/2$ as $\zeta \rightarrow i$.

3.4.3 Results: streamlines of stagnation point flow near a wall with a gap.

Now that the Goursat functions are known, we are able to determine the velocity everywhere. We now study the streamlines of this flow for a number of representative values of k and ΔP in order to present different qualitative phenomena of this flow. In what follows, we fix $\mu = k = 1$ and vary the value of ΔP . This is equivalent to varying the number, N , defined by Ko and Jeong [3] as

$$N = \frac{\Delta P}{k\mu} \quad (3.84)$$

where μ is the viscosity of the fluid [3]. The first case to consider is one where there is no stagnation point flow and only a pressure difference between the upper and lower infinities drives the flow. This corresponds to a Sampson flow [43] with $\Delta P = 1$, $k = 0$ (and hence $N = \infty$). The flow has reflectional symmetry in both the real and imaginary axes, and has no stagnation points or eddies anywhere within the fluid; see Figure 3.4.

The second fundamental case to consider is where there is no added pressure contribution, so the flow is only driven by the far field stagnation point flow in the upper half plane. Therefore $\Delta P = N = 0$ and in this case a saddle point appears at the origin. In addition to this, there are a pair of viscous eddies extending to infinity in the lower half plane, both symmetric about the imaginary axis, see Figure 3.5.

For the general case where $N \neq \{0, \infty\}$, the additional pressure contribution $2\Delta P$ acts in

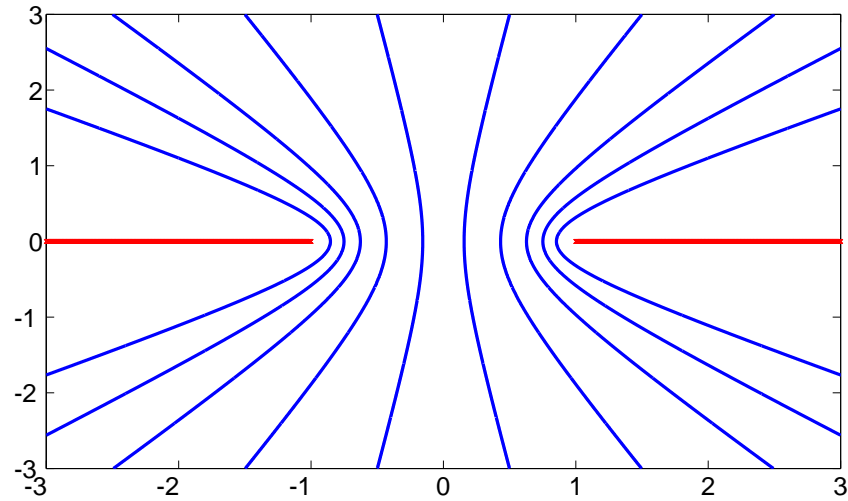


Figure 3.4: Streamlines for a flow through a gap driven only by a downwardly directed pressure gradient. Here $\Delta P = 1$ and $k = 0$ so that there is no stagnation point flow. This corresponds to $N = \infty$, as defined by Ko and Joeng [3].

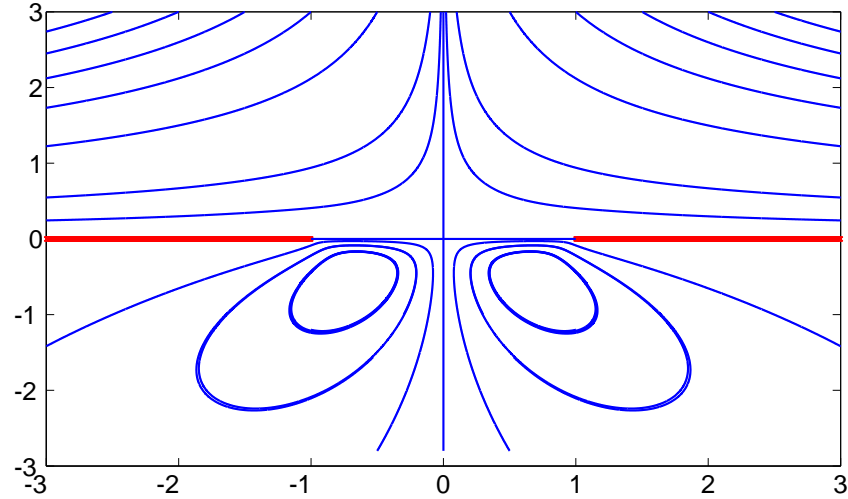


Figure 3.5: Streamlines for a stagnation point flow above a gap with no added pressure gradient and so $\Delta P = N = 0$ with $k = 1$. A single saddle stagnation point appears at the origin while two viscous eddies, both extending to infinity, are formed symmetrically in the lower half plane below the gap and the wall.

competition with the strength of the (downwardly directed) stagnation point flow: If k and ΔP are of the same sign and magnitude, and ΔP is positive, then both the stagnation point flow and the added pressure act in the same direction and fluid will be “pushed” downwards through the gap and no eddies will be formed, see Figure 3.6. If, on the other hand, k is of the same magnitude as ΔP , but this time ΔP is negative, there is an upwards pressure gradient pushing fluid against the downward stagnation point flow, as in Figure 3.7. Here there is only one saddle stagnation point in the upper half plane, and one pair of viscous eddies appearing between the ends of the plates and the streamlines which have separated from the edges. Finally, if k is larger than ΔP , then the flow will be dominated by the stagnation point flow which acts in “competition” with the pressure, as demonstrated by Figure 3.8.

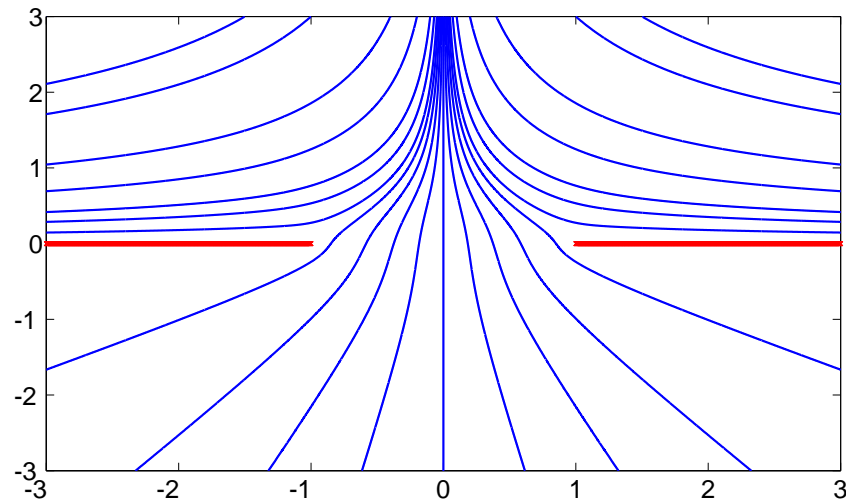


Figure 3.6: Streamlines when the added pressure gradient is in the same direction as the stagnation point flow. Here $k = \Delta P = 1$, and the fluid is pushed through the gap. There are no viscous eddies formed.

3.4.4 Comparison to Ko and Jeong’s solution [3].

Ko and Jeong [3] found that (3.11) are the appropriate analytic functions which construct the stream function of this problem. From their definition of $F_J(z)$ and $G_J(z)$ from the

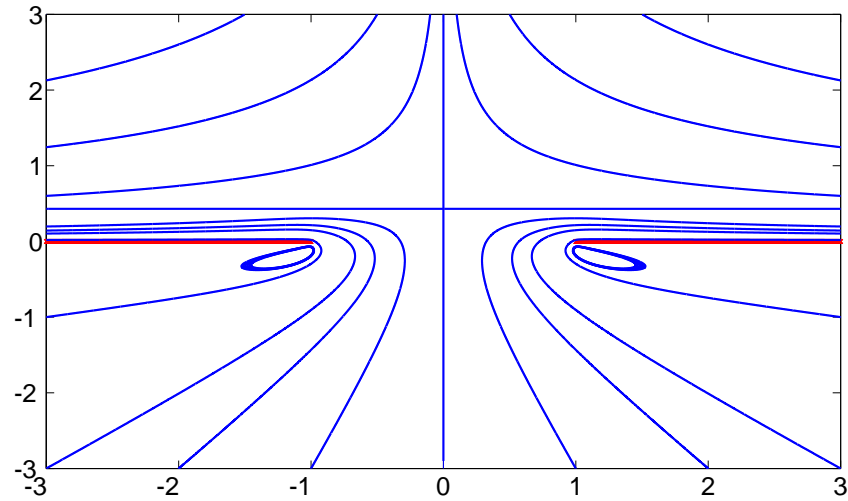


Figure 3.7: Streamlines when the added pressure gradient is in the opposite direction to the stagnation point flow. Here $\Delta P = N = -0.5$ with $k = 1$. There is one saddle stagnation point appearing above the gap while two viscous eddies formed underneath the edges of the plates and above the streamline which separates from the edge.

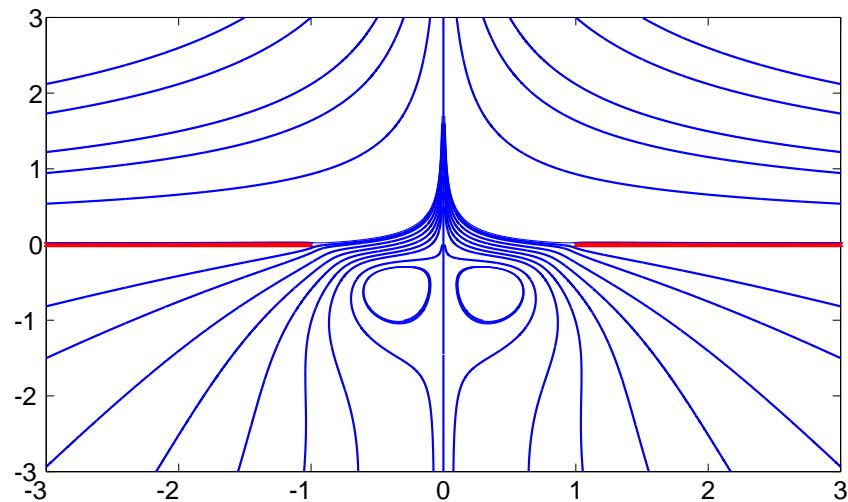


Figure 3.8: Streamlines for $k = 1$ and $\Delta P = 0.07$. The effect of the added (slight) downward directed pressure gradient is to reduce the size of the symmetric viscous eddies, visualised in Figure 3.5.

velocity condition, it can be seen that these functions are related to $f(z)$ and $g'(z)$ via the relations

$$\begin{aligned} F_J(z) &= g'(z) + zf'(z) = -\frac{ikz}{8} [z + (z^2 - 1)^{1/2}] + \frac{\Delta P}{4\mu} (z^2 - 1)^{1/2} \\ G_J(z) &= f(z) = \frac{ikz}{8} [z + (z^2 - 1)^{1/2}] + \frac{\Delta P}{4\mu} (z^2 - 1)^{1/2}. \end{aligned} \quad (3.85)$$

As a check on our method, we must show that our solutions are identical. Let us examine (3.80) for $f(z)$ and check that this is the same as $G_J(z)$: $F_J(z)$ will then necessarily follow from the no-slip boundary condition. Note that we may write expression (3.80) as

$$F(\zeta) = \frac{k\zeta}{4(\zeta - i)^2} + \frac{i\Delta P}{2\mu(\zeta^2 + 1)}. \quad (3.86)$$

Also note that from (3.23) we have that $\zeta = (1 \pm i(z^2 - 1)^{1/2})/z$, and we choose the upper branch of this so that $\zeta = 0$ is mapped to $z = 0$. Hence

$$\zeta = \frac{1 + i(z^2 - 1)^{1/2}}{z}. \quad (3.87)$$

Consider the first term of (3.86). We have that

$$\frac{1}{(\zeta - i)^2} = \frac{z(\zeta + i)}{2\zeta}, \quad \frac{1}{(\zeta - i)^2} = \frac{z^2(\zeta + i)^2}{4\zeta^2} \quad (3.88)$$

and so

$$\frac{k\zeta}{4(\zeta - i)^2} = \frac{kz}{4} \left(z\zeta + 2iz - \frac{z}{\zeta} \right). \quad (3.89)$$

Next, as we have that $z/\zeta = 1 - i(z^2 - 1)^{1/2}$, this becomes

$$\frac{ki z}{8} [z + (z^2 - 1)^{1/2}] \quad (3.90)$$

which is exactly the first term of $G_J(z)$ as given in (3.85) by Ko and Jeong [3]. Next, the second term of (3.80) is

$$\frac{i\Delta P}{2\mu} \frac{1}{(\zeta^2 + 1)} = \frac{i\Delta P z}{4\mu\zeta} \quad (3.91)$$

which can be simplified to

$$c + \frac{\Delta P}{4\mu}(z^2 - 1)^{1/2} \quad (3.92)$$

where $c = i\Delta P/4$, which is exactly the second term of $G_J(z)$ in (3.85) up to an additive constant. Note that we have set our additive degree of freedom by setting $A = 0$ in (3.74) while the authors have not, and hence the two solutions can be expected to differ by this constant. Indeed, a translation $G_J(z) \rightarrow G_J(z) + \bar{c}$ will not affect the velocity if $F_J(z) \rightarrow F_J(z) + c$. And, as $F_J(z) = g'(z) + zf'(z)$, we can expect our function $g'(z)$ to differ from $F_J(z)$ by c . In other words, we can expect that

$$g'(z) = F_J(z) - zf'(z) - c \quad (3.93)$$

We have therefore shown that the two solutions are identical, although our approach has been fundamentally different.

3.5 Summary

We have presented exact solutions for the Stokes flow past an infinite flat wall with a gap. Using the results of Dean and Montagnon [40] we have been able to characterise the flow at the sharp ends of the walls. Then, by developing a new mathematical approach based on conformal mappings, we have been able to find the flow that is driven either by a uniform shear flow or a stagnation point flow at infinity. Both of these cases have been independently solved by Smith [2] (for the former) and Ko and Jeong [3] (for the latter) using entirely different methods. We have shown that our solutions to both problems are identical to the results published by these authors.

A significant advantage of the method we have presented in this chapter is that only a slight change in far field conditions was necessary in order to solve both problems considered by the above authors. Indeed, the method may readily be modified to handle other forms of far field flows, too. In particular, Antanovskii [44] studied the Taylor four-roller mill experiment, where a deformable bubble is placed in a viscous fluid which was driven, in the far field, by four rotating cylinders. In this case, $f(z)$ tends to a cubic polynomial in the

far field, while $g'(z)$ approaches a linear function [44]. The method presented here would then be amended in such a way that the ansatz for $F(\zeta)$ would be

$$F(\zeta) = A + \frac{B}{(\zeta - i)^3} + \frac{C}{(\zeta - i)^2} + \frac{D}{(\zeta - i)} + \frac{E}{\zeta + i} \quad (3.94)$$

with the constants matched to the far field forms of the Goursat functions. Another example of a far field velocity would be one that is constructed using a combination of any, or all, of the above three.

These solutions have been documented as a contribution to the mathematical theory of Stokes flows. The solutions have been used to study the effects of an occlusion in the wall and are expected to be useful in a variety of different physical applications, in particular to the study of low Reynolds number swimming near boundaries with gap. In the following chapter, we will build on the solutions of this chapter and employ the singularity model of Crowdy and Or [1] in order to provide insight into the dynamics of such a swimmer in this complicated geometry.

Chapter 4

Swimming in low Reynolds numbers near a wall with a gap.

4.1 Introduction

Chapter 2 presented a study of a two-dimensional swimming micro-organism in the vicinity of an infinite flat wall. The next natural question to ask is how a low Reynolds number swimmer behaves in a more complicated confined geometry than that of a simple half plane above a wall. We do this by allowing the boundary to admit a finite-length gap [45]. Studying the swimmer's interaction with such a domain will provide insight on how such organisms behave in the presence of an orifice or an opening in their bounding domains. This will be the focus of the present chapter.

The fluid in this confined region fills the area above and below a no-slip wall, positioned along the real axis with a gap between $x = \pm 1$. The ends of the wall endow the domain with two sharp corners - this is an additional complication which will be resolved in this chapter.

As we have seen in chapter 3, this is not the first study of Stokes flows near such a region. In particular both Smith [2] and Ko and Jeong [3] each considered various Stokes flows past similar solid boundaries. The work within that chapter expounded a novel conformal

mapping approach which reappraised the solutions of Smith [2] and Ko and Jeong [3] in a unified fashion. This approach is a useful one as it can be generalised in a natural way to solve the problem of interest here.

4.1.1 The point swimmer model.

We will use the Crowdy and Or [1] point singularity model to study the swimming dynamics of a swimmer near a wall with a gap. Recall that using this description, the swimmer is represented by a stresslet of strength $\lambda = \exp(2i\theta)$ together with a superposed irrotational quadrupole of strength $2\epsilon^2\lambda$. As described in chapter 2, Crowdy and Or [1] derived their choice of singularities by assuming their treadmilling swimmer had radius ϵ , however in this chapter it will enter our analysis only as a parameter. The model's success in capturing the qualitative motion of swimmers near an infinite wall (as seen in numerical and laboratory experiments [23, 25]) motivates its adoption when considering swimmers in more complicated confined domains. Therefore, in order to extend this study to the case where the wall admits a finite-length gap, we focus attention on how the above *point singularity* interacts with its bounding environment. Indeed, we aim to provide a predictive theory which may be tested in future laboratory and numerical experiments.

In studying the dynamics of a swimmer above an infinite flat wall, Crowdy and Or [1] utilised the familiar method of images to determine how the swimmer interacted with the boundary. The simplicity of this method was due to the straight forward geometry of the fluid domain which made it immediately clear that the swimmer's image should be placed at its reflection in the wall. In the case where the boundary admits a gap, it quickly becomes less clear where an image system should be placed. This, together with the presence of the sharp corners at the ends of the gap, present additional complications to the model. We overcome these by using complex variables techniques to model the appropriate singularity structure of the swimmer and the corners of the wall. By introducing a conformal map to associate the physical fluid domain with a simpler one, these complications are ameliorated and an exact representation of the swimming dynamics is found.

4.2 Swimming near a gap in a wall.

With the singularity structure of the Goursat functions for this problem known, we turn our attention to finding the equations of the swimmer's motion explicitly.

4.2.1 Mathematical formulation.

Mathematically, we want to find a stream function ψ such that

$$\nabla^4 \psi(z, \bar{z}) = 0 \quad (4.1)$$

with $u + iv = 0$ on $|x| > 1$. We also require that the velocity has singularities corresponding to those of a superposed stresslet and irrotational quadrupole at the position of the swimmer, z_d . We again use the same solution for the biharmonic equation (2.13) as in previous chapters, where $f(z)$ and $g(z)$ are the usual Goursat functions which will now be analytic everywhere in the flow except at the position of the swimmer and corners. Once we have these functions, we may construct the velocity everywhere inside the fluid domain via the usual relation

$$u + iv = -f(z) + z\bar{f}'(\bar{z}) + \bar{g}'(\bar{z}). \quad (4.2)$$

We have shown that in order to attach the correct singularity model to the swimmer, we must choose

$$f(z) = \frac{\lambda}{z - z_d} + f_0 + f_1(z - z_d) + \dots \quad (4.3)$$

and also

$$g'(z) = \frac{2\epsilon^2\lambda}{(z - z_d)^3} + \frac{\lambda\bar{z}_d}{(z - z_d)^2} + g_0 + \dots \quad (4.4)$$

where $\lambda = \exp(2i\theta)$. Recall that the double pole of $g'(z)$ corresponded to the dipole that is associated with the stresslet, while the triple pole is that of the quadrupole. Also, the method of chapter 3 has taught us that near the corner at $z = \pm 1$, the Goursat functions take the local form

$$f(z) = (z \mp 1)^{1/2} H_1(z), \quad g'(z) = \frac{H_2(z)}{(z \mp 1)^{1/2}} \quad (4.5)$$

with $H_j(z)$ being analytic functions of z for $j = 1, 2$.

4.2.2 The Goursat functions for a swimmer near a wall with a gap.

In chapter 3, we studied the structure of the Goursat functions around the sharp corners within a fluid domain of identical geometry. We did this by introducing a conformal map of the form

$$z(\zeta) = \frac{2\zeta}{\zeta^2 + 1} \quad (4.6)$$

with inverse

$$\zeta(z) = \frac{1 - (1 - z^2)^{1/2}}{z} \quad (4.7)$$

which maps the interior of the unit disk to the region exterior to the walls in the physical (fluid) domain. With the map defined in this way, the points $\zeta = \pm 1$ were mapped to the right and left-most corners respectively. Note also that the points $\zeta = \pm i$ are mapped to $z = \infty^\pm$ respectively. Recall that $\zeta(z)$ has the required square root branch point singularity that is required of the Goursat functions and hence ζ may be used as a representative uniformisation variable. The problem then reduces to determining

$$F(\zeta) \equiv f(z(\zeta)), \quad G(\zeta) \equiv g'(z(\zeta)) \quad (4.8)$$

which are analytic and single-valued functions within the unit disk, except for at the position of the isolated singularities which we impose in order to incorporate the Crowdy and Or singularity structure [1].

With the form of the functions around the corners known, let us deduce what they must be at the swimmer's position. Recall that in the infinite wall case, Crowdy and Or [1] used the method of images to show that $f(z)$ requires a third order pole to be present at the image position of the swimmer. They also demonstrated that $g'(z)$ requires a fourth order pole at the same place. With this in mind, it is also reasonable to assume that the Goursat functions for this problem admit image singularities of the same type as those for the flat wall case.

The method of images used by Crowdy and Or [1] placed the image swimmer at its reflec-

tion in the wall, i.e at $z = \bar{z}_d$. However, when the wall admits a gap, the point \bar{z}_d is inside the fluid and so it is not immediately clear where the swimmer's image should be placed. Instead, recall that the conformal map (4.6) associates the entire two-dimensional ζ -plane to *two* sheets of Riemann surface in the z -plane. The interior of the unit ζ -disk is mapped to the “physical” fluid domain - the first sheet of the Riemann surface - while the exterior of the unit ζ -disk is mapped to the second sheet of the same surface. We therefore choose the image of the swimmer to be on the second sheet and, as $\zeta = \zeta_d$ is the preimage point of the swimmer in the unit disk, the point of reflection in the unit circle

$$\zeta = \frac{1}{\bar{\zeta}_d} \quad (4.9)$$

is the point *outside* the unit disk corresponding to the image of the swimmer on the second sheet. See Figure 4.1 for a diagrammatic representation of the two-sheeted Riemann surface with the swimmer and its image. Thus, we conclude that $F(\zeta)$ will admit a first order pole at $\zeta = \zeta_d$ (corresponding to a stresslet) together with, at most, a third order pole at the image point $\zeta = 1/\bar{\zeta}_d$. Meanwhile $G(\zeta)$ admits a third order pole at $\zeta = \zeta_d$ (allowing for the quadrupole) as well as, at most, a fourth order pole at $\zeta = 1/\bar{\zeta}_d$. These singularities will be in addition to those that arise from the corners at $\zeta = \pm 1$, as discussed above.

Keeping this in mind, we may take the ansatz

$$F(\zeta) = \frac{\hat{F}(\zeta)}{(\zeta - \zeta_d)(1 - \bar{\zeta}_d \zeta)^3}, \quad G(\zeta) = \frac{\hat{G}(\zeta)}{(\zeta - \zeta_d)^3(1 - \bar{\zeta}_d \zeta)^4(\zeta^2 - 1)} \quad (4.10)$$

where $\hat{F}(\zeta)$ and $\hat{G}(\zeta)$ are analytic functions of ζ with no poles inside the unit disk.

4.2.3 Determining $\hat{F}(\zeta)$ and $\hat{G}(\zeta)$ from the no-slip boundary condition.

We now refer to the fact that the fluid is stationary on the walls, which correspond to the boundary of the unit disk in the ζ -plane. On here, we have that

$$\bar{\zeta} = \frac{1}{\zeta} \quad (4.11)$$

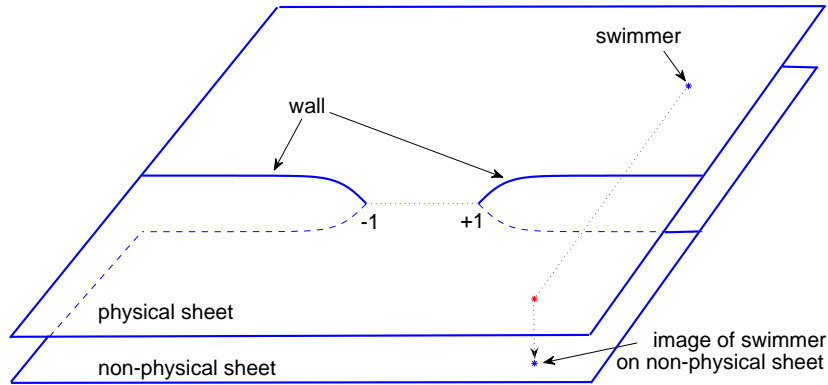


Figure 4.1: The two sheets of the Riemann surface associated with the conformal map (4.6). The upper sheet corresponds to the “physical” fluid domain, in which the swimmer resides. The lower sheet is the non-physical sheet, in which swimmer’s image will remain. In the analysis, the two sheets are glued together along the branch cuts taken as the walls: here the sheets are shown “unglued” along the walls to indicate that the image singularity is at the swimmer’s reflection in the wall on the lower sheet.

as well as the relation

$$\frac{\bar{z}(1/\zeta)}{z'(\zeta)} = \frac{\zeta(\zeta^2 + 1)}{1 - \zeta^2} \quad (4.12)$$

which we define as $R(\zeta)$. Next, the no-slip velocity condition on the boundary is

$$0 = u + iv = -F(\zeta) + \frac{z(\zeta)}{\bar{z}'(1/\zeta)} \bar{F}'(1/\zeta) + \bar{G}(1/\zeta). \quad (4.13)$$

Upon substituting the ansatz (4.10) and the conformal map into this, we have that

$$\begin{aligned}
0 = & -\frac{\hat{F}(\zeta)}{(\zeta - \zeta_d)(1 - \bar{\zeta}_d\zeta)^3} \\
& + \frac{\zeta^3(1 + \zeta^2)}{(\zeta^2 - 1)(\zeta - \zeta_d)^4(1 - \bar{\zeta}_d\zeta)^2} \left[(\zeta - \zeta_d)(1 - \bar{\zeta}_d\zeta)\overline{\hat{F}}'(1/\zeta) \right. \\
& \quad \left. - \zeta(\zeta - \zeta_d)\overline{\hat{F}}(1/\zeta) + 3\zeta_d\zeta(1 - \bar{\zeta}_d\zeta)\overline{\hat{F}}(1/\zeta) \right] \\
& + \frac{\zeta^9\overline{\hat{G}}(1/\zeta)}{(1 - \bar{\zeta}_d\zeta)^3(\zeta - \zeta_d)^4(1 - \zeta^2)}.
\end{aligned} \tag{4.14}$$

This can be rearranged to give

$$\begin{aligned}
0 = & -(\zeta^2 - 1)(\zeta - \zeta_d)^3\hat{F}(\zeta) + \zeta^3(1 + \zeta^2)(1 - \bar{\zeta}_d\zeta)^2(\zeta - \zeta_d)\overline{\hat{F}}'(1/\zeta) \\
& - \zeta^4(1 + \zeta^2)(\zeta - \zeta_d)(1 - \bar{\zeta}_d\zeta)\overline{\hat{F}}(1/\zeta) + 3\zeta_d\zeta^4(1 + \zeta^2)(1 - \bar{\zeta}_d\zeta)^2\overline{\hat{F}}(1/\zeta) \\
& - \zeta^9\overline{\hat{G}}(1/\zeta).
\end{aligned} \tag{4.15}$$

From here it is clear that $\hat{F}(\zeta)$ can not have any terms of the form ζ^5 , as it would not be possible to balance them with another term in the above expression. Hence, we deduce that

$$\hat{F}(\zeta) = \hat{A} + \hat{B}\zeta + \hat{C}\zeta^2 + \hat{D}\zeta^3 + \hat{E}\zeta^4. \tag{4.16}$$

Putting this together with relation (4.10), this means that

$$F(\zeta) = \frac{\hat{A} + \hat{B}\zeta + \hat{C}\zeta^2 + \hat{D}\zeta^3 + \hat{E}\zeta^4}{(\zeta - \zeta_d)(1 - \bar{\zeta}_d\zeta)^3} = \hat{E} + \dots \tag{4.17}$$

Therefore, \hat{E} acts as an additive constant to $F(\zeta)$, which can be set to zero without loss of generality. This is because the velocity condition (4.13) admits a natural additive degree of freedom to one of two functions $F(\zeta)$ or $G(\zeta)$. With this in mind, we may equivalently express (4.17) in partial fraction form as

$$F(\zeta) = \frac{A}{(\zeta - \zeta_d)} + \frac{B}{(\zeta - 1/\bar{\zeta}_d)^3} + \frac{C}{(\zeta - 1/\bar{\zeta}_d)^2} + \frac{D}{(\zeta - 1/\bar{\zeta}_d)}. \tag{4.18}$$

where A, B, C and D are constants. Written in this way, the first term of this corresponds to the stresslet singularity while the other terms account for the singularities generated by the swimmer's image. Next, the conjugate of the velocity condition (4.13), may be rewritten in the form

$$G(\zeta) = \overline{F}(1/\zeta) - \frac{\zeta(\zeta^2 + 1)}{(1 - \zeta^2)} F'(\zeta) \quad (4.19)$$

and so provides a functional relationship between $F(\zeta)$ and $G(\zeta)$ which also holds inside the unit disk. Upon using expression (4.18) in this, we have

$$G(\zeta) = \frac{\overline{A}\zeta}{1 - \zeta\overline{\zeta}_d} - \frac{\overline{B}\zeta^3\zeta_d^3}{(\zeta - \zeta_d)^3} + \frac{\overline{C}\zeta^2\zeta_d^2}{(\zeta - \zeta_d)^2} - \frac{\overline{D}\zeta\zeta_d}{(\zeta - \zeta_d)} \\ + \frac{\zeta(\zeta^2 + 1)}{(1 - \zeta^2)} \left[\frac{A}{(\zeta - \zeta_d)^2} + \frac{3B}{(\zeta - 1/\overline{\zeta}_d)^4} + \frac{2C}{(\zeta - 1/\overline{\zeta}_d)^3} + \frac{D}{(\zeta - 1/\overline{\zeta}_d)^2} \right]. \quad (4.20)$$

Notice that this expression has simple poles at $\zeta = \pm 1$; these are precisely the Moffatt-type singularities that we would expect $G(\zeta)$ to have due to the two corners at the ends of the walls. It also has a fourth order pole at $\zeta = 1/\overline{\zeta}_d$.

We have therefore reduced the problem to finding the four constants A, B, C and D . These are found by imposing four physical conditions, which come from equating the expansions of $F(\zeta)$ and $G(\zeta)$ in the z -plane to $f(z)$ and $g'(z)$ as given by equations (4.3) and (4.4). Specifically we find the constants A, B, C, D such that:

1. $f(z)$ has the correct singularity strength that corresponds to a stresslet at $z = z_d$ of strength λ .
2. $g'(z)$ must not have a simple pole at $z = z_d$, as this would correspond to a rotlet.
3. $g'(z)$ must have the correct double pole at z_d , accounting for the dipole of strength $\lambda\overline{z}_d$ that is associated with the stresslet.
4. $g'(z)$ must also have a triple pole at z_d of strength $2\epsilon^2\lambda$, corresponding to the superposed irrotational quadrupole that the model requires.

To do this we must express (4.18) and (4.20) in the z -plane and then compare the appropriate singularities. Note that by expanding expression (4.20) around $\zeta = \zeta_d$,

$$\begin{aligned} G(\zeta) &= \frac{1}{(\zeta - \zeta_d)^3} [-\bar{B}\zeta_d^6] + \frac{1}{(\zeta - \zeta_d)^2} [-3\bar{B}\zeta_d^5 + \bar{C}\zeta_d^4 + AR(\zeta_d)] \\ &+ \frac{1}{(\zeta - \zeta_d)} [-3\bar{B}\zeta_d^4 + 2\bar{C}\zeta_d^3 - \bar{D}\zeta_d^2 + AR'(\zeta_d)] \\ &+ \left[\bar{C}\zeta_d^2 - \bar{B}\zeta_d^3 - \bar{D}\zeta_d + \frac{1}{2}AR_{\zeta\zeta}(\zeta_d) \right] + \mathcal{O}(\zeta - \zeta_d) \end{aligned} \quad (4.21)$$

with $R(\zeta)$ defined in (4.12). Next, we refer to the expansion

$$\frac{1}{\zeta - \zeta_d} = \frac{\hat{\alpha}}{(z - z_d)} + \hat{\beta} + \hat{\gamma}(z - z_d) + \hat{\delta}(z - z_d)^2 + \dots \quad (4.22)$$

which is derived in the appendix A, with the constants $\hat{\alpha}, \hat{\beta}, \hat{\gamma}, \hat{\delta}$ known explicitly. Using this in the expression for $F(\zeta)$ given by (4.18) and comparing the simple poles corresponding to the stresslet singularity, gives

$$A = \frac{\lambda}{z'(\zeta_d)} = \frac{\lambda(1 + \zeta_d^2)^2}{2(1 - \zeta_d^2)} \quad (4.23)$$

and hence is known explicitly. Next, using the same expansions in equation (4.21) and comparing quadrupole strengths, we have that $-\bar{B}\zeta_d^6\hat{\alpha}^3 = 2\lambda\epsilon^2$ or

$$B = -\frac{\bar{\lambda}\epsilon^2 (1 + \bar{\zeta}_d^2)^6}{4\bar{\zeta}_d^6 (1 - \bar{\zeta}_d^2)^3}. \quad (4.24)$$

Similarly, comparing the double and simple poles results in

$$\bar{C} = \frac{\lambda\bar{z}_d(1 + \zeta_d^2)^4}{4\zeta_d^4(1 - \zeta_d^2)^2} - \frac{3\lambda\epsilon^2(1 - 3\zeta_d^2)(1 + \zeta_d^2)^5}{4\zeta_d^5(1 - \zeta_d^2)^4} - \frac{\lambda(1 + \zeta_d^2)^3}{2\zeta_d^3(1 - \zeta_d^2)^2} \quad (4.25)$$

and

$$\begin{aligned} \bar{D} &= \frac{\lambda\bar{z}_d(1 - 3\zeta_d^2)(1 + \zeta_d^2)^4}{2\zeta_d^3(1 - \zeta_d^4)(1 - \zeta_d^2)^2} + \frac{3\lambda\epsilon^2(1 + \zeta_d^2)^4(-1 + 5\zeta_d^2 - 11\zeta_d^4 - \zeta_d^6)}{4\zeta_d^4(1 - \zeta_d^2)^5} \\ &+ \frac{\lambda(1 + \zeta_d^2)^2(\zeta_d^4 + 4\zeta_d^2 - 1)}{2\zeta_d^2(1 - \zeta_d^2)^3}. \end{aligned} \quad (4.26)$$

With these constants known explicitly, we have expressions for $f(z)$ and $g'(z)$ in terms of the swimmer's position, z_d , and orientation, θ , at that instant. We will now use these to derive the full dynamical system which controls the swimmer's evolution.

4.2.4 Equations of motion.

Recall that we have shown that the swimmer's translational velocity is given by

$$\frac{dz_d}{dt} = -f_0 + z_d \overline{f_1} + \overline{g_0}. \quad (4.27)$$

This corresponds to the finite part of the fluid velocity at the swimmer's position. Expressed another way, the swimmer is convected only with the local fluid velocity which arises in response to the swimmer's interaction with the boundaries. The real and imaginary parts of this constitute two ordinary differential equations that govern the swimmer's horizontal and vertical displacements, respectively. To find the numbers f_0 , f_1 and g_0 , let us write

$$F(\zeta) = \frac{A}{\zeta - \zeta_d} + F_{NS}(\zeta) \quad (4.28)$$

where $F_{NS}(\zeta)$ corresponds to the non-singular components of $F(\zeta)$ given by the last three terms of (4.18). Upon using expansion (4.22) we find that $f_0 = \hat{\beta}A + F_{NS}(\zeta_d)$, or

$$f_0 = \frac{\zeta_d(\zeta_d^2 - 3)A}{(1 - \zeta_d^4)} + \frac{\overline{\zeta_d^3}B}{(|\zeta_d|^2 - 1)^3} + \frac{\overline{\zeta_d^2}C}{(|\zeta_d|^2 - 1)^2} + \frac{\overline{\zeta_d}D}{(|\zeta_d|^2 - 1)} \quad (4.29)$$

and

$$f_1 = \hat{\gamma}A + \frac{1}{z'(\zeta_d)} F'_{NS}(\zeta_d) \quad (4.30)$$

or

$$f_1 = -\frac{A}{2} \left[\frac{(\zeta_d^2 + 1)^2}{(1 - \zeta_d^2)^3} \right] - \frac{(1 + \zeta_d^2)^2}{2(1 - \zeta_d^2)} \left[\frac{3\overline{\zeta_d^4}B}{(|\zeta_d|^2 - 1)^4} + \frac{2\overline{\zeta_d^3}C}{(|\zeta_d|^2 - 1)^3} + \frac{\overline{\zeta_d^2}D}{(|\zeta_d|^2 - 1)^2} \right]. \quad (4.31)$$

Comparing $\mathcal{O}(1)$ terms of $g'(z)$ from (4.21) reveals that

$$\begin{aligned}
g_0 = & -\overline{B}\zeta_d^6[3\hat{\alpha}^2\hat{\delta} + 6\hat{\alpha}\hat{\beta}\hat{\gamma} + \hat{\beta}^3] + [-3\overline{B}\zeta_d^5 + \overline{C}\zeta_d^4 + AR(\zeta_d)] [2\hat{\alpha}\hat{\gamma} + \hat{\beta}^2] \\
& + \hat{\beta} [-3\overline{B}\zeta_d^4 + 2\overline{C}\zeta_d^3 - \overline{D}\zeta_d^2 + AR'(\zeta_d)] \\
& + \frac{\overline{A}\zeta_d}{1 - |\zeta_d|^2} + R(\zeta_d) \left[\frac{3\overline{B}\zeta_d^4}{(|\zeta_d|^2 - 1)^4} + \frac{2\overline{C}\zeta_d^3}{(|\zeta_d|^2 - 1)^3} + \frac{D\zeta_d^2}{(|\zeta_d|^2 - 1)^2} \right] \\
& - \overline{B}\zeta_d^3 + \overline{C}\zeta_d^2 - \overline{D}\zeta_d + \frac{1}{2}AR''(\zeta_d).
\end{aligned} \tag{4.32}$$

Recall that the evolution of the swimmer's head angle, θ , was taken as half of the finite part of the local fluid vorticity. Given that the vorticity is given by equation (2.21), the evolution of the head angle is governed by the single real ordinary differential equation

$$\frac{d\theta}{dt} = -2\text{Im}[f_1] \tag{4.33}$$

and so, given the above expression for f_1 , we also know this explicitly. Notice that the only free parameters are the swimmer's initial position, orientation and ϵ . Its subsequent motion is then determined by three ordinary differential equations: two from the real and imaginary parts of (4.27) and one from (4.33).

Deriving the governing dynamical system explicitly, as we have done above, has a significant advantage over other methods. For example, one may study this (and similar problems, as in [34]) using numerical boundary integral methods at each time step in order to compute the flow and hence the subsequent swimming dynamics. However, the analytic methods presented here obviate this and provide a more direct way to explore the full range of possible swimming trajectories that may be taken. Indeed, the analytic approach is also computationally cheaper than a numerical one.

4.3 Dynamics of a swimmer near an orifice.

Recall that the dynamics of the swimmer are fully determined by three ordinary differential equations; one for the development of the swimmer's orientation angle and two for its hor-

horizontal and vertical displacement. Therefore the initial orientation $\theta(0)$, the initial position, $z_d(0)$, and ϵ are the only free parameters of this model.

When the swimmer is placed above a wall which doesn't have a gap, the resultant motion is given by Crowdy and Or [1], where the swimmer follows the periodic “bouncing orbit” depicted in Figure 2.2. As a check on the analysis, when the swimmer is initially placed on one side of the gap, and given an initial orientation such that it travels away from it, the effect of the gap becomes minimal and the subsequent motion should be in accord with the bouncing orbits of the flat wall case. Indeed, as shown in Figure 4.2, this physically intuitive result is confirmed.

Placing a gap in the wall breaks the translational symmetry associated with displacements along the wall. We can expect these to lead to interesting dynamical scenarios, which we explore next. We set $\epsilon = 0.2$ and present possible trajectories which the swimmer may undertake. These are shown as solid lines with smaller lines added at intervals to present the angle θ . While they differ qualitatively, all the possible paths fall into one of the following few categories.

4.3.1 Deflection from the wall.

When the swimmer is initially pointed directly downwards (which corresponds to $\theta(0) = \pi/2$) above a wall without a gap, Crowdy and Or [1] demonstrated that the swimmer will move directly downwards coming to a halt at a distance ϵ away from the wall. In the current study, the gap in the wall provides an asymmetry which acts to repel the swimmer away from it. This is shown in Figure 4.3 for two scenarios - one where the organism starts on the left of the gap, and one where it starts on the right.

4.3.2 Jumping over the gap.

Another interesting possibility is that the swimmer may avoid the gap by jumping over it, as in Figure 4.4. Once it has passed the gap, its subsequent motion is a different bouncing orbit and so the gap may act as a “switching device” between different nonlinear periodic



Figure 4.2: A swimmer moving away from a gap (positioned at $x = \pm 1$) above a wall, with $z_d(0) = -3 + 0.3i$, $\epsilon = 0.2$ and has initial orientation $\theta(0) = 0.24$. The swimmer is placed away from the gap and is initially oriented away from it. As the effect of the gap is small, the swimmer's trajectory is reminiscent of the bouncing orbits exhibited by Crowdy and Or [1].

orbits. As the figures demonstrate, while the swimmer moves on a nonlinear periodic orbit before and after the gap, the height of the jump above the gap, as well as its periodic motion before and after the gap, may vary dramatically according to the swimmer's initial position and orientation. In the bottom right of Figure 4.4, the swimmer jumps over the gap but appears to return to a period bouncing orbit afterwards which is almost identical to the approaching orbit.

4.3.3 Rebounding from the gap.

Another category of motion is shown in Figure 4.5. Here the initial conditions are such that as the swimmer approaches the gap region, it is reversed at some critical position that always appears to be close to the first edge of the gap that it encounters. After the swimmer has been repelled from the gap, it will continue to swim along another bouncing orbit away from it. The gap affects the height and wavelength of this subsequent periodic motion and



Figure 4.3: Two swimmers starting at $z_d(0) = \pm 5 + i$, both initially directed downwards with $\theta(0) = \pi/2$. The presence of the gap “breaks” the symmetry and the swimmer results in moving away from the gap. It then continues along the a bouncing orbit in the respective direction.

in Figure 4.5 the “rebounded” orbit has a larger amplitude than the incoming one.

4.3.4 Trapping near the gap: equilibrium points.

We have seen instances where the swimmer either jumps over the gap or is repelled away from it. In addition to this, we have recorded some cases the swimmer approaches the gap in such a way that it becomes trapped inside the gap’s vicinity. In doing so, it enters the gap and may draw close to an “attracting point”, upon which the swimmer will spiral in towards it. We have found, at most, four such points. These are positioned at the four vertices of a rectangle which, by symmetrical arguments, is expected. As we shall see later,

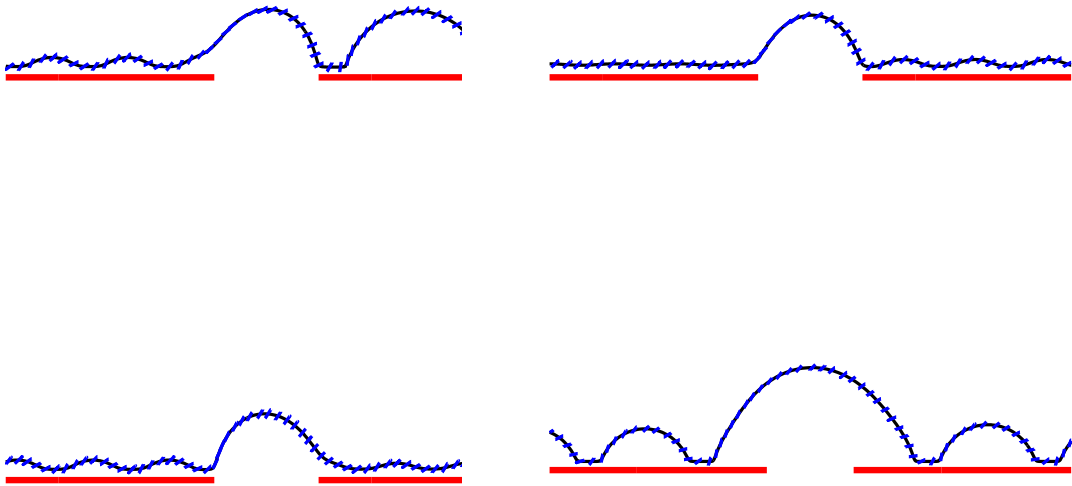


Figure 4.4: The gap provides a “switching mechanism” from one bouncing periodic orbit to another. The dynamics near the gap region are shown. Upper right figure: The orbit switches to a trajectory which is close to the steadily translating state found in [16]. Bottom right figure: The approaching and departing orbits (before and after the gap, respectively) are almost identical. Clockwise from top left $\theta(0) = 0.15\pi, 0.25\pi, 0.3\pi, 0.1\pi$ with initial positions $z_d(0) = 6.8 + i, 8 + 0.21i, 5 + 0.3i, 10.5 + 0.6i$.

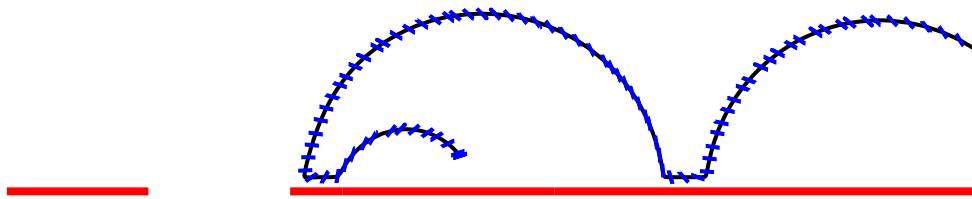


Figure 4.5: The gap may act to repel the swimmer, sending it back in the direction from which it came from. Here, we have $\theta(0) = 0.1\pi$ with initial condition $z_d(0) = 3.4 + 0.5i$.

the precise geometry of this rectangle depends on the parameter ϵ . Figure 4.6 shows four different choices of initial conditions which result in the swimmer ultimately spiralling in towards each of these four attracting points.

From a dynamical systems perspective, these are stationary points and, by watching trajectories draw into their basins of attraction, we may infer that these points are stable. To determine this more rigorously, we may perform a linear stability analysis. In doing so, the three (real) expressions (4.27) and (4.33), which give the equations that define the dynamical system for the swimmer's evolution, may be linearised and expressed as

$$\frac{d}{dt}\underline{\mathbf{X}} = J \underline{\mathbf{X}} \quad (4.34)$$

where $\underline{\mathbf{X}} = (\text{Re}[z_d], \text{Im}[z_d], \theta)$. Points of equilibrium are found numerically by searching

for the points where the left hand side of this is zero. We then search for solutions about this equilibrium point with exponential time dependence of the form

$$\exp(\sigma t) \quad (4.35)$$

where σ are the eigenvalues of the Jacobian matrix, J . Then, the nature of the equilibrium point's stability is determined from the values of these eigenvalues. At each of the above four stationary points, the eigenvalues appeared in a complex conjugate pair with a negative real parts, and a third negative real eigenvalue. These are therefore categorised as stable spiral points. A full bifurcation analysis, performed in the next section, reveals that these are the only stable points in this case.

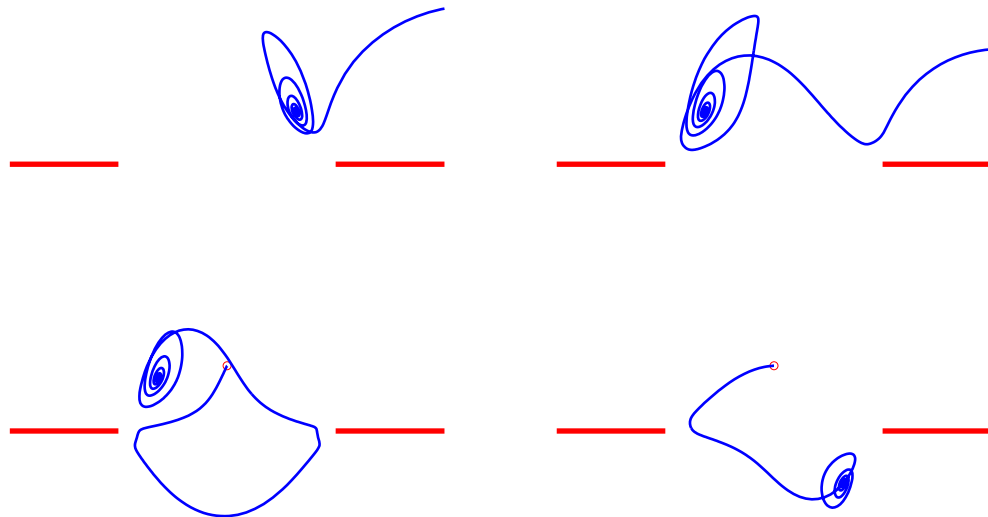


Figure 4.6: For some choices of initial conditions, the swimmer may become trapped in the gap region. The swimmers spiral into one of, at most, four attracting points. Clockwise from top left to bottom left, we have: $\theta(0) = 0.3, 0.25\pi, 0.05\pi, 0.75$ with initial positions $z_d(0) = 3.6 + 0.8i, 10.2 + i, 0.6i, 0.6i$.

That swimmers may be brought to a standstill by the strategic placement of a gap in a wall is an important result from a control theory perspective. It is therefore interesting to ask

whether there is a systematic way to determine the basins of attraction of each of these stationary points. We have found that this is not an easy matter and the initial conditions for the trajectories found in Figure 4.6 were found by trial and error. Furthermore, the ultimate fate of the swimmer's trajectory is sensitively dependent on the choice of initial conditions.

4.3.5 Escaping the gap region.

Given the above trapped orbits, it is natural to ask whether all swimmers which enter the gap region ultimately enter a basin of attraction of one of the four stable points. We have found that this is not the case. Figure 4.7 shows several examples in which the swimmer “escapes” the gap region and attaches to a nonlinear bouncing orbit away from the gap, either above or below the wall.



Figure 4.7: The swimmer may also escape the gap region to take a bouncing orbit on either side of the gap and wall. The two trajectories on the left correspond to $\theta(0) = 0.05$ with $z_d(0) = 0.1 + 0.5i, 0.5i$ (above and below the wall, respectively) while the two on the right correspond to $\theta(0) = \pm 0.05$ with $z_d(0) = -0.1 + 0.5i, 0.5i$ (also, above and below, respectively). Note the sensitivity of the swimmer's ultimate path on its initial conditions; all starting configurations are very close to each other here.

4.4 Bifurcation analysis in the parameter ϵ .

The above trajectories were found for $\epsilon = 0.2$ and were qualitatively representative of the various swimming protocols that the swimmer may undertake. In addition to the four stable

stationary points we have noted, the system may admit other stationary points which are unstable in nature, and therefore not attractors in the dynamics. These points were found by using Newton's method to locate the zeros of the left hand side of the dynamical system (4.34). Their linear stability was then determined from the method described in the last section. We will now study the structure of the stationary points as the parameter ϵ is varied.

For $0 \leq \epsilon \leq \epsilon_h^{(1)} = 0.3584$, five other stationary points have been found: three are on the real axis in the gap (one at the origin and one at each side of it) and two on the imaginary axis (one above and one below the origin). All of these are found to be linearly unstable. At $\epsilon = \epsilon_h^{(1)} = 0.3584$, the complex conjugate eigenvalues associated with each of the four stable points simultaneously become purely imaginary, all approaching from the left hand side of the σ -plane where $\text{Re}[\sigma] < 0$. This is therefore a Hopf bifurcation [46] and, for ϵ just greater than $\epsilon_h^{(1)}$, the complex conjugate eigenvalue pair acquire positive real parts. When this occurs, the dynamical simulations reveal the presence of small closed periodic orbits around each of the four stationary points, as shown in Figure 4.8. Based on these simulations, we find that these periodic orbits are stable and so we conclude that this is an example of a supercritical Hopf bifurcation. These local bifurcations are interesting because they lead to bound states meaning that a swimmer may become trapped near the gap while still engaged in a non-trivial closed period orbit, see Figure 4.8.

As ϵ is increased further, we see the occurrence of a global bifurcation. Specifically, when $\epsilon = \epsilon_g^{(1)} = 0.36895$ we have observed that pairs of periodic orbits growing around two (now unstable) spirals merge together with the unstable saddle point on the imaginary axis. This occurs symmetrically in both the upper and lower half planes, see Figure 4.9. The result of this is the formation of closed "figure of eight" orbits which, following the descriptive nomenclature introduced by Coulet *et al.* [47], are *gluing bifurcations*, see Figures 4.10 and 4.12-4.13. This orbit is found to persist for $\epsilon_g^{(1)} < \epsilon < \epsilon_g^{(2)} = 0.4805$ when, upon reaching the latter value, the gluing bifurcation reverses and the two orbits "unglue". This leaves a separate periodic orbit around each of the four (still unstable) stationary points once again, see Figure 4.11. Increasing ϵ further shows the existence of a second Hopf

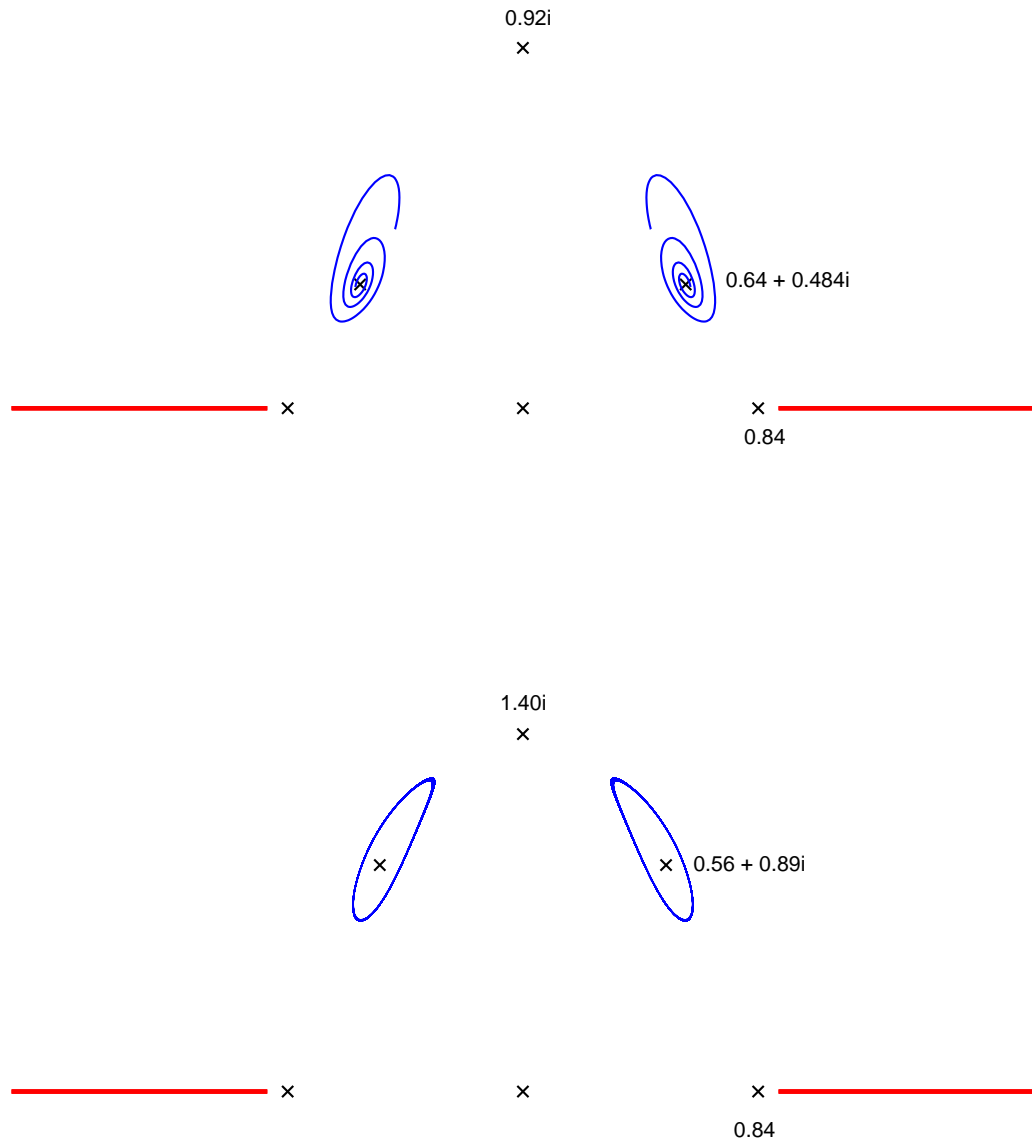


Figure 4.8: Stationary point locations before (upper figure) and after (lower figure) the Hopf bifurcation when $\epsilon = \epsilon_H^{(1)} = 0.3584$. As ϵ passes through this value, the two stable spirals become unstable spirals surrounded by fixed periodic orbits. Only the points in the upper half plane are displayed.

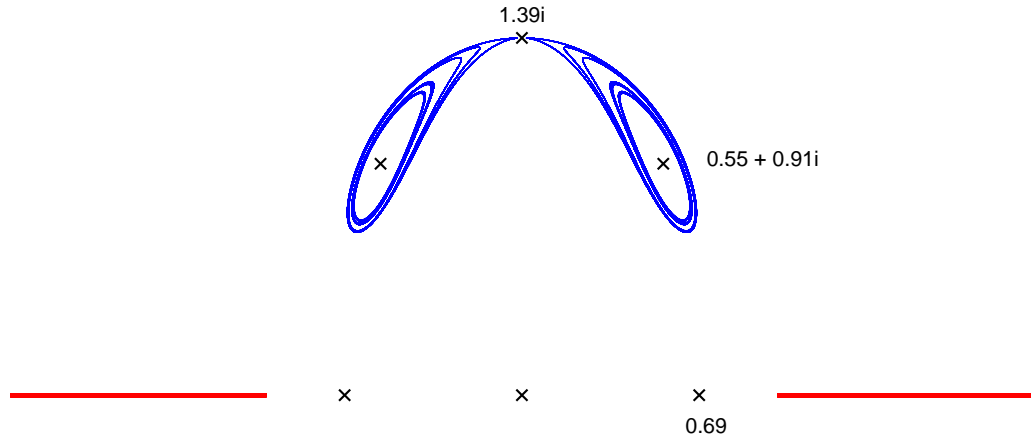


Figure 4.9: Growth of the periodic fixed orbits associated with two of the (unstable) stationary points in the upper half plane. When ϵ reaches the gluing bifurcation value ($\epsilon_g^{(1)} = 0.36895$), the two fixed orbits make contact on the imaginary axis, together with the saddle point (which was also on the imaginary axis for all $\epsilon < \epsilon_g^{(1)}$). The stationary points are shown for $\epsilon = \epsilon_g^{(1)}$.

bifurcation at $\epsilon = \epsilon_h^{(2)} = 0.5000$ at which the four stationary (previously unstable) points become stable spirals again and the fixed periodic orbits disappear. Finally these four (now stable) spiral points merge in pairs on the imaginary axis at $\epsilon = \epsilon_b = 0.5510$. Figure 4.14 shows the locus of the eigenvalues as σ is varied. The complex values of σ associated with the two Hopf and two gluing bifurcations of the stationary point in the first quadrant are clearly indicated.

4.5 Background shear effects on a swimmer near a wall with a gap.

Zilman, Novak and Benayahu [4] have studied the hydrodynamic attraction of ocean larvae (which are also swimmers that reside in a low Reynolds number environment) towards solid surfaces. They showed that when such a swimmer is placed in a uniform background shear flow parallel to a wall, the associated local flow vorticity causes the larvae to rotate their

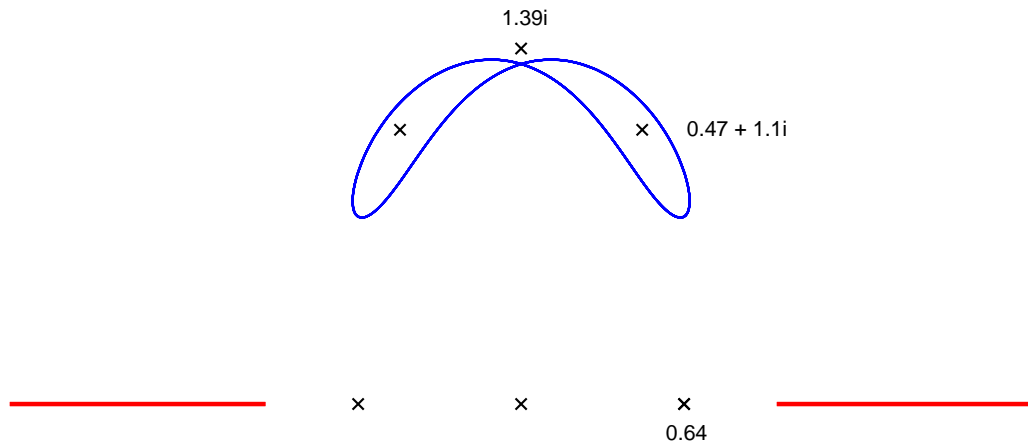


Figure 4.10: Location of stationary points just after the gluing bifurcation ($\epsilon > \epsilon_g^{(1)}$). This shows the well defined “figure of eight” fixed orbit formed after the gluing of two separate periodic orbits.

direction of self-propulsion which leads to their congregation at the surface. However, while the authors attempt to explain the larvae’s attraction to the wall, they use the wall only as a reference point of zero shear flow, but do not take into account the larvae’s direct interaction with the wall itself.

In chapter 2, we found the solution for a swimmer’s interaction with an infinite no-slip wall as well as that of a uniform shear flow of the form $\psi = \gamma y^2$. By superposing the two, we were able to properly study the swimmer’s hydrodynamic interaction with the wall in the presence of the background shear flow. In chapter 3, we considered the same uniform shear flow past the more complicated geometry of an infinite wall with a gap and found that the exact solution was given by

$$F(\zeta) = \frac{i\gamma}{2(\zeta - i)}, \quad G(\zeta) = -\frac{\gamma\zeta}{2(\zeta - i)} + \frac{i\gamma\zeta}{2} \left[\frac{1 + \zeta^2}{1 - \zeta^2} \right] \frac{1}{(\zeta - i)^2}, \quad (4.36)$$

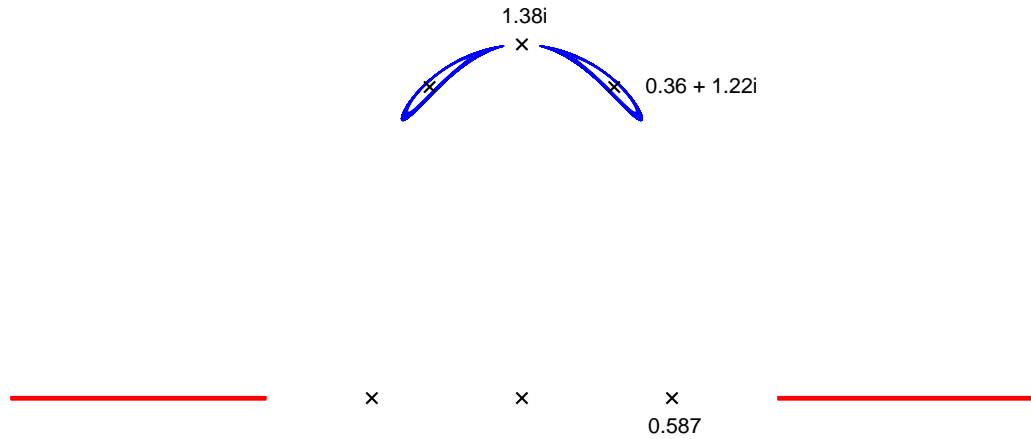


Figure 4.11: Typical periodic orbits just after the ungluing bifurcation at $\epsilon = \epsilon_g^{(2)}$, when the single figure of eight periodic orbit has split into two separate orbits, each containing an unstable spiral around both fixed points.

where $\zeta = (1 - (1 - z^2)^{1/2})/z$. In a similar fashion, we may now superpose this result with the solution presented in this chapter to accurately study a swimmer's evolution near a wall with a gap in the presence of a background shear flow. Including a this ambient flow introduces a new parameter, γ , into the model and so a new set of dynamical scenarios is expected. Here we present only a small sample of the new effects focussing on possible bound states. The results of this are depicted in Figures 4.15 - 4.17. The value of ϵ was fixed at 0.2, however the trajectories for different values of this parameter are qualitatively similar.

When no shear was present and the swimmer starts to the right of the gap such that it is attracted to one of the four stable spiral points near the gap then, as the shear rate is increased slightly, the swimmer no longer falls into the basin of attraction. Instead, it jumps over the gap and continues on a periodic orbit on the other side of the orifice, (though with a different height and amplitude). As the shear rate increases further, the background flow

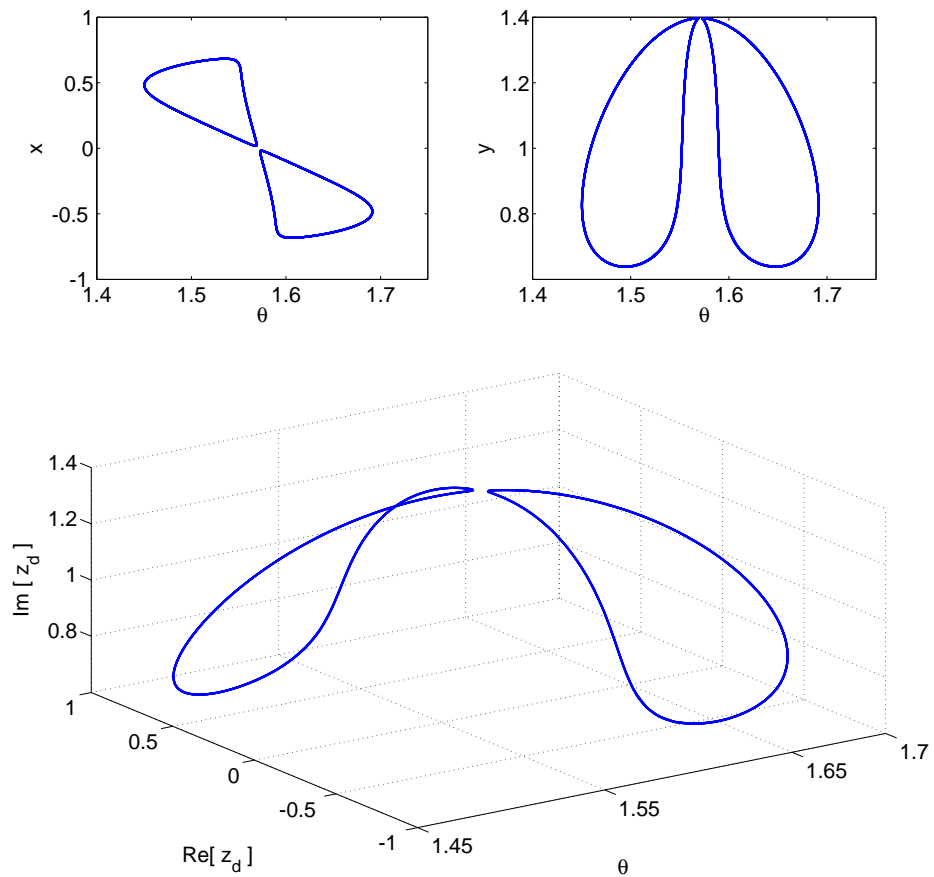


Figure 4.12: Two projections of the periodic orbits for $\epsilon = \epsilon_g^{(1)-} = 0.3689$, just before the gluing bifurcations. These are visualised in three-dimensional space ($\text{Re}[z_d]$, $\text{Im}[z_d]$, θ).

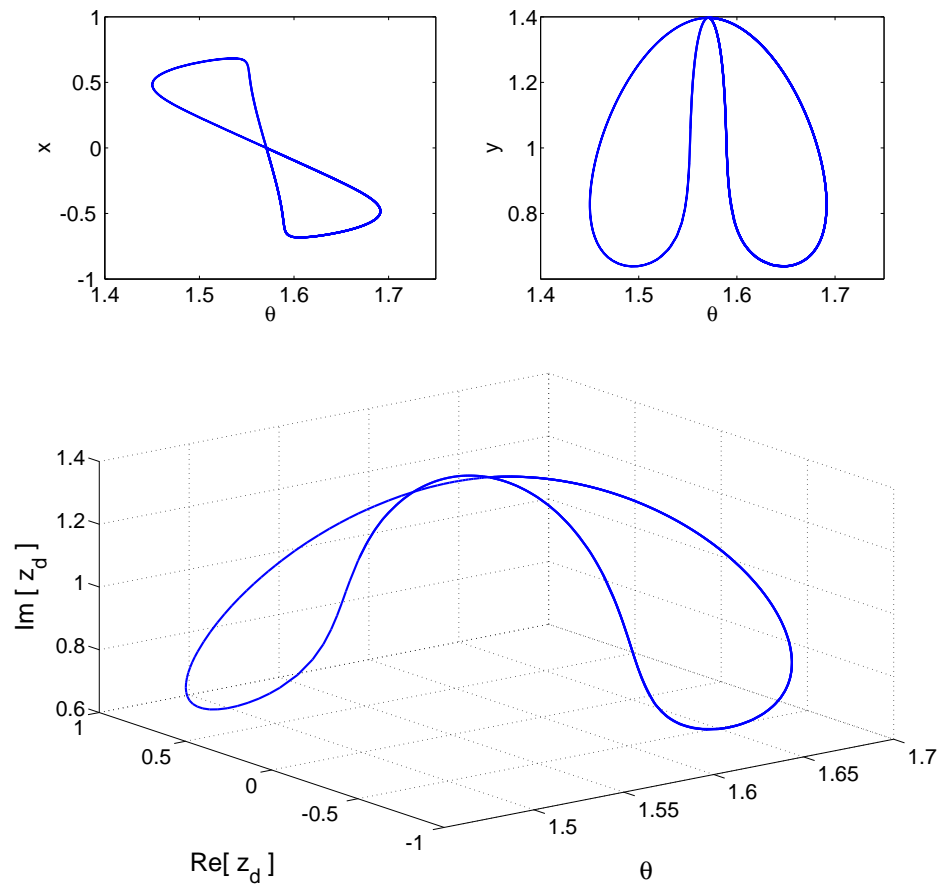


Figure 4.13: Two projections of the newly formed figure of eight orbits, just after the gluing bifurcation [73] where $\epsilon = \epsilon_g^{(1)+} = 0.369$. These are also shown in three-dimensional space ($\text{Re}[z_d]$, $\text{Im}[z_d]$, θ).

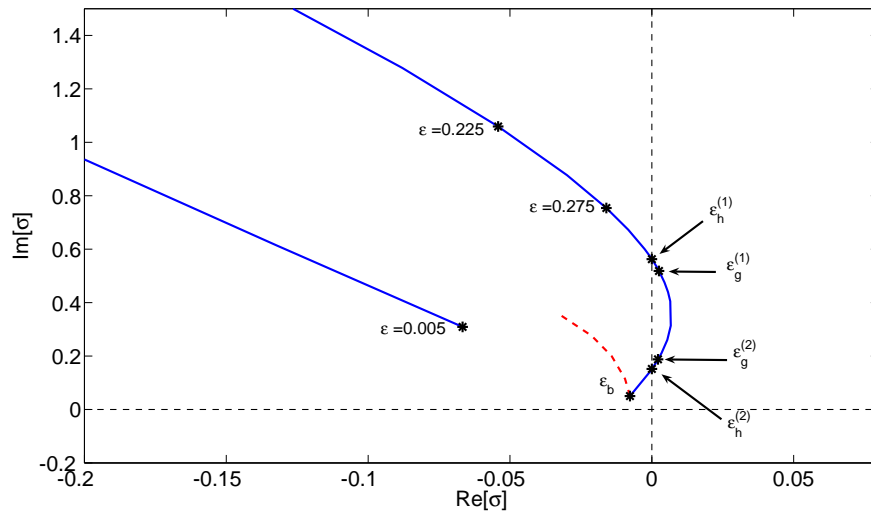


Figure 4.14: The stability diagram for one of the complex eigenvalues σ associated with the stationary point in the first quadrant as ϵ is increased. There is also another complex conjugate eigenvalue and a negative real eigenvalue, both of which are not shown here.

is eventually strong enough to reverse the direction of the swimmer and send it travelling to the right. The swimmer's eventual motion will either be that of a “spiral orbit” (akin to those reported by Zilman *et al.* [4]) if the shear rate is not too high or, for large shear rates, a bouncing orbit.

Recall that the bifurcation analysis found no periodic solutions when $\epsilon = 0.2$. Interestingly, we have found that by imposing a *symmetric* shear flow above and beneath the wall, a symmetric (diamond-shaped) closed periodic orbit exists. This is shown in Figure 4.17. They appear to be attractors in the dynamics and are different from the closed periodic orbits we have witnessed in the absence of a background shear flow in that they provide a mechanism for the swimmer to cross over from one side of the wall to the other.

4.6 Summary

We have extended the solutions presented in chapter 3 for a Stokes flows past a wall with a gap to include the singularity model presented by Crowdy and Or [1]. By studying the

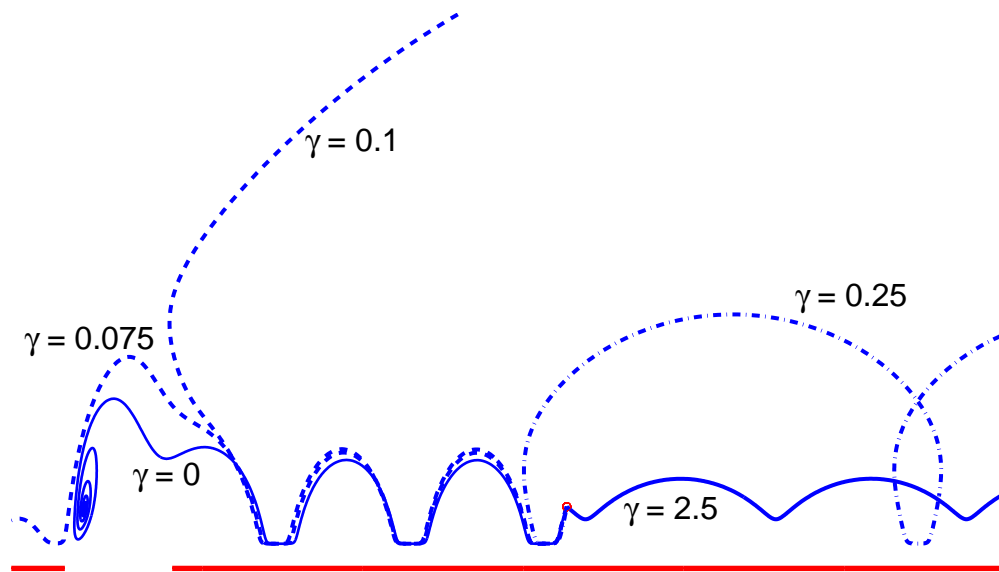


Figure 4.15: The effect of increasing the strength of a background shear flow above the wall: without shear the swimmer proceeds along the same bouncing orbit towards one of the attracting points. Increasing the shear rate further leads to the swimmer eventually moving away from the gap in another periodic bouncing orbit.

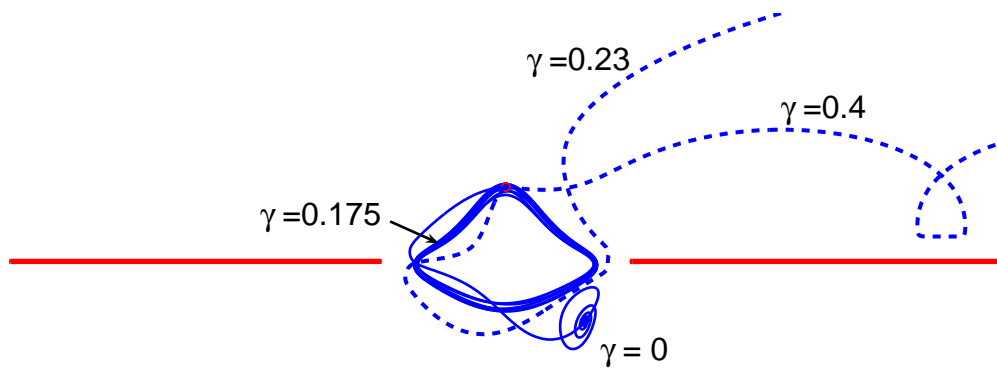


Figure 4.16: Closed periodic orbit within the gap. Without any background shear, the swimmer moves towards one of the four stable spiral. As the shear flow is introduced and increased in strength, there exists a close periodic orbit in the gap's vicinity. This orbit is not symmetric about the real axis (which is to be expected, as there is a background shear flow only in the upper half plane). As the shear rate increases further the swimmer leaves the gap region and enters into a spiral orbit.

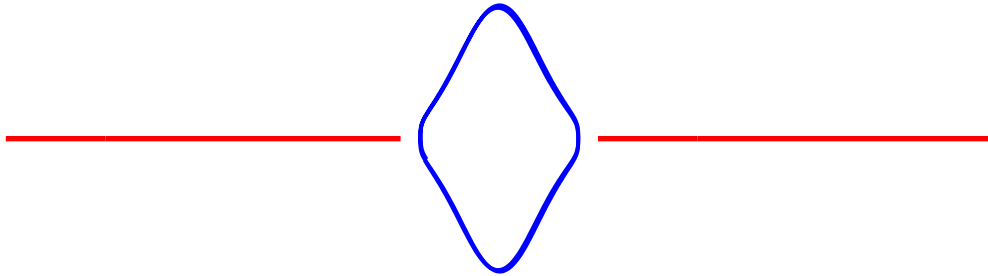


Figure 4.17: Closed periodic orbit in the gap when a uniform background shear (with $\gamma = 0.128$) flow is introduced symmetrically above and below the wall. The diamond-shaped orbit is now up-down symmetric.

interaction between the singularities within that model and the boundary, we have been able to catalogue various dynamics of a low Reynolds number swimmer near an orifice.

The results within this chapter provide a predictive theory of how such a swimmer would behave near such a boundary. These results could be tested using the laboratory experiments akin to those involving quasi two-dimensional robotic swimmers, as performed by Murray *et al.* [25] for a swimmer near a flat wall with no gaps. The singularity model of Crowdy and Or [1] has proven to provide excellent agreement with these experiments and, as we have used exactly the same model in conjunction with this more complicated domain, we have confidence that the results presented in this chapter are verifiable using similar experimental procedures. Another test of this chapter's results in a fully three-dimensional setting would be to extend the numerical experiments of Murray and Or [23] to study the dynamics of their model swimmer near a wall with a gap. As this model consists of three rotating spheres attached by rigid rods, the calculation would require the generalisation of the Swan-Brady mobility tensors [24] for spheres near a wall with a gap, which are yet to

be computed.

Or and Murray [23] studied the motion of a swimmer near a flat wall (with no gap) within the framework of control theory. The generic motion of a swimmer near such a boundary is to travel on nonlinear “bouncing orbits” along it [23]. We have noticed that a gap in the wall could be used as a control device for a low Reynolds number swimmer near an orifice. In particular, it has the ability to manipulate swimmers between its various orbits. The gaps may be used to trap swimmers in their locale: depending on ϵ , the swimmers may either spiral in towards a stationary point, or become trapped in a periodic closed orbit indefinitely. Alternatively, the gap may serve as a switching mechanism between different bouncing orbits, affecting the height and amplitude of the oncoming swimmer. It may also reverse the swimmer away from the wall, sending it back in the direction that it came from. Finally, the gap may even send the swimmer through the gap to the other side of the wall. While this is rare, we have seen that the addition of a background shear flow appears to promote this crossover by allowing closed, diamond-shaped, periodic orbits through the gap. As an application, the existence of these closed periodic orbits may be a useful mechanism for self-driven mixing devices in low Reynolds number flows.

The resulting dynamical system for a swimmer near a wall with a gap is an interesting one, in that it allows a variety of non-trivial bifurcations and possible swimming trajectories. The conformal mapping presented here may, in principle, be extensible to other planar domains. Together with the singularity description of Crowdy and Or [1], the door is opened to the construction of dynamical system models for low Reynolds number swimmers in arbitrary confined geometries. In general, however, it will not be possible to find these dynamical systems in explicit form; this is a fortuitous and rather special feature of the particular geometry and conformal map we use in this chapter. Nevertheless, the system of ordinary differential equations for the swimmer’s motion may still be computed numerically within a similar framework.

Despite this, we will now attempt to find other, more complicated, confined domains for which we are able to express the resulting dynamical system explicitly. The geometry that

we will attempt to do this in is that of a wall with *two* gaps, as this will highlight the effect of placing a finite piece of wall inside the single gap we have studied in this chapter. It is already known that even small occlusions in Stokes flows may lead to dramatic “blocking effects” [48, 49] and it will be interesting to study the influence this has on the swimmer’s behaviour. This domain is also a further complication to the single gap case and, as the length of the added wall segment presents another control parameter, it is likely that the resulting dynamical system will also produce interesting features.

Chapter 5

Stokes flows past a wall with two gaps.

5.1 Introduction

In chapter 3 we studied the slow viscous flow of fluid near an infinite no-slip wall with a gap in it. By using conformal mapping techniques we were able to characterise the behaviour near the ends of the gap (or, equivalently, the sharp corners of the wall) and retrieve previous results by Smith [2] as well as those by Ko and Jeong [3] for the Stokes flow with far field shear and stagnation point velocity fields respectively. Both of these authors used entirely different methods to solve their respective problems (the latter authors seem to have been unaware of the former's work). A clear benefit of the method that we presented was that only a slight change to the imposed far field conditions of the Goursat functions was necessary in order to model the two problems. Furthermore, we have shown in chapter 4 that our method lends itself much more readily to the study of micro-organism swimming near such boundaries.

Later, we will want to study the motion of a similar swimming organism near a no-slip wall with *two* gaps. As in the study of a swimmer above a wall with a single gap, we begin by considering a general Stokes flow around this geometrical configuration without the swimmer. We let a viscous fluid fill the entirety of the two-dimensional plane above and below an infinite no-slip wall which admits two gaps: one between $[-1, r]$ and another between $[r, 1]$ where $0 < r < 1$. The finite length plate, placed symmetrically about

the origin in $[-r, r]$, will be referred to as the *central plate*. As in the simply connected analogue of chapter 3, we will focus on the specific cases where the far field Stokes flow takes two different forms: those that in the far field above the wall tend to either a uniform shear flow or a stagnation point flow (with an added pressure gradient across the wall), while in the fluid far below the wall remains at rest.

By generalising the method presented in chapter 3 to the case where the wall admits two gaps, we will produce a range of new, exact, solutions to this problem. These results are of interest as the fluid domain is doubly connected due to the fact that there are two disconnected boundaries in the fluid. Analytical solutions for Stokes flows in multiply connected domains are few and far between. Most relevantly, Hasimoto [48] studied a purely pressure-driven flow (Sampson flow) past precisely the same geometry. By building on work by Roscoe [50], he refers to assumptions about the symmetry of certain field variables in order to form analogy with flows of ideal fluids. The approach taken here is more general than this as it does not rely on fore-aft wall symmetry and only a simple modification of the far field conditions is necessary in order to find both the shear flow and stagnation point flow solutions past the same geometry.

There have been only a small number of other studies of Stokes flows confined in doubly connected geometries: Jeffery [51] found solutions for the slow viscous flow in the annular region between two concentric cylinders (where one or both of the cylinders move and thus drives the flow) using a formulation with bipolar coordinates; Frazer [52] later used ideas based on the method of reflection to find the unbounded Stokes flow around two cylinders; later again, Jeffery and Onishi [53] used bipolar coordinates again to find closed-form formulae for the motion of a translating and rotating cylinder above a no-slip wall (as well as the forces and torques on the cylinder); lastly, Davis [54] found formulae for the Stokes flow past a cylinder over an infinite flat wall and used these to demonstrate the formation of viscous eddies when the cylinder is brought close to the plane. These classical solutions continue to be useful in the study of mixing of viscous fluids [55] as well as in the investigation of wall effects in electrophoresis [56].

5.2 The force on a central plate in a Stokes flow.

While exposed to the oncoming flow, the central plate remains in place at $[-r, r]$ and hence we must assume that there is a non-zero net force exerted on it (equal and opposite to the force that keeps it in this position). In chapter 2 we have seen that the complex form of the fluid stress, $-pn_i + 2\mu e_{ij}n_j$ where n_i are the components of the unit normal to the wall, can be written as

$$2i\frac{dH}{ds} \quad (5.1)$$

where $H = f(z) + z\bar{f}'(\bar{z}) + \bar{g}'(\bar{z})$. As this is a total derivative, the total force around the central plate is conveniently given by

$$\oint_{\Gamma} (-pn_i + 2\mu e_{ij}n_j) ds = 2i\mu[H]_{\Gamma} \quad (5.2)$$

where Γ is any contour that encircles the central plate and is positively oriented with respect to it.

5.3 Conformal mapping: a wall with two gaps.

Similarly to the simply connected case, we introduce a conformal map in order to utilize a uniformisation variable for this problem. In the case where the wall has a disconnected central plate, the fluid domain is doubly connected. It is well known [57] that there always exists a univalent conformal map to this domain from an annulus $\rho < |\zeta| < 1$ in a complex ζ -plane, with $0 < \rho < 1$: the annular region is mapped to the fluid region above and below the walls. The inner ρ circle in the annulus is mapped to the central plate, $[-r, r]$, while the outer unit circle is mapped to the walls extending to infinity. The (unique) specific conformal map that is appropriate for this is given by Crowdy and Marshall [58] as

$$z(\zeta, \rho) = \frac{P^2(-\zeta, \rho) - P^2(\zeta, \rho)}{P^2(-\zeta, \rho) + P^2(\zeta, \rho)} \quad (5.3)$$

where we shall suppress the ρ dependence in the notation for the conformal map from here on. The special function $P(\zeta, \rho)$ is defined by

$$P(\zeta, \rho) = (1 - \zeta) \prod_{k=1}^{\infty} (1 - \rho^{2k}\zeta)(1 - \rho^{2k}/\zeta) \quad (5.4)$$

which has zeros at the points $\zeta = \rho^{2n}$ for $n \in \mathbb{Z}$. The conformal map (5.3) depends on the single real parameter ρ . Different choices of this number correspond to different central plate lengths (or, equivalently, gap widths). As $\rho \rightarrow 0$, the annulus becomes the simply connected unit disk and the central plate vanishes. A graph of the width of the central plate against values of ρ is shown in Figure 5.1.

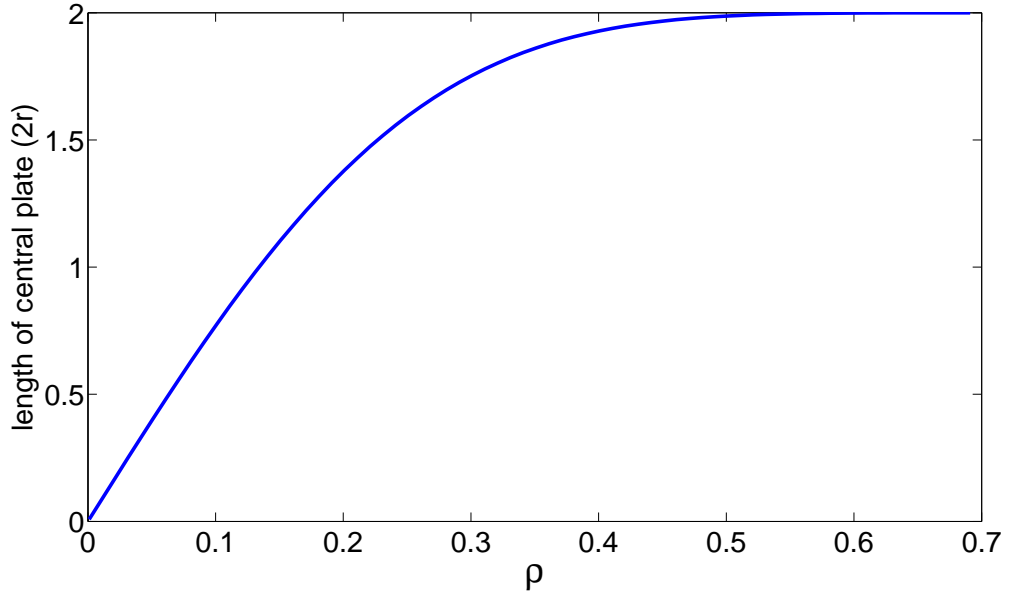


Figure 5.1: Central plate length ($2r$) in the fluid domain as a function of ρ , the radius of the inner circle of the annulus in the ζ -plane.

It follows from (5.3) that the derivative of the conformal map is given by

$$z'(\zeta, \rho) = \frac{4 [P^2(\zeta, \rho)P(-\zeta, \rho)P'(-\zeta, \rho) - P(\zeta, \rho)P^2(-\zeta, \rho)P'(\zeta, \rho)]}{(P^2(-\zeta, \rho) + P^2(\zeta, \rho))^2} \quad (5.5)$$

where $P'(\zeta, \rho) \equiv \partial P(\zeta, \rho)/\partial \zeta$. As $P(1, \rho) = 0$, we see that (5.5) vanishes at the points

$\zeta = \pm 1$. Next, the parameter ρ is chosen so that the ends of the central plate are at $z = \pm r$. This is found numerically using Newton's method. Also, for convenience, we shall also suppress the explicit ρ dependence of the conformal map from here on.

Note that it follows from the definition of $P(\zeta, \rho)$ that

$$\begin{aligned} P(\zeta^{-1}, \rho) &= (1 - \zeta^{-1}) \prod_{k=1}^{\infty} (1 - \rho^{2k}/\zeta)(1 - \rho^{2k}\zeta) \\ &= -\zeta^{-1}P(\zeta, \rho) \end{aligned} \quad (5.6)$$

and also that

$$\begin{aligned} P(\rho^2\zeta, \rho) &= (1 - \rho^2\zeta) \prod_{k=1}^{\infty} (1 - \rho^{2k}\rho^2\zeta)(1 - \rho^{2k}/\rho^2\zeta) \\ &= (1 - \rho^2\zeta)(1 - 1/\zeta) \prod_{k=1}^{\infty} (1 - \rho^{2k+2}\zeta)(1 - \rho^{2k}/\zeta) \\ &= -\zeta^{-1}(1 - \zeta) \prod_{k=1}^{\infty} (1 - \rho^{2k}\zeta)(1 - \rho^{2k}/\zeta) \\ &= -\zeta^{-1}P(\zeta, \rho). \end{aligned} \quad (5.7)$$

Next, notice that from the definition of the map (5.3) together with the above relations that the special function $P(\zeta, \rho)$ satisfies, we see that

$$\begin{aligned} z(\rho^2\zeta) &= \frac{P^2(-\rho^2\zeta, \rho) - P^2(\rho^2\zeta, \rho)}{P^2(-\rho^2\zeta, \rho) + P^2(\rho^2\zeta, \rho)} \\ &= \frac{(1/\zeta^2)P^2(-\zeta, \rho) - (1/\zeta^2)P^2(\zeta, \rho)}{(1/\zeta^2)P^2(-\zeta, \rho) + (1/\zeta^2)P^2(\zeta, \rho)} \end{aligned} \quad (5.8)$$

and hence

$$z(\rho^2\zeta) = z(\zeta), \quad \text{for all } \zeta \neq 0. \quad (5.9)$$

This is an example of a *loxodromic function* [59]: a function $u(\zeta)$ is defined to be loxodromic if it is meromorphic everywhere (i.e. it is analytic except at a discrete set of isolated singularities) inside, and on the boundary of, the *fundamental annulus* $\rho \leq |\zeta| < \rho^{-1}$ and

which satisfies the functional relation $u(\rho^2\zeta) = u(\zeta)$. Given the singularity structure of $u(\zeta)$ inside the fundamental annulus, the singularity structure in all other annuli in the complex ζ -plane follows from this functional relation. This will be a key feature and a crucial fact for what follows.

Next we may write $P(\zeta, \rho) = (1 - \zeta)Y(\zeta, \rho)$ where

$$Y(\zeta, \rho) = \prod_{k=1}^{\infty} (1 - \rho^{2k}\zeta)(1 - \rho^{2k}/\zeta). \quad (5.10)$$

Notice that the denominator of the map (5.3) vanishes at $\zeta = i$ (and also at $-i$) as

$$\begin{aligned} P^2(-i, \rho) + P^2(i, \rho) &= (1 + i)^2 Y^2(-i, \rho) + (1 - i)^2 Y^2(i, \rho) \\ &= [(1 + i)^2 + (1 - i)^2] Y^2(i, \rho) = 0 \end{aligned} \quad (5.11)$$

where we have used the fact that

$$Y(-i, \rho) = Y(i, \rho) = \prod_{k=1}^{\infty} (1 + \rho^{4k}). \quad (5.12)$$

This also follows from relation (5.6) and means that $z(\zeta)$ admits a simple pole at $\zeta = \pm i$. It is shown in the appendix B that

$$z(\zeta) = \frac{a}{\zeta - i} + b + \mathcal{O}(\zeta - i) \dots \quad (5.13)$$

where

$$a = \frac{1}{2} \left[\frac{P^2(-i, \rho) - P^2(i, \rho)}{P(i, \rho)P'(i, \rho) - P(-i, \rho)P'(-i, \rho)} \right] \quad (5.14)$$

and

$$\begin{aligned} b = & \frac{P(i, \rho)P'(i, \rho) + P(-i, \rho)P'(-i, \rho)}{P(-i, \rho)P'(-i, \rho) - P(i, \rho)P'(i, \rho)} \\ & - \frac{P^2(-i, \rho) [P'^2(i, \rho) + P'^2(-i, \rho) + P(i, \rho)P''(i, \rho) + P(-i, \rho)P''(-i, \rho)]}{2(P(-i, \rho)P'(-i, \rho) - P(i, \rho)P'(i, \rho))^2}. \end{aligned} \quad (5.15)$$

We will also use the fact that, near $\zeta = -i$, $z(\zeta)$ takes the form

$$z(\zeta) = \frac{a}{\zeta + i} + \mathcal{O}(1) + \dots \quad (5.16)$$

Next, we introduce the new function

$$K(\zeta, \rho) = \frac{\zeta P'(\zeta, \rho)}{P(\zeta, \rho)}. \quad (5.17)$$

From this, and using the relation (5.6) we have that

$$\begin{aligned} K(\zeta^{-1}, \rho) &= \frac{P'(\zeta^{-1}, \rho)}{\zeta P(\zeta^{-1}, \rho)} \\ &= -\frac{P'(\zeta^{-1}, \rho)}{P(\zeta, \rho)}. \end{aligned} \quad (5.18)$$

Differentiating relation (5.6) gives

$$P'(\zeta^{-1}, \rho) = \zeta P'(\zeta, \rho) - P(\zeta, \rho) \quad (5.19)$$

and so using this in equation (5.18) gives the result

$$K(\zeta^{-1}, \rho) = 1 - K(\zeta, \rho) \quad (5.20)$$

while it can similarly be shown that

$$K(\rho^2 \zeta, \rho) = K(\zeta, \rho) - 1. \quad (5.21)$$

Note that from its definition, $K(\zeta, \rho)$ has simple poles at $\zeta = \rho^{2n}$ for $n \in \mathbb{Z}$. Notice also that

$$\log P(\zeta, \rho) = \log(1 - \zeta) + \sum_{k=1}^{\infty} \log(1 - \rho^{2k} \zeta) + \log(1 - \rho^{2k} / \zeta) \quad (5.22)$$

and so

$$\frac{P'(\zeta, \rho)}{P(\zeta, \rho)} = \frac{1}{\zeta - 1} + \sum_{k=1}^{\infty} \left(-\frac{\rho^{2k}}{(1 - \rho^{2k} \zeta)} + \frac{\rho^{2k} / \zeta^2}{(1 - \rho^{2k} / \zeta)} \right). \quad (5.23)$$

Using this in the definition of $K(\zeta, \rho)$, we see that near $\zeta = 1$, this function takes the

leading order form

$$K(\zeta, \rho) = \frac{1}{\zeta - 1} + \text{analytic function.} \quad (5.24)$$

5.4 Shear flows past a wall with two gaps.

We now turn our attention to the problem of Stokes flow above a wall with two gaps, such that in the far field above the wall, the flow tends to that of a uniform shear flow, while in the far field below the wall, the fluid is stationary. Recall that in this case we have that

$$f(z) \sim \begin{cases} iz/2 & \text{as } z \rightarrow \infty^+ \\ f_\infty & \text{as } z \rightarrow \infty^- \end{cases} \quad (5.25)$$

and

$$g'(z) \sim \begin{cases} -iz & \text{as } z \rightarrow \infty^+ \\ g_\infty & \text{as } z \rightarrow \infty^- \end{cases}. \quad (5.26)$$

Next, using the conformal map defined above in (5.3), we define the Goursat functions

$$F(\zeta) \equiv f(z(\zeta)), \quad G(\zeta) \equiv g'(z(\zeta)). \quad (5.27)$$

While it is not easy to explicitly invert the conformal map (5.3), it is known from general arguments [60] that $z(\zeta)$ has square root branch point behaviour at the points $\zeta = \pm 1, \pm \rho$ corresponding to the preimages of the four corner-points in the fluid domain. Because of this, ζ will serve as a uniformization variable so that $F(\zeta)$ and $G(\zeta)$ may be expressed as single-valued functions, and will not admit any branch points.

We have shown that we must allow for a net force to be present on the central plate. From (5.2) it is clear that the function $H(z, \bar{z})$ must include a multi-valued component in order for a non-zero contribution to remain present after encircling the central plate. We therefore let

$$F(\zeta) = F_l \log \zeta + \hat{F}(\zeta), \quad G(\zeta) = G_l \log \zeta + \hat{G}(\zeta) \quad (5.28)$$

where F_l and G_l are numbers to be found while $\hat{F}(\zeta)$ and $\hat{G}(\zeta)$ are both analytic and single-valued inside the preimage annulus $\rho < |\zeta| < 1$. Note that while we require $H(z, \bar{z})$ to be

multi-valued, the velocity must not be. The no-slip velocity condition on the unit circle is given by

$$0 = -F_l \log \zeta - \hat{F}(\zeta) + \frac{z(\zeta)}{\bar{z}'(1/\zeta)} \left[\bar{F}_l \zeta + \bar{F}'(1/\zeta) \right] + \bar{G}_l \log \zeta + \bar{G}(1/\zeta) \quad (5.29)$$

so, in order for this to be single-valued, we must choose

$$G_l = -\bar{F}_l. \quad (5.30)$$

With this choice of coefficient, the velocity is given by

$$\begin{aligned} u + iv &= -F_l \log \zeta - F_l \log \bar{\zeta} + \text{Laurent series} \\ &= -2F_l \log |\zeta| + \text{Laurent series} \end{aligned} \quad (5.31)$$

and is therefore single-valued as well. Next, upon substitution of $H(z, \bar{z})$ into the force equation (5.2) gives the force on the central plate as

$$2i\mu[H]_\Gamma = 2i\mu \left[F_l \log(\rho^2 \eta) - F_l \log(\rho^2 / \eta) + \text{single-valued} \right]_{|\zeta|=\rho} \quad (5.32)$$

where $\zeta = \rho^2 \eta$ and $z(|\zeta| = \rho) = \Gamma$. In order for Γ to be positively oriented, we must traverse the inner ρ circle of the annulus in a positive (counter-clockwise) manner. This gives the force on the plate as

$$-8\mu\pi F_l. \quad (5.33)$$

Note also that the force on the wall is computed by performing the same calculation whilst on the *outer* (unit) circle of the annulus. In this case the $|\zeta| = 1$ circle is traversed in a negative (clockwise) fashion around the logarithmic singularity (at $\zeta = 0$) and hence the force on the wall is given by $8\mu\pi F_l$. It is precisely because the force on the wall is equal and opposite to that on the plate that there is no net force on the fluid and hence we do not encounter the Stokes paradox. Also, given the choice of constants (5.30), the velocity at a

general point in the fluid is given by

$$u + iv = -2F_l \log |\zeta| - \hat{F}(\zeta) + \frac{z(\zeta)}{z'(\zeta)} \left[\frac{\overline{F}_l}{\zeta} + \overline{\hat{F}}'(\bar{\zeta}) \right] + \overline{\hat{G}}(\bar{\zeta}) \quad (5.34)$$

and hence has no logarithmic contribution in the far field (as $\zeta \rightarrow \pm i$). Next, the no-slip condition on the unit circle takes the form

$$-F(\zeta) + \frac{z(\zeta)}{\bar{z}'(1/\zeta)} \overline{F}'(1/\zeta) + \overline{G}(1/\zeta) = 0. \quad (5.35)$$

Upon substitution of ansatz (5.28) into this, we have that

$$-\hat{F}(\zeta) + \frac{z(\zeta)}{\bar{z}'(1/\zeta)} \left[\overline{F}_l \zeta + \overline{\hat{F}}'(1/\zeta) \right] + \overline{\hat{G}}(1/\zeta) = 0. \quad (5.36)$$

Next, on the inner circle where $|\zeta| = \rho$, we have

$$-F(\rho^2 \zeta) + \frac{z(\rho^2 \zeta)}{\bar{z}'(\rho^2/\zeta)} \overline{F}'(\rho^2/\zeta) + \overline{G}(\rho^2/\zeta) = 0 \quad (5.37)$$

and, again after substitution of the same ansatz,

$$-\hat{F}(\zeta) + \frac{z(\zeta)}{\bar{z}'(\rho^2/\zeta)} \left[\frac{\overline{F}_l \zeta}{\rho^2} + \overline{\hat{F}}'(\rho^2/\zeta) \right] - \overline{F}_l \log \rho^2 + \overline{\hat{G}}(\rho^2/\zeta) = 0. \quad (5.38)$$

Making the substitution $\zeta \rightarrow \rho^2 \zeta$ into the above (5.38) gives

$$-\hat{F}(\rho^2 \zeta) + \frac{z(\rho^2 \zeta)}{\bar{z}'(1/\zeta)} \left[\overline{F}_l \zeta + \overline{\hat{F}}'(1/\zeta) \right] - F_l \log \rho^2 + \overline{\hat{G}}(1/\zeta) = 0. \quad (5.39)$$

Subtraction of (5.39) from (5.36) gives the relation

$$\hat{F}(\rho^2 \zeta) - \hat{F}(\zeta) + \{z(\rho^2 \zeta) - z(\zeta)\} \left[\frac{\overline{F}_l + \overline{\hat{F}}'(1/\zeta)}{\bar{z}'(1/\zeta)} \right] = -F_l \log \rho^2. \quad (5.40)$$

We now invoke the special loxodromic property of this map (5.9) to reduce this to

$$\hat{F}(\rho^2 \zeta) - \hat{F}(\zeta) = -F_l \log \rho^2. \quad (5.41)$$

As we shall see, is precisely this condition that will make it possible to find an exact solution to this problem.

The far field conditions for $f(z)$ and $g'(z)$ are given by (5.25) and (5.26). As $f(z)$ tends to a linear function of z in the upper far field, corresponding to $\zeta = i$, while tending to a constant at $\zeta = -i$, we let

$$\hat{F}(\zeta) = AK(\zeta/i, \rho) \quad (5.42)$$

where A is a constant to be determined. This is the analytic function that may satisfy condition (5.41) given relation (5.21) for $K(\zeta, \rho)$. Using this in (5.41) together with (5.21) reveals that

$$A = F_l \log \rho^2. \quad (5.43)$$

Notice that, as A is generally of order unity, this means that $F_l \sim 1/\log(\rho)$ which approaches zero extremely slowly. As a consequence, even exponentially small central plate lengths have non-negligible F_l , and hence finite logarithmic contributions. Following the language of Hasimoto [48] we shall refer to this as the *blocking effect*.

It now just remains to find F_l . To do this, recall that the conformal map $z(\zeta)$ takes the leading order form around $\zeta = i$ (corresponding to $z \rightarrow \infty^+$ in the fluid domain)

$$z(\zeta) = \frac{a}{\zeta - i} + \text{analytic function}, \quad \text{or} \quad \frac{1}{\zeta - i} = \frac{z}{a} + \text{analytic function}. \quad (5.44)$$

Therefore, given our solution (5.42) together with the expression for A in (5.43) and the leading order expansion of $K(\zeta, \rho)$ in (5.24), we have that

$$\begin{aligned} F(\zeta) &= AK(\zeta/i, \rho) = \frac{iA}{\zeta - i} + \dots = \frac{iA}{a}z + \dots \\ &= \frac{iF_l \log \rho^2}{a} + \dots \end{aligned} \quad (5.45)$$

and as, from equation (5.25), this must tend to $iz/2$, we see that

$$F_l = \frac{a}{4 \log \rho}. \quad (5.46)$$

Using this, we finally arrive at the result

$$F(\zeta) = \frac{a}{4 \log \rho} \left[\log \zeta + (2 \log \rho) K(\zeta/i, \rho) \right]. \quad (5.47)$$

Once we have this, $\hat{G}(\zeta)$ follows from the no-slip condition (5.36) and thus we have completely determined the flow everywhere above and below the wall.

As given by equation (5.33), the total force on the plate is given by $-8\mu\pi F_l$ and is graphed in Figure 5.2 as a function of central plate length. Interestingly, the force is horizontal and there is no vertical component to it. While this may be surprising, it is consistent with the observation by Smith [2] who, in the case of a single gap in the wall, observed that there is no mass flux or mixing of fluids through the gap. The fluid beneath the gap is stirred only by the shear stresses across the gap, generated by the motion of the fluid in the upper half plane. The force on the central plate is then a result of the differential shear stresses across it, while the absence of any fluid flux through the gap justifies the lack of vertical forces on the plate.

5.4.1 Limit of diminishing central plate length: comparison to Smith [2].

In chapter 3 we studied a shear flow past a wall which had only one gap (and no central plate). It therefore serves as an important check on the above analysis to ensure that in the limit of zero central plate length (and hence $\rho \rightarrow 0$) we retrieve the solution found in chapter 3, or that

$$F(\zeta) = \frac{i}{2(\zeta - i)} \quad (5.48)$$

plus possibly a constant (as in the double gap analysis we have not necessarily set the same additive constant of $f(z)$ to zero).

To do this, notice that from the definition of $P(\zeta, \rho)$ we see that in the limit of $\rho \rightarrow 0$,

$$P(\zeta, 0) = 1 - \zeta, \quad P'(\zeta, 0) = -1, \quad P''(\zeta, 0) = 0. \quad (5.49)$$

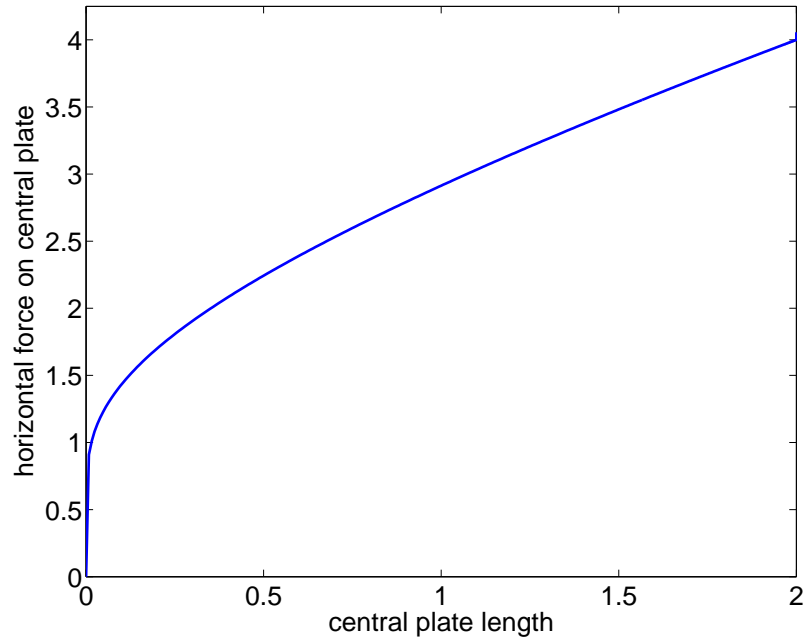


Figure 5.2: Total horizontal force on the central plate for varying plate length, for an on-coming shear flow. There is no vertical force on this.

Using these in the definition of the doubly connected conformal map (5.3) means that

$$z(\zeta) \rightarrow \frac{(1 + \zeta)^2 - (1 - \zeta)^2}{(1 + \zeta)^2 + (1 - \zeta)^2} = \frac{2\zeta}{1 + \zeta^2} \quad (5.50)$$

which is precisely the single gap map, defined in chapter 3. Furthermore, the parameter a defined in (5.14) reduces to 1. Next, using (5.17) we see that

$$K(\zeta, 0) = \frac{\zeta}{\zeta - 1}. \quad (5.51)$$

Putting these together in our function $F(\zeta)$ defined by (5.47) gives

$$\begin{aligned} F(\zeta) &= \frac{a}{4 \log \rho} \left[\log \zeta + (2 \log \rho) K(\zeta/i, \rho) \right] \\ &\rightarrow \frac{a}{2} K(\zeta/i, 0) \quad \text{as } \rho \rightarrow 0 \\ &= \frac{i}{2(\zeta - i)} + \text{constant} \end{aligned} \tag{5.52}$$

which is the required solution for the single gap case, and we conclude that the doubly connected solution is consistent with the simply connected case.

5.4.2 Results: shear flow past a wall with two gaps.

Some typical streamlines are shown in Figure 5.3, where the central plate lengths are 0.3, 1 and 1.9, (or 15%, 50% and 95%, respectively), of the gap width. When the plate length is 1.9, the gaps are narrow and the resulting streamlines resemble Figure 2 in Smith [2], who considered a shear flow past a wall with an infinite array of equally separated gaps. This gives a good qualitative verification of our results.

5.5 Stagnation point flow past a wall with two gaps.

As in the case of a single gap in the wall, we next turn our attention to the case where the same geometry is subjected to an oncoming stagnation point flow of strength k with an additional up-down pressure gradient as defined in chapter 3 for the similar flow above a wall with only one gap. Recall that, in this case, the far field forms of $f(z)$ and $g'(z)$ are given by

$$f(z) \rightarrow \begin{cases} ikz^2/4 + \Delta Pz/4\mu + \mathcal{O}(1), & \text{as } z \rightarrow \infty^+ \\ -\Delta Pz/4\mu + \mathcal{O}(1), & \text{as } z \rightarrow \infty^- \end{cases} \tag{5.53}$$

and

$$g'(z) \rightarrow \begin{cases} -3ikz^2/4, & \text{as } z \rightarrow \infty^+ \\ \mathcal{O}(1), & \text{as } z \rightarrow \infty^-. \end{cases} \tag{5.54}$$

When $k = 0$, the fluid is driven only by a pressure difference across the wall and corresponds to the problem studied by Hasimoto [48]. We follow the same solution method as

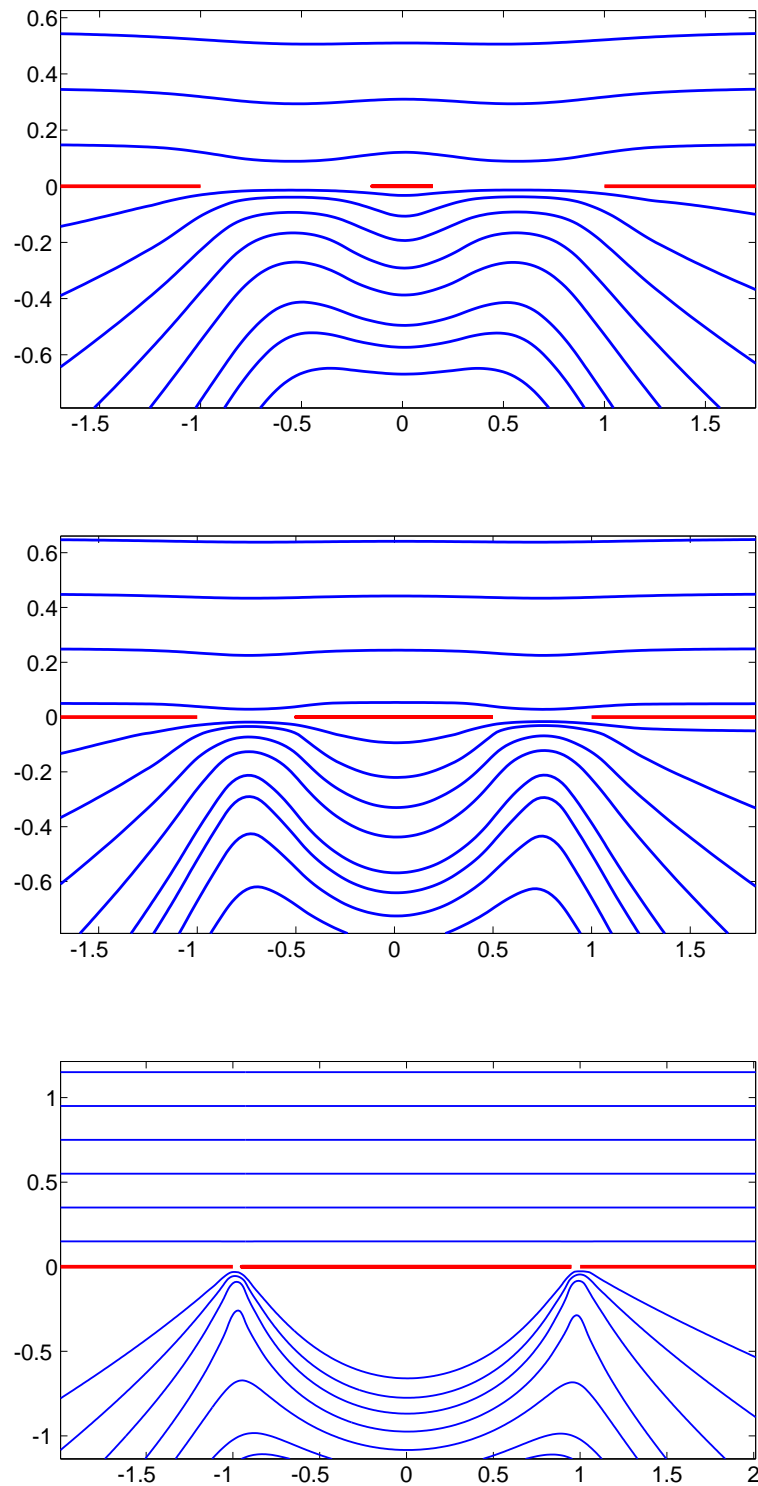


Figure 5.3: Typical streamlines for shear flow above a wall with two gaps, with varying central plate length of 0.3 (top), 1 (middle) and 1.9 (bottom). These may be qualitatively compared to Figures 1 and 2 in Smith [2].

above, so all the details carry over to this case too. In particular, $F(\zeta)$ and $G(\zeta)$ have the same functional form and relation (5.41) still holds. In order to solve for this flow, introduce the function

$$L(\zeta, \rho) = \zeta K'(\zeta, \rho). \quad (5.55)$$

From this definition we have that

$$L(\zeta^{-1}, \rho) = \frac{1}{\zeta} K'(\zeta^{-1}, \rho) \quad (5.56)$$

and, upon differentiating relation (5.20) we see that $K'(\zeta^{-1}, \rho) = \zeta^2 K'(\zeta, \rho)$ and hence

$$L(\zeta^{-1}, \rho) = L(\zeta, \rho). \quad (5.57)$$

Similarly, using the derivative of relation (5.21), it is straight forward to show that

$$L(\rho^2 \zeta, \rho) = L(\zeta, \rho). \quad (5.58)$$

Due to this relation, $L(\zeta, \rho)$ is example of a loxodromic function. It has simple pole singularities at the isolated points $\zeta = \rho^{2n}$ for $n \in \mathbb{Z}$ and, as equation (5.24) gives the leading order form of $K(\zeta, \rho)$ near the point $\zeta = 1$, we see that

$$L(\zeta, \rho) = -\frac{1}{(\zeta - 1)^2} - \frac{1}{(\zeta - 1)} + \dots \quad (5.59)$$

near the same point.

We now propose that

$$\hat{F}(\zeta) = AL(\zeta/i, \rho) + BK(\zeta/i, \rho) + CK(-\zeta/i, \rho) + D \quad (5.60)$$

with constants A, B, C and D . Without loss of generality, we choose $D = 0$ due to the additive degree of freedom in the function $f(z)$. Next, condition (5.41) together with the

above properties of $L(\zeta, \rho)$ and $K(\zeta, \rho)$, we see that

$$B + C = F_l \log \rho^2. \quad (5.61)$$

We now use the far field conditions to determine the constants. To do this, notice that since

$$z(\zeta) = \frac{a}{\zeta - i} + b + \dots \quad (5.62)$$

we may write

$$\frac{1}{\zeta - i} = \frac{z}{a} - \frac{b}{a} + \mathcal{O}(z^{-1}) + \dots \quad (5.63)$$

therefore

$$\frac{1}{(\zeta - i)^2} = \frac{z^2}{a^2} - \frac{2bz}{a^2} + \dots \quad (5.64)$$

and similarly

$$\frac{1}{\zeta + i} = \frac{z}{a} + \mathcal{O}(1) + \dots \quad (5.65)$$

Given these expansions, we see that as $\zeta \rightarrow i$ (corresponding to $z \rightarrow \infty^+$ in the physical fluid domain) we have that

$$\begin{aligned} F(\zeta) &\rightarrow A \left[\frac{1}{(\zeta - i)^2} - \frac{i}{\zeta - i} + \dots \right] + B \left[\frac{i}{\zeta - i} + \dots \right] + \dots \\ &= A \left[\frac{z^2}{a^2} - \left(\frac{2b}{a^2} + \frac{i}{a} \right) z + \dots \right] + B \left[\frac{iz}{a} + \dots \right] + \dots \\ &= \frac{A}{a^2} z^2 + \left(\frac{iB}{a} - A \left\{ \frac{2b}{a^2} + \frac{i}{a} \right\} \right) z + \mathcal{O}(1) + \dots \end{aligned} \quad (5.66)$$

Comparing this with (5.53) as $z \rightarrow \infty^+$ we see that

$$A = \frac{ika^2}{4}, \quad B = -\frac{i\Delta Pa}{4\mu} + \frac{k}{4}(ia^2 + 2ba). \quad (5.67)$$

In the limit $\zeta \rightarrow -i$ (corresponding to $z \rightarrow \infty^-$) we have

$$F(\zeta) \rightarrow -\frac{iC}{a} z + \dots \quad (5.68)$$

which, upon again comparing to the far field form of $f(z)$ in the lower plane implies that

$$C = -\frac{i\Delta Pa}{4\mu}. \quad (5.69)$$

Finally, relation (5.61) gives the last constant F_l to be

$$F_l = \frac{1}{2\log \rho} \left[-\frac{i\Delta Pa}{2\mu} + \frac{k}{4}(ia^2 + 2ab) \right]. \quad (5.70)$$

Notice again the inverse relation between F_l and $\log \rho$, implying that the blocking effect will alter this flow too even for exponentially small values ρ .

Putting this together, we find that

$$\begin{aligned} F(\zeta) = & \frac{1}{2\log \rho} \left[-\frac{i\Delta Pa}{2\mu} + \frac{k}{4}(ia^2 + 2ab) \right] \log \rho + \frac{ika^2}{4} L(\zeta/i, \rho) \\ & + \left[\frac{k}{4}(ia^2 + 2ab) - \frac{i\Delta Pa}{4\mu} \right] K(\zeta/i, \rho) - \frac{i\Delta Pa}{4\mu} K(-\zeta/i, \rho). \end{aligned} \quad (5.71)$$

Once we have this, then the no-slip condition (5.36) gives $\hat{G}(\zeta)$, and so we have fully determined the flow everywhere.

Again, we compute the force from equation (5.33) and graph this as a function of varying plate length in Figure 5.4 for the case where $\Delta P = \mu = k = 1$. This force is purely vertical, as can be expected by the left-right symmetry (about the y -axis) of the driving far field flow, the added pressure gradient and the geometrical configuration.

Hasimoto [48] also included a similar graph for the case of purely pressure-driven (Sampson) flow, corresponding to $k = 0$. Hasimoto also noted the blocking effect for very small ρ , which is also evident in Figure 5.4: From Figure 5.1, we see that the plate length ($2r$) is approximately a linear function of ρ as $\rho \rightarrow 0$, and hence the force falls off like $1/\log(2r)$ as $r \rightarrow 0$. This is a very slow decay.

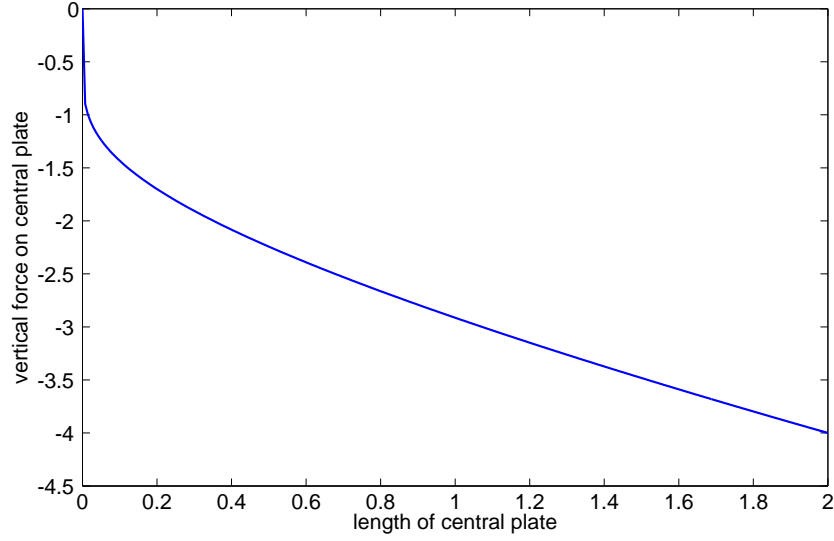


Figure 5.4: Total vertical force on the central plate as a function of varying plate length, where the fluid is driven by a far field stagnation point flow of strength $k = 1$ (with $\mu = 1$) as well as an added pressure gradient with $\Delta P = 1$ in the downward direction. Due to the symmetry of the geometry together with that of the forcing flows, there is no horizontal force on the plate.

5.5.1 Limit of diminishing central plate length: comparison to Ko and Jeong [3].

Again, as a check on the analysis, the solution given here should tend to that of the same driving flow in the simply connected case when the wall had only gap, as studied in chapter 3. Recall that $F(\zeta)$ was given by

$$F(\zeta) = \frac{k\zeta}{4(\zeta - i)^2} + \frac{i\Delta P}{2\mu(\zeta^2 + 1)}. \quad (5.72)$$

Our solution should converge to this in the limit of diminishing central plate length (or as $\rho \rightarrow 0$). To show this, recall that in this limit, $K(\zeta, \rho) \rightarrow \zeta/(\zeta - 1)$ and so

$$L(\zeta, \rho) \rightarrow -\frac{\zeta}{(\zeta - 1)^2}. \quad (5.73)$$

Using this, taking the limit of $\rho \rightarrow 0$ of $F(\zeta)$ in (5.71) gives

$$\begin{aligned} F(\zeta) &\rightarrow 0 + \frac{ka^2}{4} \frac{\zeta}{(\zeta - i)^2} + \left[\frac{k}{4}(ia^2 + 2ab) - \frac{ia\Delta P}{4\mu} \right] \left[\frac{i}{\zeta - i} + \dots \right] \\ &\quad - \frac{i\Delta Pa}{4\mu} \left[\frac{\zeta}{\zeta + i} + \dots \right] \\ &= \frac{k\zeta}{4(\zeta - i)^2} + \frac{ia\Delta P}{2\mu(\zeta^2 + 1)} - \frac{k(ia^2 + 2ab)}{4(\zeta - i)}. \end{aligned} \quad (5.74)$$

Next, in this limit, the constants a and b defined by (5.14) and (5.15) reduce to 1 and 0 respectively and hence,

$$F(\zeta) \rightarrow \frac{k\zeta}{4(\zeta - i)^2} + \frac{ia\Delta P}{2\mu(\zeta^2 + 1)} \quad (5.75)$$

which is precisely the correct function $F(\zeta)$ for the simply connected case.

5.5.2 Results: stagnation point flow past a wall with two gaps.

We now look at the flow streamlines as the oncoming flow is altered, similar to as was done in chapter 3, as well as when the geometry of the domain is changed. First we fix the strength of the stagnation point flow and the viscosity by setting $k = 1$ and $\mu = 1$, and then vary the pressure difference between the upper infinity and lower infinity, $2\Delta P$. This gives the number

$$N = \frac{\Delta P}{k\mu} \quad (5.76)$$

as defined by Ko and Jeong [3]. When N is positive, it corresponds to there being a pressure gradient in the downwards direction. When $N = 0$, the flow is driven by the stagnation point flow only, and finally, when N is negative, there is an upwards pressure gradient. The competition between the two drivers, together with the length of the central plate (and therefore the gaps), determines the nature of the flow above and below the walls.

First, we set the pressure gradient in the downwards direction so that $\Delta P = N = 1$. When there is no central plate, the streamlines pass downwards through the gap as in Figure 3.6, as well as Figure 5(a) of Ko and Jeong [3]. When the central plate is present, but is small in length, small (Moffatt-type) eddies are formed underneath it. The size of these eddies

grow as the central plate length grows and the gap width decreases; see Figure 5.5.

When $N = 0.07$ there is only a slight pressure gradient in the downwards direction and so the fluid motion is driven predominantly by the stagnation point flow. When there is no central plate and the gap width is 2, the streamlines are as given by Figure 3.8, as well as in Figure 5(b) of [3]. When the central plate is introduced and varied in length, eddies form once again underneath the wall and appear to be almost vertically oriented, see Figure 5.6. As the gap width is reduced and the central plate is made longer, the eddies “emanate” from the gap. When the central plate is long (and fills 95% of the gap), the streamlines below the wall are strongly reminiscent of those depicted in Figure 2 of Smith [2] for the case of shear flow past an infinite array of very narrow gaps. This is to be expected, as when the gaps are narrow and sufficiently far from the center of the plate, then in the region above the gap the oncoming flow locally resembles a shear flow.

Finally when we introduce a negative pressure gradient, N is negative and the flow is forced upwards from below in competition with the stagnation point flow which sends fluid downwards. In the absence of a central plate, the streamlines are as in Figure 3.6 as well as in Figure 5(c) of [3]. The flow creates eddies underneath the walls in the vicinity of the sharp edges. When a central plate is introduced, we see that the same eddies are present, but vary their position as the central plate length is increased and the gap width becomes smaller. In particular, the eddies do not form beneath the plate but underneath the sidewalls instead; see Figure 5.7.

On comparison of three cases from Figures 5.6-5.7 for $N = 1, 0.07, -0.5$ respectively, we see that in all cases viscous eddies are formed beneath the plate or sidewall, and the presence of the pressure gradient causes these eddies to be inclined at different angles: when the pressure gradient is almost absent ($\Delta P = N = 0.07$), the eddies are almost vertically oriented below the gaps; as the pressure gradient becomes increasingly positive and hence forces the fluid downwards ($\Delta P = N = 1$), the eddies rotate towards the plate; if the pressure gradient becomes increasingly negative and hence forces the fluid upwards against the driving stagnation point flow, the eddies rotate to incline themselves away from

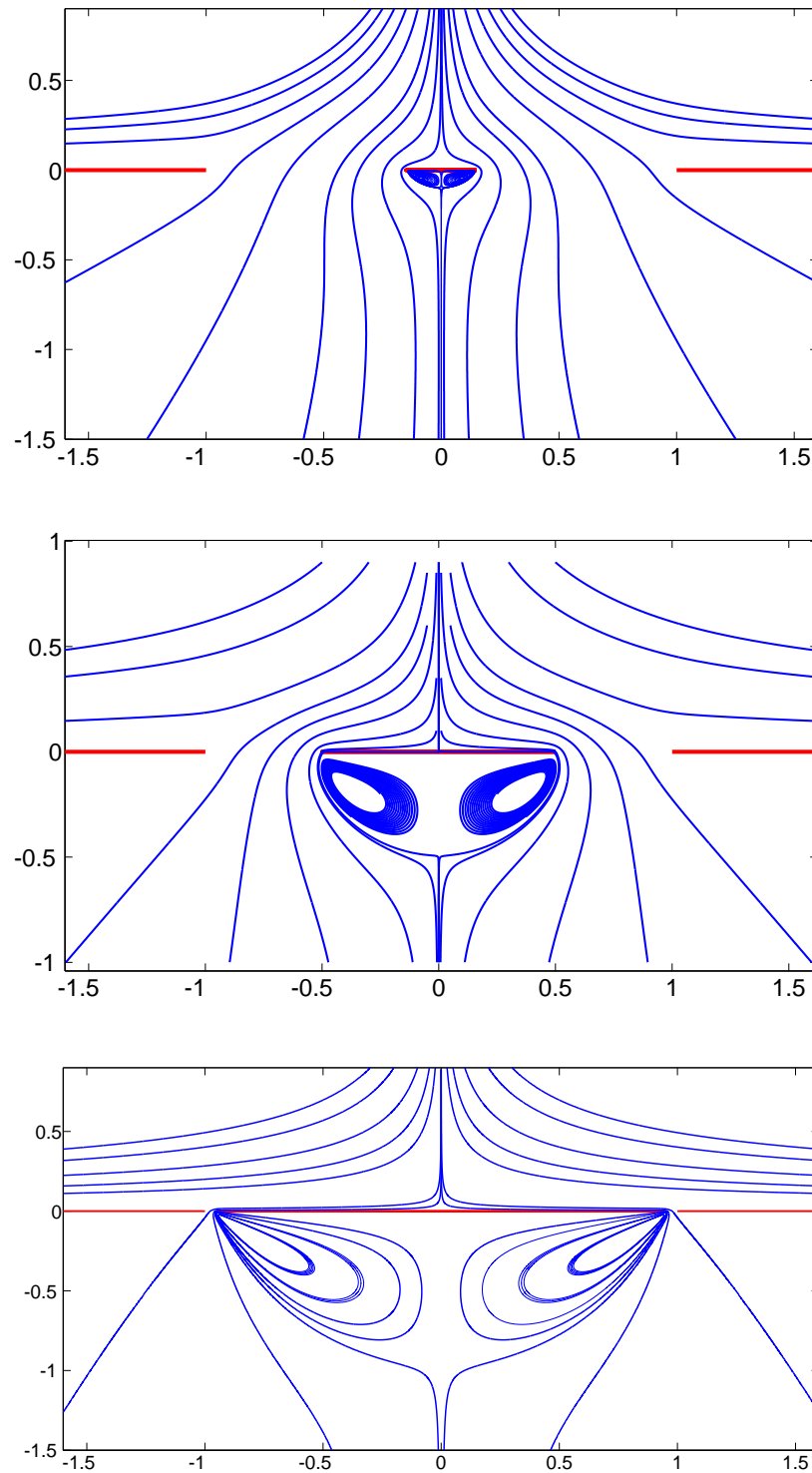


Figure 5.5: Flow streamlines for $N = 1$ and central plate length = 0.3, 1, 1.9 (top to bottom). This corresponds to an additional (downward directed) pressure gradient. The effect of this pressure gradient is to incline the viscous eddies inwards beneath the central plate.

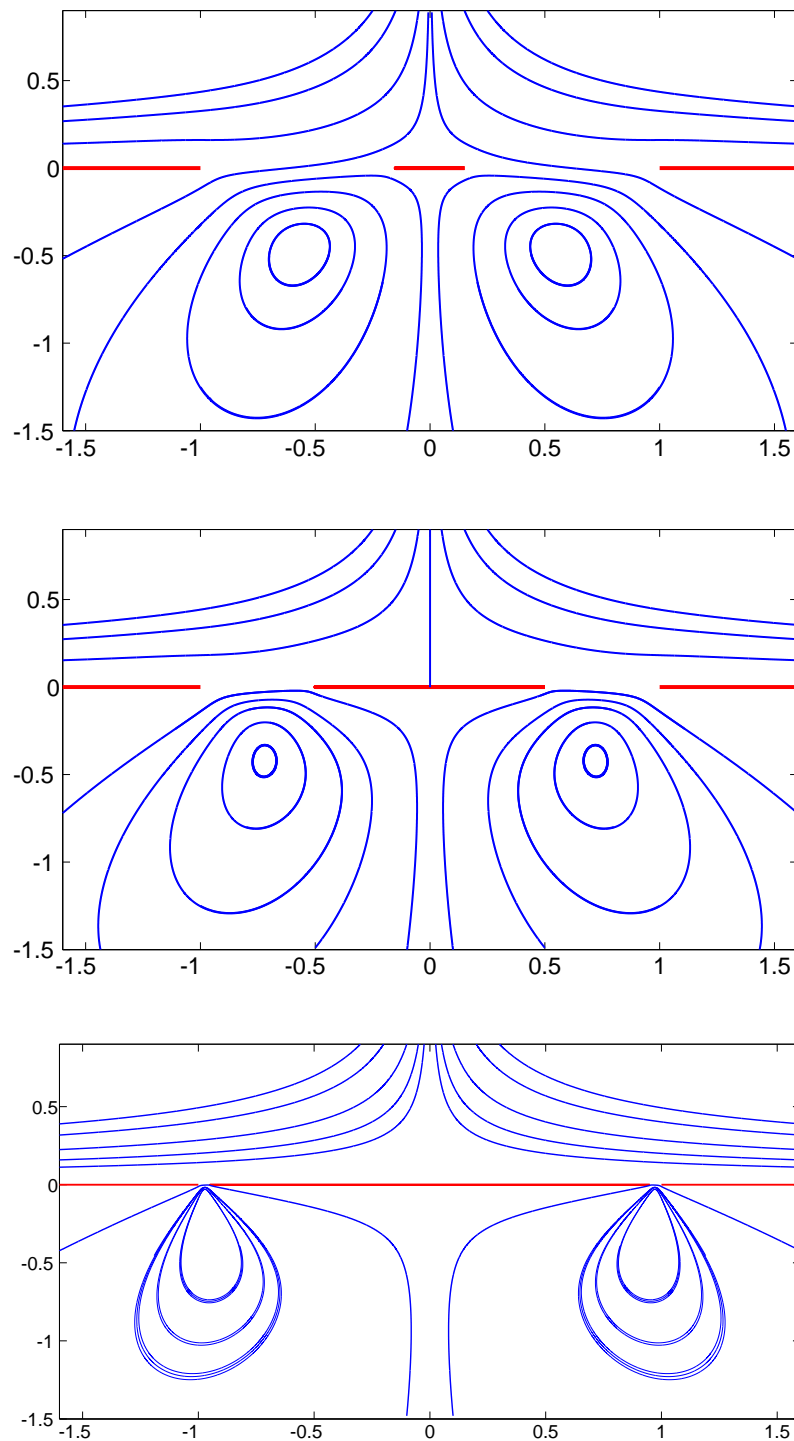


Figure 5.6: Flow streamlines for $N = 0.07$ and central plate length = 0.3, 1, 1.9 (top to bottom). In this case, $\Delta P = 0.07$ and hence there is almost no additional pressure gradient and the flow is predominantly driven by the far field stagnation point flow. In this case, the viscous (Moffatt-type) eddies are almost vertically oriented below the gaps.

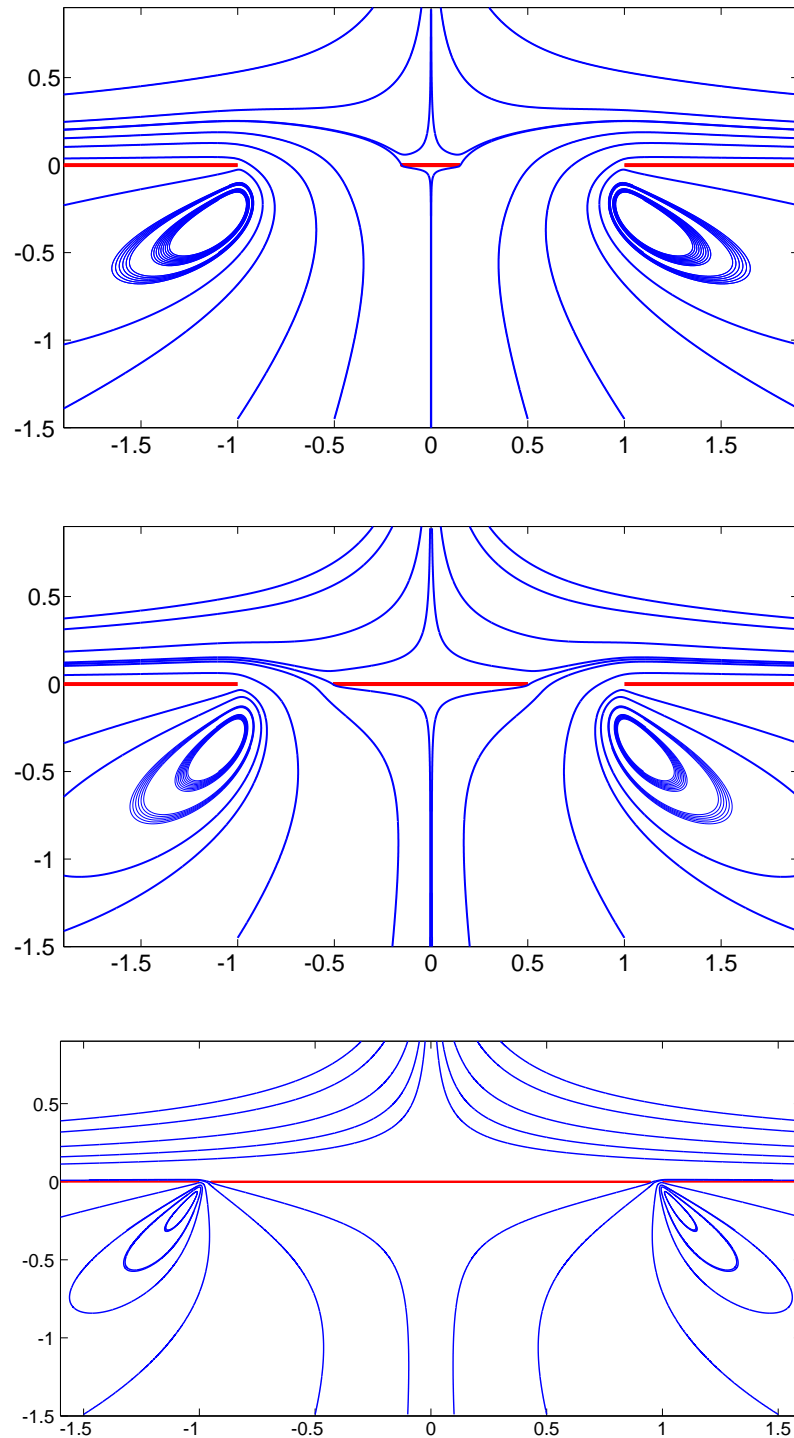


Figure 5.7: Flow streamlines for $N = -0.5$ and central plate length = 0.3, 1, 1.9 (top to bottom). In this case, a pressure gradient is introduced in the upward direction, against the oncoming (downward) stagnation point flow. The effect of this is to orient the viscous eddies away from the central plate and beneath the sidewalls.

the plate and settle underneath the sidewall.

5.6 Summary

We have presented exact solutions for Stokes flows past a no-slip wall with two gaps for the cases where the fluid is driven at the far field either by a uniform shear flow, or a stagnation point flow together with an added pressure gradient. As the only difference between the methods of solution for both these cases was a change in far field boundary condition, it should be clear that this technique is easily amendable to cases where the fluid is driven by other far field flows.

Following Hasimoto [48], this study has been focussed on the case where the gaps on either sides of the central plate have been symmetric. In general, one could perform the same analysis for when the gaps are asymmetric. The appropriate conformal map for this case would be

$$z(\zeta) = \frac{P^2(-\zeta, \rho) - R^2 P^2(\zeta, \rho)}{P^2(-\zeta, \rho) + R^2 P^2(\zeta, \rho)} \quad (5.77)$$

from the annular region $\rho < |\zeta| < 1$ in the ζ -plane to the asymmetric double gap plane. This map is also loxodromic and the case $R = 1$ corresponds to the symmetric case above. It is straightforward to generalise the analysis to the asymmetric domain when $R \neq 1$.

This work is analogous to the motion of a point vortex around geometrically complicated domains, as was studied by Crowdy and Marshall [58]. In this work, the authors considered the same symmetric double gap domain and find the trajectories that a point vortex takes around such a boundary. The authors then present explicit formulae for the conformal map (from an appropriate preimage domain) to the exterior of *any* finite number of gaps in the wall. Therefore, by analogy, one should ask whether the above Stokes flow problem may be similarly extended to the case where there are *more* than two gaps present in the wall. We have investigated this and have found the simply and doubly connected cases (where the wall admits one or two gaps) are rather special, and have been unable to generalise the above analysis to a triply connected fluid domain. In particular, the loxodromic condition

(5.9) can not be extended to a triply connected case. It should be noted that numerical solutions can, of course, be found.

The special functions $P(\zeta, \rho)$, $K(\zeta, \rho)$ and $L(\zeta, \rho)$ used in the analysis here have a close connection to the Weierstrass sigma, zeta and \mathcal{P} functions [61]. While the solutions may be rewritten in the language of elliptic function theory, as Hasimoto [48] did, we believe that for both theoretical and computational purposes, the approach we have taken here is clearer and, as the analysis is self-contained, we have not had to invoke any results from special function theory.

These solutions have been documented as a contribution to the mathematical theory of Stokes flows and the solutions will become useful in a variety of different contexts. In the following chapter, we will build on these solutions by incorporating the singularity model of Crowdy and Or [1] in order to study the motion of a swimming micro-organism in the same geometry.

Chapter 6

Swimming in low Reynolds numbers near a wall with two gaps.

6.1 Introduction

In chapter 4 we studied the motion of a swimming micro-organism in the presence of an infinite flat wall with a gap. We derived exact expressions for the swimmer's governing dynamical equations and from this we were able to find the swimmer's subsequent evolution. We also considered the position and stability of the stationary points of those dynamics, and determined the associated bifurcations as the parameter, ϵ , was increased.

In this chapter we extend the study to the case where the wall admits *two* gaps. As in the case of a swimmer by one gap, we aim to derive three ordinary differential equations for the swimmer's position, $z_d(t)$, and orientation, $\theta(t)$. These expressions will then be used to deduce interesting features of the swimmer's dynamics.

In chapter 5, we considered the slow viscous shear and stagnation point flows in the same confined domain as we consider here. The far field velocities were represented by appropriate singularities at infinity. An advantage of the method is that it may be generalised in a natural way to the case where the flow is driven by a set of singularities at a finite position in the fluid, such as those of the Crowdy and Or [1] singularity structure which

model a swimmer. We will therefore build upon the results found in chapter 5 to construct the appropriate Goursat functions for a swimming organism within this confined domain.

As in chapter 5, the presence of the central plate means that there is a non-zero net force on the wall. We account for this force by including appropriate logarithmic singularities in the relevant Goursat functions.

6.2 Conformal mapping: the symmetric double gap.

Let the central plate occupy the interval $[-r_0, r_0]$ and let the infinite walls lie along the real axis where $|x| > r_0 + W$. Hence, the central plate has a length $2r_0$ while each gap has width W and is at $[\pm r_0, \pm(r_0 + W)]$. These are parameters that we are free to specify.

We now introduce a conformal map, $z(\zeta)$, which is a slight variation to that given by (5.3). The appropriate map is

$$z(\zeta, \rho) = R \left(\frac{P(-\zeta, \rho)^2 - P(\zeta, \rho)^2}{P(-\zeta, \rho)^2 + P(\zeta, \rho)^2} \right) \quad (6.1)$$

where, from here on, we suppress the ρ dependence in $z(\zeta, \rho)$ for convenience. This map associates the interior of an annulus $0 < \rho < |\zeta| < 1$ with the fluid region and the real numbers R and ρ are found numerically so that

$$z(\rho) = r_0 \quad \text{and} \quad z(1) = r_0 + W. \quad (6.2)$$

In this manner, the image of inner circle of the annulus, $|\zeta| = \rho$, is the central plate. As $z(\zeta)$ admits simple poles at the two points $\zeta = \pm i$ on the boundary of the outer circle of the annulus, the image of this circle are the walls $|x| > r_0 + W$ extending out towards infinity. It is known [60] that $z(\zeta)$ has the appropriate square root branch point behaviour at $\zeta = \pm\rho, \pm 1$ which are the preimages of the corners in physical fluid domain. Therefore, using this map allows us to treat ζ as a uniformization variable for the Goursat functions for this problem, which may now be expressed as single-valued functions of ζ . This will

simplify the analysis greatly.

Note also that we must assume that there exists a non-zero force on the central plate. The expression for this force was given in chapter 5 by equation (5.2) as

$$2\mu i \oint_{\Gamma} \frac{dH}{ds} ds = 2\mu i [H]_{\Gamma} \quad (6.3)$$

where Γ is any closed contour encircling the central plate with positive orientation and the square bracket denotes the change in the quantity $H(z, \bar{z}) = f(z) + z\bar{f}'(\bar{z}) + \bar{g}'(\bar{z})$ as this curve is traversed.

6.3 Swimming near two gaps.

In chapter 4 we were able to find the equations of motion for a low Reynolds number swimmer in the vicinity of a single gap within the wall. We will now attempt to find the dynamical system which describes the swimmer's evolution when around two gaps.

6.3.1 The Goursat functions for swimming near a wall with two gaps.

Once we have introduced the conformal map, we will attempt to construct the Goursat functions within the preimage ζ -plane. Define

$$F(\zeta) \equiv f(z(\zeta)) \quad \text{and} \quad G(\zeta) \equiv g'(z(\zeta)) \quad (6.4)$$

which must be analytic everywhere inside the annulus, except for at the positions of the isolated singularities which model the swimmer. We have shown that the presence of the force on the central plate necessitates a logarithmic singularity in the Goursat functions at some point within it. They may therefore be decomposed as

$$F(\zeta) = F_l \log \zeta + \hat{F}(\zeta), \quad G(\zeta) = -\bar{F}_l \log \zeta + \hat{G}(\zeta) \quad (6.5)$$

where the coefficients of the logarithmic terms are again chosen so that the velocity is single-valued everywhere in the fluid. Then, equation (6.3) gives the total force on the central wall as

$$2i\mu \left[F_l \log \left(\frac{\zeta}{\bar{\zeta}} \right) + \hat{F}(\zeta) + z(\zeta) \frac{\overline{\hat{F}}'(\rho^2 \zeta^{-1})}{\overline{z}'(\rho^2 \zeta^{-1})} + \overline{\hat{G}}(\rho^2 \zeta^{-1}) \right]_{|\zeta|=\rho} = -8\pi\mu F_l. \quad (6.6)$$

Once again the Stokes paradox does not present itself here as the force on the infinite wall is equal and opposite to the force on the central plate. This crucial observation means that a solution is not precluded by this paradox.

6.3.2 Determining the Goursat functions from the no-slip boundary condition.

The fluid is stationary on both the infinite walls as well as the central plate. Considering the walls first, we that on its primage, $|\zeta| = 1$, the no-slip condition takes the form

$$-F(\zeta) + \frac{z(\zeta)}{\overline{z}'(\zeta^{-1})} \overline{F}'(\zeta^{-1}) + \overline{G}(\zeta^{-1}) = 0 \quad (6.7)$$

while on the inner ρ -circle of the annulus, we have

$$-F(\zeta) + \frac{z(\zeta)}{\overline{z}'(\rho^2 \zeta^{-1})} \overline{F}'(\rho^2 \zeta^{-1}) + \overline{G}(\rho^2 \zeta^{-1}) = 0. \quad (6.8)$$

Next, substitution of ansatz (6.5) into (6.7) and (6.8) gives

$$-\hat{F}(\zeta) + \frac{z(\zeta)}{\overline{z}'(\zeta^{-1})} \left[\overline{F}_l \zeta + \overline{\hat{F}}'(\zeta^{-1}) \right] + \overline{\hat{G}}(\zeta^{-1}) = 0 \quad (6.9)$$

and

$$-\hat{F}(\zeta) + \frac{z(\zeta)}{\overline{z}'(\rho^2 \zeta^{-1})} \left[\frac{\overline{F}_l \zeta}{\rho^2} + \overline{\hat{F}}'(\rho^2 \zeta^{-1}) \right] - 2F_l \log \rho + \overline{\hat{G}}(\rho^2 \zeta^{-1}) = 0. \quad (6.10)$$

Making the substitution $\zeta \mapsto \rho^2\zeta$ in (6.10) gives

$$-\hat{F}(\rho^2\zeta) + \frac{z(\rho^2\zeta)}{\bar{z}'(\zeta^{-1})} \left[\bar{F}_l\zeta + \bar{F}'(\zeta^{-1}) \right] - 2F_l \log \rho + \bar{G}(\zeta^{-1}) = 0 \quad (6.11)$$

and so subtracting equation (6.9) from (6.11) gives the relation

$$\hat{F}(\zeta) - \hat{F}(\rho^2\zeta) + \{z(\rho^2\zeta) - z(\zeta)\} \left[\frac{\bar{F}_l\zeta + \bar{F}'(\zeta^{-1})}{\bar{z}'(\zeta^{-1})} \right] = 2F_l \log \rho. \quad (6.12)$$

However, $z(\zeta)$ is a loxodromic conformal map and hence satisfies the property

$$z(\zeta) = z(\rho^2\zeta) \quad \text{for all } \zeta \neq 0. \quad (6.13)$$

Therefore, relation (6.12) is reduced to

$$\hat{F}(\rho^2\zeta) - \hat{F}(\zeta) = -2F_l \log \rho \quad (6.14)$$

and it is precisely this condition that allows us to find closed form analytic expressions for the swimmer's governing equations.

6.3.3 The form of $\hat{F}(\zeta)$ and $\hat{G}(\zeta)$.

In light of the special functions $K(\zeta, \rho)$, $L(\zeta, \rho)$ introduced in chapter 5, the special function $M(\zeta, \rho)$ is defined by

$$M(\zeta, \rho) = \zeta L'(\zeta, \rho) \quad (6.15)$$

and can be shown to satisfy

$$M(\zeta^{-1}, \rho) = M(\zeta, \rho), \quad M(\rho^2\zeta, \rho) = M(\zeta, \rho) \quad (6.16)$$

in a similar fashion to the equivalent relations for $K(\zeta, \rho)$ and $L(\zeta, \rho)$, also presented in that chapter. From the definition of $M(\zeta, \rho)$ and from the limiting form of $L(\zeta, \rho)$, we have

that

$$\begin{aligned} M(\zeta, \rho) &= \zeta \frac{d}{d\zeta} \left[-\frac{1}{(\zeta-1)^2} - \frac{1}{(\zeta-1)^2} + \text{analytic function} \right] \\ &= \frac{2}{(\zeta-1)^3} + \frac{3}{(\zeta-1)^2} + \frac{1}{(\zeta-1)} + \text{analytic function.} \end{aligned} \quad (6.17)$$

Recall that in order to model a swimmer by this singularity configuration, we must allow the function $f(z)$ to admit a simple pole, corresponding to the stresslet, at the swimmer's position. In addition to this, we must allow it to admit a third order pole at the swimmer's image position, too. As the conformal map preserves singularity structure, we must allow $\hat{F}(\zeta)$ to also admit a simple pole at ζ_d (where $z(\zeta_d) = z_d$) as well as up to a third order pole at $1/\bar{\zeta}_d$, the image of the swimmer in the annulus.

We have seen that the special functions $K(\zeta, \rho)$, $L(\zeta, \rho)$ and $M(\zeta, \rho)$ are analytic functions everywhere inside the annulus $\rho < |\zeta| < 1$ and that they also have first, second and third order simple poles respectively. This means that they may potentially be useful functional tools to model the swimmer, as they would provide the appropriate singularity structure that the Goursat functions require. However, due to the condition (6.14) together with the functional relations (5.21), (5.58) and (6.16) for $K(\zeta, \rho)$, $L(\zeta, \rho)$ and $M(\zeta, \rho)$ respectively, we conclude that these are the only analytic functions that may be used here.

With this in mind, we deduce that $\hat{F}(\zeta)$

$$\hat{F}(\zeta) = AM(\zeta\bar{\zeta}_d, \rho) + BL(\zeta\bar{\zeta}_d, \rho) + CK(\zeta\bar{\zeta}_d, \rho) + DK(\zeta\bar{\zeta}_d^{-1}, \rho) + E \quad (6.18)$$

where A, B, C, D and E are constants to be determined. With $\hat{F}(\zeta)$ written in this way, the first three terms allow $\hat{F}(\zeta)$ to admit a first, second and third order pole at the position $1/\bar{\zeta}_d$ while the fourth term is included to ensure that $\hat{F}(\zeta)$ has a simple pole at the point $\zeta = \zeta_d$. Finally, the constant term, E , may be set to zero without loss of generality due to the additive degree of freedom in $f(z)$.

6.3.4 Determining the constants of $\hat{F}(\zeta)$.

Using this form of $\hat{F}(\zeta)$ in the condition (6.14) and using the relation

$$K(\rho^2\zeta, \rho) = -\zeta^{-1}K(\zeta, \rho) \quad (6.19)$$

(together with similar relations for $L(\zeta, \rho)$ and $M(\zeta, \rho)$ presented in chapter 5) gives the condition

$$C + D = 2F_l \log \rho. \quad (6.20)$$

Next, note that near $\zeta = \zeta_d$, we may express the map $z(\zeta)$ using its Taylor expansion as

$$z(\zeta) = z_d + z'(\zeta_d)(\zeta - \zeta_d) + \mathcal{O}(\zeta - \zeta_d)^2 + \dots \quad (6.21)$$

or

$$\frac{1}{\zeta - \zeta_d} = \frac{z'(\zeta_d)}{z - z_d} + \mathcal{O}(1) + \dots \quad (6.22)$$

while using the limiting form of $K(\zeta, \rho)$ given in chapter 5, we have that

$$K(\zeta\zeta_d^{-1}, \rho) = \frac{\zeta_d}{\zeta - \zeta_d} + \mathcal{O}(1) + \dots \quad (6.23)$$

and so upon use of expansion (6.22) in this,

$$K(\zeta\zeta_d^{-1}, \rho) = \frac{\zeta_d z'(\zeta_d)}{z - z_d} + \mathcal{O}(1) + \dots \quad (6.24)$$

Therefore, near the swimmer's physical position, the function

$$F(\zeta) \sim \frac{D\zeta z'(\zeta_d)}{z - z_d} + \dots \quad (6.25)$$

As we require this to be stresslet of strength λ , we must choose

$$D = \frac{\lambda}{\zeta_d z'(\zeta_d)} \quad (6.26)$$

to ensure the stresslet singularity is of the correct strength.

Next, it follows from equation (6.9) that

$$\overline{\hat{G}}(\zeta^{-1}) = \hat{F}(\zeta) - \frac{z(\zeta)}{\bar{z}'(\zeta^{-1})} \left[\overline{F}_l \zeta + \overline{\hat{F}}'(\zeta^{-1}) \right]. \quad (6.27)$$

Letting $\zeta \mapsto 1/\bar{\zeta}$ and then taking the conjugate gives

$$\hat{G}(\zeta) = \overline{\hat{F}}(\zeta^{-1}) - \frac{\bar{z}(\zeta^{-1})}{z'(\zeta)} \left[\frac{F_l}{\zeta} + \hat{F}'(\zeta) \right]. \quad (6.28)$$

Substituting the expression (6.18) for $\hat{F}(\zeta)$ into this results in

$$\begin{aligned} \hat{G}(\zeta) = & \overline{A}M(\zeta_d \zeta^{-1}, \rho) + \overline{B}L(\zeta_d \zeta^{-1}, \rho) + \overline{C}K(\zeta_d \zeta^{-1}, \rho) + \overline{D}K(\overline{\zeta}_d^{-1} \zeta^{-1}, \rho) \\ & - \frac{\bar{z}(\zeta^{-1})}{z'(\zeta)} \left[F_l \zeta + \overline{\zeta}_d A M'(\zeta \overline{\zeta}_d, \rho) + \overline{\zeta}_d B L'(\zeta \overline{\zeta}_d, \rho) \right. \\ & \left. + \overline{\zeta}_d C K'(\zeta \overline{\zeta}_d, \rho) + D \zeta_d^{-1} K'(\zeta \zeta_d^{-1}, \rho) \right]. \end{aligned} \quad (6.29)$$

Notice that the first term takes the leading order form

$$\begin{aligned} M(\zeta^{-1} \zeta_d, \rho) &= M((\zeta/\zeta_d)^{-1}, \rho) = -\frac{\zeta_d}{\zeta} M(\zeta/\zeta_d, \rho) \\ &= -\frac{\zeta_d}{\zeta} \left[\frac{2\zeta_d^3}{(\zeta - \zeta_d)^3} + \dots \right] \sim -\frac{2\zeta_d^3}{(\zeta - \zeta_d)^3} + \dots \end{aligned} \quad (6.30)$$

near the point $\zeta = \zeta_d$. Therefore, $\hat{G}(\zeta)$ has a third order pole at this point, but this is exactly the condition that is required of it in order to account for the quadrupole at the swimmer's position. Comparing this to the form of $g'(z)$ near the swimmer's position $z = z_d$ gives the relation

$$A = -\frac{\bar{\lambda} \epsilon^2}{\overline{\zeta}_d^3 \bar{z}'(\overline{\zeta}_d)^3} \quad (6.31)$$

which ensures $\hat{G}(\zeta)$ has the correct quadrupole strength at the swimmer's position.

We see that expression (6.29) for $\hat{G}(\zeta)$ admits simple poles at the points $\zeta = \pm 1, \pm \rho$ as these are the zeros of the derivative of the map, $z'(\zeta)$. However, these are precisely the

simple pole singularities that $G(\zeta)$ is expected to admit at the sharp ends of the walls and plate (i.e. the images of $\zeta = \pm 1, \pm \rho$ respectively). This is therefore consistent with the form of the stream function near a sharp corner, as given by Dean and Montagnon [40] in equation (3.12). Furthermore, the function also incorporates “image singularities” at an infinite set of other points in the ζ -plane, but as these are outside the annulus, they are not physically relevant to the problem at hand. As a result, $\hat{G}(\zeta)$ has exactly the correct singularity structure needed inside $\rho < |\zeta| < 1$.

Expressions (6.26) and (6.31) give two of the five unknowns A, B, C, D, F_l while relation (6.20) provides one additional constraint. Two additional conditions may be found by equating the coefficient of $(z - z_d)^{-2}$ in $\hat{G}(\zeta)$ to $\lambda \bar{z}_d$, while setting the coefficient of the simple pole, $(z - z_d)^{-1}$, to zero. This ensures that the Goursat functions admit the appropriate (stresslet-associated) dipole at the swimmer’s position while disallowing a simple pole (a rotlet) to be present. This can be done by using expressions (6.20), (6.26) and (6.31) to substitute for A, C, D and, upon using the residue theorem, B and F_l may be determined from the two conditions

$$\begin{aligned} \lambda \bar{z}_d &= \frac{1}{2\pi i} \oint_{C_\delta} G(\zeta)(z(\zeta) - z_d) \frac{dz}{d\zeta} d\zeta, \\ 0 &= \frac{1}{2\pi i} \oint_{C_\delta} G(\zeta) \frac{dz}{d\zeta} d\zeta \end{aligned} \quad (6.32)$$

where C_δ is a small circle that encircles the ζ_d in the annulus.

6.3.5 The blocking effect.

It can be shown that in the limit of vanishing central plate length, and hence $\rho \rightarrow 0$, the functions $\hat{F}(\zeta)$ and $\hat{G}(\zeta)$ tend to the Goursat functions for the equivalent single gap problem, as expected. The only difference between them, therefore, is in the logarithmic term which is present in the two gap case but not in the single gap case.

Equation (6.20) shows that

$$F_l \sim \mathcal{O}\left(\frac{1}{\log \rho}\right) \quad (6.33)$$

as the constants C and D are generally of order unity. Therefore, this term vanishes exponentially slowly as ρ tends to zero. For example, when $\rho = 10^{-10}$ (and $r_0 \approx \rho$), $F_l \sim 10^{-2}$ and hence is not negligible. As a consequence of this inverse logarithmic dependence, we expect the convergence of the two-gap solution to the single gap solution to be extremely slow.

6.4 Dynamical system of a swimmer near a wall with two gaps.

Once the above five constants have been found, $F(\zeta)$ and $G(\zeta)$ are then known. These are then used to update the swimmer's position, which varies as a result of its own hydrodynamic interaction with the boundaries. As this is the only method of propulsion for the swimmers in question, we do not allow for any self propagation effects and hence the swimmer's velocity is taken to be only the finite part of the velocity

$$-f(z) + z\bar{f}'(\bar{z}) + \bar{g}'(\bar{z}) \quad (6.34)$$

at $z = z_d$. This means that the horizontal and vertical components of the swimmer's velocity are given by the real and imaginary part of the ordinary differential equation

$$\frac{dz_d}{dt} = -f_0 + z_d\bar{f}_1 + \bar{g}_0 \quad (6.35)$$

with f_0, f_1 and g_0 defined by equations (4.3) and (4.4). The equation for the evolution of head angle, $\theta(t)$ relates the local solid body rotation to the finite part of the local vorticity generated by the flow at $z = z_d$, or

$$\frac{d\theta}{dt} = -2\text{Im}[f'(z)] = i(f_1 - \bar{f}_1). \quad (6.36)$$

Thus, once the initial conditions $(z_d(0), \theta(0))$ for the swimmer and the length of the central plate have been set, these three ordinary differential equations determine the subsequent motion of the swimmer. We will now use them to study some interesting features of the swimmer's dynamics.

6.4.1 Stationary points and their linear stability.

In chapter 4 we considered the dynamics of the swimmer in the vicinity of one gap and found the stationary points together with their associated stability. We found that when ϵ is small enough, there were four stable spiral points at the vertices of a rectangle. When the swimmer was near such a point, it spiralled in towards it, ultimately remaining in that position and, as the value of ϵ was increased, we noted some interesting bifurcations to that stability.

We follow a similar strategy in order to find interesting dynamical features of low Reynolds number swimming near to a wall with two gaps. However, the presence (and length) of the central plate adds another parameter, and hence degree of complication, to the dynamical system. As this widens the parameter space, we restrict our attention to two physically relevant studies. Firstly, we consider the case where the parameter, ϵ , is fixed while the separation of the two gaps is varied. This will demonstrate how the position and stability of the stationary points are gradually affected by the presence of the other gap as they get closer to each other. Furthermore, when the central plate length is very small, the blocking effect on the dynamics of a swimmer around a single gap will become evident. Secondly, we fix the plate length at some small value and consider the effect of varying ϵ . This will demonstrate how the bifurcations which we have seen in the single gap study are affected by the presence of a small solid boundary.

6.4.2 Varying the parameter ϵ with fixed gap separation.

During the study of a swimmer around a wall with a single gap in chapter 4, we saw how the stability of the stationary points changed as ϵ , was varied. By increasing its size, we noticed an interesting sequence of bifurcations which the swimmer underwent, including instances where the stationary points changed from being stable to unstable in nature, as well as the gluing of fixed orbits to form figure-of-eight trajectories.

It is interesting to see whether the addition of a small central plate would disturb this sequence of bifurcations. To this end, we keep the ends of the walls at $x = \pm 1$ and place a

central plate of length 0.1 symmetrically inside the gap, so that its ends are at $x = \pm 0.05$. Note that keeping the plate length small is not a necessary detail for the analysis (indeed, the conformal map is constructed to allow central plates of any length, as long as it “fits” within the gap). Keeping the plate short enables it to be used as a small perturbation to the single gap case, and therefore to isolate its effect on the bifurcations.

As ϵ is increased from 0.1 to 0.5, the structure of the stationary points allows for only four stable points, (marked as the point C in the figures below), while the others remain unstable. These stable points are again at the four corners of a rectangle, with their positions near to the corresponding stable point locations within the single gap case (for the same value of ϵ). When $\epsilon = 0.1$, the point C is a stable spiral; see Figure 6.1. However, as ϵ is increased, it ultimately becomes unstable at the first Hopf bifurcation value

$$\epsilon_h^{(1)} = 0.1722. \quad (6.37)$$

At this stage, although the swimmer may not be attracted towards a single stagnation point, it may nevertheless become trapped within an interesting figure-of-eight period orbit, see Figure 6.3. While these look qualitatively similar to the figure-of-eight trajectories which arose from the dynamics around a single gap, there is a crucial difference between them: the orbits within the single gap study were generated by the gluing of two fixed orbits (each associated with an unstable stationary point). However, in this two-gap case there is a stationary point within only one of the “lobes” of the figure-of-eight. If the governing dynamical system was dependent on the swimmer’s position only, then this transition from a stable spiral to this more complicated orbit (which crosses over itself, without an additional equilibrium point) as ϵ is slightly increased would be impossible. However, recall that in addition to the swimmer’s position, the governing dynamical system is also a function of the swimmer’s orientation, θ . Hence, any fixed orbit of this system is, in fact, a closed curve within the three-dimensional space $(\text{Re}[z_d], \text{Im}[z_d], \theta)$. The trajectories we see in Figure 6.3 are simply the projections of this three-dimensional curve onto the two-dimensional $(\text{Re}[z_d], \text{Im}[z_d])$ plane. This is consistent with the fact that the three-dimensional fixed orbit near to the stationary point C, drawn in Figure 6.4, does not overlap itself.

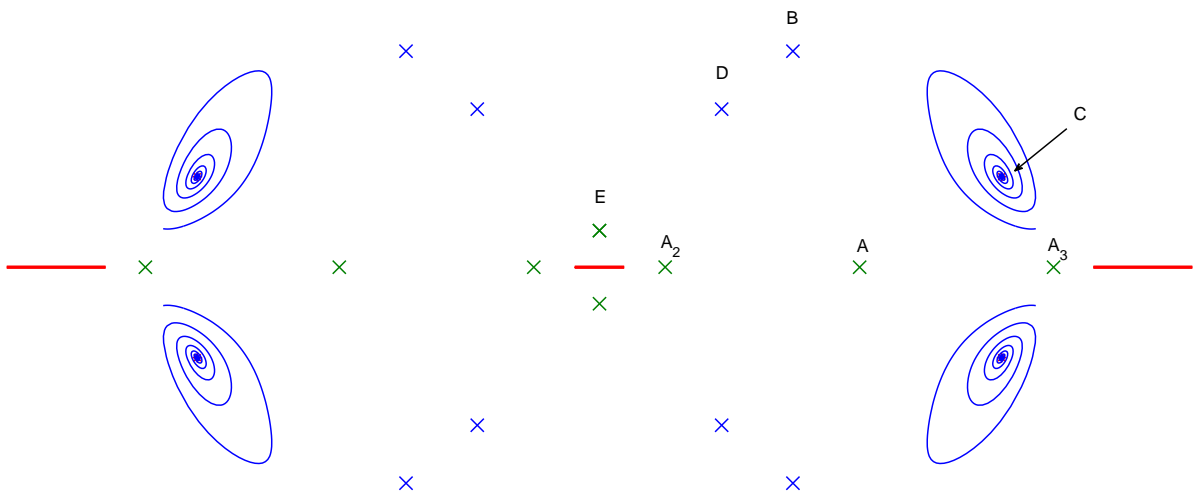


Figure 6.1: Here $\epsilon = 0.1$. The point C (and its corresponding reflections in the real and imaginary axes) are the only stable points.

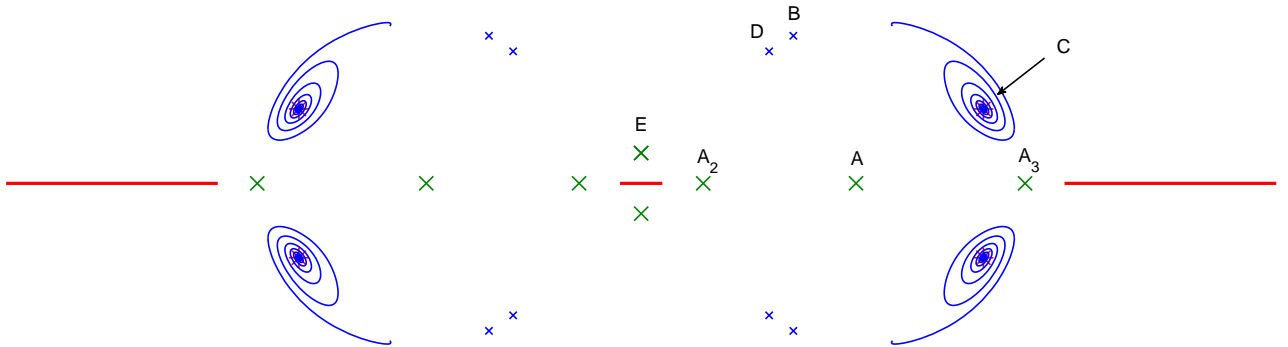


Figure 6.2: Here $\epsilon = 0.115$. The points B and D, both of which are unstable points, are near to each other. They meet and cancel each other out when ϵ reaches the value of 0.1175. The point C is still the only stable point.

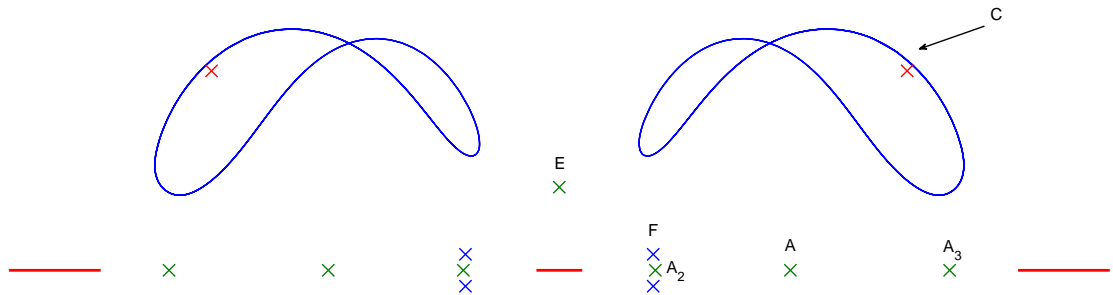


Figure 6.3: Two figure-of-eight fixed orbits when $\epsilon = 0.18 > \epsilon_h^{(1)}$. Each one is the projection on to the $(\text{Re}[z_d], \text{Im}[z_d])$ plane of the orbit which lies in the three-dimensional space (where the third axis corresponds to the swimmer's orientation, θ). Point F has emerged as a result of a saddle-node bifurcation.

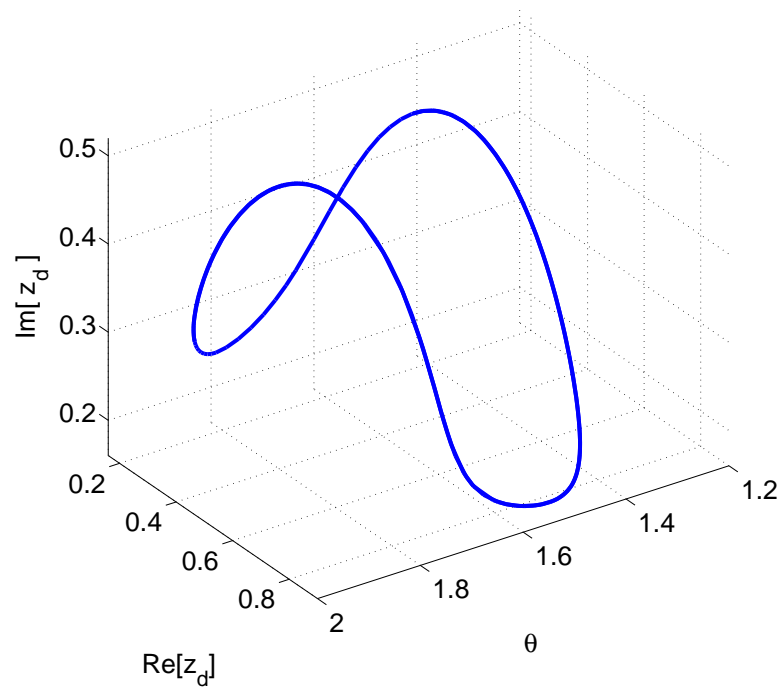


Figure 6.4: Fixed orbit around the stagnation point C when $\epsilon = 0.18$. It does not cross itself. Projecting this onto the $(\text{Re}[z_d], \text{Im}[z_d])$ plane retrieves one of the figure-of-eight orbits drawn in Figure 6.3.

As the value of ϵ is increased further, we notice another Hopf bifurcation point when

$$\epsilon_h^{(2)} = 0.3360, \quad (6.38)$$

where the stagnation point C becomes stable once again. The eigenvalues of the linear stability of point C are shown in the dispersion diagram 6.5 as ϵ is increased. The point C is unstable (during which the trajectories follow a figure-of-eight orbit) when the real part of its eigenvalue is positive and this occurs when $\epsilon_h^{(1)} < \epsilon < \epsilon_h^{(2)}$.

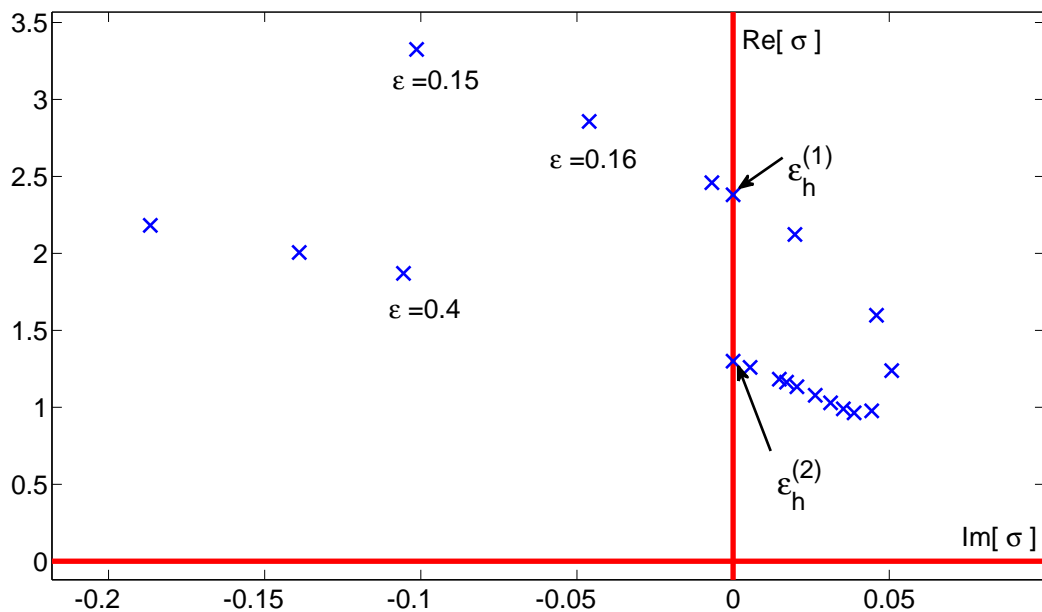


Figure 6.5: Eigenvalues, σ , for the linear stability of point C as ϵ is increased. When $\text{Re}[\sigma] < 0$, it is a stable spiral point while when $\text{Re}[\sigma] > 0$, the points becomes unstable.

Another interesting phenomenon occurs to the stagnation points as ϵ increases from 0.1 to 0.5. There are specific values for ϵ at which two stagnation points undergo a saddle-node bifurcation, defined as a local bifurcation in which two equilibria of a dynamical system collide and annihilate each other [62] or, alternatively, two equilibrium points are

created. For example, recall that when $\epsilon = 0.1$, the positions of the stationary points are demonstrated in Figure 6.1. However, as ϵ is increased, the two points A and A_2 get closer together and ultimately collide on the real axis. When they do this, their effects cancel each other out and, from then on, there are no more stagnation points in either of the two positions. Figure 6.6 shows how the saddle-node bifurcation process evolves as ϵ is increased.

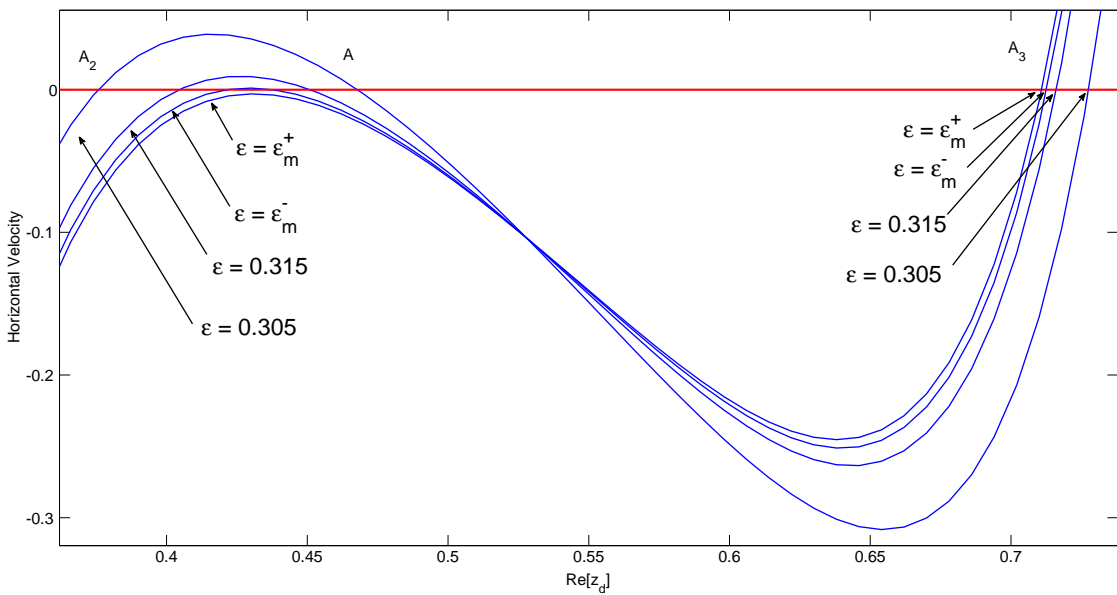


Figure 6.6: A saddle point bifurcation: the points A , A_2 and A_3 all lie on the horizontal axes inside the gaps. Any swimmer placed inside a gap with initial orientation $\theta = \pi/2$ will only swim horizontally. Here we chart the horizontal swimming velocity as a function of its position as ϵ is increased. Both $\dot{\theta}$ and $\text{Im}[\dot{z}_d]$ are zero at all times and so a stagnation point is attained when the horizontal velocity is zero. We see that when ϵ approaches the value $\epsilon_m = 0.3183$, A and A_2 cancel each other out. This is an example of a saddle-node bifurcation.

The points B and D also meet as ϵ is increased to the value of $\epsilon = 0.1175$ and again cancel each other out in the process. This can be seen in Figure 6.2, when $\epsilon = 0.115$ and therefore shows the positions of B and D just before they meet. Shortly after this, the system undergoes another saddle-node bifurcation on the real axis within the gap, creating two

more stagnation points: the point F emerges just above the gap (together with its reflection in the real line) and can be seen in Figure 6.3. Finally, when $\epsilon_s = 0.4343$, the points C and F meet and also cancel each other out. Once this has happened, E and A_3 (both of which are unstable) are the only remaining stagnation points left in the fluid, as is seen in Figure 6.7.

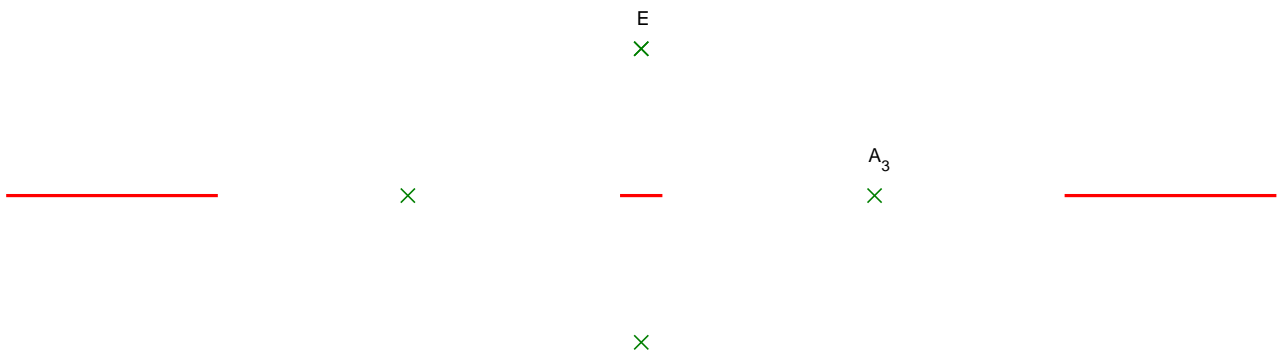


Figure 6.7: The positions of the only remaining stationary points when $\epsilon > \epsilon_s = 0.4343$ (here $\epsilon = 0.5$), and all points are unstable. There are no more saddle-node bifurcations as ϵ increases further.

6.4.3 Varying gap separation with fixed ϵ .

We now fix the value of $\epsilon = 0.1$ and begin by keeping the gaps, each of unit width, away from each other at large distances. We find that the stationary points are in the same position (relative to the gap's position) as in the single-gap study: in the case where $r_0 = 5$, there are four stable points at $(5.5 \pm 0.82 \pm 0.24i)$ each of which are stable spiral points. There are also two saddle points directly above the center of the gap at the points $(5.5 \pm 0.70i)$ as well as at the three unstable stagnation points on the real line between the edges of the gap at $(5.5, 5.5 \pm 0.41)$. In addition to these points, which are present around both gaps, there is

another unstable stagnation point both above and below the origin (the center of the plate), at the points $(\pm 0.1i)$. These stationary points are depicted in Figure 6.8 where the stable spiral points are highlighted. Figure 6.9 shows a magnified view of one of the gaps and labels the stagnation points for future reference. The point E is the (unstable) stagnation point that appears directly above the center of the plate.

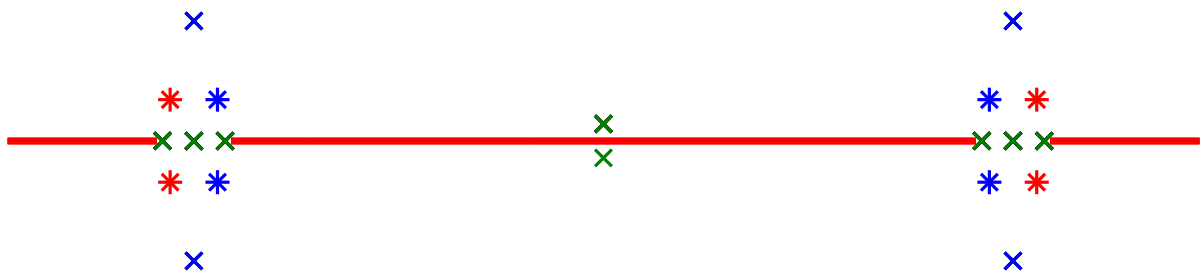


Figure 6.8: The stationary points around two widely separated gaps ($r_0 = 5$) with unit width. The stars highlight the stationary points which are stable while the crosses correspond to unstable stagnation points. ϵ is fixed at 0.1.

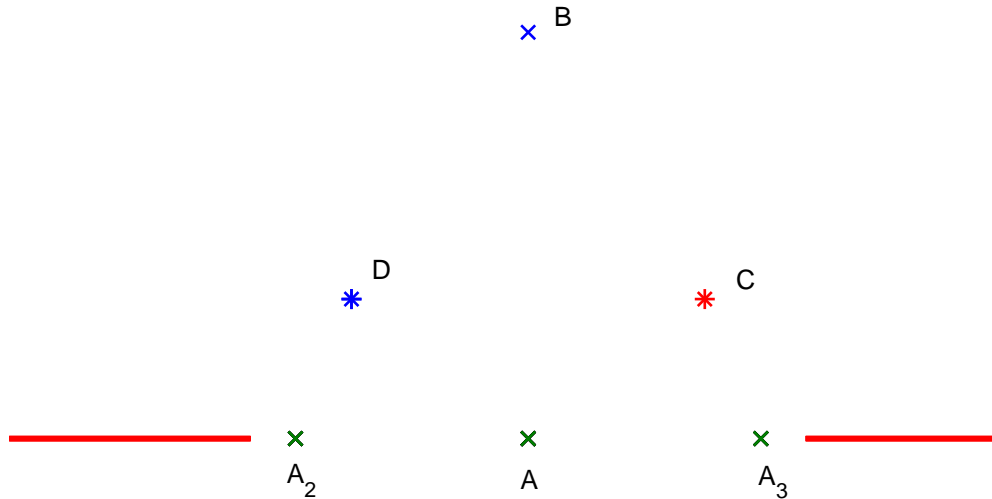


Figure 6.9: A close-up view of the stationary points in Figure 6.8 with $r_0 = 5$. Points C and D are stable spiral points, B is an unstable saddle point while the others are unstable points. Point E (not shown) is on the imaginary axis above the center of the plate and is an unstable point.

An interesting phenomenon occurs as the distance between the gaps is decreased. The unstable saddle point, B, and the stable point D move towards each other and, as r_0 approaches the value

$$r_{0h}^{(1)} = 0.06446, \quad (6.39)$$

the point D undergoes a Hopf bifurcation and becomes unstable. When the gap is decreased further, (and $r_0 \approx 0.016$), they collide (a saddle-node bifurcation) and their effects cancel each other out. See Figures 6.10 - 6.12.

When r_0 is decreased further to the value of 2×10^{-5} , two new stationary points are “born” on the imaginary axis directly above the (small) central plate. Both of these are unstable

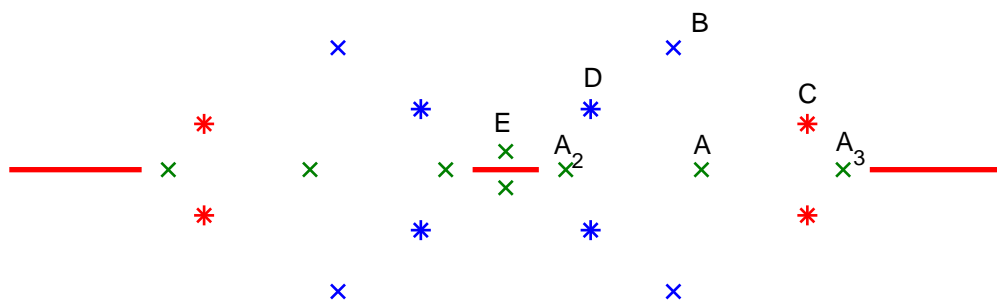


Figure 6.10: Stagnation points as the length of the central plate diminishes. Here we have $r_0 = 0.1 > r_h^{(1)}$ and the stagnation points have the same stability structure as those in Figure 6.8. The presence of the other gap, however, moves them off slightly off the “standard” positions, as seen in Figure 6.8.

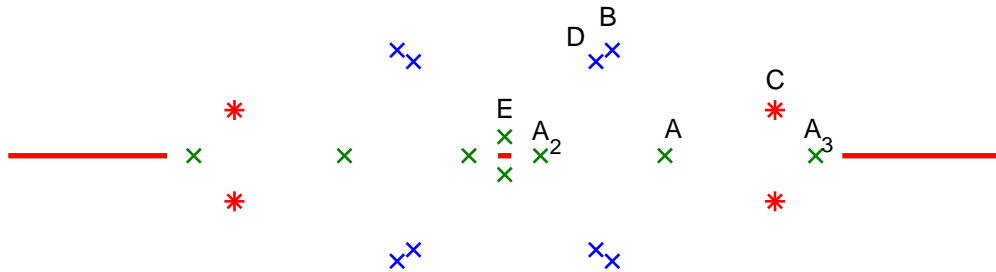


Figure 6.11: Here $r_0 = 0.02 < r_h^{(1)}$, just before points B and D meet and cancel each other out during a saddle-node bifurcation. Here, the stability of point D has changed from a stable spiral to that of an unstable spiral.

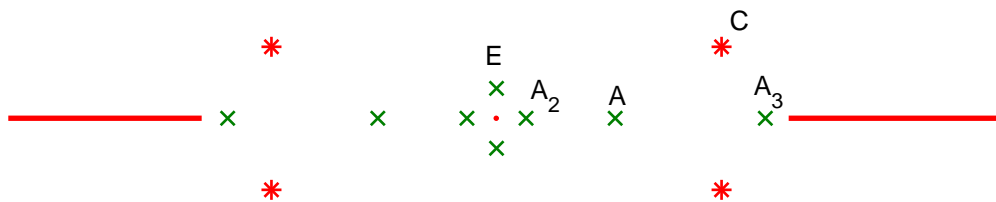


Figure 6.12: Here $r_0 = 0.01$, just after points B and D have met.

points; one of which, E_3 , is a saddle point which moves upwards as r_0 is further decreased to zero, while the other, E_2 , is an unstable point which moves downwards in the same limit. When r_0 is taken to be extremely small (at a value of 10^{-16}), the saddle point E_3 tends to the position of the saddle point that we have seen on the imaginary axis in the single-gap study; see Figure 6.13 - 6.14.

It is interesting to note that due to the blocking effect, even an exponentially small r_0 will give rise to a slight disturbance in the position of the stationary points when compared to the case where there is no wall at all. Indeed, this phenomenon allows a number of new stagnation points to appear within the flow, as highlighted in Figure 6.14.

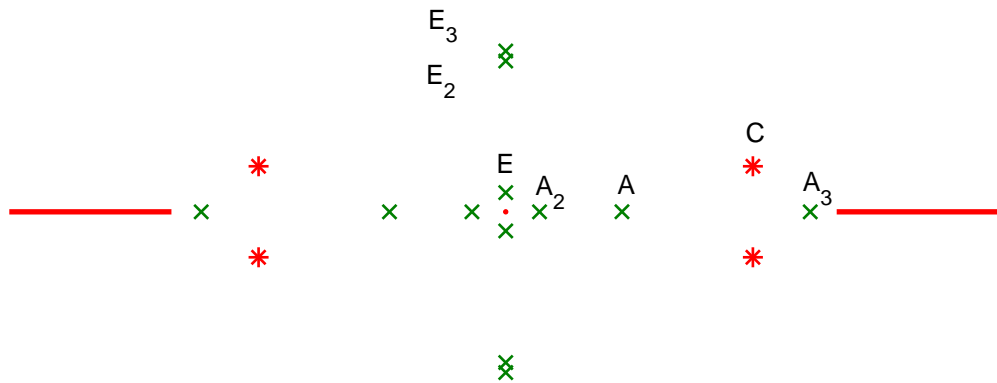


Figure 6.13: As r_0 is decreased further to 2×10^{-5} , two new points are born on the imaginary axis. The upper stagnation point, E_3 is an unstable saddle point while the lower stationary point, E_2 is an unstable point.

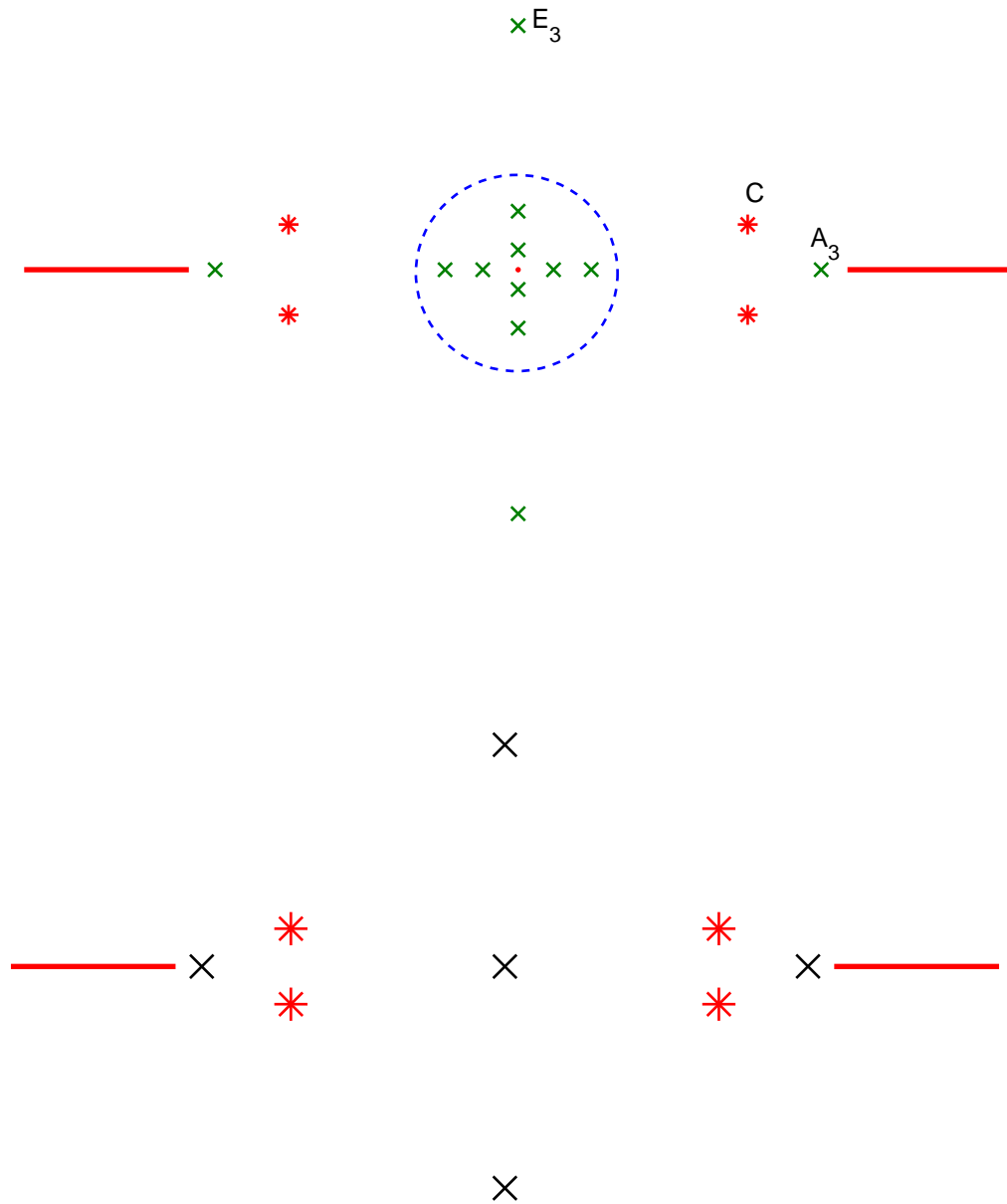


Figure 6.14: Even when r_0 is exponentially small, the blocking effect (top figure) ensures that the flow is altered from the single gap counterpart, (bottom figure), where r_0 is exactly zero. The effect of the blocking effect is highlighted by the dotted circle.

6.5 Summary

We have extended the ideas of chapter 5 to model a swimming micro-organism moving in the vicinity of an infinite wall with two symmetric gaps. By building on the Crowdy and Or [1] model for such a swimmer, we have been able to determine the flow and note some interesting dynamical features of the system. Due to the close agreement which this model has with experimental findings for a swimmer near a flat wall without gaps, we believe that the dynamics presented here provide a predictive theory for how a similar swimmer would evolve near the present confined geometry in three dimensions.

The dynamics presented chapter 4 for a swimmer near an infinite wall with only one gap experienced some interesting phenomena such as gluing, saddle-node and Hopf bifurcations as ϵ was increased. In this case, however, the addition (and length) of a central plate introduces an extra variable which widens the parameter space. We have therefore focused on two limits which have exposed some interesting dynamical features of the system.

By placing a small plate symmetrically inside a gap between $x = \pm 1$, we have been able to see how this introduction affects the bifurcations of the single gap case as ϵ is increased. For small ϵ , we saw four stable-spiral stagnation points which are in similar positions to their single gap counterparts. As ϵ was increased to $\epsilon_h^{(1)}$, these points underwent a Hopf bifurcation, after which a swimmer may have its trajectory trapped in a figure-of-eight pattern indefinitely. We have noted that while they may look qualitatively similar to the figure-of-eight trajectories of the single gap swimmer in chapter 4, they did not form as a result of a gluing bifurcation of two fixed orbits (like the single gap swimmer did). As ϵ was made even larger, the dynamics underwent a second Hopf bifurcation at $\epsilon = \epsilon_h^{(2)}$, after which the four points became stable once again. Ultimately, as ϵ approached ϵ_s , each of these stable points were annihilated during a saddle-node bifurcation. After $\epsilon > \epsilon_s$, there were only four other stagnation points left - one on either side of the central plate on the real axis, and one above and below the central plate on the imaginary axis - none of which were stable. Recall that as ϵ was made large in the single-gap case, the two remaining stagnation points on the imaginary axis (one above and one below the origin) were stable.

This therefore further illustrated how the stability of the single gap stationary points were altered by the introduction of a small central plate.

Turning to the other limit, we studied the effect of the two gaps on each other by controlling their separation and determining the dynamics around each (for a fixed value of ϵ). We saw that when the gaps were sufficiently separated, each had little effect on the other and hence a swimmer near one of the gaps behaved in much the same way as it did in the single gap study. As the gaps' separation was decreased, the system underwent a number of saddle-node bifurcations, resulting in the annihilation of stable-spiral points and the creation of new unstable saddle points. In the limit of exponentially small plate length, we saw a similar stagnation point structure to that of the single gap: there were four stable spiral points at the four corners of a rectangle; two unstable points near the ends of the gaps on the real axes and two unstable saddle points above and below the origin, on the imaginary axis. All of these points were in much the same position as their single gap counterparts. The key difference was manifested in the stationary points around the origin - there were eight new stagnation points around the exponentially small wall. This demonstrated the blocking effect, where an extremely short wall had a non-negligible effect on the flow. However, all of these points were unstable and no trajectories were found to accumulate at any of them.

Chapter 7

Numerical solutions to Stokes flows in complex geometries.

7.1 Introduction

In previous chapters, we have employed various methods of complex analysis to find exact solutions to Stokes flows near walls with gaps. A common feature of the fluid domains in question was that they all admitted sharp corners. By building on the form of the stream function in the vicinity of these corners, as first proposed by Dean and Montagnon [40], we deduced the singularities that the Goursat functions were forced to admit there. Conformal maps which had the same singularity structure as the Goursat functions were then introduced which allowed us to utilise a uniformization variable. Doing this meant that the corresponding Goursat functions in the preimage domain of the conformal map were single-valued and analytic. The problem was then reduced to determining these analytic functions and we were able to call upon a variety of complex variable techniques in order to do this. For example, by virtue of the fact that the conformal map of chapter 5 was loxodromic, we were able to find the Goursat functions explicitly and find exact solutions for the uniform shear and stagnation point flow around a wall with two gaps.

A natural question to ask is whether all Stokes flows near domains of double, or even higher, connectivity are solvable using the same techniques. We have studied this and have

found that this is not the case: not all conformal maps between annuli and doubly connected fluid regions with sharp corners are loxodromic and so, for some domains, the techniques presented in chapter 5 would not necessarily generate exact solutions. While numerical solutions have been used to solve problems which would otherwise be intractable to solve analytically [63], the presence of boundary discontinuities at sharp corners often makes it hard to find solutions even by numerical means. However, the introduction of a conformal map which has the same singularity structure as the Goursat functions in the fluid domain means that, even if they can not be found exactly, their counterparts in the preimage domain will be analytic and free of branch cuts. These problems therefore often lend themselves well to study using numerical techniques.

In this chapter we will demonstrate how the combination of conformal mapping theory with numerical methods may be used to solve Stokes flow problems near various doubly connected fluid regions. By retrieving a result found by Davis and O'Neill [54] for the uniform shear flow past a cylinder above a wall, we demonstrate a numerical procedure which we shall use in other, more complicated, fluid geometries. Then, by combining this numerical approach with the ideas presented in earlier chapters for the flow around sharp edges, we find the shear flow around a finite vertical, and inclined, plate above a wall. We will demonstrate the formation of viscous eddies in such regions and show that this has an interesting relevance to the problem considered by Moffatt [64] for the viscous flow in a wedge. Finally, we apply a similar method to find the viscous flow generated by the *Weis-Fogh* mechanism for lift generation [65].

7.2 Slow viscous shear flow past a cylinder above a wall.

We begin by presenting a new approach to the problem of an oncoming slow viscous uniform shear flow past a cylinder placed above an infinite flat wall. The cylinder is centered on the imaginary axis at a height α and has radius $r < \alpha$. A viscous fluid fills the upper half plane above the wall and exterior to the cylinder where, on both, the no-slip condition holds and so the fluid is stationary. We also assume that the cylinder is held in place and can oppose any fluid force that is exerted on it.

This problem has been previously solved by Davis and O'Neill [54]. With the use of bipolar coordinates, they map the fluid domain to the region between two parallel lines and solve the transformed biharmonic equation there with the use of Fourier transforms. We shall refer to their solution as a basis of comparison to ours.

As before, we seek the stream function in terms of a complex variable z with the general solution (2.13) where, again, $f(z)$ and $g(z)$ are two analytic functions everywhere in the fluid domain, except perhaps at specified positions where singularities are imposed in order to model the problem at hand. Assume that in the far field the fluid is driven by a uniform shear flow with velocity

$$(u, v) = (2Uy, 0) \quad (7.1)$$

with $U = 1$ from here on and so $\psi(z, \bar{z}) \rightarrow y^2$ as $z \rightarrow \infty^+$. We aim to find the flow structure everywhere in the fluid and study any interesting phenomena that occur as the cylinder is brought down towards the plane.

7.2.1 Conformal map: a cylinder above a plane.

Next, let us consider the physical fluid domain as the image of an annulus $\rho < |\zeta| < 1$ in a preimage ζ -plane under a conformal map $z \equiv z(\zeta)$. The form of this will be a Möbius map, as this maps one circle onto another (the real axis can be thought of as an arc of a circle of infinite radius). The specific Möbius map can be written as

$$z(\zeta) = A \left(\frac{\zeta - i}{\zeta + i} \right) \quad (7.2)$$

where $A \in \mathbb{C}$ and the radius of the annulus, ρ , are found by imposing the condition that the unit disk, C_0 , is mapped to the infinite (horizontal) no-slip wall while the inner ρ -circle, C_1 , in the annulus is mapped to the boundary of the cylinder. Upon doing so, it is shown in appendix C that

$$A = -i\sqrt{\alpha^2 - r^2}, \quad \rho = \sqrt{\frac{1 + \delta}{1 - \delta}}, \quad \delta = -\frac{\sqrt{\alpha^2 - r^2}}{\alpha}. \quad (7.3)$$

Written in this way, the origin is mapped to a point inside the cylinder and the point $\zeta = -i$ is mapped to infinity. This is the appropriate conformal Möbius map which associates the preimage annulus to a cylinder of radius r centered at $z = i\alpha$ above the plane.

7.2.2 Constructing the Goursat functions.

As the fluid flows past the cylinder, it exerts a force on it. In chapter 5, we showed that the net force around any object bounded by the curve Γ in the fluid is given by

$$2i\mu \left[H \right]_{\Gamma} \quad (7.4)$$

where $H(z, \bar{z}) = f(z) + z\bar{f}'(\bar{z}) + \bar{g}'(\bar{z})$. Once we have determined the flow, we will use this expression to compute the force on the cylinder.

Defining two Goursat functions in the ζ -plane by

$$F(\zeta) \equiv f(z(\zeta)), \quad G(\zeta) \equiv g'(z(\zeta)) \quad (7.5)$$

then, apart from the singularity at infinity which drives the background shear flow, these functions are completely analytic inside the annulus and hence admit a Laurent series in ζ . As these Laurent series are single-valued and hence give no contribution to the force, we must also allow $H(z, \bar{z})$ to take a multi-valued component. Thus, they also incorporate a logarithmic contribution, the coefficient of which is proportional to the force on each of the solid boundaries, as in chapter 5. The force on the cylinder is equal and opposite to the force on the wall.

Next we know that as we move away from the cylinder and the wall, the velocity tends to that of a uniform shear flow $u + iv = 2y$, which is equivalent to $f(z) \rightarrow iz/2$ and $g'(z) \rightarrow -iz$. As these are linear functions of z then, given the form of the conformal map (7.2), we see that

$$F(\zeta) = \frac{A}{\zeta + i} \quad \text{and} \quad g'(z(\zeta)) = -\frac{2A}{\zeta + i} \quad (7.6)$$

as $\zeta \rightarrow -i$. With this in mind, we may decompose our Goursat functions further as

$$F(\zeta) = F_l \log \zeta + \frac{\hat{F}(\zeta)}{(\zeta + i)} \quad (7.7)$$

and

$$G(\zeta) = -\bar{F}_l \log \zeta + \frac{\hat{G}(\zeta)}{(\zeta + i)} \quad (7.8)$$

where

$$\hat{F}(\zeta) = \sum_{j=0}^N F_j \zeta^j + \sum_{j=1}^N F_{-j} \frac{\rho^j}{\zeta^j}, \quad (7.9)$$

and where $\hat{G}(\zeta)$ admits a similar Laurent series too. Notice that we have scaled the coefficients within the second summation; without doing so, it would be numerically unstable when evaluated on the inner circle of the annulus where $|\zeta| = \rho$. Finally, we may choose

$$F_0 = 0 \quad (7.10)$$

without loss of generality due to the additive degree of freedom in the function $f(z)$.

7.2.3 The no-slip boundary conditions.

The velocity of the fluid on any boundary is zero and hence is also zero on the corresponding boundary in the ζ plane. Therefore we have

$$u + iv = 0 \quad \text{on} \quad \zeta \in C_0, C_1. \quad (7.11)$$

Let us first consider the velocity on the unit circle C_0 , on which $\bar{\zeta} = 1/\zeta$. We have the relations

$$z(\zeta) = A \left(\frac{\zeta - i}{\zeta + i} \right) \quad \text{and} \quad z'(\zeta) = \frac{2iA}{(\zeta + i)^2} \quad (7.12)$$

and hence

$$\frac{z(\zeta)}{\bar{z}'(1/\zeta)} = -\frac{iA}{2A\zeta^2} (\zeta - i)(\zeta + i) = \frac{i}{2\zeta^2} (\zeta^2 + 1) \quad (7.13)$$

where we have used the fact that A is purely imaginary and so $\bar{A} = -A$. Next, using the chain rule we differentiate expression (7.7) to get

$$f'(z) = \frac{1}{z'(\zeta)} \left[\frac{F_l}{\zeta} + \frac{\hat{F}'(\zeta)}{(\zeta + i)} - \frac{\hat{F}(\zeta)}{(\zeta + i)^2} \right] \quad (7.14)$$

and hence

$$\overline{f'(z)} = \frac{1}{\bar{z}'(1/\zeta)} \left[\bar{F}_l \zeta + \frac{i\zeta \overline{\hat{F}'(1/\zeta)}}{(\zeta + i)} + \frac{\zeta^2 \overline{\hat{F}(1/\zeta)}}{(\zeta + i)^2} \right]. \quad (7.15)$$

Putting this into the no-slip boundary condition, we have that

$$0 = -\frac{1}{(\zeta + i)} \hat{F}(\zeta) + \frac{i(\zeta^2 + 1)}{2\zeta^2} \left[\bar{F}_l + \frac{i\zeta \overline{\hat{F}'(1/\zeta)}}{(\zeta + i)} + \frac{\zeta^2 \overline{\hat{F}(1/\zeta)}}{(\zeta + i)^2} \right] + \frac{i\zeta \overline{\hat{G}(1/\zeta)}}{(\zeta + i)} \quad (7.16)$$

Multiplying this expression by $(\zeta + i)$ results in

$$\begin{aligned} 0 &= \frac{1}{2\zeta} (1 + \zeta^2)(1 - i\zeta)F_l - i\zeta \overline{F}(1/\zeta) - \frac{i}{2\zeta} (1 + \zeta^2)\zeta F'(\zeta) \\ &\quad + \frac{1}{2}(1 + i\zeta)F(\zeta) + G(\zeta). \end{aligned} \quad (7.17)$$

We now consider the boundary condition on C_1 , the inner circle of the annulus on which we have $\bar{\zeta} = \rho^2/\zeta$. Note that here it is convenient to write

$$\zeta = \rho\eta \quad (7.18)$$

and consider the curve where $|\eta| = 1$. We then have that

$$\bar{z}'(\rho/\eta) = \frac{2i\bar{A}\eta^2}{(\eta + i\rho)^2} \quad (7.19)$$

and therefore arrive at the relation

$$\frac{z(\rho\eta)}{\bar{z}'(\rho/\eta)} = \frac{i}{2\eta^2} \left(\frac{\rho\eta - i}{\rho\eta + i} \right) (\eta + i\rho)^2. \quad (7.20)$$

Also on this curve we have that

$$\overline{f'(z)} = \frac{1}{\overline{z}'(\rho/\eta)} \left[\frac{\eta \overline{F}_l}{\rho} + \frac{i\eta \widehat{F}'(\rho/\eta)}{(\eta + i\rho)} + \frac{\eta^2 \widehat{F}(\rho/\eta)}{(\eta + i\rho)^2} \right]. \quad (7.21)$$

Using these in the no-slip condition on C_1 gives

$$\begin{aligned} 0 = & -i(1 - i\rho\eta) \log \rho^2 \overline{F}_l + \frac{1}{2\rho\eta} \left(\frac{\rho + i\eta}{\rho - i\eta} \right) (1 - i\rho\eta)^3 F_l \\ & + \frac{1}{2} \left(\frac{\rho + i\eta}{\rho - i\eta} \right) (1 - i\rho\eta) \widehat{F}(\rho\eta) - \frac{i}{2} \left(\frac{\rho + i\eta}{\rho - i\eta} \right) (1 - i\rho\eta)^2 \widehat{F}'(\rho\eta) \\ & - i\eta \left(\frac{1 - i\rho\eta}{\rho - i\eta} \right) \widehat{F}(\rho/\eta) + \widehat{G}(\rho\eta). \end{aligned} \quad (7.22)$$

Equations (7.16) and (7.22) constitute two functions relations on the $\widehat{F}(\zeta)$ and $\widehat{G}(\zeta)$ and hence provide a linear relation between their Laurent coefficients. Furthermore, the two far field conditions (7.6) mean that

$$\widehat{F}(-i) = A \quad \text{and} \quad \widehat{G}(-i) = -2A. \quad (7.23)$$

7.2.4 Numerical procedure

These conditions can be used together to find the coefficients of $\widehat{F}(\zeta)$ and $\widehat{G}(\zeta)$ either by a spectral analysis or by the method of least squares. For the former, as the system is linear in the coefficients of the Laurent series, the functions may be found from a direct comparison of the powers of ζ from the no-slip conditions (7.16) and (7.22) together with the far field conditions (7.23). In the latter, the method of least squares enforces the no-slip conditions by attempting to “fit” a set of Laurent coefficients to the right hand side of equations (7.16) and (7.22), such that they also satisfy the far field conditions, at a set of collocation points distributed across both boundaries. In doing so, these conditions will not be satisfied exactly; the method of least squares converges to a solution by minimising the sum of the squares of the errors encountered at each collocation point.

	$z = 0.6 + 0.3i$	$z = 1 + i$
Davis and O'Neill	$0.0449101332 + 0.0215225474i$	$0.1500124809 - 0.0884469812i$
Spectral analysis	$0.0449101331 + 0.0215225474i$	$0.1500124808 - 0.0884469811i$
Least squares	$0.0449101331 + 0.0215225473i$	$0.1500124808 - 0.0884469810i$

Table 7.1: Comparison of velocities as worked out by Davis and O'Neill [54], as well as those computed using a spectral analysis and a least squares analysis. The results are the same to within an accuracy of $\mathcal{O}(10^{-10})$ of each other.

Davis and O'Neill [54] have presented a solution to this problem using bipolar coordinates together with Fourier transform methods. Their solution therefore serves as a useful check on both of the above numerical methods. Indeed the use of a spectral and least squares method to determine the Laurent coefficients of $\hat{F}(\zeta)$ and $\hat{G}(\zeta)$ yields extremely similar results to Davis and O'Neill [54]. This is demonstrated in Table 7.1 by comparing the velocities at a few locations inside the fluid, as computed by a spectral analysis, a least squares method and finally from the form of the velocity given by Davis and O'Neill [54].

Both spectral and least squares methods produce accurate results for $N = 64$ coefficients of the Laurent series together with 128 collocation points. These choices of parameters will also be appropriate when solving similar problems of Stokes flows past multiply connected fluid regions, including those with sharp corners. As the above results for the shear flow past a cylinder differ from each other only in their tenth decimal place, we have confidence that these numerical methods may also be useful in these (more complicated) geometries.

7.2.5 Results: shear flow past a cylinder above a wall.

We now consider the flow in the vicinity of the cylinder for a variety of different configurations. When the cylinder is placed far away from the plane, the streamlines pass above and below the cylinder as they would if it was placed in free space with an oncoming shear flow, see Figure 7.1. As the cylinder is moved closer to the plane, Figure 7.2, the presence of the wall attracts streamlines downwards towards it in the fore and aft of the cylinder.

As the cylinder is brought further down towards the plane, we see the same behaviour as

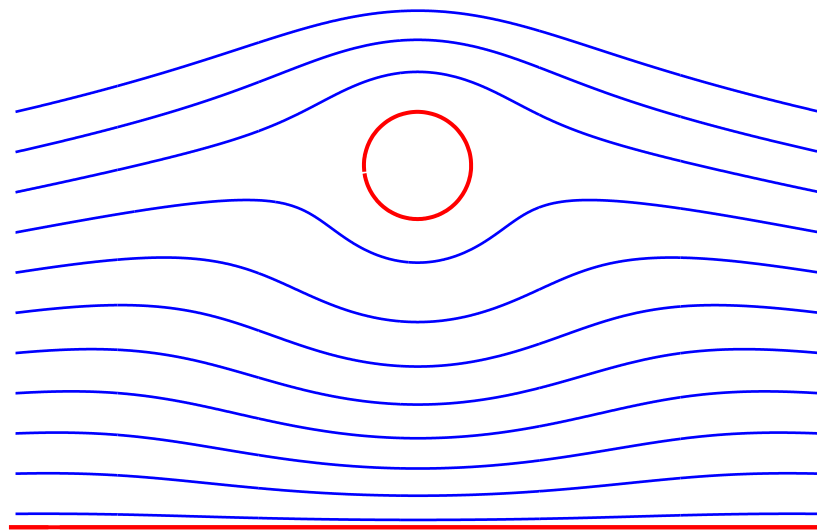


Figure 7.1: Here the cylinder is far away from the no-slip wall and hence the wall's effect on the fluid around the cylinder is minimal. The cylinder is centered above the origin with height $\alpha = 2.7$ and $r = 0.4$. The streamlines are attracted slightly downwards towards the plane before and after the cylinder.

exhibited by Davis and O'Neill [54]. The authors find that when the gap width is less than (approximately) 0.865 times the cylinder radius the streamlines separate and single eddies are formed. Placing the cylinder just above this critical distance ensures that no eddies appear, as shown in Figure 7.3. Lowering the cylinder further to just below the critical height, we see that a single eddy is formed adjacent to the plane at the base of the cylinder as shown in Figures 7.4 and 7.5. This is consistent with the results of Davis and O'Neill [54].

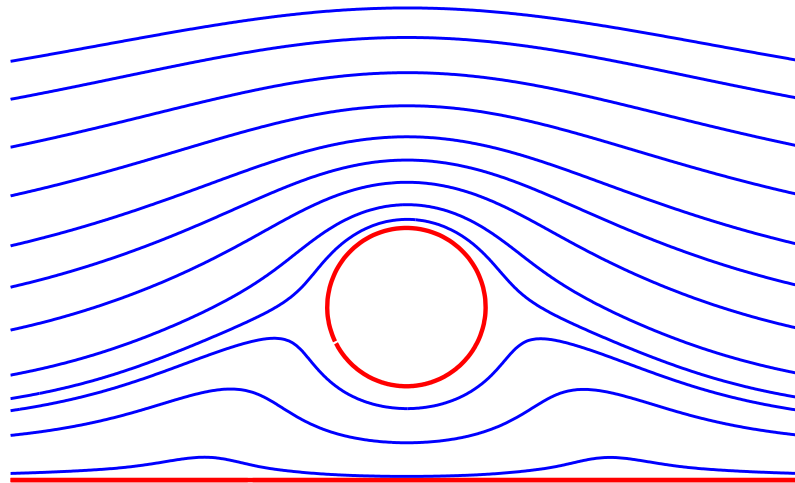


Figure 7.2: As the cylinder is brought downwards, the effect of the wall on the fluid around the cylinder becomes more evident. Here, $\alpha = 0.8$ and $r = 0.4$.

These results demonstrate that both the spectral analysis and least squares method yield, to excellent accuracy, the same results as those found by Davis and O'Neill [54] using the Fourier transform methods. The success of the authors' method relied on the specific geometry of the domain which enabled exact solutions to be found. However, it is not

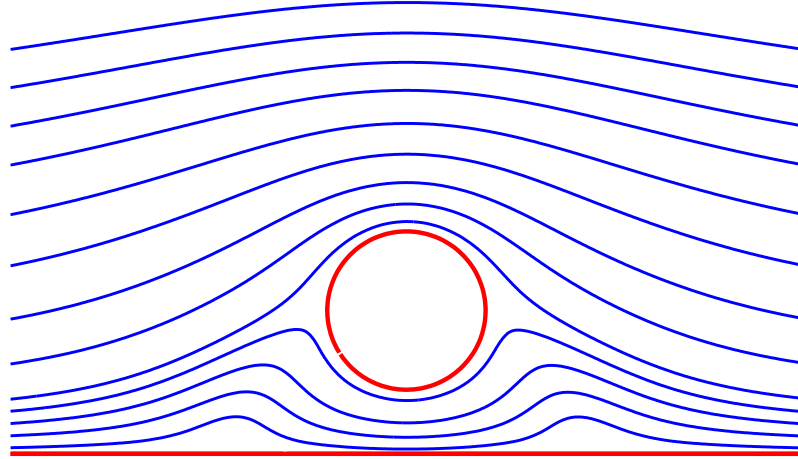


Figure 7.3: Streamlines for when the ratio of gap width to cylinder radius is 0.935. Eddies have not formed yet.

immediately clear how their method would be adapted to accommodate, say, a sharp edge in the fluid domain. It is this that we turn our attention to now. By using the methods that we have developed in previous chapters regarding sharp corners together with the numerical techniques we have demonstrated here, we will attempt to find numerical solutions to the Stokes flow past a finite length plate above a wall.

7.3 Shear flow past a finite perpendicular plate above a wall.

We now consider a similar problem in which a uniform shear flow is present above an infinite no-slip wall but, instead of a cylinder, a finite length plate is placed vertically above, and perpendicular to, the wall. Assume that the lower end of the plate is at height $z = ia$ while the upper end is at $z = ib = i(\alpha + L)$, so that it has length L . Unlike the case of the cylinder above the wall, the sharp ends of the plate present an additional complication

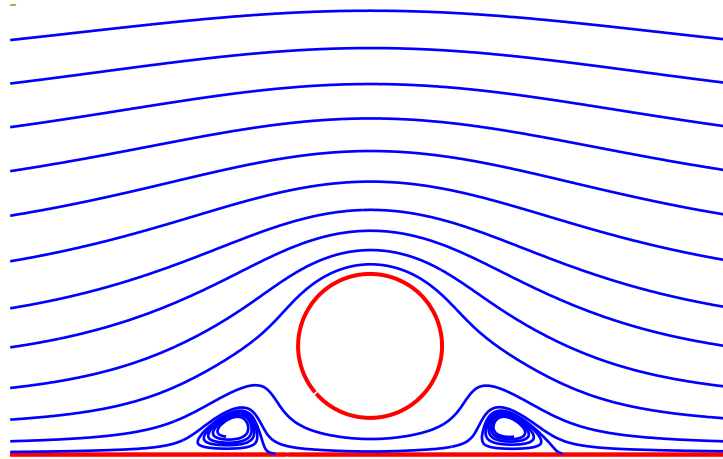


Figure 7.4: Eddies begin to form as the cylinder is brought towards the plane. Here $\alpha = 0.5$ and $r = 0.4$.

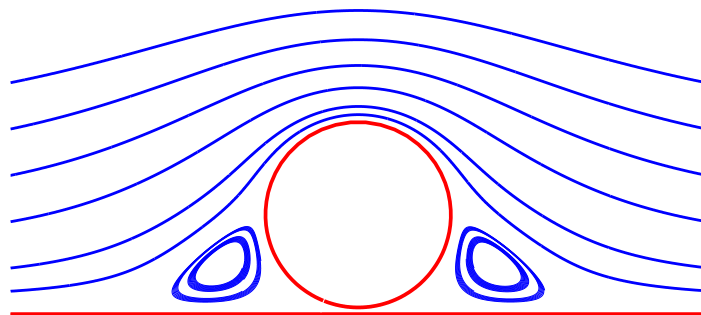


Figure 7.5: When the ratio of the gap width to cylinder radius is much less than the critical value of 0.865 (as found by Davis and O'Neill [54]) the eddies become fully formed. Here $\alpha = 0.43$ and $r = 0.4$.

which must be resolved in order to accurately find the flow. We take the same approach as we have done in previous chapters, namely that the Goursat functions take the form $f(z) \sim a_0(z - z_0)^{1/2}$ and $g'(z) \sim b_0(z - z_0)^{-1/2}$ in the vicinity of a 2π -corner at $z = z_0$ (where a_0 and b_0 are constants). Modelling the exact nature of this singularity is essential in guaranteeing convergence of solution at points near to the ends of the plate. Therefore the ansatz for the Goursat functions will be chosen in such a way that it exploits the above behaviour near these points.

7.3.1 Conformal mapping: finite plate above a wall

We shall consider the physical fluid region to be the image of the same annulus as used in the case of a cylinder above a plane. The appropriate map can be constructed in terms of special transcendental functions, $\omega(\zeta, \gamma)$, which consists of an infinite products depending only on the inner radius of the annulus, ρ . The required map is then represented as

$$z_0(\zeta) = R \frac{\omega(\zeta, \gamma_1)}{\omega(\zeta, \gamma_2)} \quad (7.24)$$

where R is a complex constant scaling parameter and γ_1 and γ_2 are taken to be two distinct points in the closure of the annulus [60]. While this map can be extended to any number of plates (constructing a map to a wall with n plates requires the same connectivity inside the unit disk and hence will be the image of a unit ζ -disk with n holes inside), the form of the map for the current study requires that

$$\omega(\zeta, \gamma) = -\gamma C^{-2} P(\zeta/\gamma, \rho) \quad (7.25)$$

where

$$P(\zeta, \rho) = (1 - \zeta) \prod_{k=1}^{\infty} (1 - \rho^{2k} \zeta)(1 - \rho^{2k} \zeta^{-1}) \quad (7.26)$$

and $C = \prod_{k=1}^{\infty} (1 - \rho^{2k})$. Full details of this map are discussed by Crowdy and Marshall in [58, 60]. There are a few notable properties of this function. Firstly, it is clear to see that $\omega(\zeta, \gamma)$ has a simple zero at $\zeta = \gamma$ and hence the map (7.24) admits a simple zero at $\zeta = \gamma_1$ and a simple pole at $\zeta = \gamma_2$. Therefore, if we choose $|\gamma_1| = |\gamma_2| = 1$, then since

the map has a zero and a simple pole on the unit disk, it follows that C_0 is mapped to a line that passes through the origin and infinity. Secondly, it will also map the inner circle, C_1 , to a finite length radial plate emanating from the origin in the z -plane. By choosing

$$\gamma_1 = 1, \quad \gamma_2 = -1, \quad R \in \mathbb{R}^- \quad (7.27)$$

we have that the point $\zeta = 1$ is mapped to the origin, while the point $\zeta = -1$ is mapped to infinity. Also, the image of the interior of the annulus is the right half plane, except for a finite plate which lies purely on the real axis. The length of this plate, L , and its minimum distance away from the wall will be determined by an appropriate choice of R and ρ . Indeed, these numbers are found numerically from the two equations

$$z(\rho) = a \quad \text{and} \quad z(-\rho) = b \quad (7.28)$$

using Newton's method, where the numbers $a < b$ define the start and end points of the plate. Lastly, note that this map does not satisfy the loxodromic condition (5.9) and so the analytic methods presented in chapters 5 and 6 are not applicable to this problem.

Once R and ρ have been found, we then rotate the above map by an angle of $\pi/2$ counter-clockwise in order to ensure that the unit disk is mapped to the real line. The required conformal map is then given by

$$z(\zeta) = iz_0(\zeta) = -iR \frac{P(\zeta, \rho)}{P(-\zeta, \rho)}. \quad (7.29)$$

Note that we may write this as

$$z(\zeta) = \frac{\hat{z}(\zeta)}{\zeta + 1} \quad (7.30)$$

where we have used the fact that $z(\zeta)$ admits a simple pole at $\zeta = -1$. Here $\hat{z}(\zeta)$ is given by

$$\hat{z}(\zeta) = -iR \frac{(1 - \zeta)T(\zeta, \rho)}{T(-\zeta, \rho)} \quad \text{with} \quad T(\zeta, \rho) = \prod_{k=1}^{\infty} (1 - \rho^{2k}\zeta)(1 - \rho^{2k}\zeta^{-1}). \quad (7.31)$$

It also follows from this that the derivative of the conformal map is given by

$$z'(\zeta) = \frac{\hat{z}'(\zeta)}{(\zeta + 1)} - \frac{\hat{z}(\zeta)}{(\zeta + 1)^2} \quad (7.32)$$

where, using some elementary manipulations, it is readily seen that

$$\hat{z}'(\zeta) = -iR \left[-\frac{T(\zeta, \rho)}{T(-\zeta, \rho)} + \frac{(1 - \zeta)T'(\zeta, \rho)}{T(-\zeta, \rho)} + \frac{(1 - \zeta)T(\zeta, \rho)T'(-\zeta, \rho)}{T(-\zeta, \rho)^2} \right],$$

$$T'(\zeta, \rho) = T(\zeta, \rho) \sum_{k=1}^{\infty} \rho^{2k} \left[\frac{1}{\zeta^2(1 - \rho^{2k}\zeta^{-1})} - \frac{1}{(1 - \rho^{2k}\zeta)} \right].$$

These are the expressions that will be useful when defining the equations that need to be solved in order to find the appropriate Goursat functions.

7.3.2 Constructing the Goursat functions

Using the map we may, again, define the Goursat functions in the ζ -plane by the relation

$$F(\zeta) \equiv f(z(\zeta)), \quad G(\zeta) \equiv g'(z(\zeta)). \quad (7.33)$$

We know that at a far distance from the plate and plane, the fluid motion tends to a uniform shear flow and hence the stream function for this problem must converge to y^2 . We have seen that this is equivalent to requiring that the Goursat functions have simple poles at infinity and, specifically, they must take the far field form of $f(z) \rightarrow iz/2$ and $g'(z) \rightarrow -iz$. As a simple pole in the z -plane corresponds to a simple pole in the ζ -plane, we allow $F(\zeta)$ and $G(\zeta)$ to both admit simple poles at $\zeta = -1$. Additionally, our choice of parameters ensured that the two points in the annulus at $\zeta = \pm\rho$ are mapped to the two ends of the plate. Recall that $F(\zeta)$ will be regular while $G(\zeta)$ will admit simple poles at these points.

Putting these properties together, we assume that

$$\begin{aligned} F(\zeta) &= F_l \log \zeta + \frac{\hat{F}(\zeta)}{(\zeta + 1)} \\ G(\zeta) &= -\bar{F}_l \log \zeta + \frac{\hat{G}(\zeta)}{(\zeta + 1)(\zeta^2 - \rho^2)} \end{aligned} \quad (7.34)$$

where we have ensured that the functions behave appropriately near the three singularity points corresponding to infinity and the two edges of the plate in the fluid domain. As $\hat{F}(\zeta)$ and $\hat{G}(\zeta)$ are analytic everywhere inside the annulus, they admit a Laurent series as in (7.9). Also, given the far field conditions on the Goursat functions, it follows that

$$F(\zeta) \rightarrow R \frac{T(-1, \rho)}{T(1, \rho)} \quad \text{and} \quad G(\zeta) \rightarrow -2R \frac{(1 - \rho^2)T(-1, \rho)}{T(1, \rho)} \quad (7.35)$$

as $\zeta \rightarrow -1$.

7.3.3 The no-slip boundary conditions

Next we refer to the no-slip condition on the plate as well as on the plane. Therefore, on the corresponding curves C_0 and C_1 in the ζ plane, we have the condition that

$$0 = -F(\zeta) + \frac{z(\zeta)}{\bar{z}'(\bar{\zeta})} \bar{F}'(\bar{\zeta}) + \bar{G}(\bar{\zeta}) \quad (7.36)$$

First consider the unit disk C_0 where the relation $\bar{\zeta} = 1/\zeta$ holds. Differentiating the first expression of (7.34) gives

$$\overline{f'(z)} = \frac{1}{\bar{z}'(1/\zeta)} \left[\bar{F}_l \zeta + \frac{i\zeta \bar{\hat{F}}'(1/\zeta)}{(\zeta + i)} + \frac{\zeta^2 \bar{\hat{F}}(1/\zeta)}{(\zeta + i)^2} \right] \quad (7.37)$$

and similarly

$$\bar{G}(1/\zeta) = F_l \log \zeta + \frac{\zeta^3 \bar{\hat{G}}(1/\zeta)}{(\zeta + 1)(1 - \rho^2 \zeta^2)}. \quad (7.38)$$

Putting this together, we see that after some arrangement the boundary condition on the unit disk in the annulus is

$$\begin{aligned} -\hat{G}(\zeta) = & -\zeta \overline{\hat{F}}(1/\zeta) + \left[\frac{(1+\zeta)\overline{z}(1/\zeta)}{\zeta z'(\zeta)} \right] F_l + \left[\frac{\overline{z}(1/\zeta)}{z'(\zeta)} \right] \hat{F}'(\zeta) \\ & + \left[-\frac{\overline{z}(1/\zeta)}{(1+\zeta)z'(\zeta)} \right] \hat{F}(\zeta) \end{aligned} \quad (7.39)$$

while on C_1 , where $\bar{\zeta} = \rho^2/\zeta$, the velocity condition becomes

$$\begin{aligned} 0 = & \left[-\frac{2\rho^2}{\eta^2} \log \rho(\eta + \rho)(1 - \eta^2) \right] F_l + \left[\frac{\rho z(\zeta)(\eta + \rho)(1 - \eta^2)}{\eta^2 \overline{z}'(\rho/\eta)} \right] \overline{F}_l \\ & + \left[-\frac{\rho^2(\eta + \rho)(1 - \eta^2)}{\eta^3(1 + \rho\eta)} \right] \hat{F}(\rho\eta) + \left[\frac{\rho^2(1 - \eta^2)z(\rho\eta)}{\eta^2 \overline{z}'(\rho/\eta)} \right] \overline{\hat{F}}'(\rho/\eta) \\ & + \left[-\frac{\rho^2(1 - \eta^2)z(\rho\eta)}{\eta(\rho + \eta)\overline{z}'(\rho/\eta)} \right] \overline{\hat{F}}(\rho/\eta) + \overline{\hat{G}}(\rho/\eta). \end{aligned} \quad (7.40)$$

Together with the far field conditions (7.35), the no-slip conditions (7.39) and (7.40) are used to find the coefficients of the Laurent expansions of $\hat{F}(\zeta)$ and $\hat{G}(\zeta)$. Using the same method that was demonstrated for the shear flow past a cylinder over a plane, we do this either by a spectral analysis or by a least squares method.

7.3.4 Results: shear flow past a finite plate above a wall.

We will now look at the solutions of the above equations with their generated streamlines. As the strength of the shear flow is constant, the only parameters we vary are a and b which determines the length and position of the plate. We begin by placing the plate far away from the wall, so that it has little effect. The streamlines pass by the wall in a similar fashion to if the plate was it a free space shear flow. The effect of the wall, while being weak, nevertheless provides a slight downwards attraction towards it, as it did in the case of a cylinder above a wall. This is shown below in Figure 7.6. As the plate is brought nearer to the wall, the effect of the wall becomes more apparent in its attraction of streamlines; see Figures 7.7 and 7.8.

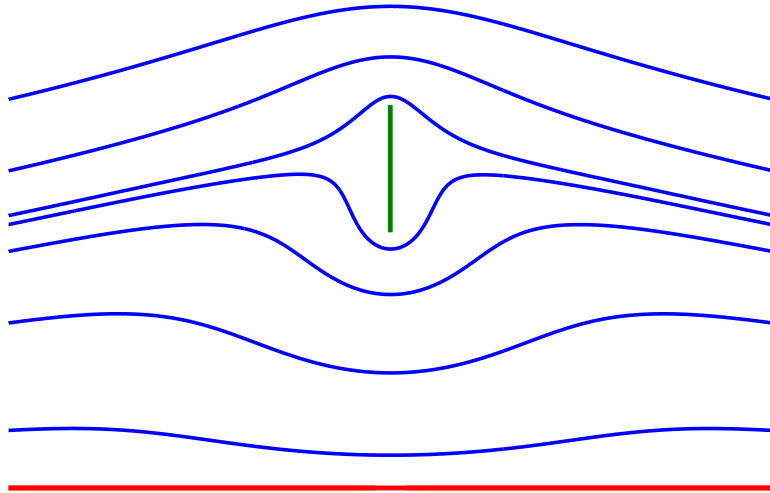


Figure 7.6: When the plate is far away from the wall, the streamlines behave similarly to when in a free space shear flow past a plate. Here $a = 2$ and $b = 3$.

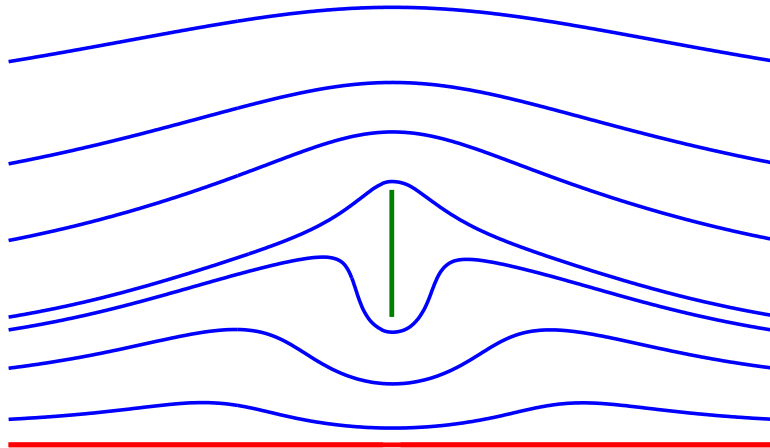


Figure 7.7: When the plate is brought further down, the effect of the wall becomes more evident and streamlines are pulled downwards towards it. Here $a = 1$ and $b = 2$, and so the plate is unit length.

Recall that in the case of a cylinder instead of a plate, single eddies are formed when the cylinder is brought close to the plane. We saw that the closer the cylinder was to the plane, the larger the eddies became. The same phenomenon occurs in the case of the plate above a wall. Notice that in the above two examples, while the wall had a slight effect on the streamlines, they did not separate and thus no eddies were created. However, as the plate is brought close to the wall, we see a single viscous eddy being formed on each side of the plate. The eddy increases in size as the gap between the plate and the wall is reduced to zero. This is illustrated in the Figures 7.9-7.11 below.

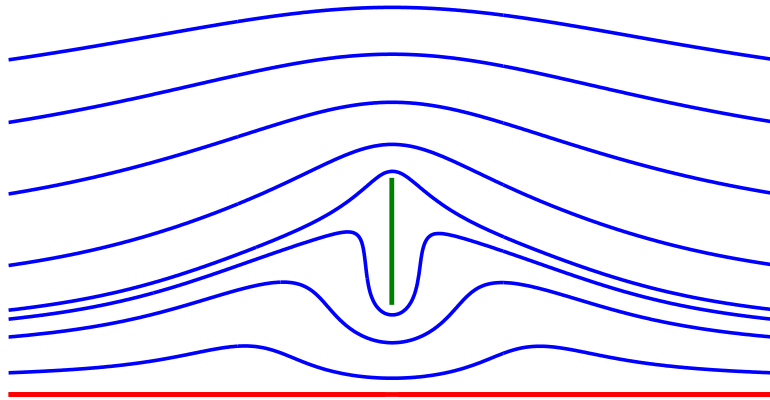


Figure 7.8: The plate is of unit length and the gap width is 0.7. The effect of wall becomes even more pronounced as the plate is brought down further. The plate has unit length.

7.3.5 Limiting case: diminishing gap width.

The method of least squares provides the coefficients of the Laurent series of the Goursat functions which satisfy conditions (7.35), (7.39) and (7.40). When the plate is brought down towards the wall, the gap width decreases and the fluid domain approaches one that has a perpendicular corner. The boundaries of such domains are associated with discontinuities and so it is necessary to increase the number of collocation points near the contact

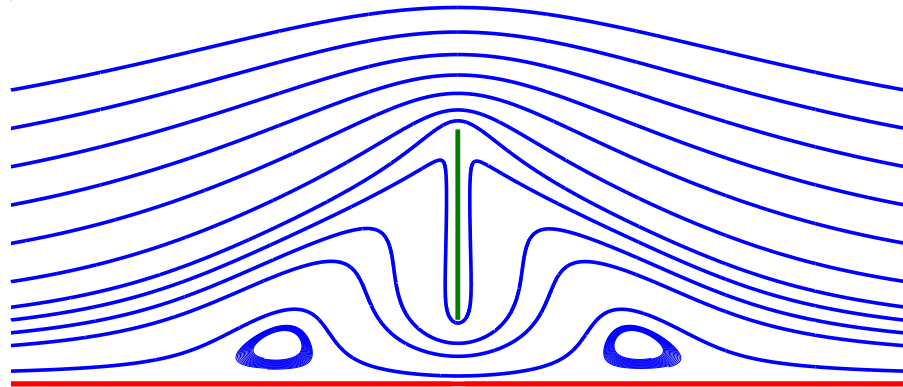


Figure 7.9: Eddies begin to form as the plate becomes close to the wall. Here, the gap width is 0.5 and the plate's length is 1.5.

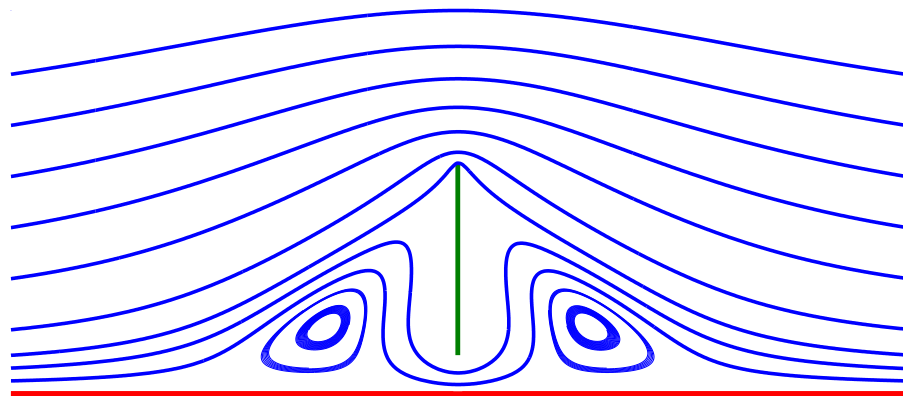


Figure 7.10: Here the gap between the plate and the plane is 0.3 and the plate's length is 1.8. The eddies become more pronounced as the plate is brought even further down towards the wall.

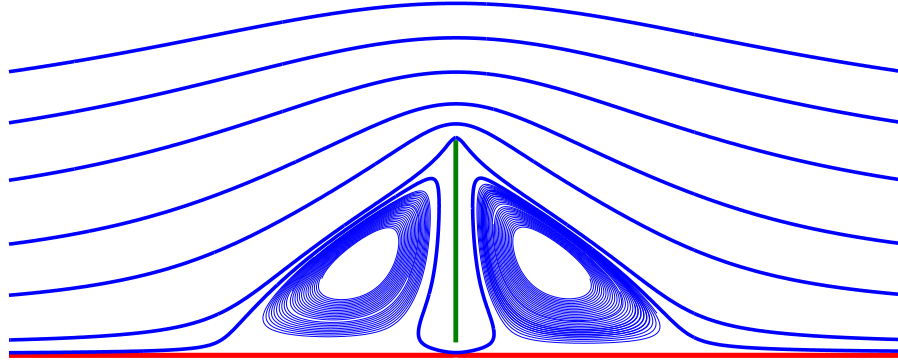


Figure 7.11: The plate length is 1.5 and the gap width is further reduced to 0.1. At this stage the separation of the streamlines create eddies which prevent the fluid from travelling through the small gap between the plate and the wall.

points in order to establish an accurate solution in this limit. The case when the plate is directly in contact with the plane, and so $a = 0$, has been solved by Kim [5] with use of Weiner-Hopf techniques. The author computes that the force on the wall by the oncoming shear flow is

$$F_k = 5.817\alpha\mu \quad (7.41)$$

where α is the strength of the oncoming flow (equal to -2 in our case: this is because he considers a flow of half the strength from the opposite direction) and μ is the coefficient of viscosity (equal to one here). In our study it was shown that we may compute the force on the plate by the quantity

$$F = -8\pi F_l. \quad (7.42)$$

As a useful check on our method, the force in the doubly connected regime (7.42) should approach the result of Kim [5] as the gap width is reduced to zero. Indeed, this is confirmed and a graph of the force on the plate as it is brought closer to the wall is shown in Figure

7.12.

It should be noted, however, that when the gap width is exactly zero we can not accurately solve the problem using the numerical method we have presented above. This is because when $a = 0$, the domain becomes simply connected and the vicinity of the contact points on both sides of the plate forms a perpendicular wedge shaped region. The locale of these points are precisely the flow regions studied by Moffatt when demonstrating the existence of eddies in wedge shaped domains [64]. Based on his results, it can be shown that whenever the wedge angle is less than roughly 146.6° , the Goursat functions necessarily take the form

$$f(z) = Az^\lambda + Bz^{\bar{\lambda}} \quad (7.43)$$

with $\lambda \in \mathbb{C}$ related to the wedge angle $\sin(\pi\lambda/2) = \pm\lambda$. The positive sign relates to flow that is symmetric about the line $\theta = \pi/4$ while the negative relates to the antisymmetric flow about the same line. When $a \rightarrow 0$ the angle between the wall and the plate is $\pi/2$ and hence, in order to correctly solve this problem using the above conformal mapping method, we would be required to include such singularities into our ansatz for $f(z)$ as well as for $g'(z)$. However, any term of the form

$$z^\lambda \quad (7.44)$$

introduces a branch cut, as well as being divergent as $|z| \rightarrow \infty$. This presents significant difficulties to the method presented here and, as yet, it is not known how to accurately include these singularities in our model. However, we have shown that we can retrieve accurate solutions in the *limit* of diminishing gap width, while still in the doubly connected regime. This supports the idea that, by using the numerical method presented here, determining the flow near two (slightly) disconnected sections of wall may be used to provide a good approximation to the flow in the wedge-shaped region when the walls touch.

Indeed, this idea is not specific to the perpendicular wedge and hence considering the flow past an inclined plate provides the equivalent doubly connected approximation to a non-perpendicular wedge shaped region. This will be the focus of the next section and, later in the chapter, we will use the same proposition when studying the Weis-Fogh mechanism in

low Reynolds numbers.

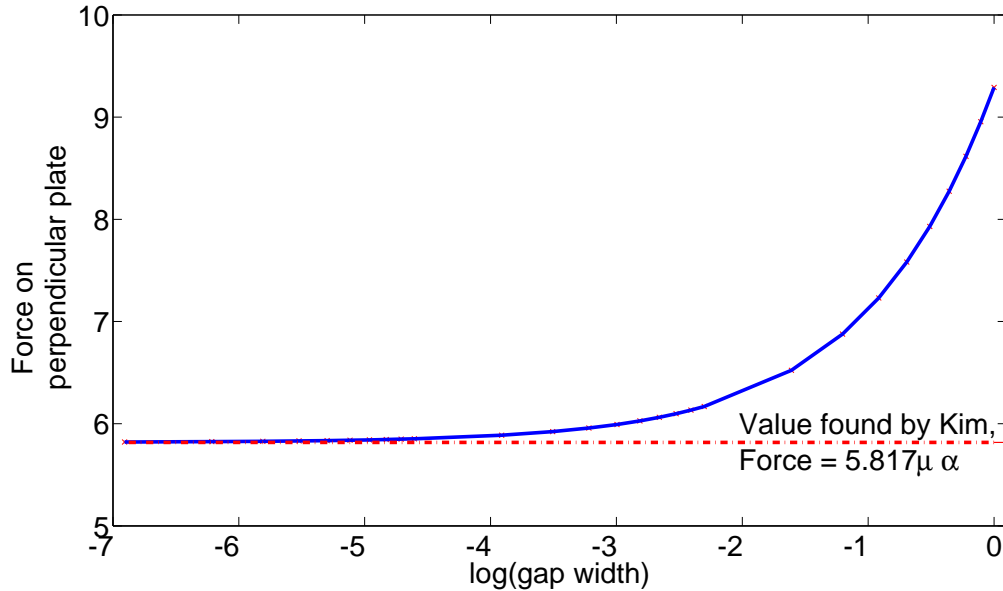


Figure 7.12: Force on the plate as a function of gap width (solid, blue). We see that as the width is reduced to zero, the force tends to the value of 5.817 (dashed, red) as predicted by Kim [5].

7.4 Shear flow past a finite inclined plate above a wall.

We now consider the case where the finite plate is not perpendicular to the no-slip wall but is radially inclined, while still above it. Let ϕ be the inclination angle of the plate relative to the horizontal and let r_0 be the distance of the near edge to the origin, as depicted in schematic Figure 7.13. In this case, a gap of size $r_0 \sin \phi$ will be present between the wall and the plate, allowing a net fluid flux through it. We will again study the formation of viscous eddies as the plate is brought downwards towards the wall and hence the gap becomes smaller.

Many of the details of the perpendicular plate carry over to this case, except that the conformal map is changed and, therefore, the preimage points of the plate's sharp ends may not

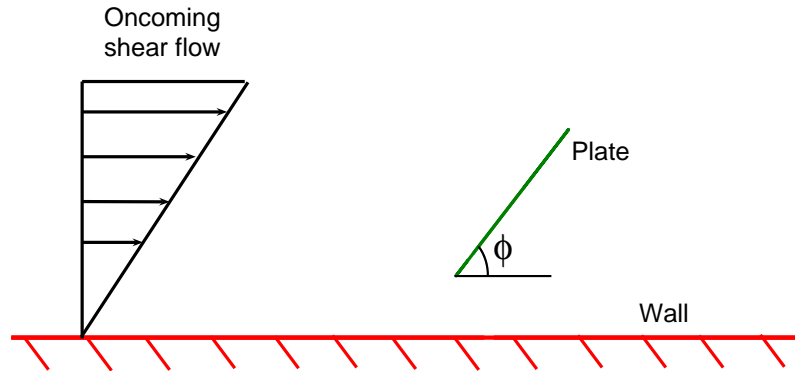


Figure 7.13: Schematic diagram of the shear flow past an inclined plate above a wall. The on-coming shear flow has strength $U = 1$.

necessarily be at $\zeta = \pm\rho$. Recall that when $\gamma_1 = 1$ and $\gamma_2 = -1$, expression (7.24) mapped the ρ -circle of the annulus to a radial plate emanating from the origin along the real axis, while mapping the unit circle to an infinite vertical line passing through the origin. Now, we take

$$z_0(\zeta) = -R \frac{P(\zeta, \rho)}{P(\zeta/\gamma_2, \rho)} \quad (7.45)$$

where it then remains to find the values of R , ρ and $\gamma_2 \in \mathbb{C}$. This will map the inner circle of the annulus to a finite line along the real axis, starting at r_0 and ending at $r_0 + L$, (where L is the chosen length of plate).

Choosing $\gamma_1 = 1$ also means that the point $\zeta = 1$ will be mapped to the origin and hence the image of the unit circle will pass through the origin. Additionally, selecting $|\gamma_2| = 1$ will ensure that $z_0(\zeta)$ admits a simple pole at $\zeta = \gamma_2$ and so will be mapped to infinity. Therefore, the unit circle will be mapped to an infinite straight line which passes through the origin. Crowdy and Marshall [60] have shown that the explicit angle made by the

straight line image of the unit circle to the positive real axis is given by

$$\arg[R] - \frac{1}{2} \arg[\gamma_2]. \quad (7.46)$$

Therefore, the condition

$$\arg[R] - \frac{1}{2} \arg[\gamma_2] = \pi - \phi \quad (7.47)$$

together with the requirements that the minimum and maximum real values of the radial plate are at $x = r_0, r_0 + L$ respectively gives a system of three nonlinear equations for $\rho, R, \arg \gamma_2$, which may be solved numerically using a Newton method. Once these are found, we rotate the domain by an angle ϕ so that the infinite line lies along the real axis. The required conformal map is therefore given by

$$z(\zeta) = e^{i\phi} z_0(\zeta). \quad (7.48)$$

Next, in order to account for the singularities at the end of the plate in the “physical” fluid domain, we must find their preimage points on the ρ -circle in the annulus. We again find these two points ζ_1 and ζ_2 numerically from the condition that the derivative of the conformal map, $z'(\zeta)$, vanishes there.

With these parameters found, the Goursat functions take the modified form

$$F(\zeta) = F_l \log \zeta + \frac{\hat{F}(\zeta)}{(\zeta - \gamma_2)} \quad (7.49)$$

and

$$G(\zeta) = -\bar{F}_l \log \zeta + \frac{\hat{G}(\zeta)}{(\zeta - \gamma_2)(\zeta - \zeta_1)(\zeta - \zeta_2)} \quad (7.50)$$

with $\hat{F}(\zeta)$ and $\hat{G}(\zeta)$ again admitting Laurent series in the annulus. In this case, the far field conditions on $f(z)$ are applied as $\zeta \rightarrow \gamma_2$. To simplify this, notice that the conformal map (7.45) takes the form

$$z_0(\zeta) = \left\{ \frac{R\gamma_2 e^{i\phi} P(\zeta, \rho)}{T(\zeta/\gamma_2, \rho)} \right\} \frac{1}{(\zeta - \gamma_2)} \quad (7.51)$$

and so we see that $\hat{F}(\zeta)$ tends to

$$\hat{F}(\zeta) = \frac{i}{2} R \gamma_2 e^{i\phi} \frac{P(\gamma_2, \rho)}{T(1, \rho)} \quad (7.52)$$

as $\zeta \rightarrow \gamma_2$ while $\hat{G}(\zeta)$ tends to

$$\hat{G}(\zeta) = -i R \gamma_2 e^{i\phi} \frac{P(\gamma_2, \rho)(\gamma_2 - \zeta_1)(\gamma_2 - \zeta_2)}{T(1, \rho)} \quad (7.53)$$

in the same limit. The coefficients of the Laurent series are again found either by a spectral method or by a least squares algorithm.

Below are some typical streamlines around a plate with varying inclination angle, ϕ , and gap width. Kim and Jeong [66] studied the problem of an oncoming shear flow past an infinite no-slip wall with a protruding fence (attached to the wall) at different angles, using Wiener-Hopf techniques. This is a limiting case of the present study as the gap width is reduced to zero, and so the below figures should be compared to Figure 2 of [66].

In the plots of Figure 7.14, the inclination angle is kept constant at $\phi = \pi/3$ while the distance of the nearest edge to the origin, r_0 , is reduced. Similarly to the case of the perpendicular plate, we see that viscous eddies are formed as the gap width, given by

$$\frac{\sqrt{3}}{2} r_0 \quad (7.54)$$

is reduced. The size of these eddies grow as the gap width is reduced and, when the gap width is very small, eddies also form on the left (or upstream) of the plate. When the plate is made longer and again brought very close to the no-slip wall, but kept at the same inclination angle $\phi = \pi/3$, a secondary set of eddies appears in the vicinity of the resultant wedge, see Figure 7.15. This is consistent with the theory by Moffatt [64] that when the fluid is driven by some far field flow, viscous eddies appear sequentially in a wedge. The eddies on the left (upstream) of the plate grow also as the length of the plate is increased. Note that even a very small gap allows for a small volume of fluid to pass through it and

distorts the eddies that would be formed if the fluid domain was an exact wedge.

In Figure 7.16, we demonstrate the effect of varying inclination angle while keeping the length of the plate at a constant length. We see that eddies may form on both sides of the plate, but that upstream eddies will not form when $\phi < 33^\circ$, as then the upstream angle will be greater than 147° , in agreement with Moffatt [64].

7.5 The Weis-Fogh mechanism: the low Reynolds number limit

In the observation and study of the hovering motion of insects, Weis-Fogh proposed a mechanism [65] by which many of these insects, such as the *Encarsia formosa* (wing chord $\sim 0.2\text{mm}$) [67] generate their required lift. This is often referred to as the *clap and fling* mechanism: an insect “claps” both its wings together so that they meet along the (say) vertical line of contact. It then rotates both wings around the common point of contact at the bottom of both wings (the “opening phase”) and in doing so, air quickly fills the gap generated. It then moves its wings apart horizontally, (the “spreading phase”) by which time the circulation around each wing is of the correct sign to provide upward lift. The remarkable feature of this mechanism is that it does not depend on the usual vortex shedding method of generating lift and hence it is applicable to a hovering insect in a purely inviscid fluid. Instead, its success relies on the instantaneous circulation that is generated around each wing as the two wings separate from each other and thus change the flow domain topology.

In the same year, Lighthill [68] provided a mathematical rationalisation of this process by considering an irrotational, inviscid, two-dimensional model. With the use of a Schwarz-Christoffel mapping, he produced an explicit mathematical representation for the “opening out” phase of the motion. However, as the connectivity of the flow domain is changed (from simply to doubly connected) when the wings begin to separate, the expression for the lift which Lighthill computed was not extensible to the spreading phase of the mechanism. Using conformal mapping techniques in the doubly connected regime, Crowdy [69]

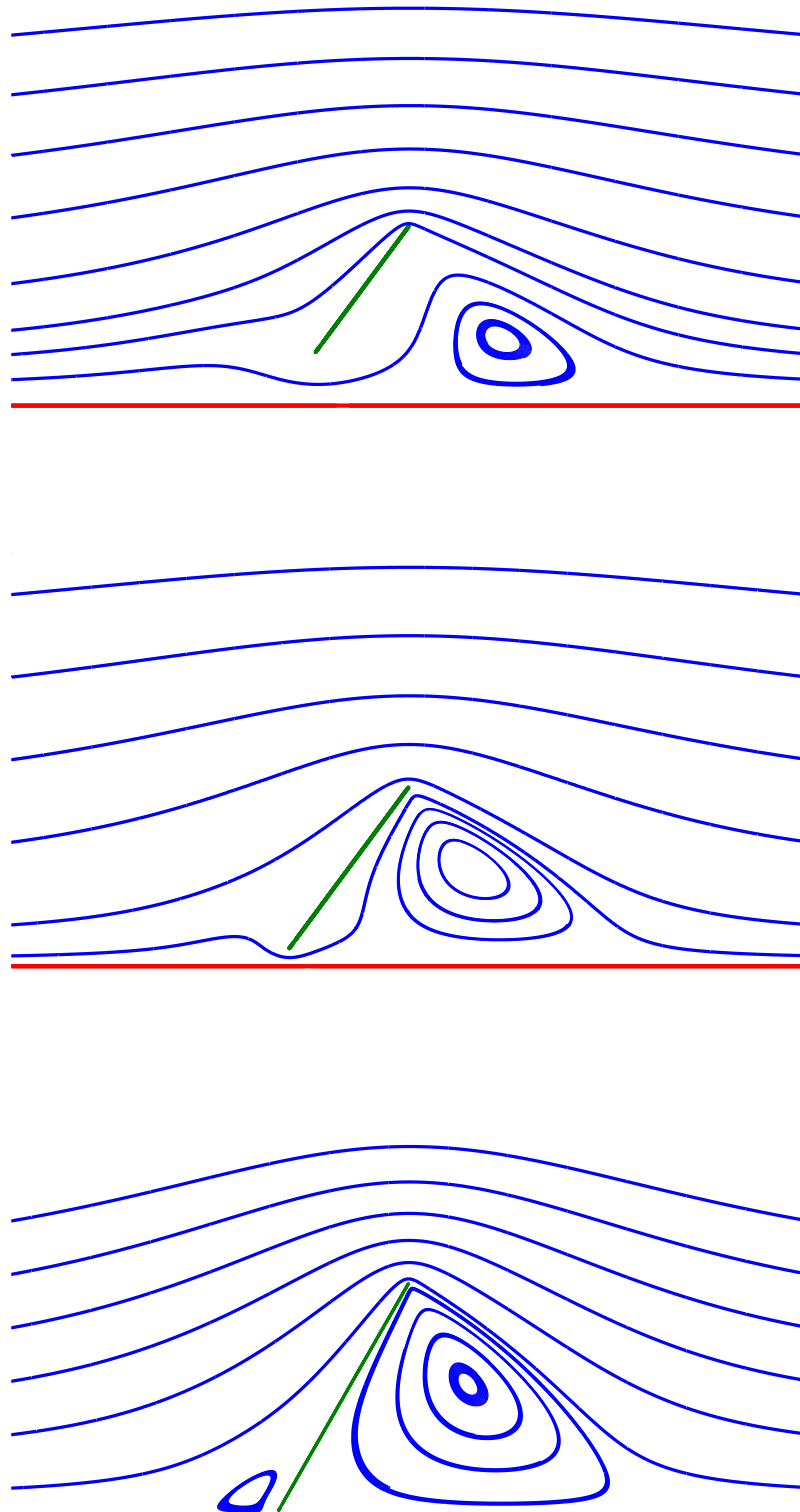


Figure 7.14: A plate, inclined at angle of $\pi/3$ from the horizontal is gradually brought downwards towards the no-slip wall. Here the gap has widths 0.26, 0.08 and 0.02 (top to bottom). As the gap becomes narrower, less fluid may pass through it and the resulting viscous eddies increase in size.

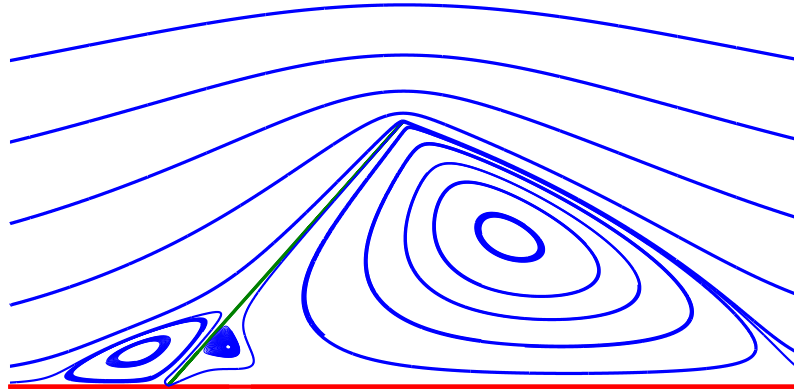


Figure 7.15: As the plate is made longer $L = 3$ and kept very close to the wall, with gap width 0.02 (and inclined with $\phi = \pi/3$), a secondary set of eddies appear in the immediate vicinity of the wedge, to the right of the plate.

presented analytical expressions for the lift generated during the spreading phase in the infinite Reynolds number regime.

The focus of the section is to study the spread out phase of the Weis-Fogh mechanism in the *low* Reynolds number regime. The two plates are separated by an angle $\phi(t)$ at their lowest point and move away from each other with speed U (so that their total speed of separation is $2U$), as shown in Figure 7.17.

We again aim to find the Goursat functions that satisfy the appropriate boundary conditions for this problem, i.e that

$$-f(z, t) + z\bar{f}'(\bar{z}, t) + \bar{g}'(\bar{z}, t) = \pm U \quad \text{for } z \in \Gamma_{1,2} \quad (7.55)$$

where $\Gamma_{1,2}$ corresponds to the right and left wings respectively. To do this, we introduce a (time dependent) conformal map from the annulus $\rho(t) < |\zeta| < 1$ to the fluid domain

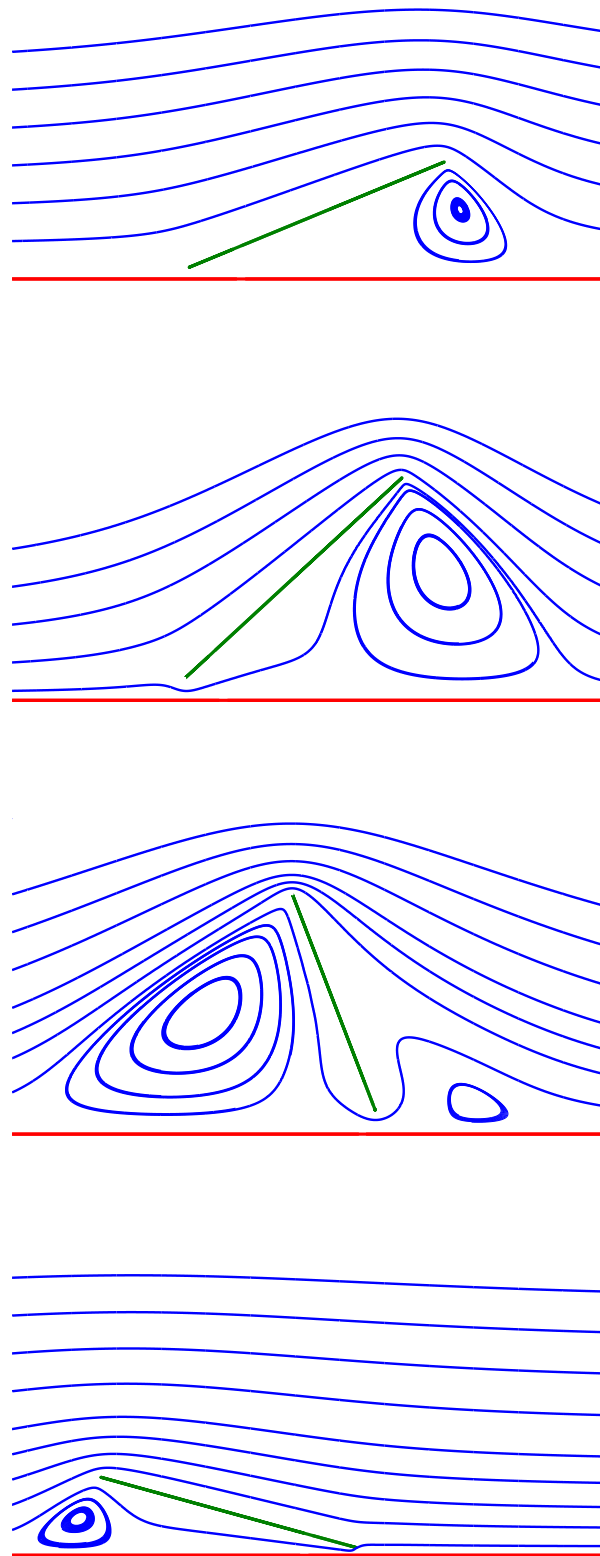


Figure 7.16: Typical streamlines around a plate with varying inclination angle. In all cases, $r_0 = 0.2$ and $r_0 + L = 2$, and $\phi = \pi/10, \pi/5, 3\pi/5, 9\pi/10$ (top to bottom, respectively).



Figure 7.17: Schematic diagram for the spreading out phase of the Weis-Fogh mechanism. Both wings are separated by an angle $\phi(t)$ at their lowest point and move away from each other with relative speed $2U$.

exterior to the two wings. This map is given by

$$z(\zeta) = iA(t)e^{-i\phi(t)/2}R(\zeta, \rho(t)) - id(t) \quad (7.56)$$

where $A(t)$ and $\rho(t)$ are real functions of time. Here, $R(\zeta, \rho(t))$ is given by

$$R(\zeta, \rho(t)) = A(t) \frac{P(\zeta \sqrt{\rho(t)}^{-1} e^{i\phi(t)}, \rho(t)) P(\zeta \sqrt{\rho(t)} e^{i\phi(t)}, \rho(t))}{P(\zeta \sqrt{\rho(t)}^{-1}, \rho(t)) P(\zeta \sqrt{\rho(t)}, \rho(t))} \quad (7.57)$$

with the usual $P(\zeta, \rho)$ given by (7.26). This is a doubly connected case of the so called *radial slit map* as discussed in [70]: the unit circle, C_0 where $|\zeta| = 1$ is mapped onto the a finite straight line along the ray $\arg R = \phi(t)$; the inner circle of the annulus, C_1 where $|\zeta| = \rho(t)$, is mapped to another ray of the same length lying along the real axis. The parameters $\rho(t), A(t) \in \mathbb{R}$ are found numerically from the condition

$$\text{Max} [R(\rho(t)\eta, \rho(t))] = r_0 + L, \quad \text{Min} [R(\rho(t)\eta, \rho(t))] = r_0, \quad |\eta| = 1 \quad (7.58)$$

using a Newton solver where r_0 is the minimum distance from the origin and L is the length of the wings. This function $R(\zeta, \rho(t))$ is then multiplied by

$$ie^{-i\phi(t)/2} \quad (7.59)$$

to ensure that the wings lie symmetrically about the vertical axis, and then translated by a distance

$$d(t) = (r_0 + L/2) \sin [(\pi - \phi(t))/2] \quad (7.60)$$

downwards so that their centers lie along the real axis. From here on, we suppress the time dependence in the notation for convenience. Once again the preimages of the sharp ends of the plates are at $\zeta = \zeta_j$, with $j = 1, \dots, 4$, and are found numerically from the condition that the derivative of the conformal map vanishes at these points of non-conformality.

With the conformal map known, we propose that the Goursat functions $F(\zeta) \equiv f(z(\zeta))$ and $G(\zeta) \equiv g'(z(\zeta))$ are given by

$$F(\zeta) = F_l \log \zeta + \hat{F}(\zeta), \quad G(\zeta) = -\bar{F}_l \log \zeta + \frac{\hat{G}(\zeta)}{\prod_{j=1}^4 (\zeta - \zeta_j)} \quad (7.61)$$

with the logarithmic singularities included to account for the force required to move each wing, and their coefficients chosen so that the velocity remains single valued along on each wing. Once again, the functions $\hat{F}(\zeta)$ and $\hat{G}(\zeta)$ are both analytic and single valued in the closure of the annulus. It should be noted that this condition circumvents the Stokes paradox and the force on one wing is both equal and opposite to the force on the other.

Using this ansatz in the two no-slip conditions (7.55) gives, on $|\zeta| = 1$,

$$U = -\hat{F}(\zeta) + \frac{z(\zeta)}{\bar{z}'(\zeta^{-1})} \left[\bar{F}_l \zeta + \bar{F}'(\zeta^{-1}) \right] + \frac{\zeta^4 \bar{\hat{G}}(\zeta^{-1})}{\prod_{j=1}^4 (1 - \bar{\zeta}_j \zeta)} \quad (7.62)$$

while on the inner circle of the annulus, $|\zeta| = \rho$, we have

$$-U = -2F_l \log \rho - \hat{F}(\rho\zeta) + \frac{z(\rho\zeta)}{\bar{z}'(\rho/\zeta)} \left[\frac{\bar{F}_l \zeta}{\rho} + \bar{F}'(\rho/\zeta) \right] + \frac{\zeta^4 \bar{G}(\rho/\zeta)}{\prod_{j=1}^4 (\rho - \bar{\zeta}_j \zeta)} \quad (7.63)$$

The conformal map for this fluid domain does not satisfy the loxodromic condition and hence $z(\rho^2\zeta) \neq z(\zeta)$ for all ζ in the annulus. The two equations (7.62) and (7.63) are linear in the coefficients of the Laurent series of the Goursat functions and hence this system can once again be solved by either a spectral analysis or by a least squares method.

Snapshots of typical streamlines associated with the flow around the two wings are shown in Figure 7.18 for the “opening” phase and in Figure 7.19 for the “spreading” phase. As they open, the lower ends of the wings are kept close together (but not in contact) during which time their angle of separation increases. When the wings reach an inclination angle of $\pi/6$ (and hence have a separation of $\phi = \pi/3$) they complete the first part of their motion and commence the spreading phase. At this point, they maintain this inclination and move apart at constant speed at which point a pair of viscous eddies are formed in the vicinity of the lower ends of the two wings only and, as the wings move further apart, these eddies increase in size.

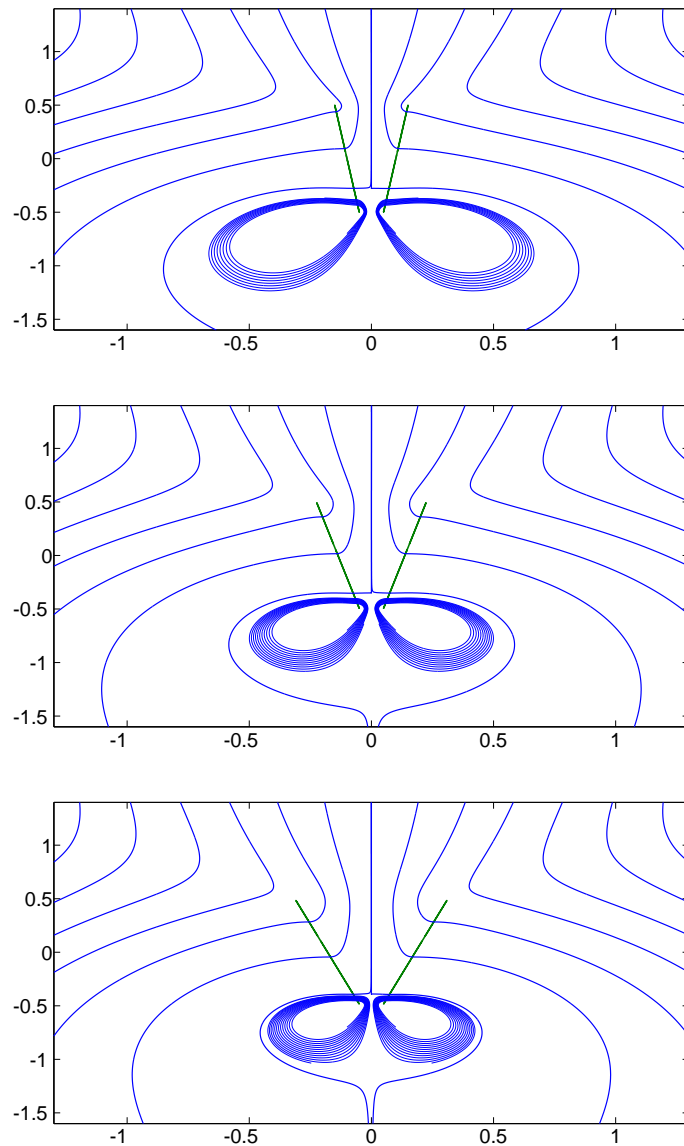


Figure 7.18: Typical streamlines around two wings during the “opening” phase of the Weis-Fogh mechanism. They rotate with angular velocity U until reaching a separation angle of $\phi = \pi/3$. Here they are pictured at separation angles $\phi = 0.2, \pi/9, \pi/6$ (top to bottom). The wings have unit length and their lower corners are at a distance of 0.1 away from each other (or 10% of the wing’s length).

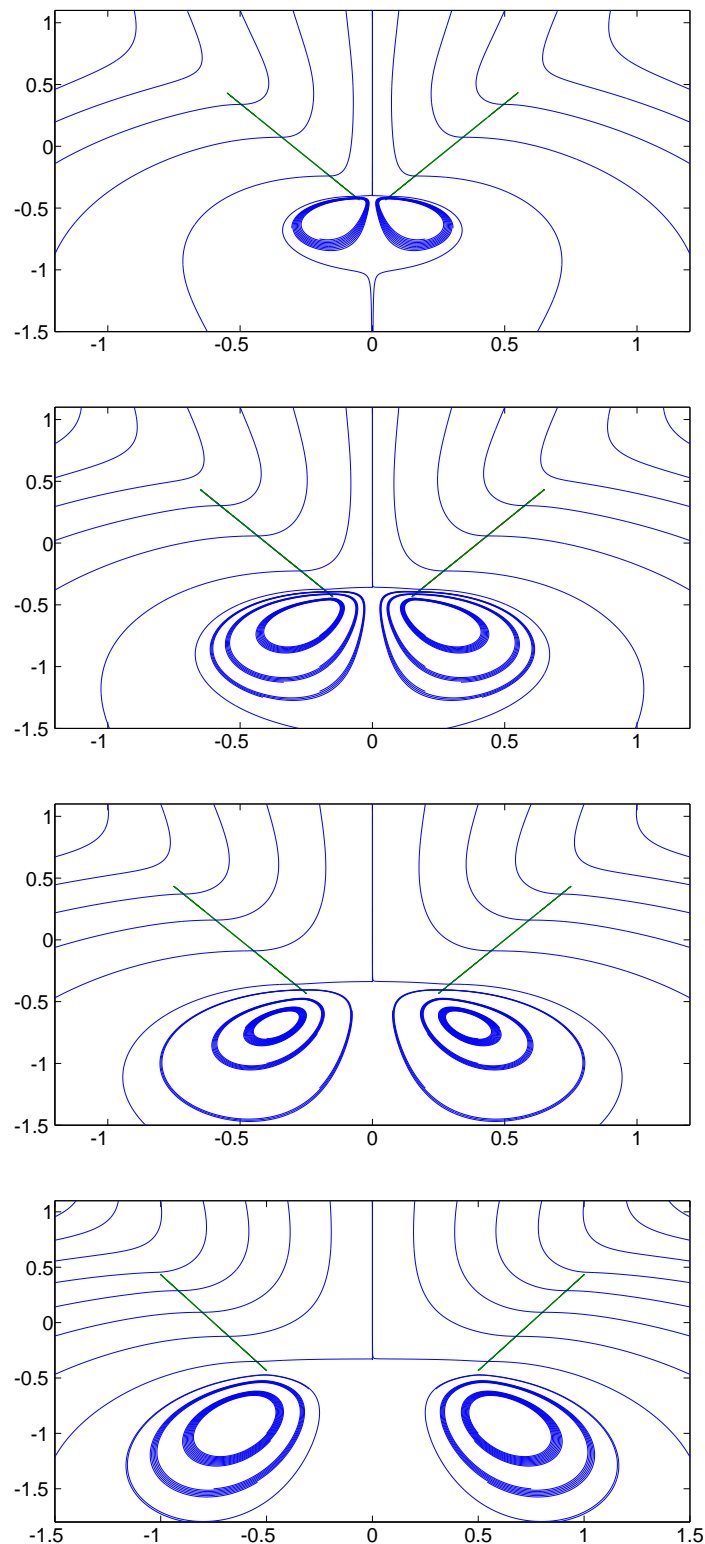


Figure 7.19: Typical streamlines around two wings during the “spreading” phase. They are inclined with separation angle $\phi = \pi/3$ and move with speed $U = 1$ away from each other.

7.6 Summary

We have presented a numerical procedure which is useful for determining solutions for Stokes flows past domains of complicated geometry. By retrieving a previous result by Davis and O'Neill [54] for the uniform shear flow past a cylinder above a wall, we have demonstrated the accuracy of this method which motivates its use in problems which have not been previously considered. In particular, we turned our attention to fluid domains whose boundaries included sharp corners. These problems could, in theory, be solved using standard boundary integral methods [34], however the discontinuities at these corners would present severe complications to this. By calling on the results from previous chapters, we have been able to characterise the singularity structure of the Goursat functions at these sharp corners and, by introducing a conformal map, we have reformulated the problem in terms of analytic functions that have (well-behaved) Laurent expansions.

Following this procedure has allowed us to find the uniform shear flow past a finite length plate above a wall, at any angle of inclination, and study the formation of eddies as the plate is brought down towards the wall. These results are of interest as in the limit of diminishing gap width (between the wall and the plate's lowest corner), we retrieve a wedge shaped fluid domain, similar to those considered by Moffatt [64]. Moffatt's analysis was a local one from which we may infer the local singularity structure of the Goursat functions at the wedge corner, however these singularities are divergent and a method for including them in a global expression for the stream function is currently unknown. However, an inclined plate above a wall provides a good approximation to this and hence the numerical method presented here could be used as a first approximation for the global solution of fluid flows near wedge shaped regions.

We have also used this method to find the Stokes flow around two wings during the opening out and spreading phase of the Weis-Fogh mechanism [65]. While we are unable to determine the flow while the lower ends of the wings are in contact, separating them by a small length provides a good approximation to this stage of the mechanism.

Special care must be taken when considering two-dimensional Stokes flows past solid surfaces due to the Stokes paradox. The presence of the fluid's force on the object necessitates a logarithmically divergent velocity field. However, the scenarios we have considered here has been concerned with doubly connected fluid regions and we have shown that the force exerted on one object is equal and opposite to the force exerted on the other. Because of this, the forces cancel each other out and therefore these problems are not susceptible to this paradox.

Chapter 8

Conclusions and future work.

Problems of low Reynolds number swimming have received a great deal of attention recently. Most of the interest has been devoted to swimmers in an unbounded fluid, while the studies of swimming in bounded domains has been limited to cases where the fluid is confined by a simple boundary, such as an infinite flat wall. This thesis has extended the study to cases where the confining geometries of the swimmer are more complicated.

In order to do so, we have first studied general Stokes flows near complicated boundaries. By presenting a new approach using conformal mapping theory, we have been able to find exact solutions for the uniform shear flow and stagnation point flow past a wall with one or two gaps in such a way that retrieves, in a unified manner, the results previously found by Smith [2] and Ko and Jeong [3].

Then, by incorporating the singularity model proposed by Crowdy and Or [1], we have been able to explicitly determine the dynamical system which governs low Reynolds number swimming in these complicated geometries. Their model, which was based on a non self-propelling treadmilling swimmer of radius ϵ in free space, is a two-dimensional one and provides excellent qualitative agreement with numerical and laboratory experiments for the case of a fully three-dimensional motion of a swimmer near a flat wall. Therefore, we have confidence that the results presented in this thesis establish a predictive theory for how similar swimmers will behave around walls with one or two gaps.

A characteristic feature of the boundaries of the domains we have studied is that they admit sharp corners at the ends of their boundaries. One can construct many other fluid domains that have similar corners, however it may not always be possible to find analytical solutions to Stokes flows in these domains. Nevertheless, the numerical procedures used to solve these problems are greatly ameliorated by incorporating the ideas introduced within this thesis and we have presented a number of Stokes flows in doubly connected domains with sharp corners in order to demonstrate this.

The idea of modelling a swimmer as a two-dimensional point singularity is also currently being employed within other contexts. For example, a similar model is being used to provide insights into low Reynolds number swimming beneath a deformable free surface [9].

The singularity model that was proposed by Crowdy and Or [1] was chosen in a passive way, such that the swimmer is always described by a stresslet together with a superposed irrotational quadrupole. This model could be extended to a non-passive one where the swimmer reacts to its surroundings by changing its singularity structure appropriately. One could, in principle, perform a full matched asymptotic expansion to deduce the dynamics of the swimmer. In doing so, one would match the “inner” flow generated by a small, finite-area swimmer of radius ϵ with the “outer” solution in which the flow generated by that swimmer interacts with the solid boundary. The implicit assumptions in this method would be that ϵ is small relative to its distance from the boundary. This would result in corrections to the singularity strengths in powers of ϵ while the leading order term of this would be the Crowdy and Or [1] singularity model. The solutions found in this thesis would then serve as the “outer” solution in such a scheme. Antanovskii [44] used precisely the same strategy of matched asymptotic expansions to present a complex variable formulation of a deformable bubble in Taylor’s four-roller mill. We have not pursued this asymptotic approach for two reasons: firstly, such a strategy would be necessarily more complicated than the simpler point model which, as we have shown, already captures key features of low Reynolds number swimming dynamics near walls. Secondly, in order to do this matching

accurately, one would need to make assumptions as to *how* the treadmiller responds to its surrounds. As this is dependent on the precise details of the fluid domain the swimmer is in, these are challenges left for the future.

The results presented here are interesting from the viewpoint of dynamical systems. Gluing bifurcations have been observed in only a few other fluid dynamical systems [71, 72, 73] and this study adds to the short list. An intriguing possibility is that the presence of the gaps provide a route to chaos for the swimmer's dynamics. The single and symmetric double gap cases we have considered in this thesis provide one and two parameters for the dynamical system respectively, and we have not witnessed any chaotic behaviour. However, the two-gap study may be extended to the case where the gaps are asymmetrically placed about the origin. In this case, the required conformal map is

$$z(\zeta) = R \left(\frac{P(-\zeta, \rho)^2 - \lambda P(\zeta, \rho)^2}{P(-\zeta, \rho)^2 + \lambda P(\zeta, \rho)^2} \right) \quad (8.1)$$

where λ is real. The positions of a non-symmetric central plate would add a third parameter into the dynamics and it would be interesting to determine whether doing so would result in a chaotic system.

In presenting the numerical procedure for determining the Stokes flow past stationary surfaces, such as cylinders or inclined plates, the flows were driven by a far field uniform shear flow. Another advantage of the method we have presented here is that it may readily adopt other forms of far field flow. For example, the stagnation point flow considered in chapters 3 and 5 could equally drive the fluid in these problems. The formulation we have presented would remain largely unchanged, except for a slight modification of value of the Goursat functions at one point in the preimage domain; that which corresponds to infinity (in the fluid domain). Moreover, by incorporating the Crowdy and Or [1] singularity structure, it would be interesting to use this numerical approach in order to study the dynamics of a low Reynolds number swimmer in these complicated geometries.

Finally, there are other physical scenarios where the ideas of this thesis may be useful. Zhao

and Bau [56] have studied the two-dimensional problem of the induced electro-osmosis on a cylindrical particle placed near to an infinite no-slip flat wall. The governing equations are very similar to those of a swimmer confined within the same geometry, except that the motion of the charged, or dielectric, object is induced by its interaction with an ambient electric field. In a similar approach that we have taken to low Reynolds number swimming, it would be interesting to extend Zhao and Bau's work [56] to study the dynamics of this cylinder near to a wall with a gap, using the techniques presented in this thesis.

Appendix A

Analysis of single gap conformal map.

The conformal map for the single gap studies of chapters 3 and 4 is given by

$$z(\zeta) = \frac{2\zeta}{(\zeta^2 + 1)} \quad (\text{A.1})$$

This is analytic inside the unit disk in the ζ -plane and has the Taylor expansion

$$\begin{aligned} z(\zeta) = z_d + z'(\zeta)(\zeta - \zeta_d) + \frac{1}{2}z''(\zeta)(\zeta - \zeta_d)^2 \\ + \frac{1}{6}z'''(\zeta_d)(\zeta - \zeta_d)^3 + \frac{1}{24}z''''(\zeta_d)(\zeta - \zeta_d)^4 \dots \end{aligned} \quad (\text{A.2})$$

Rearranging this, we can write (A.2) as

$$(z - z_d) = (\zeta - \zeta_d) \left[z'(\zeta) + \frac{1}{2}z''(\zeta)(\zeta - \zeta_d) + \frac{1}{6}z'''(\zeta_d)(\zeta - \zeta_d)^2 + \dots \right]. \quad (\text{A.3})$$

Dividing by the square bracket and expanding, we have

$$\begin{aligned} \zeta - \zeta_d = \frac{z - z_d}{z'(\zeta)} \left[1 - \frac{z''(\zeta_d)}{2z'(\zeta_d)}(\zeta - \zeta_d) \right. \\ \left. + \left\{ \frac{z''(\zeta_d)^2}{4z'(\zeta_d)^2} - \frac{z'''(\zeta_d)}{6z'(\zeta_d)} \right\} (\zeta - \zeta_d)^2 + \mathcal{O}((z - z_d)^3) \dots \right] \end{aligned} \quad (\text{A.4})$$

which can be written as

$$\begin{aligned}
 (\zeta - \zeta_d) &= \frac{1}{z'(\zeta_d)}(z - z_d) - \frac{z''(\zeta_d)}{2z'(\zeta_d)^2}(z - z_d)(\zeta - \zeta_d) + \\
 &+ \frac{1}{z'(\zeta_d)} \left\{ \frac{z''(\zeta_d)^2}{4z'(\zeta_d)^2} - \frac{z'''(\zeta_d)}{6z'(\zeta_d)} \right\} (z - z_d)(\zeta - \zeta_d)^2 + \dots
 \end{aligned} \tag{A.5}$$

Using this expression in itself again, we get

$$(\zeta - \zeta_d) = a_1(z - z_d) + a_2(z - z_d)^2 + a_3(z - z_d)^3 + \dots \tag{A.6}$$

where

$$a_1 = \frac{1}{z'(\zeta_d)}, \quad a_2 = -\frac{z''(\zeta_d)}{2z'(\zeta_d)^3}, \quad a_3 = \frac{z''(\zeta_d)^2}{2z'(\zeta_d)^5} - \frac{z'''(\zeta_d)}{6z'(\zeta_d)^4} \tag{A.7}$$

Furthermore, from expansion (A.3), we have

$$\begin{aligned}
 \frac{1}{(\zeta - \zeta_d)} &= \frac{1}{(z - z_d)} \left[z'(\zeta_d) + \frac{1}{2}z''(\zeta_d)(\zeta - \zeta_d) + \frac{1}{6}z'''(\zeta_d)(\zeta - \zeta_d)^2 \right. \\
 &\quad \left. + \frac{1}{24}z''''(\zeta_d)(\zeta - \zeta_d)^3 + \dots \right].
 \end{aligned} \tag{A.8}$$

Upon using (A.6) in this, we have

$$\frac{1}{(\zeta - \zeta_d)} = \frac{\tilde{\alpha}}{(z - z_d)} + \tilde{\beta} + \tilde{\gamma}(z - z_d) + \tilde{\delta}(z - z_d)^2 \tag{A.9}$$

where

$$\tilde{\alpha} = z'(\zeta_d), \quad \tilde{\beta} = \frac{z''(\zeta_d)}{2z'(\zeta_d)}, \quad \tilde{\gamma} = \frac{z'''(\zeta_d)}{6z'(\zeta_d)^2} - \frac{z''(\zeta_d)^2}{4z'(\zeta_d)^3}$$

$$\tilde{\delta} = \frac{z''(\zeta_d)^3}{4z'(\zeta_d)^5} - \frac{z''(\zeta_d)z'''(\zeta_d)}{4z'(\zeta_d)^4} + \frac{z''''(\zeta_d)}{24z'(\zeta_d)^3}.$$

Note that cubing this, we get the expression

$$\frac{1}{(\zeta - \zeta_d)^3} = \frac{\omega_{-3}}{(z - z_d)^3} + \frac{\omega_{-2}}{(z - z_d)^2} + \frac{\omega_{-1}}{(z - z_d)} + \omega_0 \tag{A.10}$$

where

$$\omega_{-3} = z'(\zeta_d)^3, \quad \omega_{-2} = \frac{3}{2}z'(\zeta_d)z''(\zeta_d), \quad \omega_{-1} = \frac{1}{2}z'''(\zeta_d)$$

$$\omega_0 = \frac{z''''(\zeta_d)}{8z'(\zeta_d)} - \frac{z''(\zeta_d)z'''(\zeta_d)}{4z'(\zeta_d)^2} + \frac{z''(\zeta_d)^3}{8z'(\zeta_d)^3}.$$

Appendix B

Analysis of double gap conformal map.

We have seen that the conformal map (5.3) admits a simple pole at the points $\zeta = \pm i$. Therefore, we may write

$$\begin{aligned}
 z(\zeta) &= \frac{A(\zeta)}{B(\zeta)} \\
 &= \frac{A(i) + A'(i)(\zeta - i) + \dots}{B'(i)(\zeta - i) + B''(i)(\zeta - i)^2/2 + \dots} \\
 &= \frac{A(i)}{B'(i)} \frac{1}{(\zeta - i)} + \left[\frac{A'(i)}{B'(i)} - \frac{A'(i)B''(i)}{2B'(i)^2} \right] + \mathcal{O}(\zeta - i) + \dots
 \end{aligned} \tag{B.1}$$

where we have used the fact that $B(i) = 0$. From the Taylor expansion of $A(\zeta)$ and $B(\zeta)$ we see that

$$A(i) = P^2(-i, \rho) - P^2(i, \rho) = 2P^2(-i, \rho) \tag{B.2}$$

using property (5.6) of the special function $P(\zeta, \rho)$. We also have that

$$A'(i) = -P(i, \rho)P'(i, \rho) - P(-i, \rho)P'(-i, \rho). \tag{B.3}$$

The Taylor expansion of $B(\zeta)$ reveals that $B(i) = 0$ while

$$B'(i) = P(i, \rho)P'(i, \rho) - P(-i, \rho)P'(-i, \rho) \tag{B.4}$$

and

$$B''(i) = 2[P'^2(i, \rho) + P(i, \rho)P''(i, \rho) + P'^2(-i, \rho) + P(-i, \rho)P''(-i, \rho)]. \quad (\text{B.5})$$

Putting these together in expansion (B.1) gives the required constants a and b , given by equations (5.14) and (5.15)

Appendix C

Derivation of conformal map for a cylinder above a plane.

Let us assume that the Mobius map may be written in the form

$$z(\zeta) = A \left(\frac{\zeta - i}{\zeta + i} \right) \quad (\text{C.1})$$

Written in this way, the point $\zeta = -i$ is mapped to infinity in the z -plane. As a point on the unit disk is also mapped to the origin, this allows us to map the outer circle to a line that passes through the origin and extends towards infinity. We also ensure that A is chosen so the image of the interior of the unit disk lies only in the upper half complex plane.

We prescribe the radius, r , of the cylinder and its height above the plane, $\alpha > 0$, so that its center is at $z_0 = i\alpha$. In order to determine the map, we must find $A \in \mathbb{C}$ and $\rho \in \mathbb{R}$ in terms of r and α . We have that

$$r^2 = |z(\zeta) - d|^2 \quad (\text{C.2})$$

This means that

$$r^2 = \left[A \left(\frac{\zeta - i}{\zeta + i} \right) - d \right] \left[\overline{A} \left(\frac{\bar{\zeta} + i}{\bar{\zeta} - i} \right) - \bar{d} \right] \quad (\text{C.3})$$

Using the fact that $\bar{\zeta}\zeta = \rho^2$, this can be rearranged to give

$$\gamma(\rho^2 + 1) = |A|^2(\rho^2 + 1) - (\rho^2 - 1)d\bar{A} - (\rho^2 - 1)\bar{d}A \quad (\text{C.4})$$

where $\gamma = r^2 - |d|^2 = r^2 - \alpha^2 < 1$. Next, we may compare different orders of ζ . At the order of ζ we have

$$\gamma = d\bar{A} - \bar{d}A - |A|^2 = 2i\alpha A_x - |A|^2 \quad (\text{C.5})$$

while the order of $\bar{\zeta}$ gives

$$\gamma = -2i\alpha A_x - |A|^2 \quad (\text{C.6})$$

from which we can conclude that

$$A_x = 0 \quad A = iA_y \quad A_y^2 = -\gamma = d^2 - r^2 \quad (\text{C.7})$$

At the order of unity, we have

$$\gamma(\rho^2 + 1) = -\alpha A_y(\rho^2 - 1) \quad (\text{C.8})$$

which simplifies to

$$\frac{\rho^2 - 1}{\rho^2 + 1} = \frac{A_y}{\alpha} = \delta \quad (\text{C.9})$$

and hence

$$\rho = \sqrt{\frac{1 + \delta}{1 - \delta}} \quad (\text{C.10})$$

Note that for $\rho < 1$, we must take the negative square root for A_y and thus we are left with

$$A = -i\sqrt{\alpha^2 - r^2}, \quad \rho = \sqrt{\frac{1 + \delta}{1 - \delta}}, \quad \delta = -\frac{\sqrt{\alpha^2 - r^2}}{\alpha} \quad (\text{C.11})$$

These parameters give the required map.

References

- [1] D. G. Crowdy and Y. Or. Two-dimensional point singularity model of a low Reynolds number swimmer near a wall. *Phys. Rev. E.*, **81**:036313, (2010).
- [2] S. H. Smith. Stokes flow past slits and holes. *Int. J. Multi. Flow*, **13**(2):219–231, (1987).
- [3] H. J. Ko and J. T. Jeong. Two-dimensional slow stagnation flow near a slit. *J. Phys. Soc. Japan*, **63**(8):3288–3294, (1994).
- [4] G. Zilman, J. Novak, and Y. Benayahu. How do larvae attach to a solid in a laminar flow? *Marine Biology*, **154**:1–26, (2008).
- [5] M. U. Kim. Slow viscous flow around a vertical fence on a plane. *J. Phys. Soc. Jap*, **49**(4):23872391, (1980).
- [6] A. Shapere and F. Wilczek. Geometry of self-propulsion at low Reynolds numbers. *J. Fluid Mech.*, **189**:557–585, (1989).
- [7] J. E. Avron, O. Gat, and O. Kenneth. Optimal swimming at low Reynolds number. *Phys. Rev. Lett.*, **93**:186001, (2004).
- [8] A. Najafi and R. Golestanian. Simple swimmer at low Reynolds number: three linked spheres. *Phys. Rev. E*, **69**:062901, (2004).
- [9] D. G. Crowdy, S. Lee, O. Samson, A. E. Hosoi, and E. Lauga. A two dimensional model of low Reynolds number swimmers beneath a free surface. (*Submitted*), (2010).

- [10] H. A. Stone and A. D. T. Samuel. Propulsion of microorganisms by surface distortions. *Phys. Rev. Lett.*, **77**(19):41024104, (1996).
- [11] E. Lauga, W. R. DiLuzio, G. M. Whitesides, and H. A. Stone. Swimming in circles: motion of bacteria near solid boundaries. *Biophys. J.*, **90**:400–412, (2006).
- [12] J. Cosson, P. Huitorel, and C. Gagnon. How spermatozoa come to be confined to surfaces. *Cell Motility and the Cytoskeleton*, **54**:56–63, (2003).
- [13] A. Berke, L. Turner, H. Berg, and E. Lauga. Hydrodynamic attraction of swimming microorganisms by surfaces. *Phys. Rev. Lett.*, **101**:038102, (2008).
- [14] K. Drescher, K. C. Lptos, I. Tuval, T. Ishikawa, T. J. Pedley, and R. E. Goldstein. Dancing Volvox: hydrodynamic bound states of swimming algae. *Phys. Rev. Lett.*, **102**, (2009).
- [15] L. J. Fauci and A. McDonald. Sperm motility in the presence of boundaries. *Bull. Math. Biol.*, **57**:679–699, (1995).
- [16] D. F. Katz. Propulsion of microorganisms near solid boundaries. *J. Fluid Mech.*, **64**:33–49, 1975.
- [17] D. F. Katz, J. R. Blake, and S. L. Paverifontana. Movement of slender bodies near plane boundaries at low Reynolds number. *J. Fluid Mech.*, **72**:529–540, (1975).
- [18] A. J. Reynolds. The swimming of minute organisms. *J. Fluid Mech.*, **23**:241–260, (1965).
- [19] L. Rothschild. Non-random distribution of bull spermatozoa in a drop of sperm suspension. *Nature*, **198**:1221–1222, (1963).
- [20] H. Winet, G. S. Bernstein, and J. Head. Observations on the response of human spermatozoa to gravity, boundaries and fluid shear. *J. Reprod. Fert.*, **70**:511–523, (1984).
- [21] D. M. Wolley. Motility of spermatozoa at surfaces. *Reproduction*, **126**:259–270, (2003).

- [22] J. P. Hernandez-Ortiz, C. G. Stoltz, and M. D. Graham. Transport and collective dynamics in suspensions of confined swimming particles. *Phys. Rev. Lett.*, **95**:204501, (2005).
- [23] Y. Or and R. Murray. Dynamics and stability of a class of low Reynolds number swimmers near a wall. *Phys Rev E.*, **79**:045302, (2009).
- [24] J. W. Swan and J. F. Brady. Simulation of hydrodynamically interacting particles near a no-slip boundary. *Phys. Fluids*, **19**:113306, (2007).
- [25] S. Zhang, Y. Or, and R. M. Murray. Experimental demonstration of the dynamics and stability of a low Reynolds number swimmer near a plane wall, (2010).
- [26] T. Ishikawa, M. P. Simmonds, and T. J. Pedley. Hydrodynamic interaction of two swimming model micro-organisms. *J. Fluid Mech.*, **568**:119–160, (2006).
- [27] J. R. Blake. Self propulsion due to oscillations on the surface of a cylinder at low Reynolds number. *Bull. Austral. Math. Soc.*, **3**:255–264, (1971).
- [28] M. J. Lighthill. On the squirming motion of nearly spherical deformable bodies through liquids at very small Reynolds numbers. *Comm. Pure Appl. Math*, **5**:109–118, (1952).
- [29] J. R. Blake. A spherical envelope approach to ciliary propulsion. *J. Fluid Mech.*, **46**:199–208, (1971).
- [30] K. M. Ehlers, A. D. T. Samuel, H. C. Berg, and R. Montgomery. Do cyanobacteria swim using travelling surface waves? *Proc. Natl. Acad. Sci*, **93**(16):8340–8343, (1996).
- [31] J. R. Blake and A. T. Chwang. Fundamental singularities of viscous flow. part 1: the image systems in the vicinity of a stationary no-slip boundary. *J. Eng. Math.*, **8**:23–29, (1974).
- [32] N. I. Muskhelishvili. *Some basic problems of the mathematic theory of elasticity*. P. Noordhoff, (1953).

- [33] S. Richardson. Two-dimensional bubbles in slow viscous flows. *J. Fluid Mech.*, **33**:476–493, (1968).
- [34] C. Pozrikidis. *Boundary Integral And Singularity Methods For Linearized Viscous Flow*. Cambridge University Press, Cambridge, (1992).
- [35] S. Weinbaum. On the singular points in the laminar two-dimensional near wake flow field. *J. Fluid Mech.*, **33**:39–63, (1968).
- [36] Z. Dagan, S. Weinbaum, and R. Pfeffer. An infinite series solution for the creeping motion through an orifice of finite length. *J. Fluid Mech.*, **115**:505–523, (1982).
- [37] A. Erdelyi. *Tables of Integral Transforms*. New York, NY, McGraw-Hill, (1954).
- [38] M. E. O’Neill. On the separation of a slow linear shear flow from a cylindrical ridge or trough in a plane. *Z. Angew. Math. Phys.*, **28**:439–448, (1977).
- [39] S. Wakiya. Application of bipolar coordinates to the two dimensional creeping motion of a liquid. III: separation in stokes flows. *J. Phys. Soc. Japan*, **45**(5):1756–1763, (1978).
- [40] W. R. Dean and P. E. Montagnon. On the steady motion of a viscous fluid in a corner. *Proc. Camb. Phil. Soc.*, **45**:389–394, (1949).
- [41] A. M. J. Davis. Shear flow disturbance due to a hole in the plane. *Phys. Fluids*, **A3**:478–480, (1991).
- [42] Z. Y. Yan, A. Acrivos, and S. Weinbaum. Fluid skimming and particle entrainment into a small circular side pore. *J. Fluid Mech.*, **229**:1–27, (1991).
- [43] R. A. Sampson. On Stokes current function. *Phil. Trans. Roy. Soc. Lond. A*, **182**:449–518, (1891).
- [44] L. K. Antanovskii. Formation of a pointed drop in Taylor’s four-roller mill. *J. Fluid Mech.*, **327**:325–341, (1996).

- [45] D. G. Crowdy and O. Samson. Hydrodynamic bound states of a low-Reynolds-number swimmer near a gap in a wall. (*Submitted*), (2010).
- [46] J. Guckenheimer and P. Holmes. *Nonlinear oscillations, dynamical systems and bifurcations of vector fields*. Springer-Verlag, New York, (1993).
- [47] P. Coulet, J. M. Gambaudo, and C. Tresser. Une nouvelle bifurcation de codimension-2: le collage de cycles. *C. R. Acad. Sci. Paris*, **299**:253–256, (1984).
- [48] H. Hasimoto. On the flow of a viscous fluid past a thin screen at small Reynolds numbers. *J. Phys. Soc. Japan*, **13**(6):633–639, (1958).
- [49] K. Stewartson. On mass flux through a torus in Stokes flow. *J. Appl. Math. Phys.*, **34**:567–574, (1983).
- [50] R. Roscoe. The flow of viscous fluids round plane obstacles. *Phil. Mag*, **40**:338–351, (1949).
- [51] G. B. Jeffery. The rotation of two circular cylinders in a viscous fluid. *Proc. Roy. Soc. A*, **101**:169–174, (1922).
- [52] R. A. Frazer. On the motion of circular cylinders in a viscous fluid. *Phil. Trans. R. Soc. Lond. A*, **225**:93–130, (1926).
- [53] D. J. Jeffrey and Y. Onishi. The slow motion of a cylinder next to a plane wall. *Q. J. Mech. Appl. Math*, **34**:129–137, (1981).
- [54] A. M. J. Davis and M. E. O’Neill. Separation in a slow linear shear flow past a cylinder and a plane. *J. Fluid Mech*, **81**:551–564, (1977).
- [55] M. D. Finn and S. M. Cox. Stokes flow in a mixer with changing geometry. *J. Eng. Math.*, **41**:75–99, (2001).
- [56] H. Zhao and H. H. Bau. On the effect of induced electro-osmosis on a cylindrical particle next to a surface. *Langmuir*, **23**(7):4053–4063, (2007).
- [57] Z. Nehari. *Conformal mapping*. New York, NY, McGraw-Hill, (1952).

- [58] D. G. Crowdy and J. S. Marshall. The motion of a point vortex through gaps in walls. *J. Fluid Mech.*, **551**:31–48, (2006).
- [59] G. Valiron. *Cours d'Analyse Mathematique*. Masson et Cie., Paris, France, 2nd edn. edition, (1947).
- [60] D. G. Crowdy and J. S. Marshall. The motion of a point vortex around multiple circular islands. *Phys. Fluids*, **17**:056602, (2005).
- [61] E. T. Whittaker and G. N. Watson. *A Course Of Modern Analysis*. Cambridge University Press, Cambridge, (1996).
- [62] A. A. Andronov, E. A. Leontovich, I. I. Gordon, and A. G. Maier. *Theory of bifurcations of dynamical systems on a plane*. Israel Prog. Sci. Transl., (1971).
- [63] J. Higdon. Stokes flow in arbitrary two-dimensional domains: shear flow over ridges and cavities. *J. Fluid Mech.*, **159**:195–226, (1985).
- [64] H. K. Moffatt. Viscous and resistive eddies near a sharp corner. *J. Fluid Mech.*, **18**(1):1–18, (1964).
- [65] T. Weis-Fogh. Quick estimates of flight fitness in hovering animals, including novel mechanisms for lift production. *J. Exp. Biol.*, **59**:169–230, (1973).
- [66] J. T. Jeong and M. U. Kim. Slow viscous flow around an inclined fence on a plane. *J. Phys. Soc. Japan*, **52**(7):2356–2363, (1983).
- [67] D. Acheson. *Elementary fluid dynamics*. Oxford University Press, (1990).
- [68] M. J. Lighthill. On the Weis-Fogh mechanism of lift generation. *J. Fluid. Mech.*, **60**:1–17, (1973).
- [69] D. G. Crowdy. The spreading phase in Lighthill's model of the Weis-Fogh lift mechanism. *J. Fluid Mech.*, **641**:195–204, (2009).
- [70] D. G. Crowdy and J. S. Marshall. Conformal mappings between canonical multiply connected domains. *Comp. Meth. Funct. Theory*, **6**(1):59–76, (2006).

-
- [71] J. Abshagen, G. Pfister, and T. Mullin. Gluing bifurcations in a dynamically complicated extended flow. *Phys. Rev. Lett.*, **87**(22):224501, (2001).
- [72] A. M. Rucklidge. Chaos in models of double convection. *J. Fluid Mech.*, **237**:209–229, (1992).
- [73] T. Peacock and T. Mullin. Homoclinic bifurcations in a liquid crystal flow. *J. Fluid Mech.*, **432**:369–386, (2001).